ISTITUTO ITALIANO
DI TECNOLOGIA

Università degli Studi di Genova

Doctorate in Sciences and Technologies of Chemistry and Materials

Curriculum: Nanochemistry

PhD Cycle: XXXVII

Design, Synthesis, and Characterization of 2D halide Perovskite Lateral heterojunctions

by

Mehrdad Faraji

Supervisors:

Dr. Roman Krahne (IIT)

and

Prof. Davide Comoretto (Unige)

Table of contents

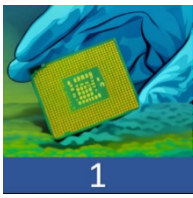

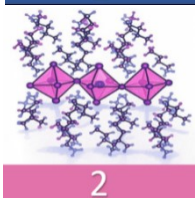

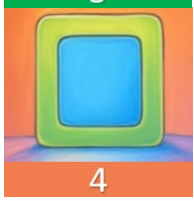

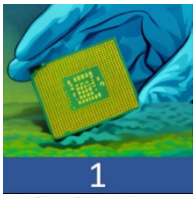

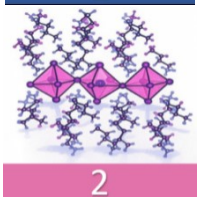

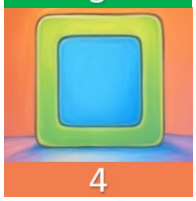

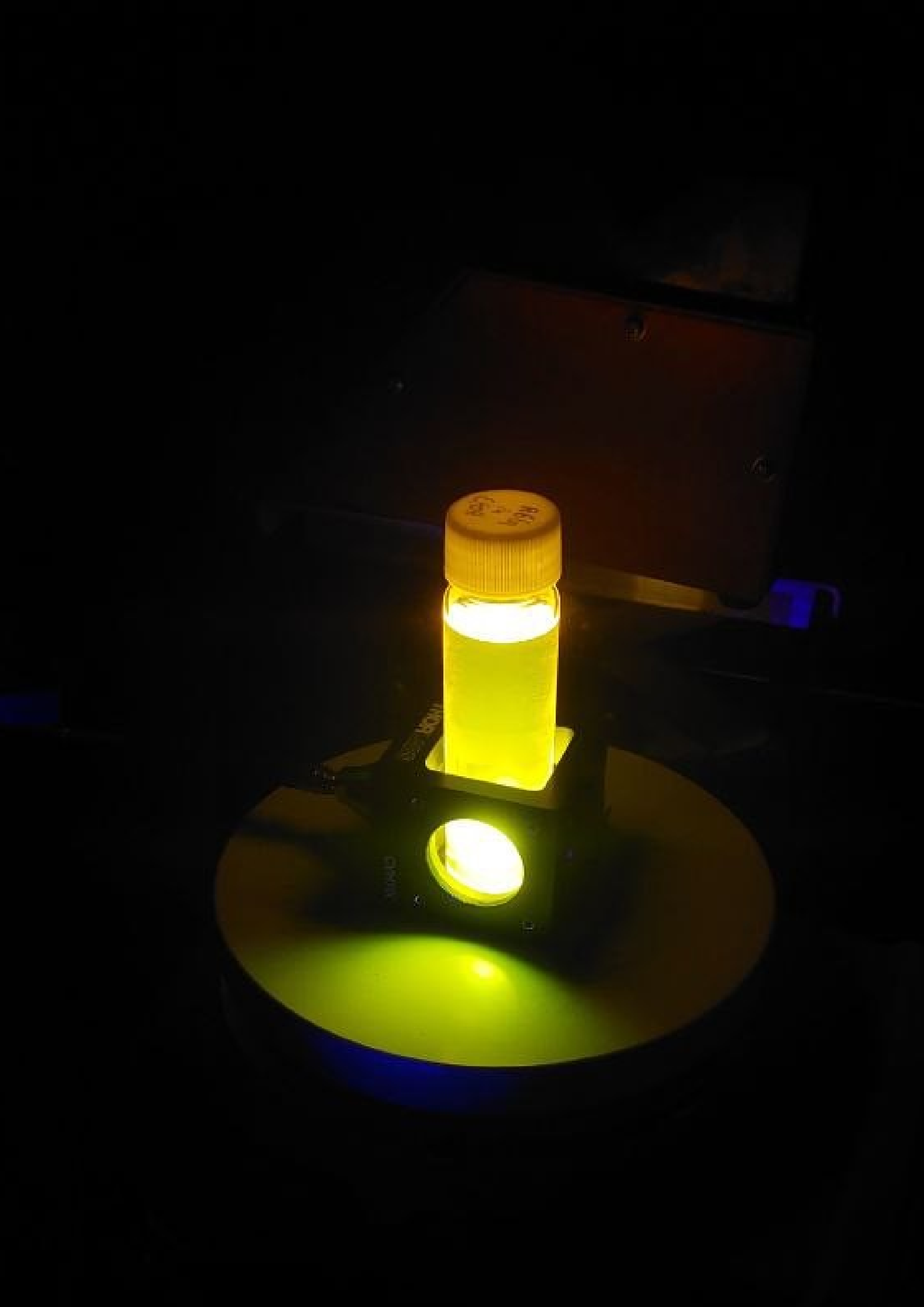

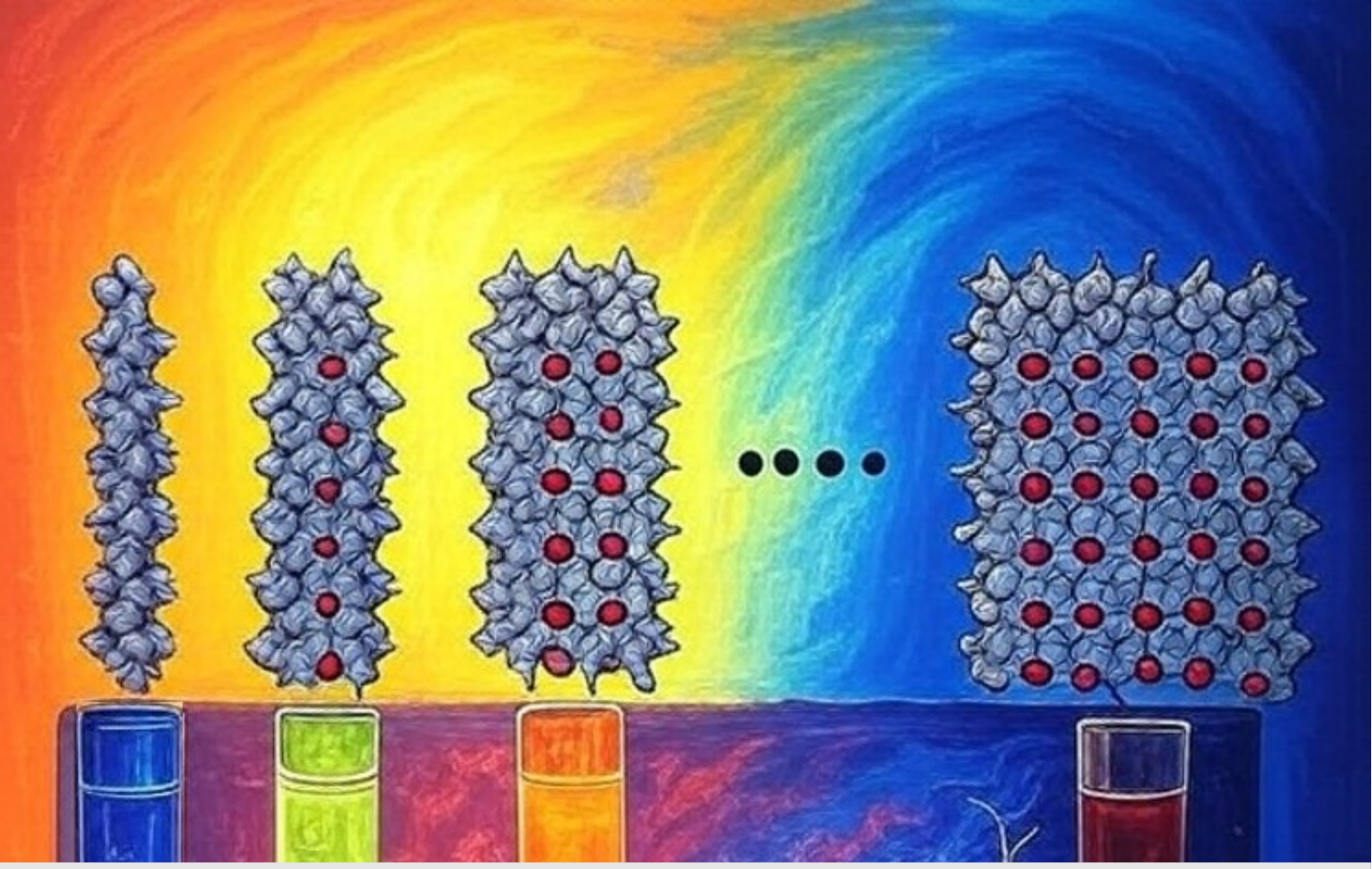

Chapter I:

The Physics of Semiconductors and Quantum Confinement

Chapter I: The Physics of Semiconductors and quantum confinement

Semiconductors are significant materials in electronic industries and our modern life, and they have electrical conductivity between insulators (like plastic) and conductors (metals). This unique conductivity makes them potential applications in electronics and optoelectronics devices such as circuit boards, LEDs, and solar cells. Semiconductor devices are essential to industries and societies. Hence, significant investigation has been implemented to produce efficient semiconductors with unique properties and find innovative ways to fulfill them. The chemical solution-based approach is an interesting way to implement and produce semiconductors. The method enables their characterizations to be modified because they are cost-effective, scalable, have low energy consumption, and are versatile in materials. Moreover, the solution-based process can be easily implemented in liquid form, facilitating room temperature and simple device fabrication. This thesis mainly focuses on 2D materials, such as 2D layered perovskites and metal organic chalcogenides, and the fabrication and characterization of lateral heterostructures using chemical solution-based methods. The 2D layered perovskites and metal organic chalcogenides have higher stability, excellent tunable properties, material and environmental versatility, and lower ion migration. In this thesis, 2D lateral heterostructure perovskites are produced based on chemical anion exchange and sequential growth approaches on large scales, along with metal organic chalcogenides lateral heterostructures. Heterostructures are made using the sequential growth approach for different spacers, metals, and halides regarding 2D perovskites and various metals and chalcogenides regarding metal organic chalcogenides. This chapter briefly introduces semiconductors and nanostructured materials, explaining their history, physics, and properties, and summarizing other main chapters.

1.1 Conductivity, optical absorption, and emission properties of semiconductors

To be electrically conductive, the electrons should be capable of moving in a material freely [1,2]. It means electrons can contribute to the current and are not permanently bound to atoms. Consequently, they should move through empty orbitals. In semiconductors, a bandgap separates the filled orbitals in the VB from the empty orbitals in the CB. At thermodynamic equilibrium, all electrons are confined to the VB since there are no accessible states in the VB and no electrons in the CB. Insufficient energy prevents the electrons from crossing the bandgap and getting into the CB. By absorbing a photon of light, electrons can get to the CB, as seen in **Figure 1.1a**. Consequently, the photon requires more energy than the bandgap of the semiconductor. The process resulting in an excited electron in the CB, which can freely

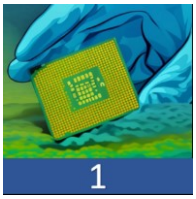

move through the empty orbitals, is called photon excitation. The so-called hole is the lack of an occupied orbital with an electron (empty orbital) in the VB, including the presented excited electron.

An analogy is an air bubble moving through a liquid; the missing electron, or hole, behaves like a positively charged particle moving through the crystal in the opposite direction of an electron. Like an excited electron freely moving in the CB, a hole moves freely in the VB. It is important to note that the promotion of an electron from the VB and the simultaneous creation of a hole can only occur if, at the moment of their formation, the electron and hole have equal magnitudes of momentum but opposite signs. This stems from the fundamental law of momentum conservation: because a massless photon carries negligible momentum compared to a massive particle, the electron-hole pair created must have nearly zero total momentum, the sum of the individual momenta of the electron and hole. The so-called “direct bandgap” semiconductor arises from this direct transition. In other words, the electron in the band edge of VB and CB should have the same momentum [2]. For example, in indirect bandgap silicon, electron excitation requires a combined interaction involving a photon and a lattice vibration (phonon). Since the two-body photon-electron interaction in direct bandgap semiconductors is much more likely than this three-body interaction, electron excitation through light absorption is much less effective in indirect bandgap materials. For example, the solar light absorption in direct bandgap semiconductors like GaAs or lead halide perovskites is several orders of magnitude greater than in indirect bandgap silicon, despite silicon’s smaller bandgap that enables absorption over a broader range of the solar spectrum [2]. This thesis primarily focuses on direct bandgap organic-inorganic 2D lead halide perovskites and metal-organic chalcogenides.

As previously mentioned, in a direct semiconductor, the excitation of an electron can occur via the absorption of any energy (even X-ray or high-energy electrons) that is larger than the bandgap. As shown in **Figure 1.1b**, highly excited electrons in the CB can relax, or release excess energy as heat, and settle into states close to the band edge. The excited electron can subsequently recombine with the hole to reverse the excitation process and release the gained energy as a photon. Due to the photon emission, the related energy transitioning from the CB edge to the VB edge corresponds to the bandgap. The process is called radiative recombination and is a primary mechanism of photoluminescence (PL) in semiconductors. It is important to note that this process occurs mainly in direct bandgap semiconductors, as exciton recombination requires a momentum change facilitated by photon interaction, an event much less probable in indirect bandgap materials [2]. The so-called "radiative recombination decay rate" is the rate at which electrons are recombined with the holes and is strongly material-dependent. Moreover, it should be noted that not all excited electrons are combined with holes via the emission of a photon. **Figure 1.1d** shows that the traps usually result in fewer combined molecular orbitals. Thus, they form states

around their atomic orbitals and, therefore, in the bandgap. Since trap states lie just above the VB or below the CB, holes and electrons migrate to these defect states and recombine there, typically releasing energy as heat. Consequently, trap states lead to non-radiative recombination. The radiative recombination can be quenched by defects, which can harm optoelectronic devices that are required to extract the holes and electrons (solar cells) or that need either radiative recombination (lasers, LEDs, etc.). The *surface trap state* is a trap state arising from undercoordinated atoms at a material's surface. These states primarily introduce energy levels within the bandgap [3] as lattice defects. This flaw is less harmful because there are fewer surface atoms in bulk materials. However, their high surface-to-volume ratio makes them more noticeable in nanomaterials.

As mentioned, the radiative recombination produces light emission, requiring the material to be as trap-free as possible. To determine the radiative recombination and, therefore, to calculate a performance indicator for the efficiency of emission, the rates of both non-radiative recombination and radiative recombination can be compared. The rate of radiative recombination of excited electrons can be described by **equation 1.1** [4].

$$(1.4)\ \text{quantum efficiency}\ (\eta) = \frac{\gamma\text{rad}}{\gamma\text{rad} + \gamma\text{nrad}}$$

Where γrad and γrad are radiation and non-radiative recombination decay rates, respectively, the ratio between radiative and non-radiative recombination describes the *photoluminescence quantum yield* (PLQY) or quantum efficiency (η) of a material [4]. PLQY is not an inherent property of a material; rather, it depends on the fabrication method and the material's quality.

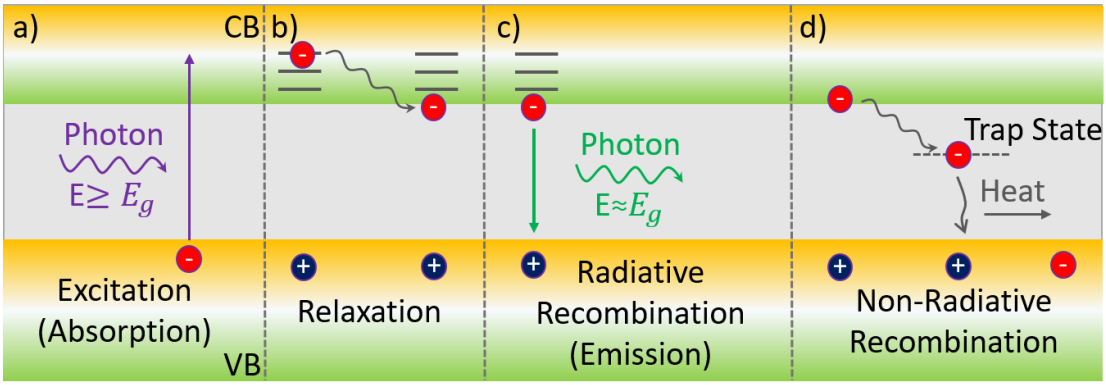

Figure 1.1. Semiconductor excitation and interaction with photons. a) absorption of photons, b) relaxation of electrons, c) radiative recombination due to photon emission, and d) non-radiative recombination.

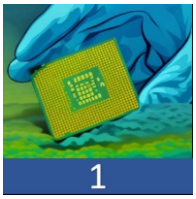

1.2 Quantum confinement in nanostructured materials

As discussed, nanostructured semiconductors have unique optical properties compared to their bulk counterpart. To observe the alterations in the optical properties of a semiconductor going from bulk to lower dimensions is by considering a nanomaterial as giant molecules that contain approximately 0.1 – 100 kiloatoms. Single-molecule characteristics, hybrid bulk materials with quasi-continuous CBs and VBS, and DOS discrete states at the band edge have all been demonstrated by nanostructured materials. The combination of linear atomic orbitals systematically explains this hybrid behavior. Numerous atomic orbitals, like the s and p orbitals in semiconductors, combine as the system scales from a few atoms (a molecule) to a few hundred atoms (nanoscale), creating quasi-continuous bands made up of numerous molecular orbitals, as shown in **Figure 1.2**. However, these small molecules still possess discrete energy levels for their most bonding and antibonding states, with the HOMO and LUMO remaining the most isolated states. When the size of the nanomaterials increases (approximately 2-10 nm, or 0.1 – 100 kilo atoms), not only does the energy separation between the bands decrease, but also the energy separation between individual molecular orbitals within each band decreases. Yet, as shown in **Figure 1.2**, the states closer to the band edges are discrete for the intermediate case. The energy gap between bands is smallest in bulk solids. As is commonly shown in **Figure 1.2**, all states within a band combine to form a continuum.

On the other hand, the development from a bulk crystal to nanomaterials and ultimately to a cluster of only a few atoms can be seen in **Figure 1.2** (left to right). As the nanomaterial's size decreases, the band edges' energy levels become more discrete, leading to an increased bandgap. The so-called “quantum confinement effect” is coupled to the bandgap's widening, which leads to the two most dominant alterations in semiconductor nanomaterials.

Looking at the electron-hole pairs is one of the ways to look at quantum confinement. An excited electron in the CB stays attached to its matching hole in the VB due to Coulomb interactions. This bound electron-hole pair that occupies a specific spatial region is called an exciton. **Equation 1.2** illustrates how the exciton Bohr radius (a_o) defines its size.

$$(1.5)\text{Exciton Bohr radius (a0)} = \frac{\hbar^2 \varepsilon}{e^2}\left(\frac{1}{m_e^*} + \frac{1}{m_h^*}\right)$$

The effective masses of the electron and hole determine the exciton Bohr radius, which makes it highly material-dependent. For instance, the reported exciton Bohr radii for PbTe, CdSe, and InAs are 104, 5, and 29 nm, respectively. The exciton can travel freely through a semiconductor much larger than a_0. As the semiconductor size approaches a_0, the exciton may become spatially confined and lose mobility. The exciton loses mobility and becomes spatially confined when the semiconductor size approaches

a_0. As a result, the exciton undergoes confinement and energy increase when the nanostructured material is smaller than a_0. Accordingly, the exciton acts as a particle inside a box, gaining energy as the "box" gets smaller. For example, the bandgap of nanomaterials with different shapes can be described by **Equations 1.6–1.8**:
For spherical or quantum dots, the Brus equation:

$$(1.6)\ E_{QD} = E_{gap} + \frac{h^2}{8r^2}\left(\frac{1}{m_e^*} + \frac{1}{m_h^*}\right) - \frac{1.8e^2}{4\pi\varepsilon R}$$

For cylindrical or quantum rods:

$$(1.7)\ E_{QR} = E_{gap} + \frac{h^2}{8r^2}\left(\frac{1}{m_e^*} + \frac{1}{m_h^*}\right)$$

For nanosheets or quantum wells:

$$(1.8)\ E_{QR} = E_{gap} + \frac{h^2\pi^2}{2L^2}\left(\frac{1}{m_e^*} + \frac{1}{m_h^*}\right)$$

The so-called quantum dot examples all describe the effects of quantum confinement on nanomaterials in which 3D structures are confined. Typically, nanomaterials of various shapes and sizes can be fabricated. Thus, each of their dimensions can be of multiple sizes. The different shapes can generally be grouped by their dimensionality. For example, 3D or bulk materials have no quantum confinement in their dimensions and represent properties close to their bulk counterpart. 2D nanomaterials represent quantum confinement in only one dimension and can be described as quantum wells or nanosheets. One-dimensional nanomaterials are elongated nanomaterials with two dimensions showing quantum confinement, including quantum wires or nanowires. Finally, zero-dimensional nanomaterials, including clusters or quantum dots, have all 3D structures representing quantum confinement and generally show the most substantial effects.

Figure 1.3 represents that any alteration in the dimensionality would strongly affect the DOS of 3D, 2D, 1D, and 0D semiconductor nanostructures [5]. However, in 2D quantum well structures, excitons are free to move in two dimensions but confined in the remaining dimensions, in contrast to bulk semiconductors, where the DOS varies with the square root of energy (~$E^{½}$). Because of this, 2D quantum wells show a step-function DOS, which results in an effectively larger bandgap by making energies available in discrete steps with a constant value (~E0). Excitons can only travel along the wire in 1D structures, also known as quantum wires, and the DOS has an inverse square-root dependence on energy (~$E^{-½}$). The DOS is completely discrete, rising in quantized steps and falling precipitously in between. Lastly, the DOS only occurs at particular energy levels in 0D structures, or quantum dots, as shown in the pattern in **Figure 1.3**.

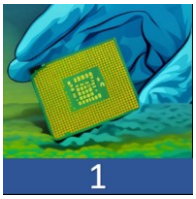

Significantly, nanomaterials can have different shapes and sizes and cannot always be described by the DOS of 0D, 1D, 2D, and 3D models. For example, CsPbBr3 nanoplatelets with an exciton Bohr radius of 7 nm could be fabricated with dimensions of 2 by 5 by 20 nm and are a quasi-2.5D model. Thus, these nanoplatelets represent one dimension of extreme quantum confinement with a significant increase in bandgap and strongly confined exciton with very discrete states, 1D with only weak quantum confinement, and the bandgap only showing a modest growth and weakly confined exciton. Another shows bulk properties without any quantum confinement.

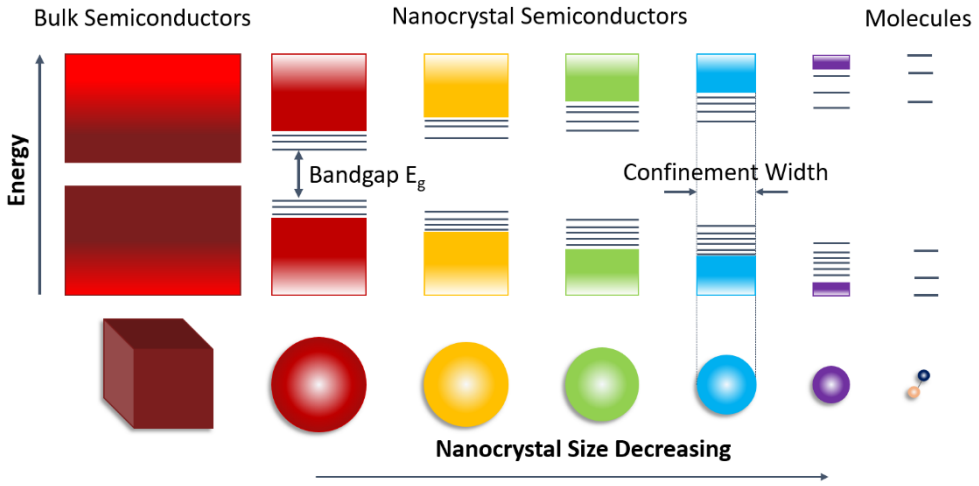

Figure 1.2. Size-dependent quantum confinement effect. Size-dependent bandgap and discrete states formation near the band edge of nanocrystals, as well as comparisons of bulk (3D), nanocrystals, and molecules.

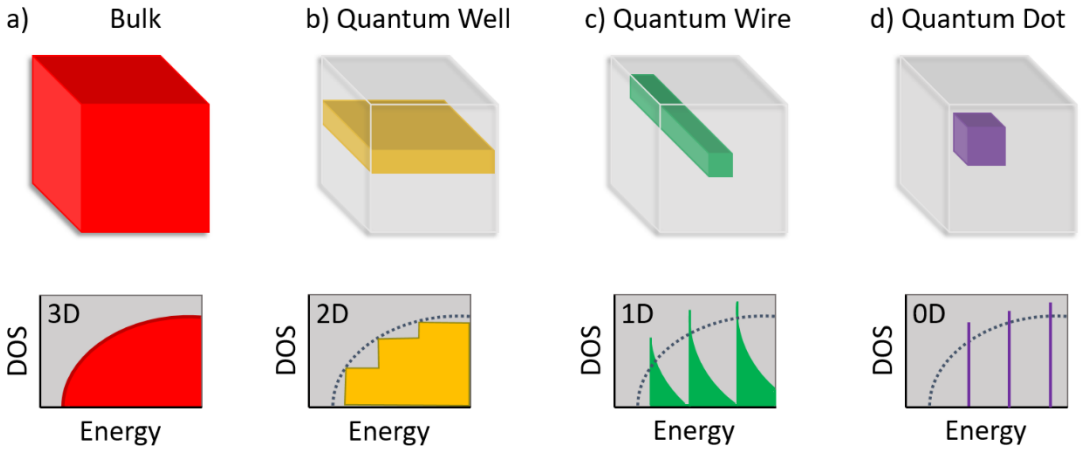

Figure 1.3. Influence of size-dependent confinement on the DOS. a) continues DOS of bulk (3D), b) step-like DOS of quantum wells (2D), c) saw-tooth dependent DOS of quantum wires (1D), and the availability of discrete states of quantum dots (0D).

1.3 Quantum confinement in 3D semiconductors

Regarding 3D or bulk semiconductors, when the size of the crystal is significant with respect to the distance between the ions. Thus, an infinite lattice is employed. In the real space, the wavefunctions are completely delocalized, and the band structure possesses a continuous dispersion of energy as a function of momentum. If the semiconductor is decreased to the nanoscale in one or more dimensions, the assumption of an infinite lattice expansion no longer holds [6]. Quantum confinement effect can be observed if the carrier motion in a semiconductor is restricted in one dimension to the order of the mean free path and the de Broglie wavelength (λ_B), if this number is smaller. As shown in Figure 1.3, the DOS for electrons in 0D, 1D, 2D, and 3D semiconductor nanostructures indicates that reducing the dimensionality of a semiconductor from 3D to 2D results in the localization of electron and hole wave functions. Consequently, a step-like DOS distribution and a larger band gap appear.

1.4 Quantum confinement in 2D semiconductors

When exciton motion is limited along one dimension in a 2D semiconductor, especially if that dimension is smaller than the exciton's mean free path and de Broglie wavelength, quantum confinement takes place. The temperature, the electron's effective mass (m*), and the hole in the crystal all affect the de Broglie wavelength (λ_B)[7]:

$$(1.9)\ \lambda_B = \frac{h}{p} = \frac{h}{\sqrt{3m^* kT}} = \frac{1.22\ nm}{\sqrt{\frac{E_{kin}}{[eV]}}}$$

The 2D semiconductors, particularly the layered 2D perovskites and metal organic chalcogenides studied in this thesis, can be fabricated with large lateral dimensions of several hundred nanometers in two directions. In contrast, their thickness in the third dimension is limited to just a few nanometers. Thus, quantum confinement should be considered when mathematically describing the nanocrystals' properties. In such 2D semiconductors, the exciton can extend in 2D homogenously but is limited in 3D by the surrounding materials, such as the crystals' ligand or solvent.

To explain this mathematically, the dielectric mismatch of the crystal and its impact on excitonic properties must be considered by extending the quantum mechanics of the hydrogen atom to include a spatially dependent dielectric constant (ε). Spatial factors also affect the electron affinity (X), the energy needed to extract an electron from a material and place it in a vacuum.

1.5 Infinitive quantum well and two-step infinite quantum well

In a first approximation, a real crystal can be modeled as an infinite-depth quantum well (QW), in which the electron and hole wave functions are spatially confined. By solving Schrödinger's equation and considering $V(x) = 0$ and the boundary condition (B.C) of **equation 1.10**, the eigenenergies E_n can be calculated in **equation 1.12** [8].

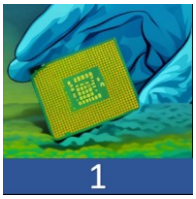

$$(1.10)\ \Psi(0) = \Psi(L) = 0$$

$$(1.11)\ H\Psi_n(x) = \left(-\frac{\hbar^2}{2m}\frac{\partial^2}{\partial x^2} + V(x)\right)\Psi_n(x) = E_n\Psi_n(x)$$

$$(1.12)\ E_n = \frac{\pi^2\hbar^2}{2mL^2}n^2$$

Here, *m* is the particle's mass, *L* is the length of the quantum well, and *n* is an integer. In 2D layered perovskites, the confinement imposed by the spacer ligands is strong but finite, so this model tends to overestimate the eigenenergies (E_n) of a real crystal.

Building on the infinite quantum well model, it can be assumed that the nanocrystals are surrounded not by vacuum but by spacer ligands. This leads to a two-step potential model, as illustrated in **Figure 1.7**. The B.C.s of 1.13 and 1.14 are determined by **equation 1.15** [9].

$$(1.13)\ \Psi_I(x_0) = \Psi_{II}(x_0)$$

$$(1.14)\ \frac{1}{m^*_{QW}}\frac{\partial^2}{\partial x}\Psi_I(x_0) = \frac{1}{m^*_B}\frac{\partial^2}{\partial x}\Psi_{II}(x_0)$$

$$(1.15)\ V(x) = \begin{cases} V_{CB(VB)} \quad for\ 0 \le x \le L_{QW} \\ 0 \quad for\ -L_B \le x \le 0\ or\ L_{QW} \le x \le L_{QW} + L_B \\ \infty\ else \end{cases}$$

In B.Cs 1.13 and 1.14, x_0 is the spacer ligand and crystal boundary, $x_0 = L_{QW}$, and $x_0 = 0$. In a real system, the assumption that crystals are isolated with an infinite potential barrier outside the spacer ligands is inaccurate, resulting in an overestimation of E_n for strongly confined crystals.

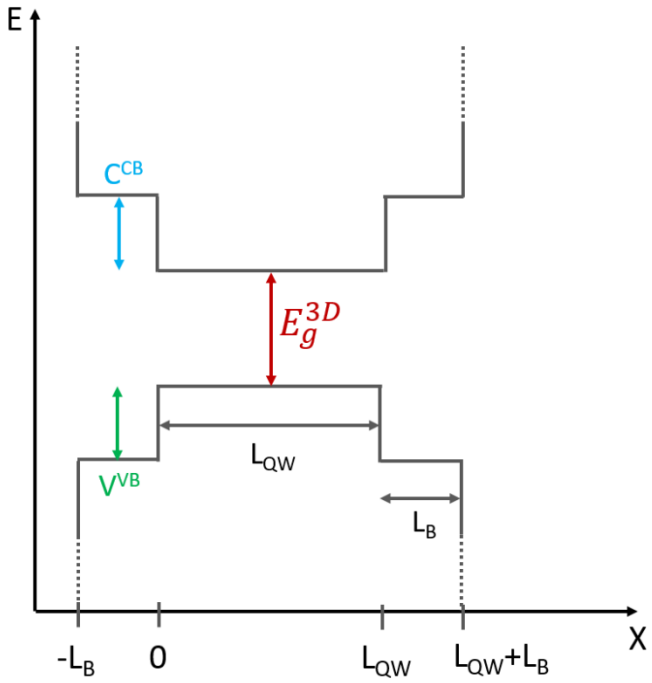

Figure 1.4. Schematic representation of an infinitive QW in real space, with L_B the length of the surrounding ligand and L_{QW} the thickness of the nanocrystal.

1.6 Outline of this thesis

2D layered halide perovskites, which are derived from the 3D perovskites by slicing the 3D configuration into the 2D layers. The layer units are stacked via van der Waals (vdW) interactions to form bulk crystals. Due to the presence of an insulating dielectric molecular space-charge layer, 2D layered perovskites can be considered a class of natural quantum wells, with the degree of quantum confinement and related optical properties tailored by varying the thickness of the inorganic layer. 2D layered perovskites, unlike their 3D counterparts, behave as semiconductors with free carriers and strong confinement, and exhibit tightly bound excitons with binding energies up to several hundred meV. Consequently, this results in intense PL with high color purity and strong exciton-photon coupling at RT. Additionally, they exhibit greater chemical stability than their 3D counterparts and have been introduced as a new class of solution-processable materials with outstanding optical properties. The chemical diversity and quantum-confinement effects of 2D layered perovskites enable strong PL tunability from the UV to the NIR spectral regions, which are not available in other 2D materials. Finally, the solution-based processibality, providing low-cost, flexible functionality across a wide range of semiconductor technologies, particularly for forming in-plane heterojunctions.

This thesis primarily focuses on the design, fabrication, and characterization of lateral heterostructures within the 2D layered metal halide perovskites. Lateral heterostructures were realized in 2D layered halide perovskites by integrating two or

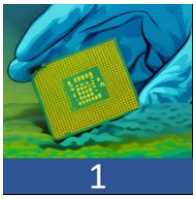

three halide species in the octahedra layer. In particular, the initially fabricated pristine 2D layered halide perovskites, produced via a fast crystallization method, exhibit large, irregular morphologies, and, using the techniques described in this thesis, have been converted into perfectly shaped lateral heterostructures.

In the second chapter of this thesis, 2D layered perovskites are introduced, with a strong focus on their unique structural properties, and the fabrication and significance of their lateral heterostructures are discussed.

In Chapter III, a versatile solution-based method is applied to fabricate a lateral heterostructure between bromide- and iodide-based 2D layered halide perovskites, yielding discrete halide phases with distinct light-emission and band-gap properties by replacing bromide with iodide and vice versa. The morphology of the phase boundary and the composition of the exchange phase are dependent on the exchange method, and are associated with the preferred localization of the halides at the axial or equatorial octahedral sites, which either led to solvation and recrystallization of the octahedral lattice for bromide to iodide, or ion diffusion within the lattice for iodide to bromide. The result of this work was published in Advanced Materials journal [10]. The content of this chapter is derived from that manuscript.

In Chapter IV, a flexible, solution-based one-pot synthesis strategy is employed to produce a wide variety of 2D-layered halide perovskite lateral heterojunctions by varying halide and metal cation compositions. Exploiting the sequential crystallization of various 2D halide perovskites and alternating the composition and injection events of solutions containing the dissolved materials enables the design of diverse heterojunction structures, including multiple heterostructures. As a result, high-quality crystalline heterostructures with multicolor emission and optical coupling among the various heterojunction regions were yielded. It is expected that such an interesting design will stimulate the development of novel optoelectronic devices with a significant electronic band gap.

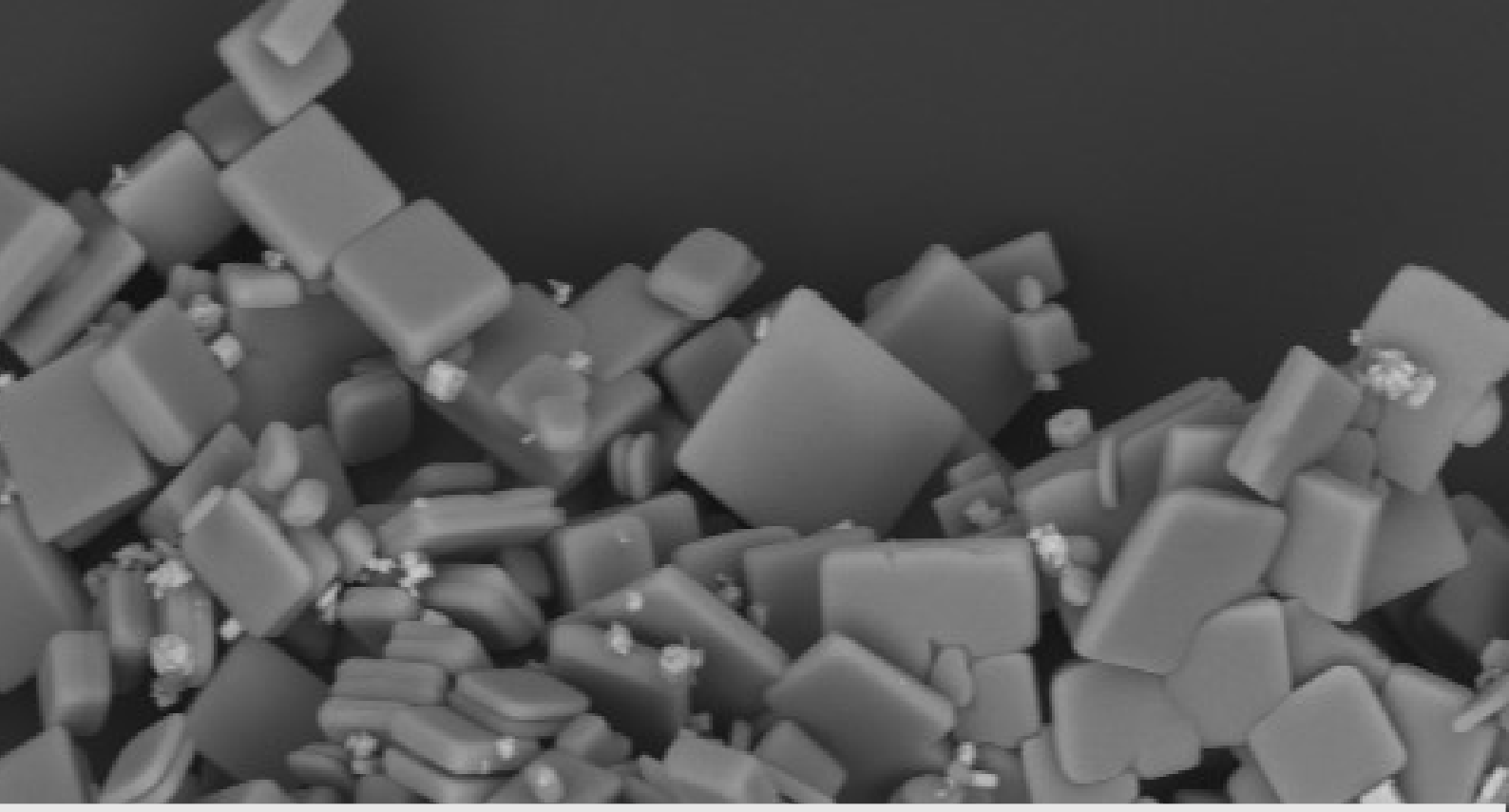

Chapter II:

2D layered halide perovskites and lateral heterostructures

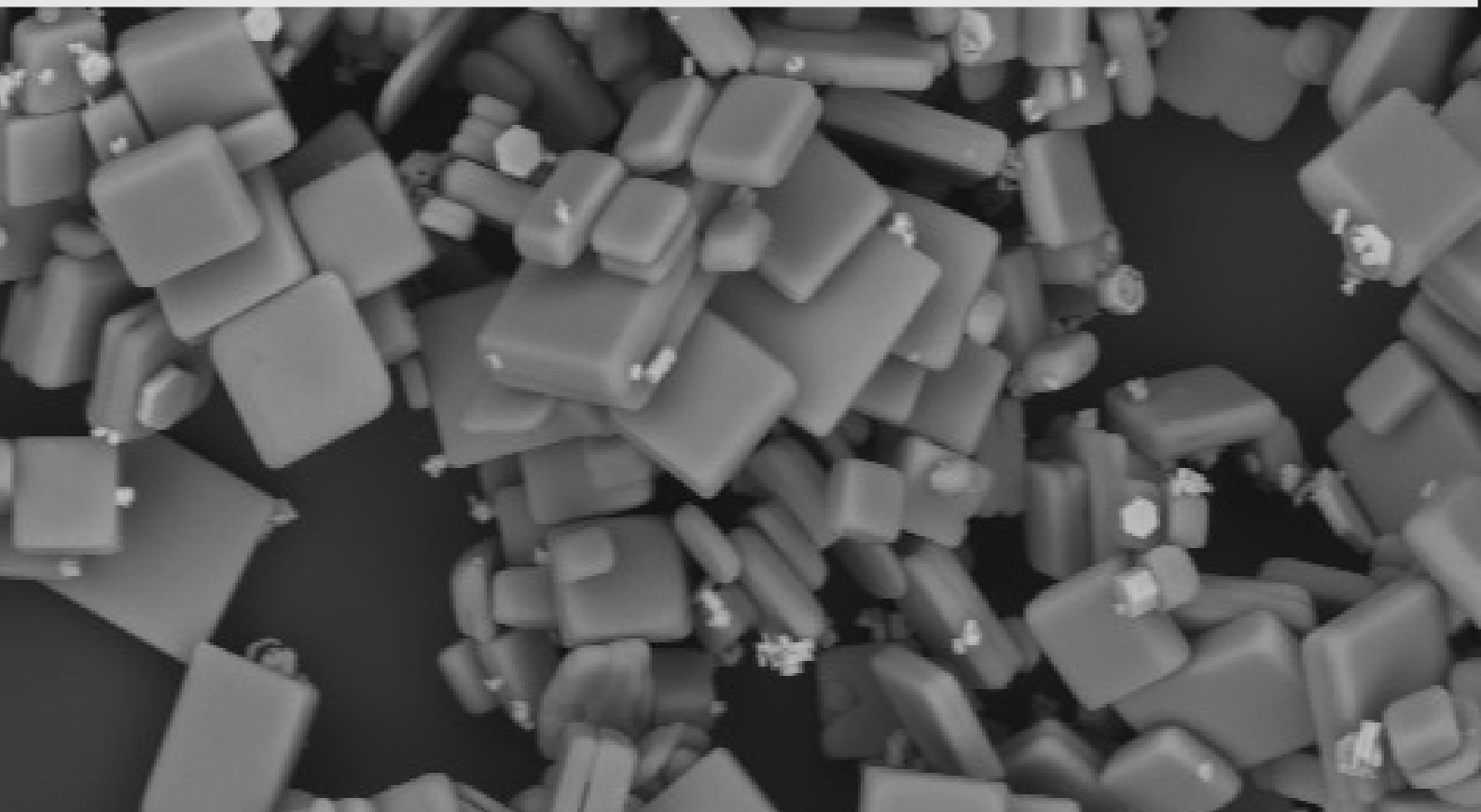

Chapter II: 2D layered halide perovskites and lateral heterostructures

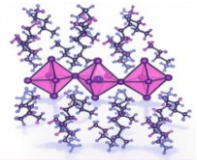

2

Abstract: *Halide perovskites are among the most promising semiconductors of the 21st century, rapidly advancing due to their remarkable properties and wide potential applications in electronics and optoelectronics. Their tunable optical properties have attracted considerable interest from researchers in a wide range of scientific and technological domains, and they can be synthesized as brightly luminescent crystals. The development of halide perovskite crystals and our understanding of their special qualities and uses have advanced significantly in recent years. 3D halide perovskites are a large class of materials with the general formula ABX_3, in which X stands for the six halide ions, B is a cation at the center of each octahedron, and A is an inorganic ion or small organic molecule occupying the interstitial sites between the octahedra. It is necessary to attain charge balance within the crystal. Thus, the B ion must be bivalent if the X and A are monovalent. The structural dimensionality of halide perovskites can be easily tunable from 3D to 2D using a long-chain organic molecule cation as a spacer in their structure, forming a 2D layered structure. The number of octahedral layers between the long-chain organic layers can control the exciton binding energy and wavelength of these 2D layered perovskites $L_2A_{n-1}B_nX_{3n+1}$ (n=1, 2, … ∞). Most of this thesis focuses on fabricating in-plane heterostructures using 2D layered perovskites, mainly in PEA_2PbBr_4-PEA_2PbI_4 heterostructures. Since these 2D layered perovskites confine the electronic carriers in the in-plane direction (because the spacer organic molecule is typically insulating), they are highly advantageous candidates to make an in-plane heterostructure. This chapter introduces 3D and 2D halide perovskites and their unique characteristics.*

2.1 Introduction

2D layered perovskites were first reported in the late 1980s [11]. With the rise of 3D perovskites in recent decades, they have been rediscovered and extensively investigated for electronic and optoelectronic applications [12,13]. 3D perovskites, generally described by the formula ABX_3, are subject to relatively strict structural constraints: beyond the requirement of charge balance, the size of each ion is limited by tolerance rules for ionic selection [14]. In contrast, 2D layered perovskites belong to extended perovskite families that also include lower-dimensional analogues. Like their 3D counterparts, they are built from corner-sharing BX_6 octahedra. Importantly, the connectivity of this octahedral network dictates the dimensionality of the resulting perovskite. In 2D layered perovskites, large A-site cations separate the corner-sharing octahedra into distinct 2D sheets. Moreover, the A site cation has no known size limitations [15,16]. It should have a functional group stabilizing it by binding ionically to the

octahedral site. The organic molecule cation can be selected from most molecular structures containing an amine group and other possible functional groups. Hence, the characteristics of the organic molecules can be, for instance, luminescent, chromophoric, conductive, polymerizable, and polarizable [15,16]. This thesis focuses on 2D layered perovskites with the general formula A_2BX_4, where the A-site is occupied by an alkylammonium or aliphatic organic molecule containing an ammonium functional group of varying chain lengths, as illustrated in **Figure 2.1**. The B site is a bivalent metal like Pb and Sn, and the X site is a halide, Cl, Br, or I. The $[MX_6]^{4-}$ octahedral composed 2D sheets in which the A-site ion's ammonium functional group stabilizes. This thesis investigated some organic molecules, but a phenethylammonium (PEA) *organic* spacer was prepared for the primary investigations, especially for lateral heterostructure formation. This thesis aims to investigate the formation of lateral heterostructure in 2D layered perovskites with PEA spacer via anion exchange process and a sequential growth approach.

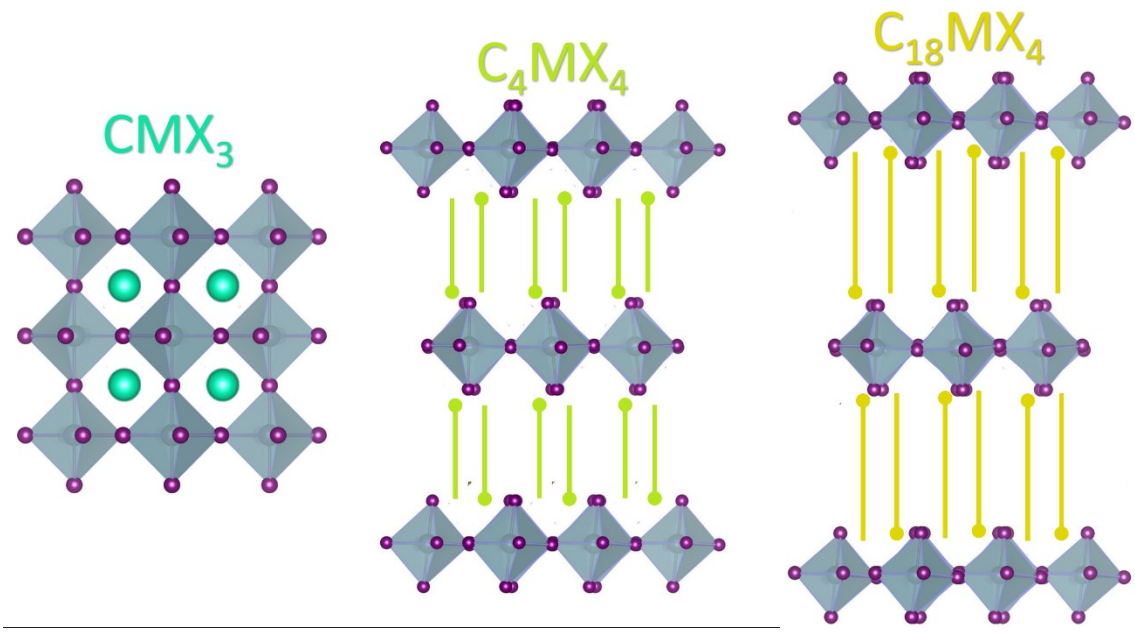

Figure 2.1. Schematic representation of 3D and 2D layered hybrid perovskite structures of CMX3 and CnMX4. Unlike 3D perovskites, 2D layered perovskites include an MX6 octahedra structure (blue). The MX6 octahedra form 2D layers in which the A-site cation's ammonium functional group stabilizes. Here, from left to right, the green shows a very short chain amine spacer like methylammonium, for the other 2D layered perovskites, the spacer could be an alkylammonium functional group and a lipophilic moiety of different length (green vertical lines for butylammonium and orange octadecylammonium).

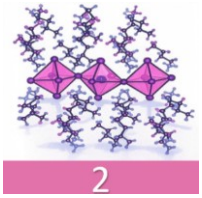

2.2 2D layered perovskites

2D layered perovskites follow the general formula $L_2A_{n-1}B_nX_{3n+1}$ (n = 1, 2, 3, …), where L is a large aromatic or aliphatic alkylammonium spacer cation, typically n-butylammonium (n-BA) or phenylethylammonium (PEA). A is a monovalent organic or inorganic cation, such as formamidinium (FA), methylammonium (MA), or cesium (Cs). M represents a divalent metal cation, such as Pb, Sn, or Ge, while **X** is a halide anion. The parameter n denotes the number of $[MX_6]^{4-}$ octahedral layers forming each QW. The crystal structures of 2D and 3D perovskites are shown in **Figure 2.1**. As previously discussed, 2D layered perovskites consist of *n* layers of inorganic $[MX_6]^{4-}$ octahedra sandwiched between two layers of large organic spacer cations. This arrangement forms natural multiple QW structures, where the organic layers act as potential "barriers" and the inorganic layers serve as potential "wells" [17]. In contrast, 3D perovskites feature each $[MX_6]^{4-}$ octahedron connected to six neighbors through halogen atoms, creating a continuous network in which small organic cations occupy the voids of the framework. [18]. **Figure 2.2** illustrates that the generated excitons can be confined within the inorganic layers. Combined with the low dielectric screening of the surrounding organic spacer cations, this confinement leads to significantly larger exciton binding energies (E_g) than their 3D counterparts. The quantum confinement effect can be reduced by increasing the well size and thickness (n), which can be precisely tuned through careful control of the precursor stoichiometry. Moreover, the van der Waals (VDW) interactions between layers and the organic spacers' hydrophobic nature endow 2D layered perovskites with superior air stability.

Nevertheless, the unique crystal structure of 2D layered perovskites also has some unfavorable properties. Accordingly, the insulating organic spacer cation can decrease carrier mobility, bring radiative recombination losses and charge accumulation, and, thereby, diminish device performance. The cations in 2D counterparts are partially restricted by intermolecular interactions and VDW, especially in the case of PEA^+, in contrast to the MA^+ cations in 3D perovskites, which are comparatively free to rotate within the lattice. Here, the positively charged amine group layers align with the negatively charged neighboring halide layers, giving rise to a polar interface between the inorganic and organic layers [19].

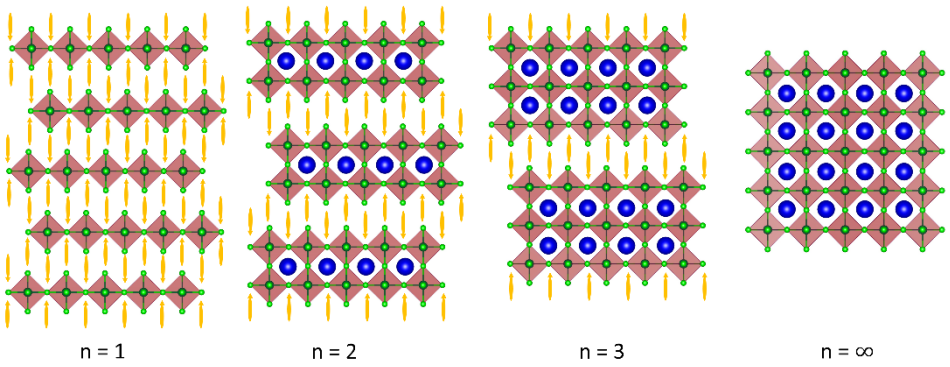

Figure 2.2. Representation of 2D layered perovskites with increasing layers, n, from 1 to 3, and ∞ for the 3D or bulk perovskite structure. The spacer molecule is shown in orange, the halogen in green, the small organic molecule in blue, and the inorganic octahedral framework in warm rose.

2.3 Organic spacer cation

One of the unique properties and advantages of 2D layered perovskites is that their facile structure can be tuned by the molecular design of the spacer cation, like ammonium dications, alkyl chain length, and insertion of π-conjugated segment, which in turn greatly influence the optoelectronic properties. These materials can be considered natural QWs, where the bandgap increases as the perovskite layer thins due to enhanced quantum confinement along the stacking direction. Additionally, similar to their role in 3D perovskites, the A-site spacer cations can modulate the metal–halide bond length (M–X) and metal–halide–metal (M–X–M) bond angles. This then alters the orbital overlap between metal and halide ions, leading to slight changes in the bandgap, though not as much as changes in layer thickness. Spacer cation is crucial to modify the properties of 2D perovskites in several ways. First, the exciton binding energy of 2D layered perovskites is changed by changing their dielectric constant. A higher dielectric constant reduces the dielectric mismatch between the inorganic and organic layers, lowering the exciton binding energy [20]. 2) It serves as a hydrophobic "raincoat" layer, improving the structural stability of 2D layered perovskites [21]. 3) It modifies the M–X–M bond angles and introduces octahedral distortions, which impact the bandgap. Electronic structure is directly affected by deviations from the ideal octahedron. Although much work has been done to add spacer cations to 2D layered perovskites, there are still no clear structural design guidelines for selecting the most effective spacer cations. A summary of organic molecular spacer cations used in 2D layered perovskites is provided in **Table 2.1**.

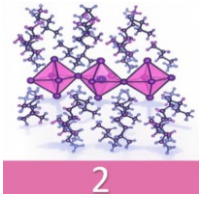

Table 2.1. List of some spacer cations incorporated in the formation of 2D layered perovskites.

Spacers	2D perovskites	E_g (eV)	References
BA	BA2PbBr4	7.2	[22]
PEA	PEA2PbBr4	6.2	[22]
BzA	BzA2PbBr4	6.6	[23]
UDA	(UDA)2PbBr4	9.0	[24]
N-MDDA	(N-MDDA)2PbBr4	9.1	[24]
1-MDA	(1-MDA)2PbBr4	9.0	[25]
N-MDA	(N-MDA)2PbBr4	9.1	[25]
TEA	(TEA)2PbI4 (TEA)2PbBr4	6.4	[26]
TMA	(TMA)2PbI4 (TMA)2PbBr4	6.0	[26]
F4Tm	(F4Tm)2PbI4	1.17	[27]
TeFBTT	(TeFBTT)2PbI4	3	[28]
TP	(TP)2PbI4	4.6	[29]
Pyr	(Pyr)2PbI4	3.7	[29]
FBTT	(FBTT)2PbBr4	2.36	[30]
FBTP	(FBTP)2PbBr4	2.61	[30]
PyBA	(PyBA)2PbI4	3.1	[31]
PP	(PP)2PbBr4	-	[32]
PPm	(PPm)2PbBr4	-	[32]
PPT	(PPT)2PbI4	-	[33]
PPT’	(PPT’)2PbI4	-	[33]
TT	(TT)2SnI4,	2.49	[34]
DTT	(DTT)2SnI4	2.39	[34]
BTm	(BTm)2SnI4	1.92	[35]
STm	(STm)2SnI4	1.9	[36]
2T	(2T)2PbI4	3.65	[37]
4T	(4T)2PbI4	2.58	[37]
4Tm	(4Tm)2PbI4	2.59	[37]
4TCNm	(4TCNm)2PbI4	2.19	[37]
4TeI	(4Te)2PbI4	1.11	[38]
4TdmI	(4Tdm)2PbI4	1.11	[38]

Butylamine (BA), Phenethylamine (PEA), Benzylamine (BzA), Undecylamine (UDA), N-methyldodecylammonium (N-MDDA), 1-methyldecylamine (1-MDA), *N*-methyldecylamine (N-MDA), 2-thiophenemethylammonium (TEA), 2-

thiopheneethylammonium (TMA), (3‴,4′-dimethyl-[2,2′:5′,2″:5″,2‴-quaterthiophen]-5-yl)ethan-1-amine (F4Tm), 2-(5-(7-(3-ethylthiophen-2-yl)-5,6 difluorobenzo[c] [1,2,5] thiadiazol-4-yl)thiophen-2-yl)ethan-1-aminium iodide (TeFBTT), 2-(triphenylene-2-yloxy) butan-1-aminium iodide (TP), 4-(pyren-1-yl)butan-1-aminium iodide (Pyr), 2-(5-(7-(9,9-dimethyl-9H-fluoren-2-yl)benzo[c][1,2,5]thiadiazol-4-yl)thiophen-2-yl)ethan-1-ammonium bromide (FBTT), 2-(4-(7-(9,9-dimethyl-9H-fluoren-2-yl)benzo[c] [1,2,5] thiadiazol-4-yl)phenyl)ethan-1-ammonium bromide (FBTP), 4-(pyren-1-yl)butan-1-amine (PyBA), [1,1″-biphenyl]−4,4″-dimethylammonium bromide (PP), 2,2″-dimethyl-[1,1″- biphenyl]−4,4″-dimethylammonium bromide (PPm), 2-(5-(3′,5′- dimethyl-[1,1′-biphenyl]−4-yl)thiophen-2-yl)ethyl-1-ammonium iodide (PPT), 2-(5-(2,2′-dimethyl-[1,1′-biphenyl]−4-yl)thiophen-2-yl)ethyl-1- ammonium iodide (PPT′), tert-Butyl-(2-(4'-methyl-5'-(5-(3-methylthiophen-2-yl)thieno[3,2-b]thiophen-2-yl)[2,2'-bithiophen]-5-yl)ethyl) amine (TT), tert-Butyl-(2-(4'-methyl-5'-(6-(3-methylthiophen-2-yl)dithieno[3,2-b:2',3'N O O d]thiophen-2-yl)-[2,2'-bithiophen]-5-yl)ethyl) amine (DTT), 7-(thiophen-2-yl)benzothiadiazol-4-yl)-[2,2′-bithiophen]-5-yl)ethylamine (BTm), 2-(40-methyl-5′-(5-(3-methylthiophen-2-yl)selenophen-2-yl)-[2,20-bithiophen]-5-yl)-ethan-1-aminium (STm), 2-([2,2'-Bithiophen]-5-yl) ethan-1-aminium iodide (2T), 2-([2,2':5',2'':5'',2'''-Quaterthiophen]-5-yl)ethan-1-aminium iodide (4T), 2-(3''',4'-Dimethyl-[2,2':5',2'':5'',2'''-quaterthiophen]-5-yl) ethan-1-aminium iodide (4Tm), 2-(3'',4''-Dicyano-3''',4'-dimethyl-[2,2':5',2'':5'',2'''-quaterthiophen]-5-yl)ethan-1 aminium iodide (4TCNm), 2-(3''',4'-diethyl-[2,2':5',2'':5'',2'''-quaterthiophen]-5-yl)ethan-1-aminium iodide (4TeI), and 2-(3',3''',4',4'''-tetramethyl-[2,2':5',2'':5'',2'''-quaterthiophen]-5-yl)ethan-1-aminium iodide (4Tdml).

2.4 2D layered perovskite band structure and band alignment

Generally, reducing the dimensionality of 3D perovskite structures increases bandgap energy, E_g [16,39]. The lowest-energy electronic transition follows the trend for a family of structures containing the same octahedral metal halide, $E_g^{3D} < E_g^{2D} < E_g^{1D} < E_{HOMO-LUMO}^{0D}$. As the dimensionality of the BX_6 octahedral network decreases, the bandwidths of both the CB and VB shrink, creating a larger energy separation between the VBM and the CBM. In 2D layered perovskites, this reduced band dispersion is particularly pronounced in the direction perpendicular to the organic–inorganic interface. **Figure 2.3a** presents a schematic illustrating the change in bandwidth as the dimensionality decreases from 3D to 2D [40]. The total DOS indicates that 2D layered crystals contain several localized bands, in contrast to the broader bands observed in their 3D counterparts. Furthermore, the bandwidth narrows even more due to octahedral tilting [40]. As a result, the M–X–M bridging angle between adjacent octahedra deviates from the ideal 180°. As schematically illustrated in **Figure 2.3b**, this difference is called the tilt angle. Theoretical studies of 2D layered perovskites have primarily focused on exciton coupling, using effective mass parameters within abrupt dielectric confinement schemes and carrier dispersion models [17,41] or have provided broader descriptions of their electronic band structure through density functional theory (DFT)

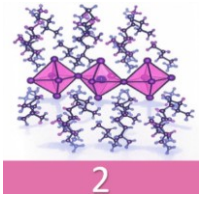

[40,42–44]. For the 2D layered perovskites needing an extensive system for DFT simulation, their calculation might encounter limitations regarding computational resources [45]. A successful option for DFT simulation has been proposed earlier by Mitzo and coworkers [15] based on a QW concept. **Figure 2.4** shows that the inorganic layers in 2D perovskites can be interpreted as QWs for electrons and holes, separated by organic ligands that act as barriers, forming a type-I heterostructure.

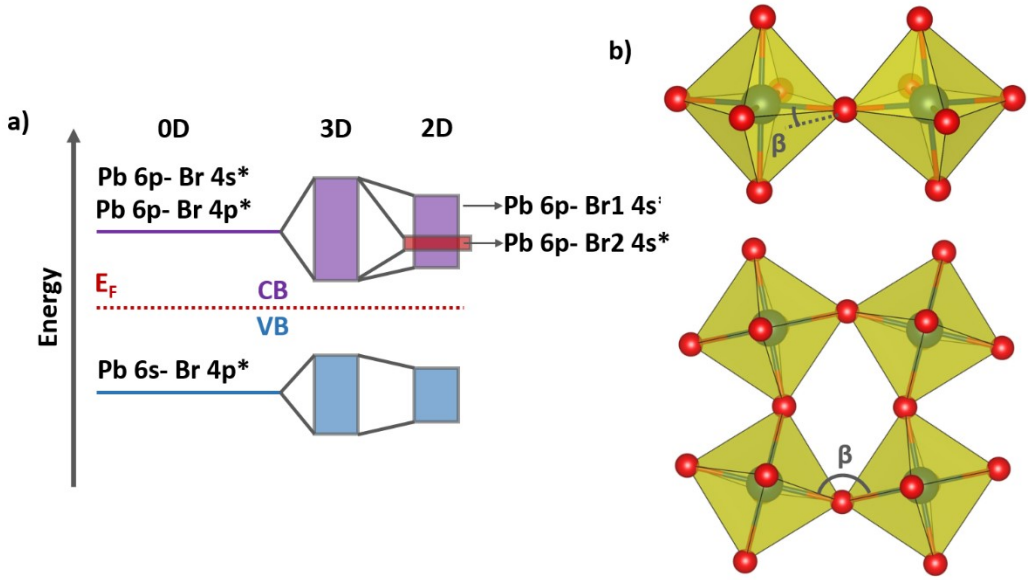

Figure 2.3. Dimensionality reduction and octahedral tilting distortions result in a narrower bandwidth in 2D layered perovskite structures compared to their 3D counterparts. a) VBM and CBM elemental contributions in 3D versus 2D perovskite, according to Umebayashi et al. [40]. b) The M–X–M tilt angle reflects the degree of tilt in the MX_6 octahedra.

2.5 Exciton and exciton binding energy

As mentioned in the first chapter, the exciton binding energy can be increased 4-fold from 3D to 2D due to spatial confinement [46]. Moreover, the mismatch of dielectric constants in QW and barrier leads to dielectric confinement and further improvement of the exciton binding energies [46]. For example, in the L_2PbI_4 structure, 360 meV and 320 meV binding energies have been reported for the C4 and C10 spacer ligands, respectively [16]. Owing to these combined dielectric and quantum confinement effects, determining the exact nature of the exciton is challenging. Nevertheless, it has been suggested that the exciton retains a Wannier-type character with a relatively small radius [16].

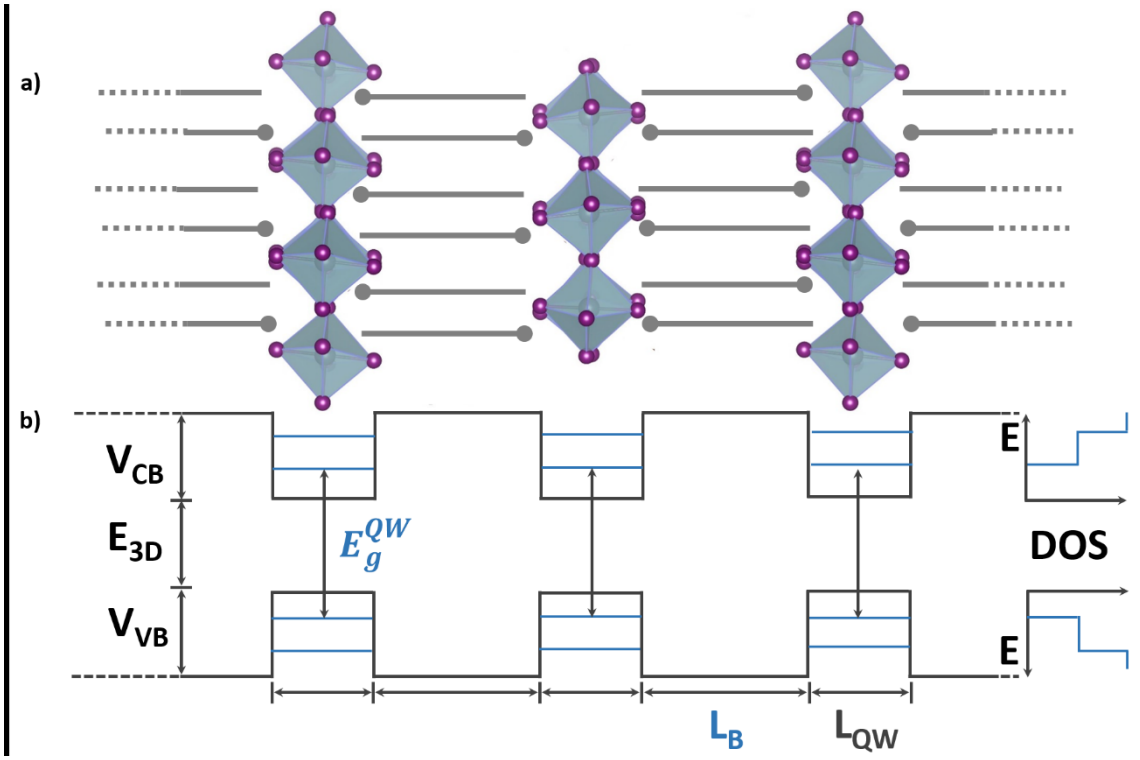

Figure 2.4. 2D layered perovskite as a quantum well heterojunction. a) Schematic illustration of 2D layered hybrid perovskites, consisting of inorganic MX_6 octahedra arranged in 2D layers, separated by organic ligand layers. b) In the QW framework, the inorganic 2D perovskite layers act as QWs for electron and hole confinement, while the organic ligands serve as insulating barriers. This configuration represents a type-I heterojunction in the energy-level scheme, as Mitzo et al. [15] reported.

2.6 Exciton confinement in 2D layered perovskites

*3*D metal halide perovskites appeared as an ionic structure of negatively charged $[MX_6]^{4-}$ octahedral and positively charged size-limited organic or inorganic spacers. Delamination along one of the crystallographic axes is necessary to transition from a 3D to a 2D layered configuration. This results in octahedral lattice extension in the other two axes and stabilization with additional large organic cation spacers. This delamination can happen along the <111>, <100>, or <110> direction of the ideal cubic lattice of the 3D structure, and the selection of the spacer can be a mono-cation. The prominent case discussion in most concerns is the combination of monoammonium cations and a <100> terminated inorganic lattice due to their superior excitonic behavior and relatively more straightforward crystal growth. In the Ruddesden Popper (RP) 2D layered perovskites with the formula of $L_2A_{n-1}B_nX_{3n+1}$, where n is the number of inorganic layers that are intercalated between spacer structural direction, generating multi-QW structures. Herein, this section is based on the popular terminology of 3D, quasi-2D, and 2D halide perovskites to denote their layered 3D ($n = \infty$), layered $n \geq 2$, and $n = 1$

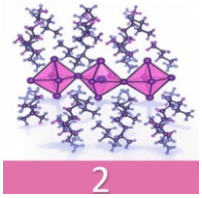

configurations, respectively. Unlike in the bulk or 3D perovskites, where organic is limited to set grain boundaries, in 2D layered structures that allow for the incorporation of complex organic spacers in the related lattice, which subsequently inspires the semiconducting or insulating organics with a tunable energy gap [47] and molecular engineering of intermolecular interactions [48,49]. These sophisticated spaces can define the exciton dynamic [37] and dielectric environment [50] of 2D layered perovskites. The exciton dynamics in 2D layered RP perovskites are represented in **Figure 2.5**.

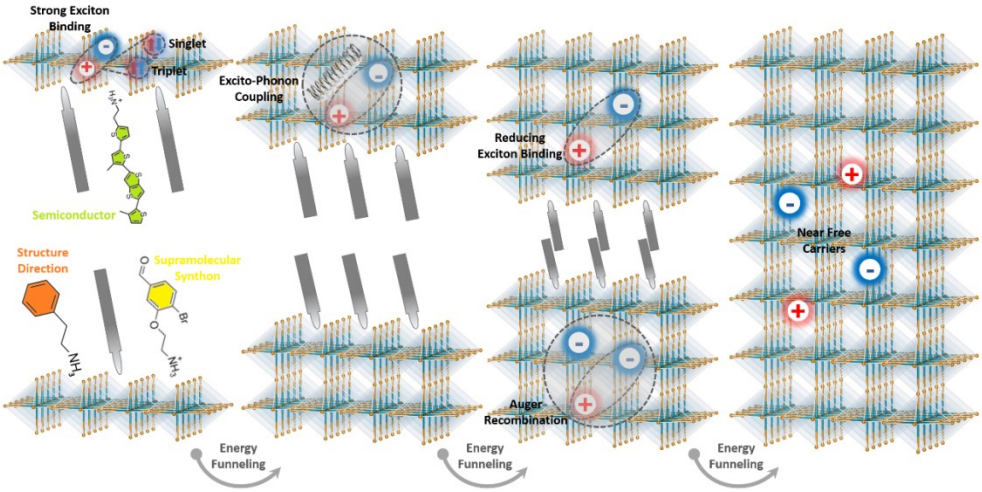

Figure 2.5. Exciton dynamics in 2D layered RP perovskites starting from n = 1 to 3, and 3D perovskite (left to right). The schematic represents energy funneling direction from wide bandgap n = 1 RP to narrow bandgap 3D perovskites.

2.7 Excitons in 2D layered perovskites

An exciton is a bound state of excited electrons and holes, attracted together by coulombic forces, and the exciton binding energy is the minimum energy needed to ionize the mentioned bound electron-hole pair from the lowest energy eigenstate into the uncorrelated free charge carriers [51]. The reduction in dimensionality from 3D (bulk) to 2D layered halide perovskites enhances quantum confinement and reduces dielectric screening (**Figure 2.6a**) [51], which in turn strengthens Coulombic interactions and leads to tightly bound exciton pairs [52]. As shown in **Figure 2.6b**, classical Wannier and Frenkel models can describe excitons in halide perovskites [46]. Frenkel excitons usually have high binding energies between 0.5 and 1 eV, while Wannier excitons have generally lower binding energies of about 10–30 meV [53]. An exciton dissociates into free charge carriers with longer diffusion lengths when its binding energy is equal to the thermal energy at room temperature, or about 26 meV. As shown in **Figure 2.6d**, experimental data confirm that exciton binding energy can be extracted from the exciton Rydberg series by analyzing optical properties such as absorption, photoluminescence (PL), and photoluminescence excitation (PLE) spectra [54]. This model, which is based on Wannier-type excitons with binding energies ranging from 2 to 60 meV [55], is commonly used to

describe excitons in 3D perovskites. On the other hand, hybrid Frenkel-Wannier excitons are present in quasi-2D and 2D layered perovskites. Strong quantum confinement is induced by the insulating organic spacers in multi-quantum well structures, resulting in tightly bound Wannier excitons inside the inorganic framework. On the other hand, Frenkel-like excitons are more likely to form in the vicinity of organic spacers [53,56]. Therefore, in low-dimensional perovskites, tightly bound excitons with binding energies reaching several hundred meV are the dominant excited-state species. However, the incorporation of semiconductor organic spacers [57], particularly those with strong electron-accepting properties, can reduce exciton binding energy by enhancing electrostatic screening [50]. This inclusion may also alter the energy gap of the organic lattice relative to the inorganic counterpart, potentially leading to exciton separation at the interface or spontaneous confinement within the organic domain [37]. Such semiconductor spacers offer a unique tunability to organic–inorganic hybrid structures, highlighting their potential in light-emitting applications.

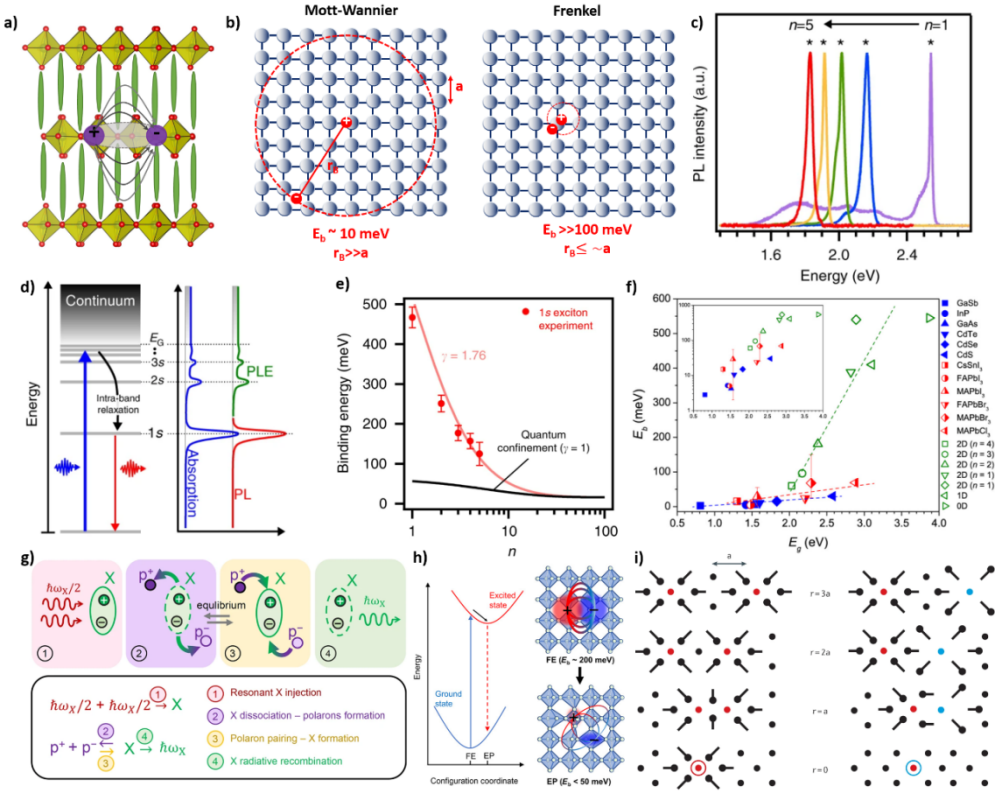

Figure 2.6. a) Schematic representation of a 2D layered perovskite structure as a natural QW system and electrons and holes bound in excitons [51]. b) Illustration of Wannier and Frenkel type excitons in an arbitrary atomic lattice [46]. c) PL spectra in RP 2D layered perovskites with different well thickness (n) . d) Schematic of the Rydberg series of the exciton ground state. e) Scaling law of the exciton binding energy with the 2D layered perovskites thickness [54]. f) The relationship between Eb and Eg in several quasi-2D and 3D perovskites has been empirically found [46]. g) Illustration of exciton

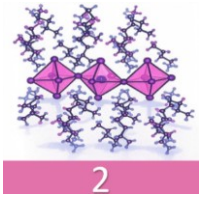

dissociation into equilibrium and free carriers dynamics [58]. h) configuration space illustration of exciton and ground state potentials with different equilibrium positions under the harmonic approximation [59]. The representation illustration of short-range repulsive overlap between electron and hole polaron [60].

2.8 Exciton energy in quasi-2D perovskites

In quasi-2D perovskites, the photophysical properties are tunable by controlling the inorganic layers (n). As a result, facile color tunability emission appears, which is the most significant benefit of these quasi-2D layered halide perovskites, as shown in **Figure 2.6c** [54]. **Figure 2.6e** shows a scaling rule for exciton binding energy developed as a function of the number of layers (n), which accounts for dielectric confinement effects [54]. Nevertheless, another empirical relationship is reported between the exciton binding energy and band gap in some 3D and quasi-2D halide perovskites (**Figure 2.6f**) [46]. Accordingly, increasing the number of layers or n-values represented a rapid decline in the exciton binding energies in the quasi-2D perovskites, as shown in a series of quasi-2D structures featuring various bulky organic spacers.

2.9 Polaron and exciton-phonon interaction

In halide perovskite structures, the electrons and holes can be easily coupled with lattice vibration to form polaron pairs, owing to the polarizable and soft lattices. The carrier mobility can be decreased; consequently, the effective mass increases, and this exciton-lattice interaction can play a vital role in exciton dynamics. **Figure 2.6g** summarizes a picture of phonon-incorporated exciton dynamics [58]. After exciting, the excitons can be formed and relaxed to an excited-state equilibrium configuration between the exciton polaron and bound states. Then, the excitons are screened and dissociated by the atomic displacement of the nearby lattice to create polaron pairs (P+ or P-). As a result, the polaronic effect reduces the exciton binding energy, where light emission occurs after equilibrium is established, as excitons undergo dissociation and subsequently recombine radiatively. Polaronic effects are generally classified into short-range deformation potential (Holstein-like interaction) and long-range electrostatic polarization response (Fröhlich-like interaction) [60]. In 3D or bulk perovskites, a long-range Fröhlich-like exciton–phonon interaction dominates, where free charge carriers are believed to exist as large polarons [61]. This behavior is responsible for the high defect tolerance and low electron–hole recombination rates observed in 3D perovskites.

In contrast, in 2D layered halide perovskites, due to the increased lattice distortion and reduced dimensionality, they possess a promoted short-range Hostein-like interaction [62]. As a result, the excitons in 2D layered halide perovskites exist as exciton polaronic and represent significant polaronic characteristics [63]. The related model is intuitively described in **Figure 2.6h** [59]. Thereafter, opposite lattice deformations associated with the electron and hole polarons can be observed, spatially separating their respective

wave functions, as shown in **Figure 2.6i** [60]. Thus, the exciton binding energy is dramatically decreased, making inter- and intra-exciton interactions weaker due to the overlaps of the electron-hole wave function. In summary, the polaronic effects strongly renormalize exciton-state carrier behaviours due to dynamic disorder and lattice anharmonicity in 2D and 3D perovskites.

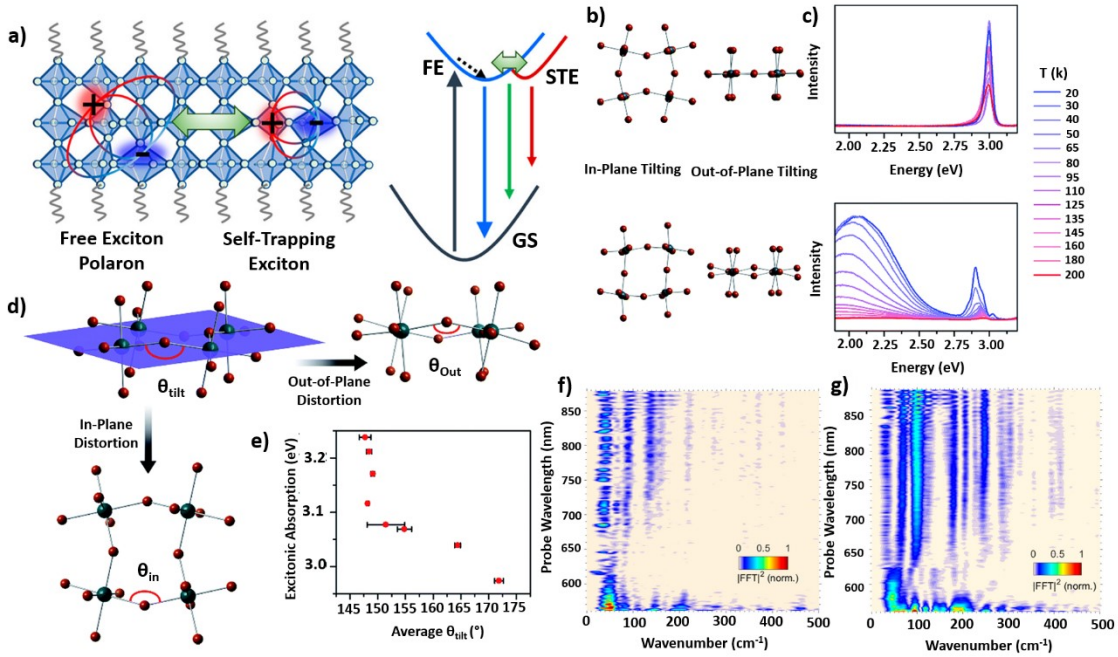

Figure 2.7. Illustration of self-trapped electrons originating from the exciton polaron [63]. b) In-plane and out-of-plane tilting in 2D perovskites of BA_2PbBr_4 (top) and HIS_2PbBr_4 (bottom), and c) related PL spectra of BA_2PbBr_4 (top) and HIS_2PbBr_4 (bottom). HIS_2PbBr_4 shows a broad emission due to octahedral distortion, free emission, and lattice reorganization. d) In-plane (ϑ_{in}) and out-of-plane (ϑ_{out}) octahedral distortion representation components in the M-X layer of a (001) 2D perovskite. The in-plane and out-of-plane can be defined as $D_{in} = 180°-\vartheta_{in}$ and $D_{out} = 180°- \vartheta_{out}$, respectively. Brown and green spheres show M and X atoms. e) The relationship between the exciton absorption energy at 298 K and tilting angle in the series of (001) M-X 2D perovskites [64]. Wavelength-resolved Fourier transform power map of f) HA_2PbI_4, and g) BA_2PbI_4 2D perovskites [65].

2.10 Self-trapping excitons in 2D perovskites

Importantly, local lattice distortion and exciton trapping in a low-energy self-trapped exciton state occur based on the exciton-phonon interaction [66]. A local potential well can be formed, and the charge carrier becomes self-trapped when a charge carrier distorts the surrounding structural lattice [67]. In 3D perovskites, while free exciton polarons are usually stable as a result of the strong short-range exciton-phonon interactions in 2D layered perovskites, the self-trapping states are more likely to be in the form of thermal equilibrium with free states as represented in **Figure 2.7a** [63]. This

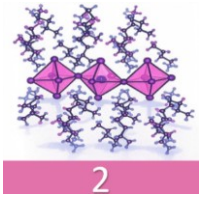

means that both dynamic exchange and states possibly coexist between them. Thus, exciton polarons in 2D layered perovskites experience ultrafast dynamic interconversion between self-trapped and free states. As a result, significant Stokes shifts with broad emission can be observed as an intrinsic phenomenon in 2D layered perovskites, as shown in **Figure 2.7b, c** [64]. Structurally, it has been demonstrated that the broad emission in perovskites was strongly correlated with the out-of-plane and in-plane inorganic lattice distortion, as shown in **Figure 2.7d, e** [64]. The choice of organic cations, which can determine the vibrational modes of the exciton couples, influences the strength of exciton-phonon interaction (**Figure 2.7f, g**) [65]. In HA2PbI4, for example, excitons interact with phonons with frequencies of 88 and 137 cm-1, while in BA2PbI4 2D perovskites, they mainly couple to a 100 cm-1 phonon mode.

2.11 Lateral heterostructure formation in 2D layered halide perovskites

Formation of epitaxial heterojunction based on transitional metal dichalcogenide semiconductor [68–71], II-VI [72], III-V [73], and perovskite oxides [74] generates the foundation of modern electronics and optoelectronics. 2D layered halide perovskites, an emerging class of tunable semiconductors with unique properties, are attractive materials for heterostructure fabrication. The compositional and structural flexibility of layered Pb-based perovskites enables their outstanding PLQY, short lifetimes, and optoelectronic tenability [75]. Their soft crystal lattice allows greater tolerance for lattice mismatch, making them a promising structure for semiconductor integration and heterojunction formation [76]. To enhance device performance and enable miniaturization, atomically sharp epitaxial interfaces are required. However, the epitaxial formation of atomically sharp heterojunctions in 3D halide perovskites has not yet been achieved, owing to their high intrinsic ionic mobility, which leads to large junction widths and interdiffusion [77], and owing to their poor chemical stability, which leads to decomposition of the prior layer during the formation of subsequent layers. Thus, evaluating effective strategies to suppress ion diffusion and understanding the origins of this instability are of great significance [78]. In this thesis, two methods, based on anion exchange and sequential growth, are employed to produce lateral heterostructures in 2D layered halide perovskites, as discussed in Chapters II and III, respectively.

The formation of lateral heterostructures was first reported by E. Shi et al. [79], who proposed a promising approach to substantially suppress lateral ion diffusion in 2D layered halide perovskites by incorporating rigid π-conjugated organic spacer ligands. They have demonstrated tunable, highly stable in-plane epitaxial heterojunctions, superlattices, and multiheterojunctions, with epitaxial growth and near-atomically sharp interfaces, as shown in **Figure 2.8**. Figures **2.8a-d** represent in-plane heterojunctions formed between two different segments with various organic spacer ligands of BTm^+, $2T^+$, $4Tm^+$, and PEA^+ (see **Table 2.1** for more details). Additionally, a

lateral heterostructure between two metals, Pb and Sn, is formed by replacing Pb with Sn and is shown in Figures 2.8b, 2.8c, and 2.8e. Due to the formation of type-II band alignment between the $[PbI_4]^{2-}$ layers and $4Tm^+$ space ligand in **Figure 2.8c**, the $(4Tm)_2PbI_4$ region represents no PL emission. A type-I band alignment between the BTm^+ layer and [PbI4]2− layer, with a broad PL emission, is formed in $(BTm)_2PbI_4$-$(4Tm)_2PbI_4$ heterojunction. Two different PL emission peaks from the $(2T)_2SnI_4$-$(2T)_2$ PbI_4 heterojunction associated with pristine $(2T)_2SnI_4$ and $(2T)_2PbI_4$, and the gap in the PL images between the Sn- and Pb-based perovskite sections is probably induced by exciton dissociation at the interface. In addition to the reported double halide concentric heterojunctions, a more complex heterojunction have also been fabricated and represented in **Figure 2.8f** and **g**, for the (2T)2PbI4–(2T)2PbBr4 × n (n = 2, 3, 4) superlattices and $(2T)_2SnI_4$-$(2T)_2PbI_4$-$(2T)_2PbBr_4$ lateral multiheterostructure, respectively, which is formed by repetitive grown steps. The PL images and schematic representation show concentric rectangles grown (**Figure 2.8f**), with quenched regions associated with the $(2T)_2PbBr_4$ layer and green-emission regions related to the $(2T)_2PbI_4$ layer. Furthermore, the multiheterojunctions are fabricated by a core-frame-frame layers with a red emission along the $(2T)_2PbI_4$-$(2T)_2PbBr_4$ layer (**Figure 2.8g**).

A. Singh et al. [80] have synthesized core-frame $(R)_2PbX_4$-$(R)_4M'M''X_8$ heterojunctions by using a two-step solution-based synthesis approach, between RP and DP phases, where R = molecular spacer ligand here PEA^+ and $2T^+$, $M' = Na^+$ or Ag^+, $M''' = In^{3+}$ or Bi^{3+} or Sb^{3+}, and X = I^- or Br^- halides. Interestingly, in these heterojunctions, the Pb-based layered perovskite is located in the core. In contrast, the Pb-free Ag-based layered DP is located in the frame, and no emission is observed under excitation for this segment. Based on heating analysis of this novel heterojunction, no anion migration is observed in the core or frame, confirming high stability relative to Pb-based heterostructures, which undergo rapid anion migration under heating. It has also been reported that layered Pb-free Ag-based perovskites are more stable than layered Pb-based perovskites due to the presence of rigid organic spacer cations, such as 2T+, and careful selection of metal cations that prevent anion migration. Different forms of heterojunctions are represented in Figure 2.9.

M. Xia et al. [81] have discovered a kinetic Wulff-shaped heteroepitaxy approach for generating 2D layered halide perovskite epitaxial heterojunctions with deterministic slab layers of n = 1-3. The method enables versatile modulation of the lattice interface mismatch, ranging from in-plane homojunctions with no lattice mismatch to in-plane heterojunctions with >11% lattice mismatch, all of which can retain single-crystal properties. Moreover, the fabrication of two-segment heterojunctions and a complete multiheterojunction may enable the development of ultranarrow segments with carrier wavelengths, thereby facilitating the construction of an epitaxial quantum well structure via a solution-based process, superlattices, and related functional systems. Based on the 2D single-crystalline layered halide perovskite in-plane heterojunctions, they have

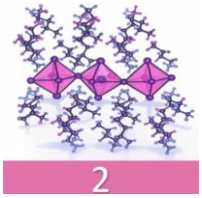

successfully produced an optoelectronic device using the vdW dry transfer technique. Under electrical or optical inputs, these heterojunction-based devices represented reliable on/off switching and substantial electrical rectification ratios. The structural and optical characteristics of the reported epitaxial dual- and multiple-heterostructures are reported in Figures 2.10 and 2.11, respectively.

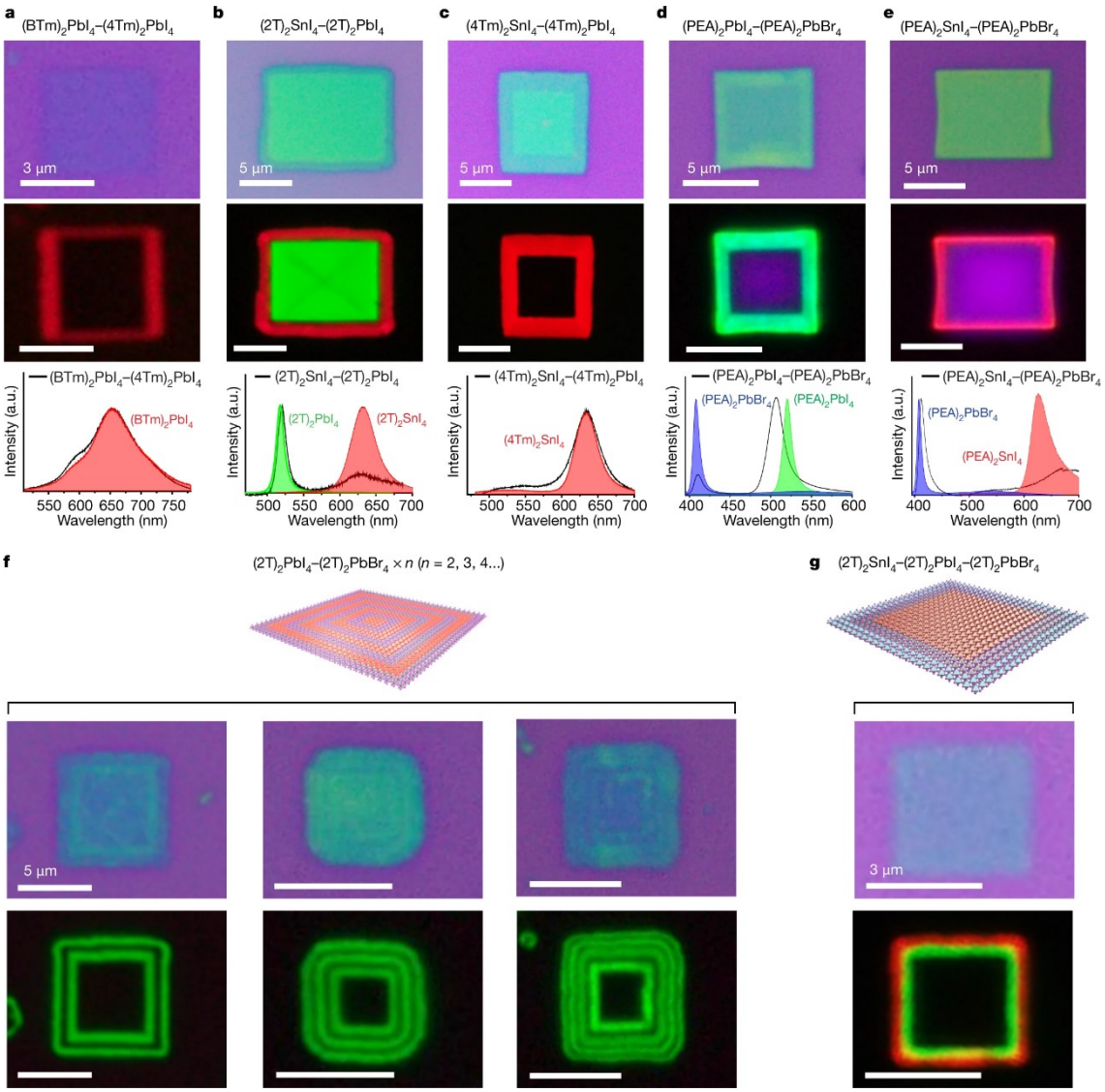

Figure 2.8. In-plan heterojunctions formation of a) $(BTm)_2PbI_4$–$(4Tm)_2PbI_4$, b) $(2T)_2SnI_4$-$(2T)_2PbI_4$, c) $(4Tm)_2SnI_4$-$(4Tm)_2PbI_4$, d) $(PEA)_2PbI_4$-$(PEA)_2PbBr_4$, and e) $(PEA)_2SnI_4$-$(PEA)_2PbBr_4$. Optical images are shown on top, PL images in the middle, and PL spectra on the bottom. f) Schematic representation of the $(2T)_2PbI_4$-$(2T)_2PbBr_4$ × *n* lateral superlattice (left to right n = 2, n = 3, and n = 4), and g) $(2T)_2SnI_4$-$(2T)_2PbI_4$-$(2T)_2PbBr_4$ in-plane multiheterojunction. Optical images on top and PL images on bottom. Reproduced with permission from ref. 79, copyright 2020 Nature.

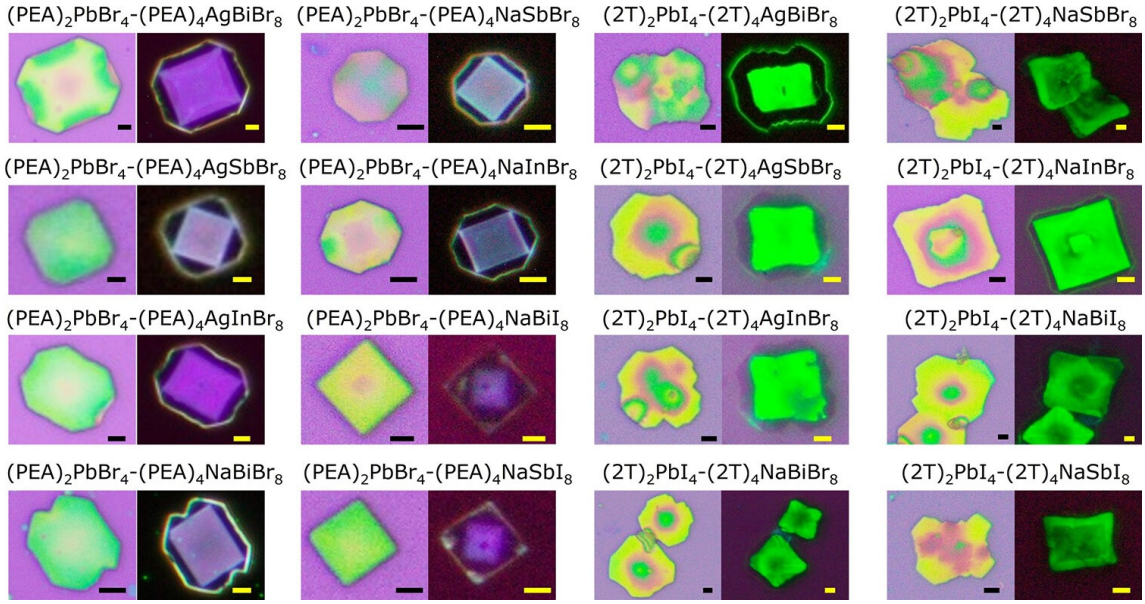

Figure 2.9. The bright-field and PL images of different heterojunctions formed between Pb-based and Pb-free Ag-based layered perovskites. All scale bars are 2 μm. Reproduced with permission from ref. 80, copyright 2023 Journal of American Chemical Society.

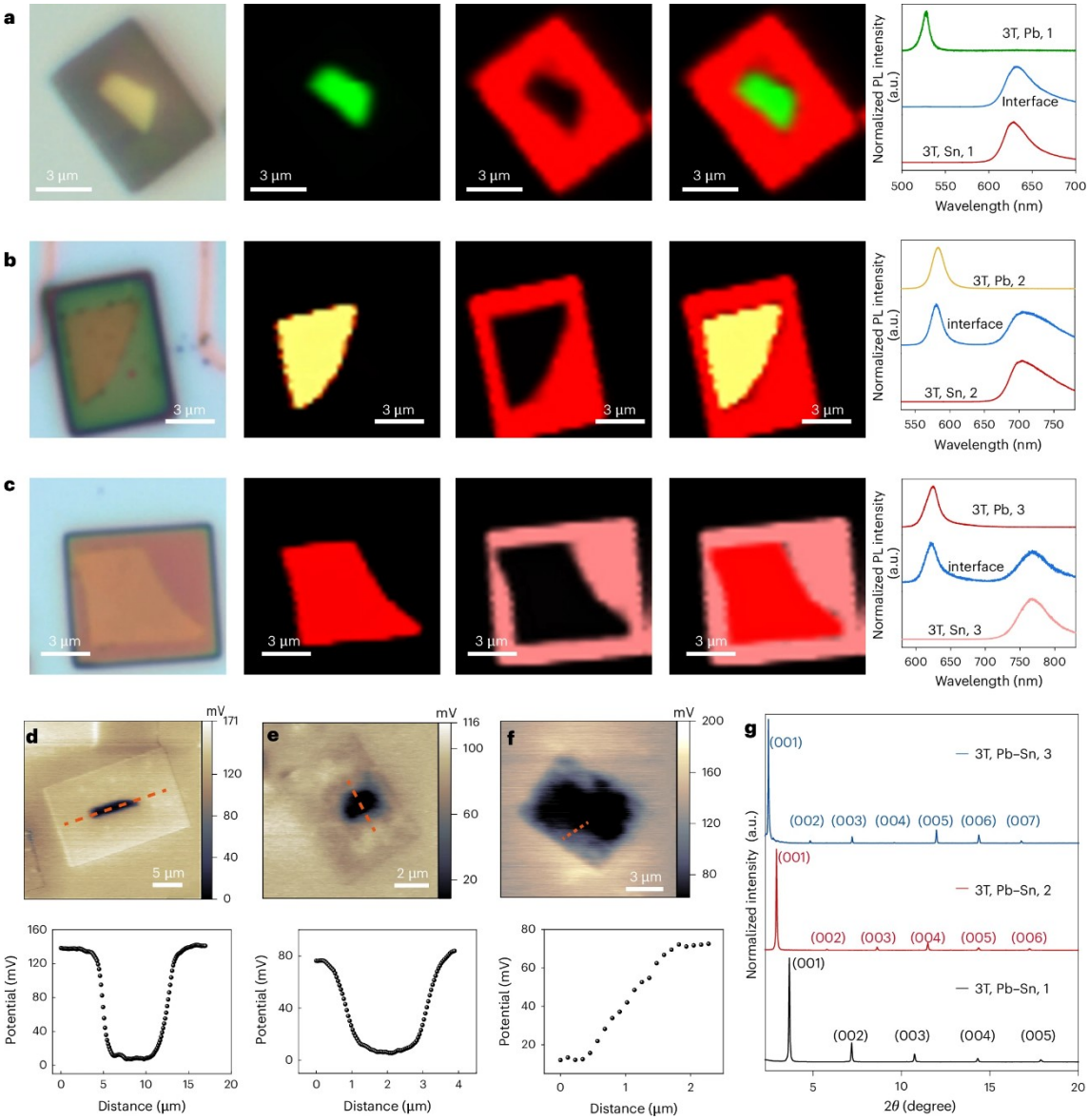

Figure 2.10. Confocal PL images of a) $(3T)_2PbI_4$–$(3T)_2SnI_4$, b) $(3T)_2MAPb_2I_7$–$(3T)_2MASn_2I_7$, c) $(3T)_2MA_2Pb_3I_{10}$–$(3T)_2MA_2Sn_3I_{10}$ heterojunctions. From left to right, each panel shows optical images, confocal PL images of the Pb domains of the heterojunctions, collected by exciting at green ranges (500-540 nm), yellow ranges (560-600 nm), and red ranges (600-640 nm), and confocal PL images of the Sn domains of the heterojunctions, collected by exciting at red ranges (610-650 nm and 680-720 nm), and pinkish red ranges (740-780 nm), and the dual-channel confocal PL image of mixed Pb and Sn domains, and PL spectra of Pb-, and Sn-domains and their interfaces of illustrated heterojunctions (n = 1-3). KPFM images (top) and surface potential profiles (bottom) of d) $(3T)_2PbI_4$–$(3T)_2SnI_4$, e) $(3T)_2MAPb_2I_7$–$(3T)_2MASn_2I_7$, and f) $(3T)_2MA_2Pb_3I_{10}$–$(3T)_2MA_2Sn_3I_{10}$. PXRD pattern of $(3T)_2MA_{n-1}Pb_nI_{3n+1}$–$(3T)_2MA_{n-1}Sn_nI_{3n+1}$ (n = 1–3) epitaxial heterojunctions. Reproduced with permission from ref. 81, copyright 2025 Nature Synthesis.

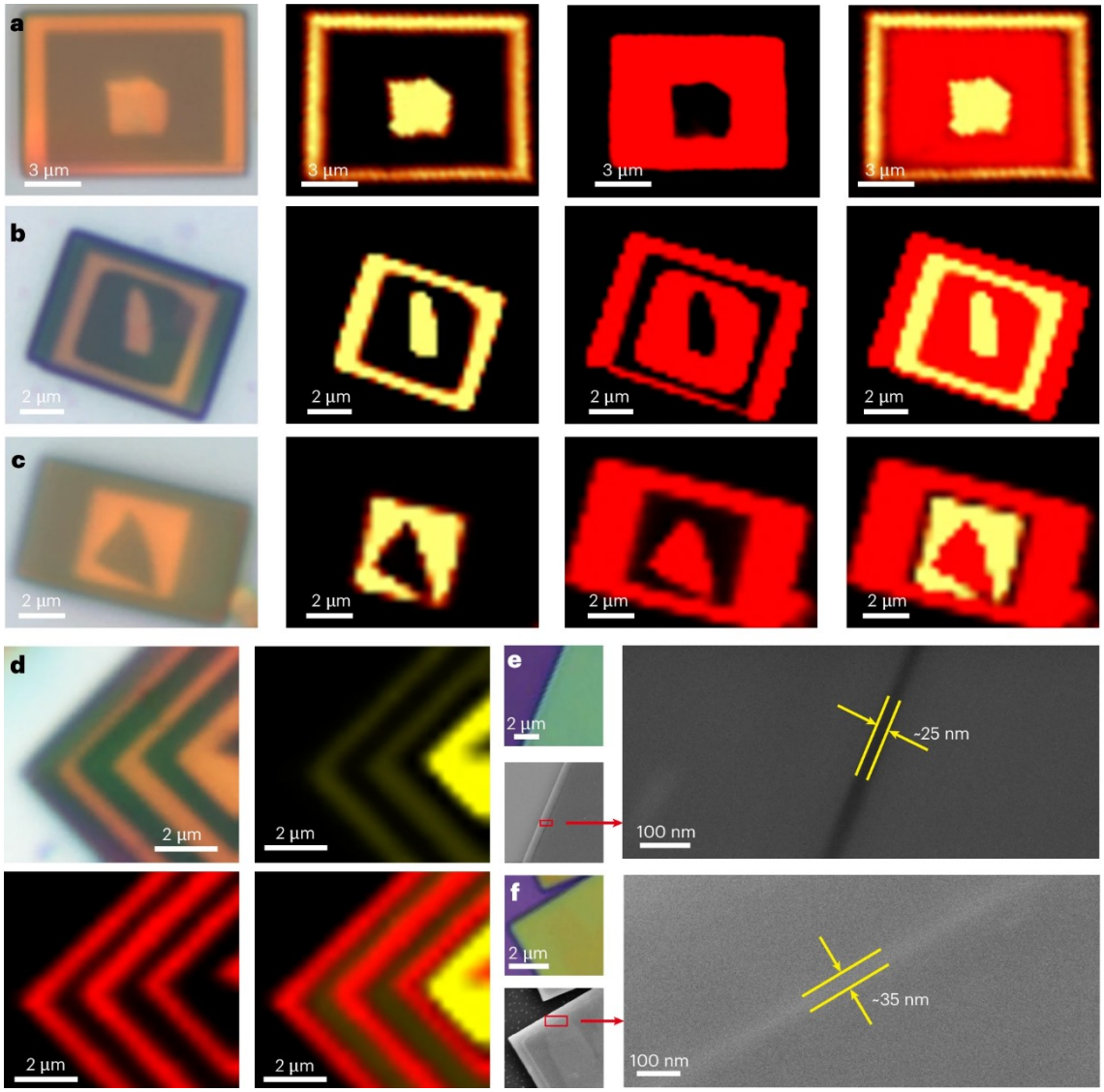

Figure 2.11. Confocal PL images of a) $(3T)_2MAPb_2I_7$–$(3T)_2MASn_2I_7$–$(3T)_2MAPb_2I_7$, b) $(3T)_2MAPb_2I_7$–$(3T)_2MASn_2I_7$–$(3T)_2MAPb_2I_7$–$(3T)_2MASn_2I_7$, and c) $(3T)_2MASn_2I_7$–$(3T)_2MAPb_2I_7$–$(3T)_2MASn_2I_7$. From left to right, each panel shows optical images, confocal PL images of the Pb segments of the heterojunctions, collected by exciting at yellow ranges (560-600 nm), and confocal PL images of the Sn domains of the heterojunctions, collected by exciting at red ranges (680-720 nm), and the dual-channel confocal PL image of mixed Pb and Sn domains. d) The $(3T)_2MASn_2I_7$–$(3T)_2MAPb_2I_7\}\times 3$-$(3T)_2MASn_2I_7$ multi-heterojunction, the optical images (top left), confocal PL image of the Pb segments recorded by exciting at yellow ranges (top righ, 560-600 nm), confocal PL image of the combined Pb and Sn domains recorded at red ranges (bottom left, 680-720nm). e) Top left and bottom left show optical and SEM images, and a magnified SEM image of $(3T)_2PbI_4$–$(3T)_2SnI_4$–$(3T)_2PbI_4$ heterojunction with an ultranarrow $(3T)_2SnI_4$ domain, respectively. f) Top left and bottom left show optical and SEM images

respectively, and magnified SEM image of $(3T)_2SnI_4$–$(3T)_2PbI_4$–$(3T)_2SnI_4$ heterojunction with an ultranarrow $(3T)_2PbI_4$ domain, respectively. Reproduced with permission from ref. 81, copyright 2025 Nature Synthesis.

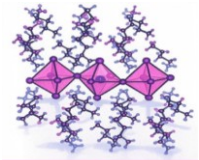

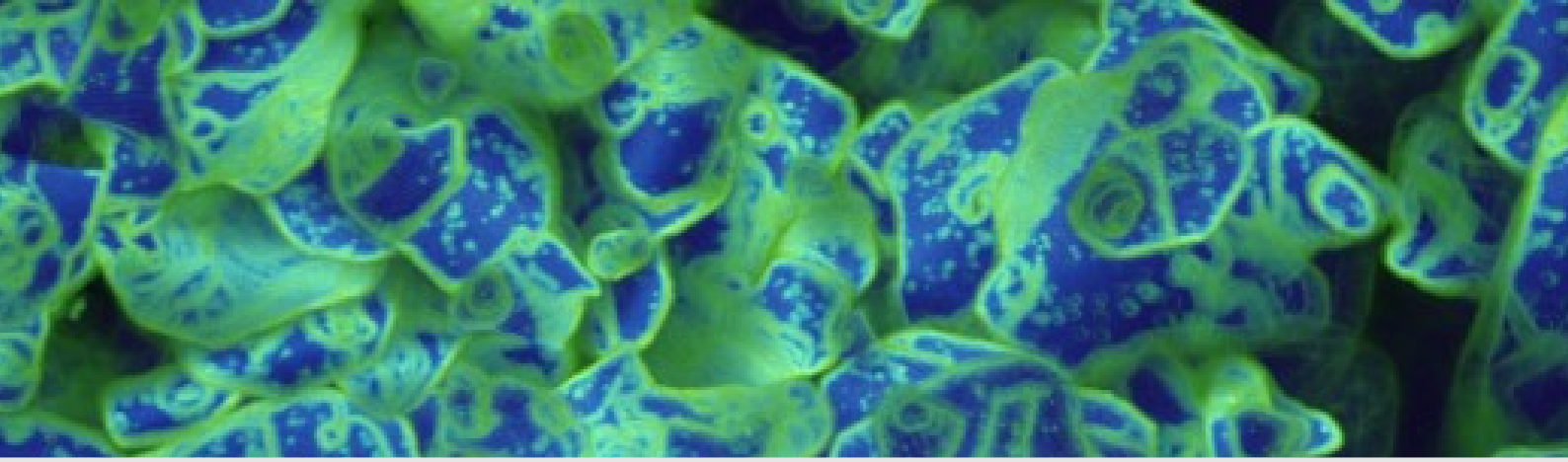

Chapter III:

Fabrication of 2D perovksite lateral heterostructure via a anion exchange

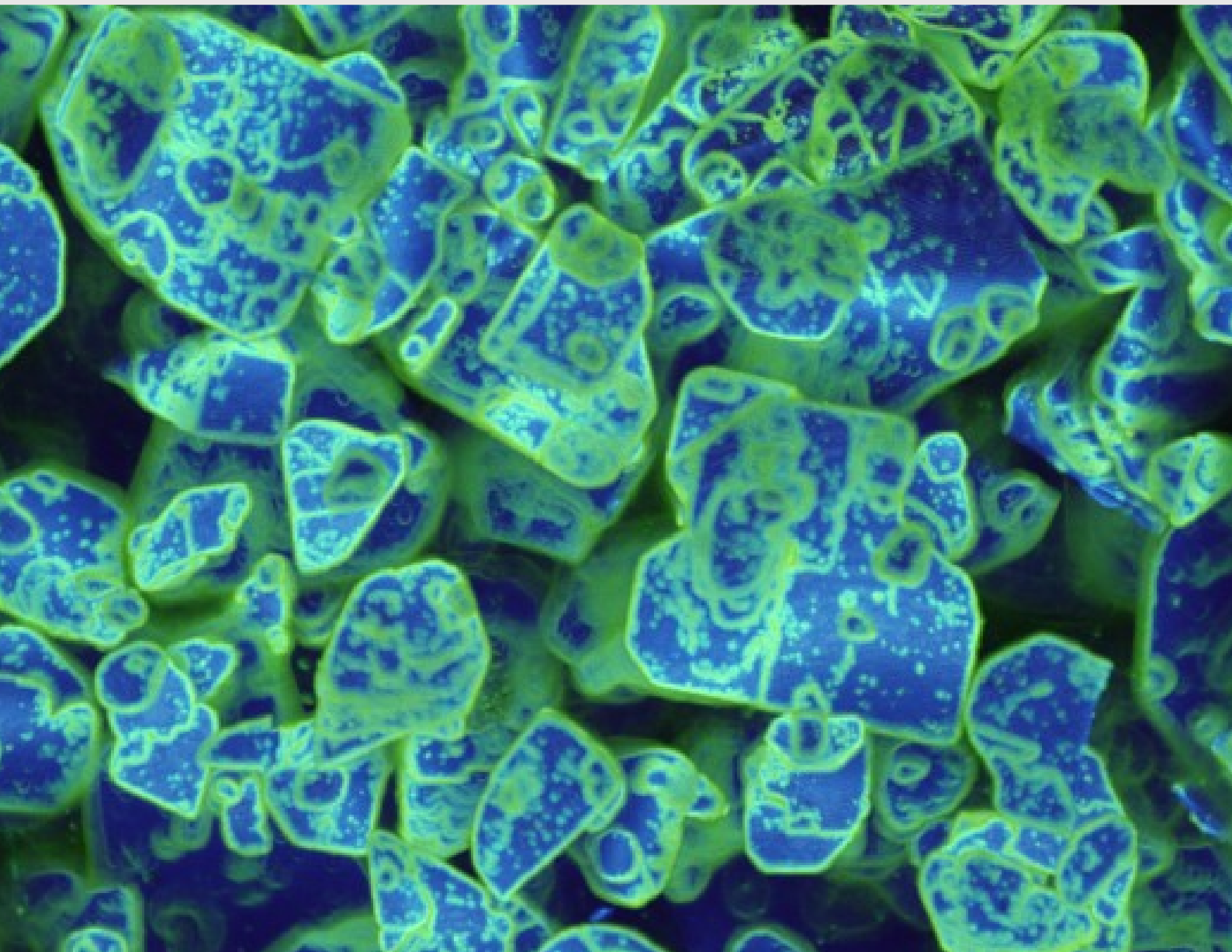

Chapter III: Fabrication of 2D perovskite lateral heterostructure via Anion exchange

Abstract: *2D layered perovskites contain organic molecule spacer layers with typical dielectric behavior, which sandwich the inorganic semiconducting metal halide octahedral lattices and make an organic-inorganic layered compound. In such 2D materials, the in-plane quantum confinement of charge carriers leads to interesting electronic and optoelectronic properties, including anisotropic charge diffusion, strong exciton binding energy, and polarization directionality. A heterojunction can provide additional control on carrier localization and diffusion, and an in-plane heterostructure is an interesting connection between the layered semiconductors due to the related high charge carrier mobility. As the title of this thesis is "The Synthesis of heterostructure perovskites," this chapter starts synthesizing and characterizing a 2D layered perovskite lateral heterostructure with different halide compositions fabricated via a versatile solution-based anion exchange strategy. This contributes to fabricating a 2D layered in-plane heterostructure with spatially separated halide phases with various light emission colors and band gaps. The results illustrated that the composition and morphology of the exchanged phase boundary depend on the exchange approach, which is linked to the preferential localization of halide atoms at the axial or equatorial octahedral positions. This localization either drives solvation and recrystallization of the octahedral lattice in the case of a bromide-to-iodide heterostructure or facilitates ion diffusion within the lattice in the case of an iodide-to-bromide heterostructure. This chapter provides comprehensive information on creating a solution-based anion exchange method for fabricating and characterizing 2D layered perovskite in-plane heterostructures.*

3.1 Introduction

As discussed in the second chapter, 2D layered perovskites are a rising family of semiconductors that present a sandwiched layered structure between organic spacer cations and an inorganic metal halide octahedral layer [82,83]. This unique layered structure provides high in-plane mobility to charge carriers and excitons while limiting out-of-plane mobility due to the mainly insulating nature of the organic spacer cations [84,85]. Consequently, energy and charge transfer across out-of-plane heterojunctions in these materials is challenging. However, one can take advantage of the strong in-plane quantum confinement that comes with 2D layered perovskites thanks to in-plane heterojunctions, where compositional variations occur along the horizontal direction [79,86,87]. An alternative and promising route for investigating charge and energy transfer across junction interfaces lies in this strategy. The earliest demonstration of in-plane heterojunctions within 2D layered perovskites, achieved through a sequential solution-

based crystallization process, was reported by E. Shi and co-workers [79]. Since then, the method has been extended to enable core–frame architectures in Pb-containing 2D layered perovskites and Pb-free layered double perovskites, and further advanced through scale-up via solution shearing techniques [80,88]. The reported sequential crystallization strategy depends upon the various solubilities of the 2D layered perovskites in the ternary solvent system. Thus, precise fine-tuning is crucial to keeping the overall structure of the 2D layered perovskites. Despite this progress, the fabrication of in-plane heterojunctions in 2D layered perovskites remains early, with most reported examples relying on anion-exchange processes.

Previously, such exchanges in 2D perovskites were only realized through solid–gas phase reactions employing butylammonium halide or hydrogen bromide (HBr) vapors [89,90]. The quality of the fabricated lateral heterostructure is comparatively high, but altering the anion exchange process into otherwise entirely solution-based process systems could be expensive, time-consuming, and challenging. In the case of 3D perovskites, the solution-based anion exchange processes were quite successful and are now generally applied to alter the characteristics of the fabricated materials [91–94]. However, the solution-based anion exchange processes in 3D perovskites were successful, while this approach has not been successfully represented in 2D layered perovskites. In this thesis, in-plane heterojunctions with unique optical characteristics were achieved based on a facile solution-based process, based on an anion exchange process in 2D layered perovskite microflakes. The exchange process is investigated using a single octahedral layer (n = 1) phenethylammonium (PEA) lead halide 2D layered perovskites, leading to the formation of PEA_2PbBr_4-PEA_2PbI_4 lateral heterojunctions. PEA spacer molecule is related to rigid aromatic spacer groups that represent higher structural stability compared to the aliphatic spacer cation groups, which could be an advantage for the solution-based anion exchange process in polar solvents as a result of the ability to keep material properties by tolerating the conditions [83]. The solution-based fabrication approach used to produce the pristine 2D layered perovskites is, in principle, compatible with the solution-based anion exchange strategy. However, the solubility of the perovskite materials and precursors in the common solvent could be challenging. In the solid-gas phase anion exchange processes in PEA-based 2D layered perovskites, there was no anion exchange when PEA2PbI4 micro flakes were exposed to HBr vapor [90]. The anion exchange method could be facilitated in an alcoholic solvent that causes the exchange process to contain halide salts of PEA. Aligning with the earlier report on solid-gas phase exchange approaches, an enhancement in in-plane exchange originates from the layered nature of the 2D layered perovskites [79,89,90]. Intriguingly, the exchange process strongly depends on the halide anion that will be exchanged. Hence, the bromide-to-iodide exchange (PEA_2PbBr_4-PEA_2PbI_4) generates an almost iodide-pure phase in the exchange area, while the iodide-to-bromide exchange process yields a mixed-phase composition. This chapter represents that the two exchange process

directions follow various mechanisms. Accordingly, in the bromide-to-iodide process, the process involved solvation and recrystallization, while in the iodide-to-bromide exchange process, the classical vacancy-assisted anion exchange process resembled [95,96]. The results agreed with halides' recently reported preferential occupancy at specific octahedral positions [97–100]. The mentioned preferential occupation mechanism can be utilized to obtain lateral heterostructures with various properties in terms of band offset and composition, in one case creating a junction of PEA_2PbI_4 with alloyed phases including $PEA_2Pb(Br_{x-1}I_x)_4$, in the other connecting relatively pure PEA_2PbI_4 and PEA_2PbBr_4. This chapter introduces a scalable method for generating in-plane heterojunctions in 2D layered perovskites, thereby enabling the progress of fully solution-based process systems that lead to control energy or charge flow in the in-plane direction.

3.2 Anion exchange process and stability of the microcrystals

Figure 3.1a shows a facile two-step formation process of 2D layered in-plane heterojunction perovskites. The first step is to include the preparation of the 2D layered perovskites by an anti-solvent-assisted fast crystallization approach previously reported in our group [101]. This method leads to microflakes forming up to a few microns in thickness and several hundreds of microns in lateral size. To achieve a facile and scalable approach toward heterojunctions, 2D layered perovskites were exposed in an alcoholic solvent to the salt of the spacer cation with a different halide from that of the starting material, as shown in **Figure 3.1b**. Alcoholic solvents are known to selectively solvate the organic cation molecules due to their strong hydrogen bond formation between the hydroxyl groups of the alcohol and –NH of the amine [102]. Thus, it has been hypothesized that the exposure to a halide salt of the respective spacer cation can stabilize the 2D layered perovskites in alcohols while at the same time implementing the anion exchange because it enables maintaining the structure of 2D layered perovskites and features sufficient solubility for the halide salts of PEA. **Figures 3.2-3.4** represent the details of the stability of 2D layered perovskites in octanol and the stabilizing effects. **Figure 3.1c** clearly shows that after the exposure of the PEA_2PbBr_4 microflakes to PEAI in octanol solution, a new PL band in the green region appears at the edge of the microflakes, forming a 2-micron (**Figure 3.5**) uniform frame thickness.

The mentioned green PL spectrum is similar to that of PEA_2PbI_4; therefore, it has been assigned to a nearly pure PEA_2PbI_4 phase. As a result, a core-frame PEA_2PbBr_4-PEA_2PbI_4 in-plane heterojunction was formed that conserves the initial morphology of the microflakes. The reaction was performed on a microscope slide to study the spatial and temporal dynamics of the anion exchange. As seen in **Figure 3.6a**, this enabled capturing real-time hyperspectral confocal images of the lone microflake. As it moves toward the center and eventually becomes the most prominent phase, the iodide phase first appears at the edge of the microflake (**Figure 3.6b, 3.6c, and 3.6d**). The reaction

develops mainly in the lateral direction, which is due to the 2D layered perovskite configuration, in which the layers of organic molecule cations make barriers for the ion diffusion in the vertical direction, in perfect agreement with C. R. Roy et al., which reported on the solid-gas phase exchange process with the difference being that this process proceeds in minutes instead of hours [90]. Moreover, the binding of the equatorial halide ions might be weaker than that of apical ones due to the N-H head group bonds of the spacer cation molecule, which additionally favors lateral over vertical ion diffusion direction [97,103].

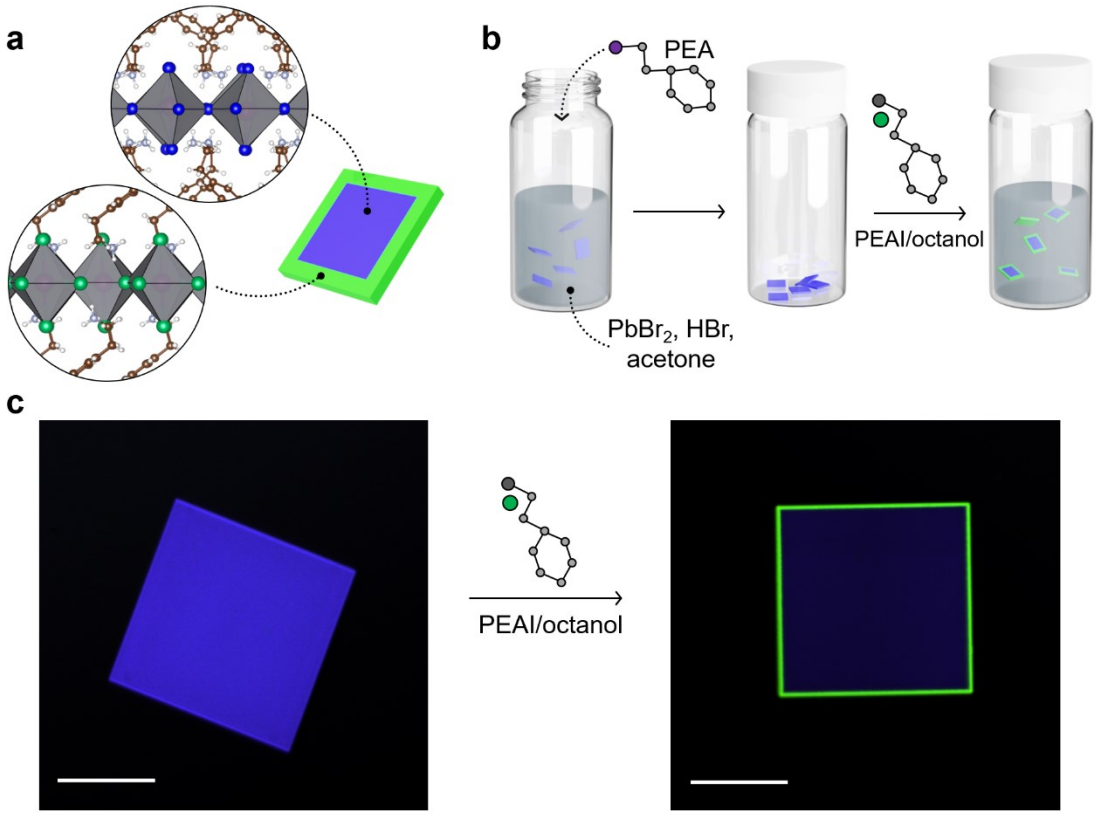

Figure 3.1. Fabrication of PEA_2PbBr_4-PEA_2PbI_4 in-plane heterojunctions by a simple two-step RT approach. a) Schematic representation of the proposed microcrystalline heterojunction architecture with the bromide phase in the center and the iodide phase positioned at the edges. b) Representation of the synthesis of microflake powders of PEA_2PbBr_4 and the fabrication of lateral heterojunctions by exposing the powder to a solution containing PEAI and octanol. c) PL confocal images of (λ_{ex} = 400 nm) of a perfect square PEA_2PbBr_4 microflake fabricated on glass before (left) and after (right) 2 min of exposure to PEAI-octanol solution (scale bar 50 µm). Reproduced with permission from ref. 81, copyright 2024 Advanced Materials.

The green PL band originating from the exchange phase remains fixed throughout the exchange process. It is located at 520 nm, even at very early times, as confirmed by a temporal resolution of 500 ms per frame in **Figure 3.8**. Thus, the iodide

phase at the edges is formed rapidly, with no sign of any intermediate phase. After the rapid formation of the PEA_2PbI_4 phase at the edges, a slower propagation of the bromide to the iodide phase boundary towards the center occurs. It is worth noting that the exchange process also happens, but much more slowly at the top surface. This is the main reason why, after long reaction times, the entire crystal region appears green in the confocal images. However, for micro flakes well stacked to the glass surface, the imaging from below through the glass substrate allows for controlling the exchange process without the bottom/top surface contribution. In this case, the blue emission in the core is preserved even for long reaction times and is surrounded by a green frame with a few microns in width, as shown in **Figure 3.9**. Thus, it has been concluded that the exchange process of microflakes resembles a core-frame structure, even after long exchange reaction times. To represent that this exchange protocol is a scalable and versatile process, the bromide-to-iodide exchange has been performed on microflake powder synthesized by the fast crystallization method, as shown in **Figure 3.1b** and the confocal image of **Figure 3.10**.

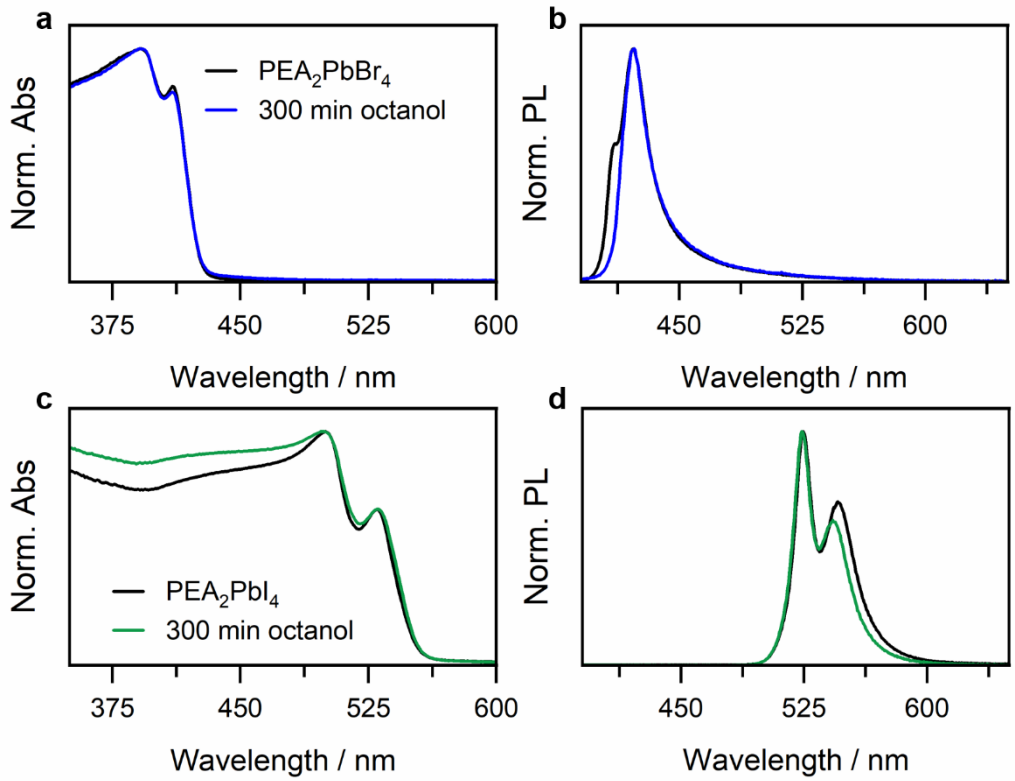

Figure 3.2. Optical properties of pristine PEA_2PbBr_4, a) Uv-vis, b) PL spectra, along with pristine PEA_2PbI_4, c) Uv-vis, d) PL spectra before and after octanol treatment for 300 min. The treatment with octanol shows a minor change in the optical properties, absorption, and PL spectra. Reproduced with permission from ref. 81, copyright 2024 Advanced Materials.

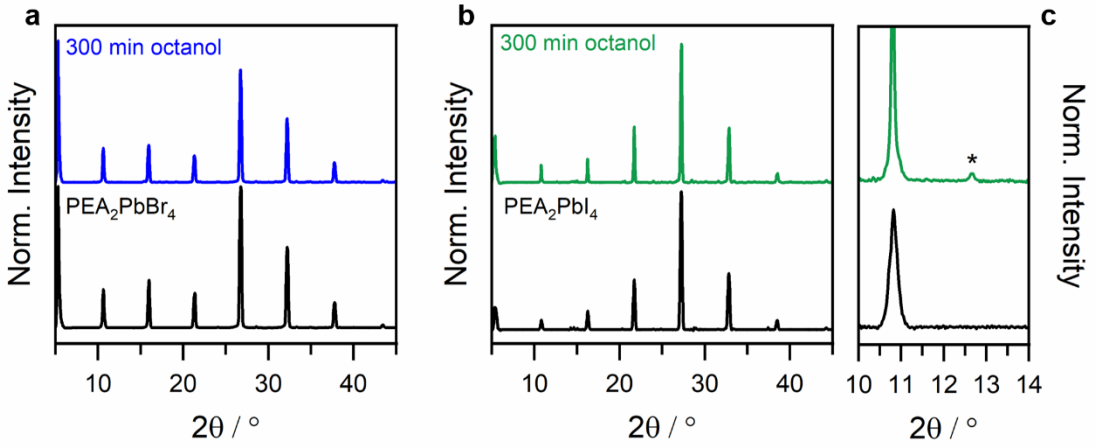

Figure 3.3. XRD pattern of a) pristine PEA_2PbBr_4, along with b) pristine PEA_2PbI_4 before and after octanol treatment for 300 min. c) Magnification region of b) representing the presence of a new reflex (12.7°, marked by an asterisk) that can be related to a minor contribution of PbI2 after the treatment with octanol [104]. Reproduced with permission from ref. 81, copyright 2024 Advanced Materials.

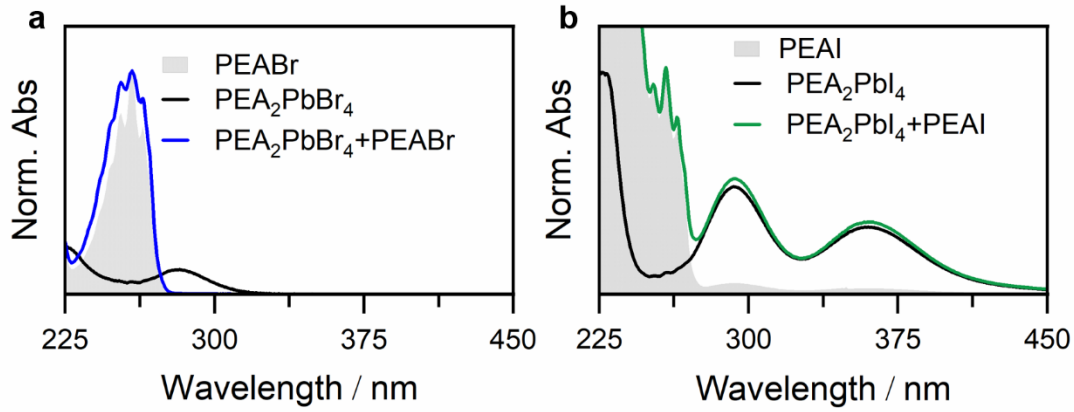

Figure 3.4. a) UV-vis absorption spectrum of PEABr-octanol solution, octanol after 300 min of exposure to PEA_2PbBr_4, and PEABr in octanol after 300 min of exposure to PEA_2PbBr_4. The recorded band at 282 nm can be related to a solvated $[PbBr_2]$ complex [105], which is not present if PEA_2PbBr_4 is exposed to PEABr in octanol. b) Uv-vis absorption spectrum of PEAI in octanol, octanol after 300 min exposure to PEA_2PbI_4, and PEAI in octanol after 300 min exposure to PEA_2PbI_4. The recorded dual bands at 293 and 360 nm can be related to I^{3-} [106,107], and the dual bands can be represented independently of the presence of PEAI, suggesting the leaching of I- species into the solution as one of the main degradation pathways. Reproduced with permission from ref. 81, copyright 2024 Advanced Materials.

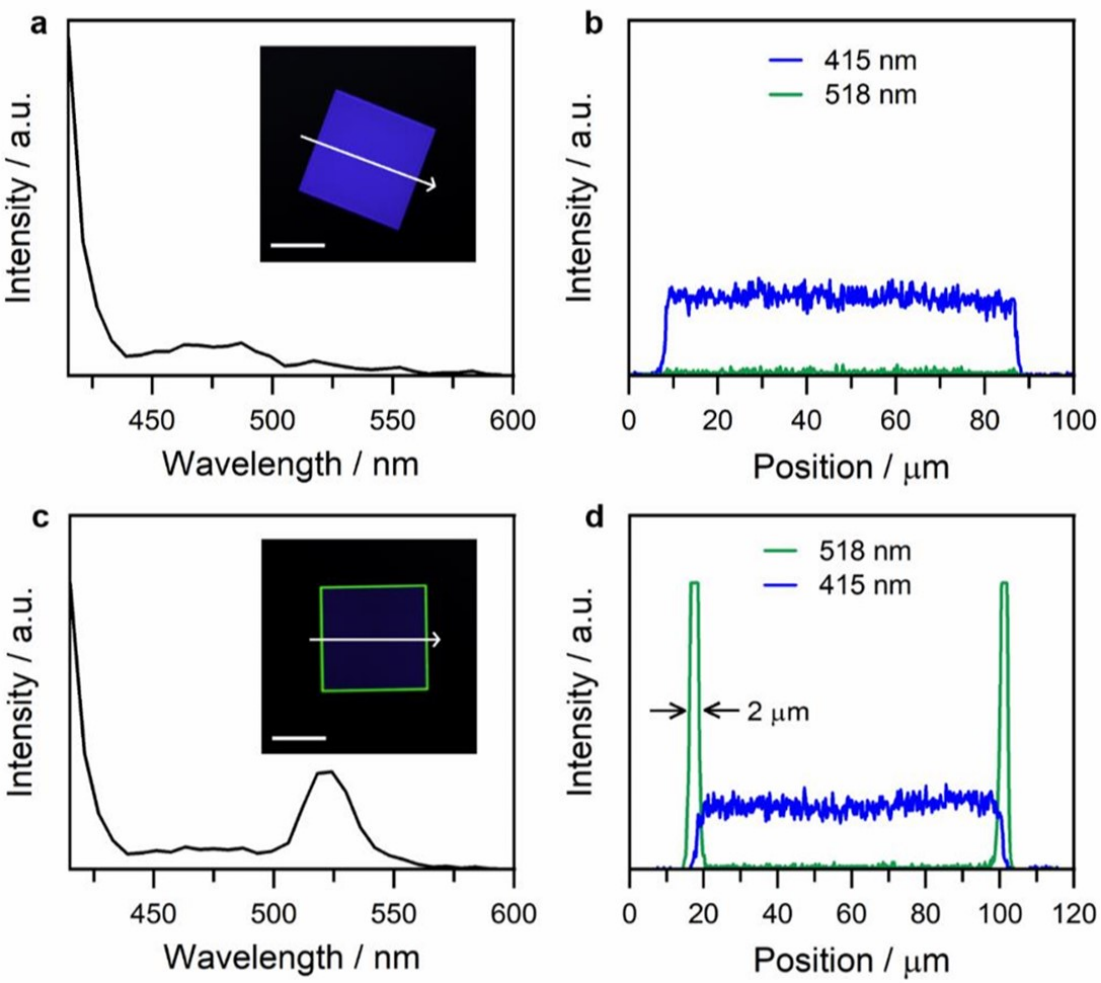

Figure 3.5. PL Spectrum and confocal image of a PEA_2PbBr_4 microflake extracted along the scan line, a) before, and c) after 2 min of bromide to iodide exchange, respectively. The intensity profiles of related scan line on the structures, b) before, and d) after exchange at 415 and 518 nm, respectively (scale bar 50 μm). Reproduced with permission from ref. 81, copyright 2024 Advanced Materials.

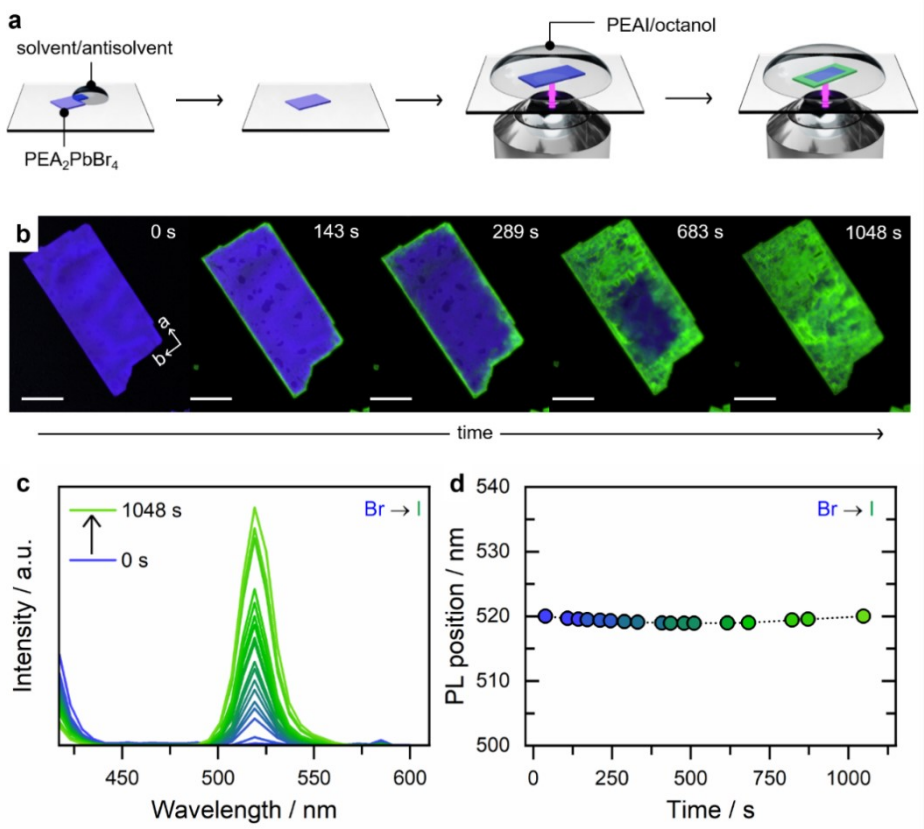

Figure 3.6. In situ tracking of the temporal and spatial dynamics in the bromide to iodide exchange. a) Schematic representation of in situ monitoring of the exchange process and the preparation of a microflake on a microscope slide. b) PL confocal images of a single PEA_2PbBr_4 miroflake before and during the exchange process, showcasing the preparation of the phase boundary toward the center (scale bar 20 µm, λex = 400 nm). c) PL spectra (integrated over the field of view) extracted from the sequence of PL confocal images in b) show that the d) green PL band is stable at 520 nm throughout the process. The whole sequence of the PL confocal images is shown in **Figure 3.7**. Reproduced with permission from ref. 81, copyright 2024 Advanced Materials.

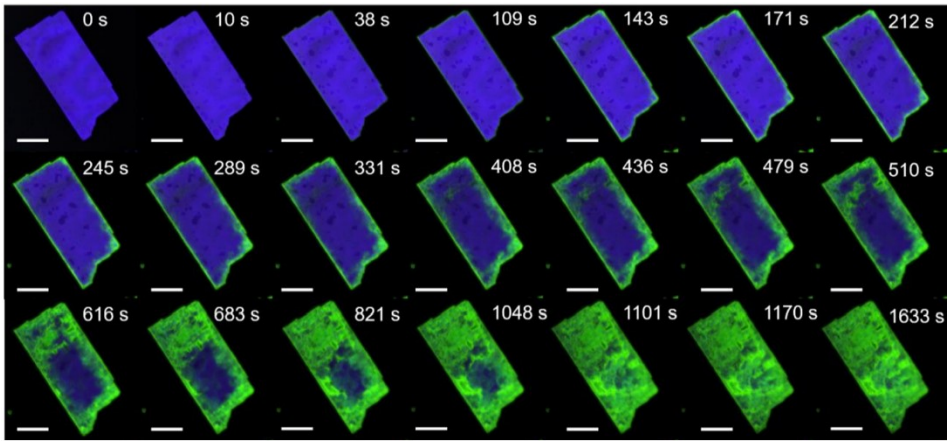

Figure 3.7. Time progression of confocal PL images of a PEA_2PbBr_4 microflake during the bromide to iodide exchange (excited at 400nm, scale bar 20 µm). Reproduced with permission from ref. 81, copyright 2024 Advanced Materials.

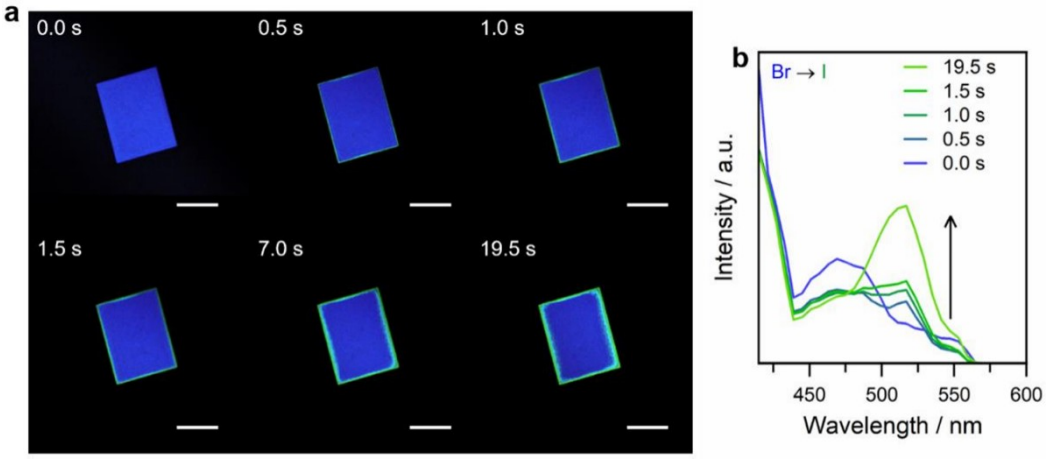

Figure 3.8. PL confocal images obtained with a time progressing resolution of 0.5 s per frame represent the appearance of the new PL feature after one single frame, showing the rapid transition from the bromide phase to the iodide phase (scale bar 20 µm, λex=400 nm). b) corresponding PL spectra extracted from the images in a). Reproduced with permission from ref. 81, copyright 2024 Advanced Materials.

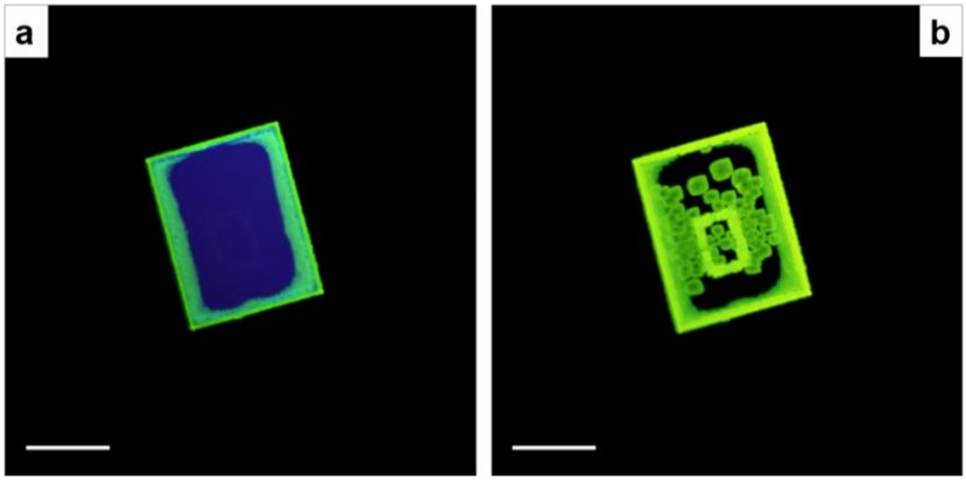

Figure 3.9. a) PEA_2PbBr_4 microflake after 5 min of bromide to iodide exchange, excited at 400 nm, and b) 485 nm, confirming a faster propagation at the exchange solution exposed top surface compared to the bulk of the crystal. Reproduced with permission from ref. 81, copyright 2024 Advanced Materials.

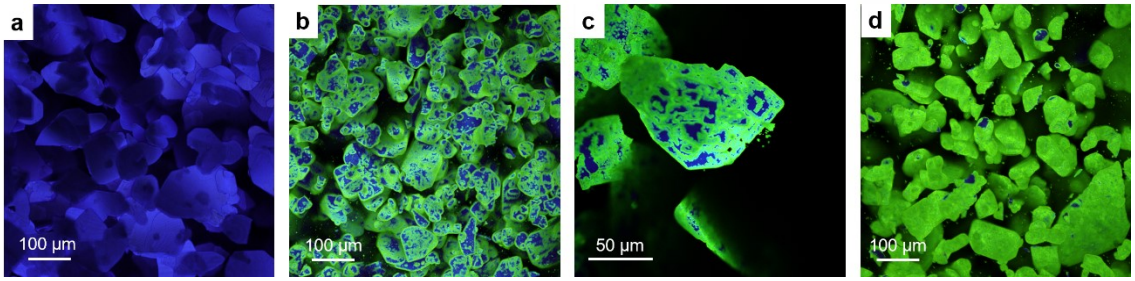

Figure 3.10. PL confocal images of PEA_2PbBr_4 microflake powders: a) before, b) after 5 min, c) 30 min, and d) 300 min of bromide to iodide exchange. Reproduced with permission from ref. 81, copyright 2024 Advanced Materials.

A spectrophotometer (Edinburgh Instruments), which provides above-bandgap excitation and improved spectral resolution in the ultraviolet region (350 nm), was used to investigate the optical characteristics of the powders and heterojunctions. Overall, the same behavior was observed in the confocal experiment, as shown in **Figure 3.6**, of single microflakes, as shown in **Figure 3.11a**. The pristine PEA_2PbBr_4 powders show dual PL bands at 411 and 422 nm. The higher energy band can be assigned to the band edge exciton emission. The lower energy band can relate to re-absorption and emission, defect state, or surface/edge [108,109]. Notably, the lower-energy band vanished after a brief exchange reaction (5 min), producing new PL emissions at 517 and 530 nm. The quenching of the lower-energy band at 422 nm can be attributed to the formation of an iodide-rich phase at the edges of the microflakes, where surface or edge states act as defective sites that facilitate the exchange process. Prolonged exchange reactions further enhance the contribution of PEA_2PbI_4-related PL while diminishing the intensity of the PEA_2PbBr_4-related band. Notably, the spectral positions of the PL bands remain unchanged throughout the exchange process (**Figure 3.12**), confirming the coexistence of two relatively pure halide phases within the powder samples. Both pristine and exchanged samples were subjected to photoluminescence excitation (PLE) and time-resolved photoluminescence (TRPL) measurements to obtain a better understanding of how the heterostructure interface controls the optical response (**Figure 3.13**). A clear peak corresponding to the bromide-phase band edge can be seen in the PLE spectrum captured in the iodide-phase emission band (522 nm), indicating that photoexcited carriers have relaxed throughout the heterostructure. In addition, the iodide phase shows a significantly lower emission quantum yield and faster PL decay (**Table 1** and **2**). This behavior indicates that the iodide phase introduces efficient pathways for rapid nonradiative recombination.

Table 1. Fitting results of the PL decay in **Figure 3.13** and **3.24**.

	λ_{ex} (nm)	λ_{em} (nm)	τ_1 (nm)	a_1	τ_2 (nm)	a_2
PEA_2PbBr_4	372	412	3.10	0.98	16.43	0.02
PEA_2PbI_4	372	524	0.82	0.98	8.05	0.02
PEA_2PbI_4	508	524	0.90	0.99	9.67	0.01
Br → I	372	412	1.77	0.95	6.31	0.05
Br → I	372	522	1.83	0.97	12.44	0.03
Br → I	508	522	0.15	0.99	2.31	0.01
I → Br	372	522	1.80	0.97	11.90	0.03
I → Br	508	522	0.91	0.98	7.17	0.02
I → Br	372	406	0.74	0.9	6.36	0.01
I → Br	372	510	2.10	0.99	12.97	0.01

Table 2. PLQY values of exchanged powder samples obtained by measurements with an integrating sphere.

	PLQY 385 (nm) – 700 nm (%)	PLQY 385 (nm) – 450 nm (%)	PLQY 450 (nm) – 700 nm (%)
PEA_2PbI_4	0.57		
Br-I 5 min	1.46	0.6	0.86
I-Br 300 min	0.76		
PEA_2PbBr_4	12.87		

X-ray diffraction (XRD) data observation represents that the exchanged structures have a new set of equidistant reflexes that agree well with the PEA_2PbBr_4 microcrystal and the PEA_2PbI_4 reflexes. Over time, the bromide-phase reflexes' intensity ratio falls compared to the iodide phase in the bromide-to-iodide case. This pattern makes sense because the iodide-phase volume increases as the phase boundary moves inward toward the microflakes' center. Notably, the composition (or volume) ratio of the bromide and iodide phases within the exchanged microcrystals can be directly inferred from the XRD data. However, because of the high surface sensitivity of PL and the distinctions between radiative and nonradiative decay pathways, PL intensity is not a good measure of the phase ratio. Based on the intensity ratio of the (0010) and (005) reflexes in XRD, extended exchange reactions produce an iodide-phase content of xI = [I]/([I]+ [Br]) = 0.34. X-ray fluorescence (XRF) verified a similar value of xI=0.26 (**Figure 3.12**). Interestingly, the exchanged samples' UV–vis spectra show a slightly blue-shifted low-energy absorption peak when compared to independently synthesized PEA_2PbI_4 microflakes (**Figure 3.11a**). A similar trend is observed in the XRD patterns (**Figure 3.11b,c**), where the bromide-phase reflexes first shift toward lower angles and

subsequently toward higher angles at the longest exchange times. The same continued shift toward the higher angles can also be observed for the iodide phase reflexes by increasing the exchange reaction time, which has a good match with the signal of the pristine PEA_2PbI_4 control for long reaction times. The results ascribe the small shifts of the XRD signals to a minor presence of alloyed mixed phases caused by the exchange reaction [98,100].

Energy-dispersive X-ray spectroscopy (EDX) and scanning electron microscopy (SEM) were used to analyze the exchanged microcrystals' composition and morphology. PEA_2PbBr_4 microflakes grown on Si substrates had distinct rectangular or square morphologies before the bromide-to-iodide exchange (**Figure 3.1 and 3.14**). The presence of the iodide phase was indicated by the appearance of a micrometer-wide bright region along the flake edges following the exchange reaction. On the other hand, EDX elemental mapping verified that the darker central region represented the bromide phase (**Figure 3.11d and 3.14**). Atomic force microscopy (AFM) height profiles showed thinner areas and an uneven interface between the frame and core with alternating stripes of reduced contrast (**Figure 3.15**). These findings are consistent with a solvation–recrystallization mechanism in which the exchange front gradually consumes the bromide phase. The bromide phase is gradually consumed at the exchange front and recrystallizes into an iodide-rich phase, according to a solvation–recrystallization mechanism supported by these observations. To sum up the Bromide to the iodide exchange process, it has been concluded that the reaction is based on solvation and recrystallization process mechanisms, which leads to the formation of a core-frame lateral heterostructure with almost pure PEA_2PbBr_4 (core) and PEA_2PbI_4 (frame) phase.

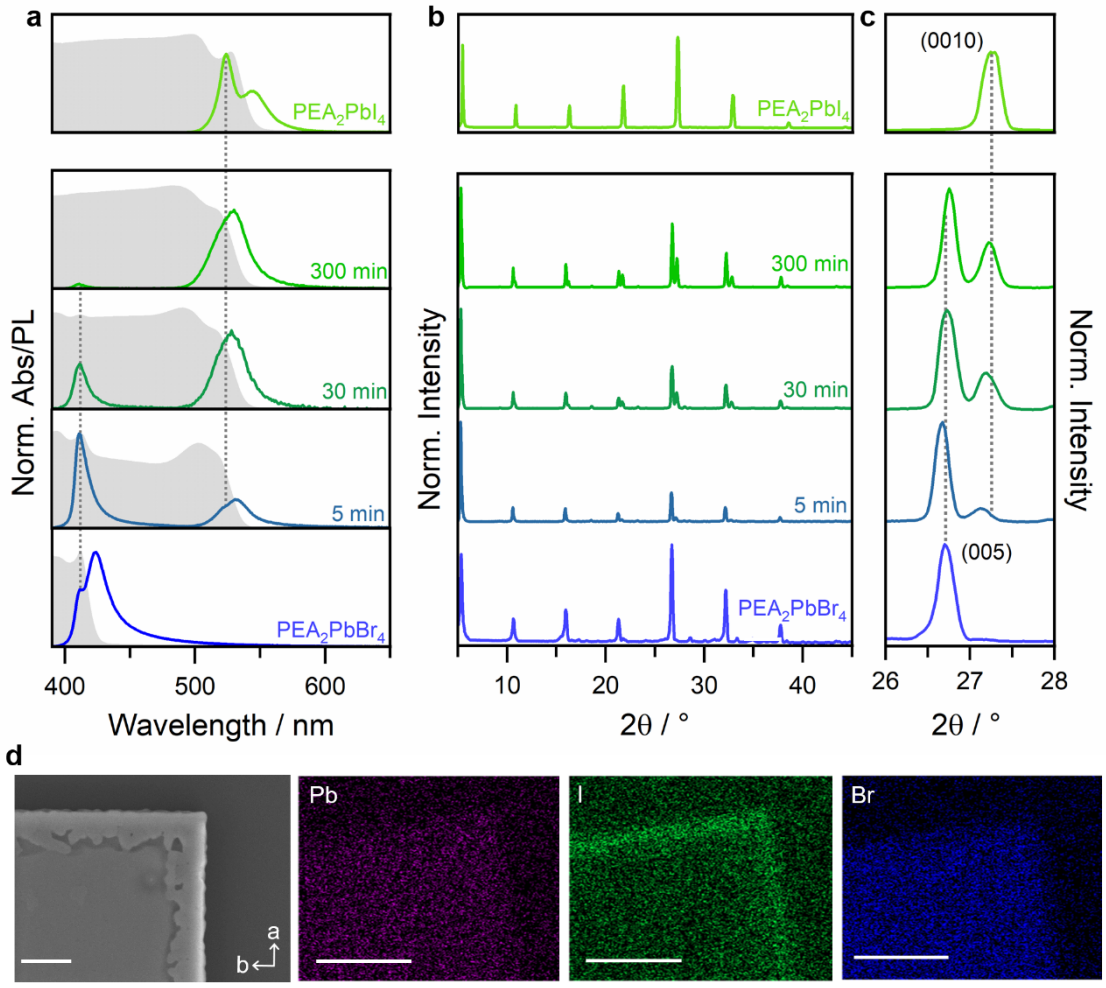

Figure 3.11. Structural and optical properties of the PEA_2PbBr_4-PEA_2PbI_4 heterojunctions recorded by bromide to iodide exchange compared to their pristine counterpart. a) Optical properties including UV-vis absorption (shaded area) and PL (continuous lines, excited at 350 nm) spectra of PEA_2PbBr_4 powders treated with PEAI in octanol for 5, 30, and 300 min. b) XRD pattern of the same powder samples as in a), and c) the magnification of the XRD pattern. d) HAADF-STEM images of a PEA_2PbBr_4 microflake after the bromide to iodide exchange process, and related STEM images corresponding to Pb, I, and Br (left to right), respectively (scale bar 1 μm). Reproduced with permission from ref. 81, copyright 2024 Advanced Materials.

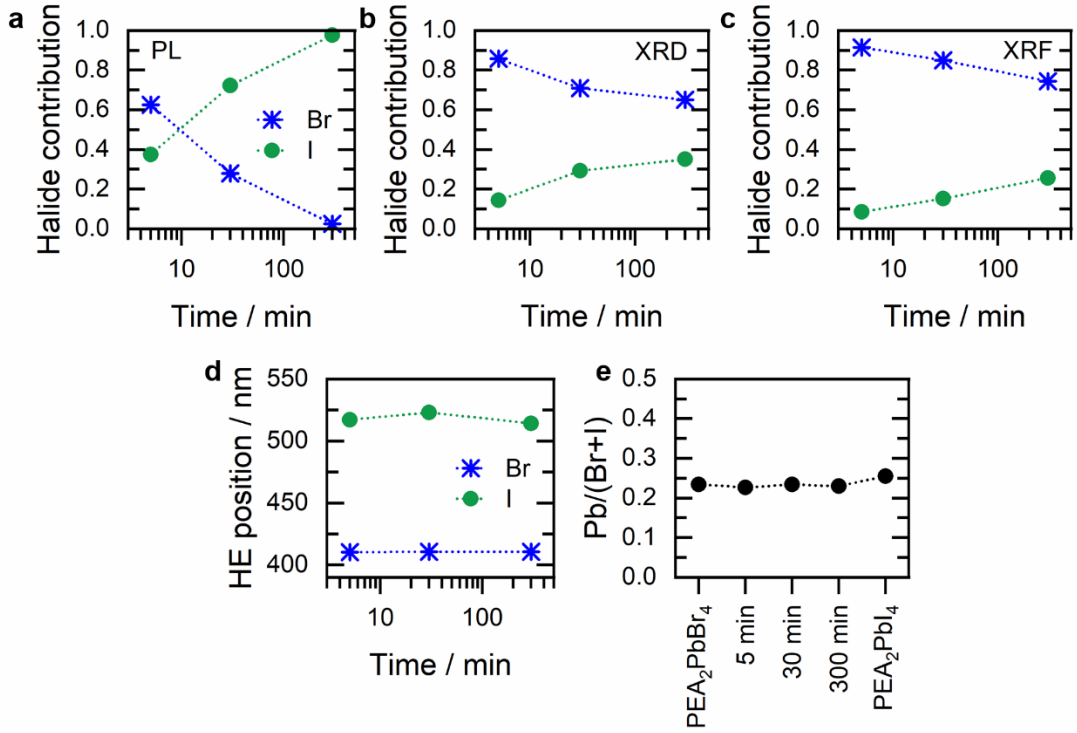

Figure 3.12. a), b), and c) contribution of the bromide and iodide signals to the PL, XRD, and XRF signals, showcasing that the contribution of the bromide and iodide signals strongly deviates between the different techniques. d) The position of the HE band for bromide and iodide, respectively, showing no shift over time. e) [Pb]/([Br]+[I]) ratio extracted from the XRF data shows no change in the ratio during the treatment with PEAI in octanol. Reproduced with permission from ref. 81, copyright 2024 Advanced Materials.

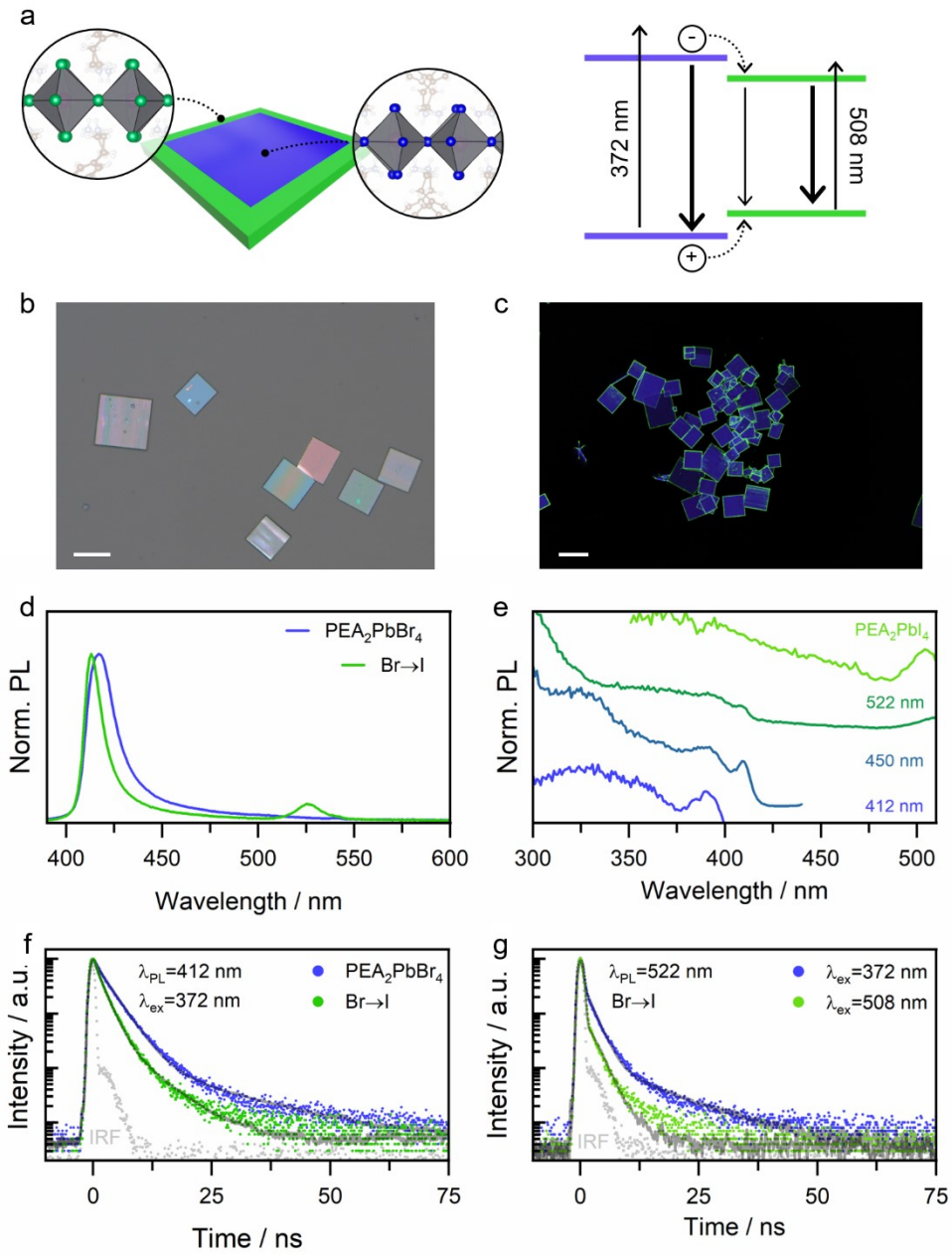

Figure 3.13. PL, PLE, and TRPL of microflakes for the bromide to iodide exchange. a) Scheme of the core-frame architecture and the excitation-relaxation mechanism in the heterojunctions for excitation above (372 nm) and below (508 nm) the band gap and alignment of PEA_2PbBr_4 and PEA_2PbI_4. Optical b) and confocal PL c) images with scale bars of 20 µm and 50 µm, respectively. d) Normalized PL spectra of pristine PEA_2PbBr_4 microflakes and bromide to iodide exchange PEA_2PbBr_4-PEA_2PbI_4 heterojunctions. e) PLE spectra measured from the heterojunctions at different detection wavelengths, and of a pristine PEA_2PbI_4 powder sample (at 525 nm) for comparison. f), and g) PL decay traces for different detection and excitation wavelengths, showing for the pristine PEA_2PbBr_4 powder samples for comparison. PL

decay traces were fitted with two components. The results are summarized in **Table 1**. Reproduced with permission from ref. 81, copyright 2024 Advanced Materials.

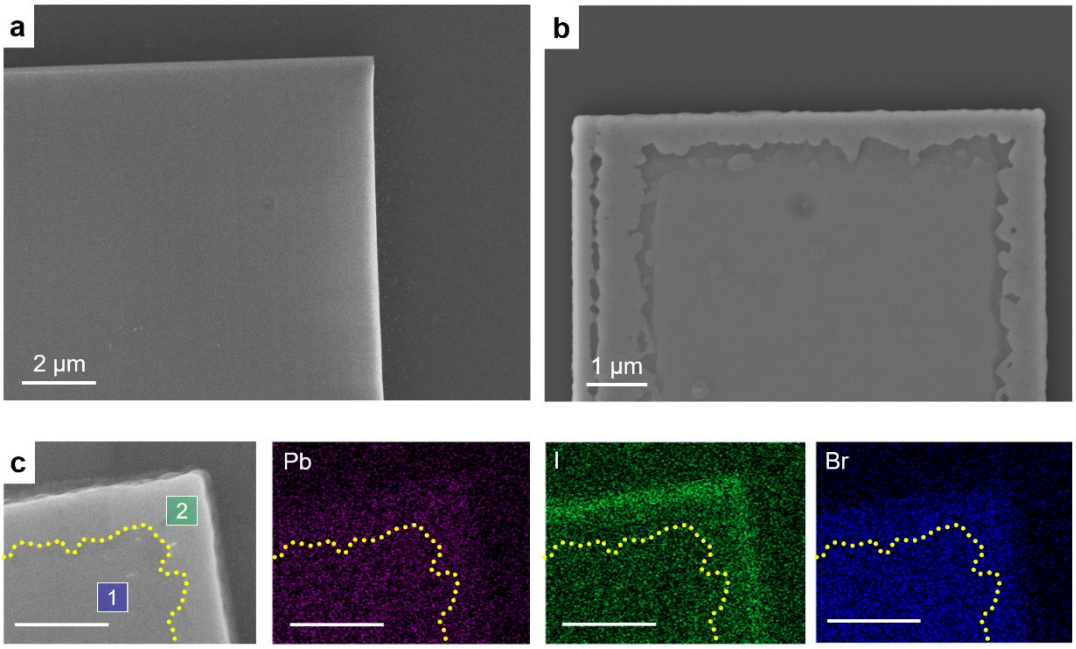

Figure 3.14. SEM images of PEA_2PbBr_4 microflake, a) before, and b) after the Bromide to iodide exchange, representing the microflake changes caused by the exchange process. c) SEM images and corresponding EDX elemental maps for Pb, I, and Br (left to right), respectively. The dotted line shows the boundary between the new microflake feature and the central region. Projecting this boundary to the EDX elemental map shows a mismatch, probably due to the thin surface layer of iodide. The elemental composition of the represented regions is provided in **Table 3**. Reproduced with permission from ref. 81, copyright 2024 Advanced Materials.

Table 3. Elemental composition of the regions 1 and 2 in **Figure 3.14**.

Spectrum 1	At. %	XBr	Spectrum 2	At. %
Br	76.80	0.77	**Br**	58.98
I	-		**I**	17.62
Pb	23.20		**Pb**	23.40

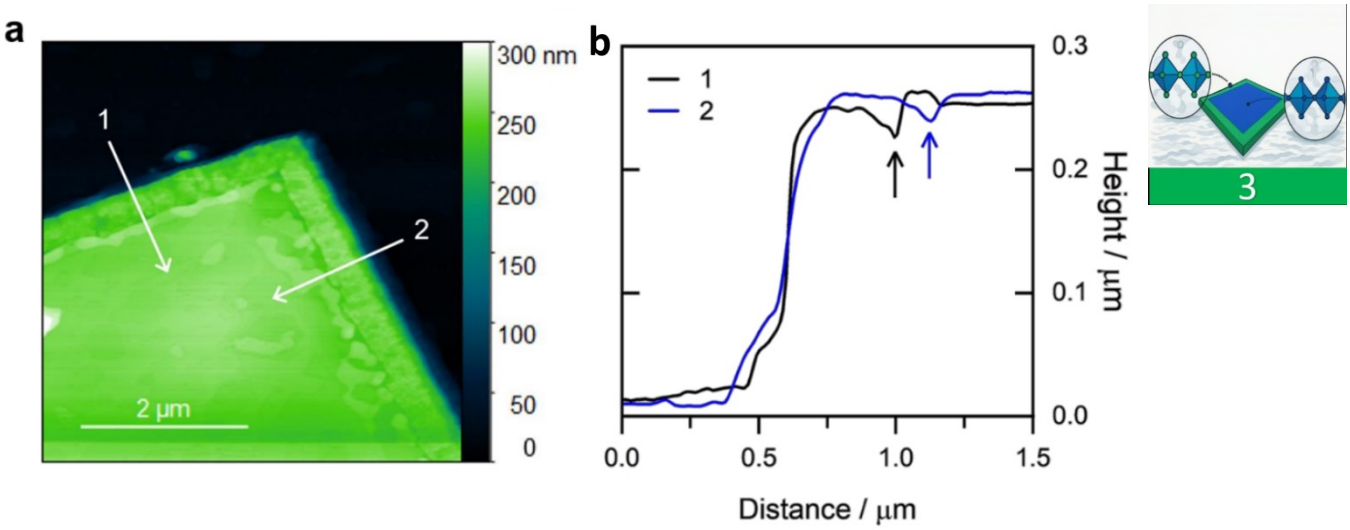

Figure 3.15. a) AFM image of a PEA_2PbBr_4 microflake after bromide to iodide exchange. b) Height profile along the arrows shown in a) confirms the existence of a gap between the central regions and the edge (marked by arrows). Reproduced with permission from ref. 81, copyright 2024 Advanced Materials.

3.3 Cathodoluminescence mapping on pristine PEA2PbBr4 and PEA2PbI4 structures

In this section, PL was employed to investigate the local optical response of the reported 2D perovskites. At the same time, cathodoluminescence (CL) measurements were performed using SEM-CL to capture the photoemission signatures of different perovskite phases. The optical characteristics of these techniques were associated with the chemical distribution, and CL made it possible to use a concentrated electron beam for nanoscale probing. Hyperspectral CL analysis was performed on the PEA_2PbBr_4–PEA_2PbI_4 core–frame heterojunction, pristine PEA_2PbBr_4, and pristine PEA_2PbI_4. Although CL remains relatively underexplored in studying 2D layered perovskites, its fundamentally distinct excitation mechanism offers valuable complementary insights into their optical properties. A pulsed electron beam was employed to mitigate potential electron beam–induced damage, such as local heating, inelastic scattering, and knock-on effects, which are common concerns in halide perovskites and other 2D materials. This operating mode enabled the collection of sufficient CL signal at currents on the order of several tens to hundreds of picoamperes [110,111]. In this regard, MultiVariate Analysis (MVA) was applied to create high-resolution emission maps and to maximize the information output from hyperspectral maps, which can be utilized to highlight correlations in the local spectral features as well as to increase the signal-to-noise ratio (SNR) significantly [112]. It can provide certain proof of a successful halide exchange process by enabling accurate spatial localization and recognizing the unique components within the heterojunction.

First, pristine PEA_2PbBr_4 and PEA_2PbI_4 microflakes were analyzed to create a reference for comparison with the CL mapping of heterojunctions. Measurements were conducted at an acceleration voltage of 10 kV with an average integrated pulsed beam current of ~100 pA, effectively minimizing surface-induced damage to the microflakes. The hyperspectral maps represent an apparent and distinctive spatial distribution of emission that was recorded for both pristine PEA2PbBr4 and PEA2PbI4 microcrystals. Accordingly, a predominant strong radiative emission was observed at the edge of the microflakes. At the same time, the central regions show a spectral and lower emission, as shown in **Figure 3.16**. For the bromide- and iodide-based compounds, the primary emission peaks were observed at 407 nm and 528 nm, respectively, accompanied by weaker secondary emissions at longer wavelengths. The regions where measurements were made for the corresponding pristine microflakes are confirmed by the PL spectra displayed in **Figures 3.16g, h**. Without the apparent resolution of two separate peaks, the PL spectrum for the bromide-based sample showed a broad emission resembling that seen in CL. Aside from a minor shift in absolute wavelength, which is a frequently mentioned discrepancy between the two methods, the iodide-based sample, on the other hand, showed a splitting of PL peaks that matched the CL results quite well. Two different emission contributions, located at the edges and in the bulk, are reflected in this spectral complexity. It's also important to keep in mind that the CL process is made up of several sequential steps, each of which has an impact on the signal that is detected: (i) interaction between the material and the primary electrons; (ii) carrier diffusion; (iii) radiative recombination; and (iv) photon extraction. To get higher emissions along the edges, there are several potential phenomena, depending on the morphology and chemical composition of the microflakes under testing. Moreover, 2D layered perovskites are especially vulnerable to the high-energy electron beam, which can cause damage through chemical changes, introduction of defects, and sample heating [111]. The beam damage can influence the intrinsic factors and optical emission [111]. For instance, spatial heterogeneity of the CL signal can be influenced by an inhomogeneous distribution of halide species (from beam damage, synthesis, or aging). The morphological features and defects can influence the local radiative recombination efficiency, including the rough exposed edges of microflakes that constitute the edges of crystals. It is important to note that carriers in 2D layered perovskites exhibit lateral diffusion lengths on the order of micrometers [113,114], which are significantly longer than their vertical diffusion lengths due to the intrinsic anisotropy of these materials. As a result, carriers can readily migrate to recombination sites at the crystal edges [114–116]. The distinction between primary and secondary emission signals can thus be attributed to this anisotropic diffusion, in combination with the complex microflake morphology, both of which contribute to spatial heterogeneity in the emission. Since detectable photons are less likely to be produced by radiative recombination, which takes place deeper in the crystal, photon reabsorption in the perovskite further complicates the response.

Thus, self-absorption modifies the spectral profile of the CL signal, attenuating higher-energy photons in particular. This mechanism explains the red-shifted nature of the secondary emission, which originates predominantly from the bulk. To estimate the volume sampled during CL analysis, the interaction of the electron beam with the microflakes was simulated. As shown in **Figure 3.17**, the calculated interaction volume for both bromide- and iodide-based samples was less than the microsheet thickness ascertained by profilometry. Since the resulting emissions mainly originated from a depth of 100-500 nm, the detected signals reveal the bulk properties of the crystals. A thorough investigation was conducted to determine the source of the secondary emission. The SEM images revealed that the microflakes had irregular morphologies and varied thicknesses (**Figure 3.17**). Areas with greater overall thickness or greater thickness variation had the majority of secondary emission. Several of the previously mentioned factors, such as differences in photon extraction geometry and defects, can be responsible for this behavior. Additionally, increasing the intensity of the CL signal in regions that are thicker and have substantial thickness differences is caused by the carriers excited in-depth, which can move in-plane and recombine in areas that are close to the top surface (shallower), from which photons are more likely to be collected. The luminescence in neighbouring areas can be due to the electrons being injected in thick areas, and thinner areas at the same depth in the sample as the volume where carriers are created. Because the CL signal intensity is assigned to the pixel being scanned, while photons are collected from the entire sample, this process results in apparently stronger luminescence being mapped to thicker (elevated) areas relative to their surroundings.

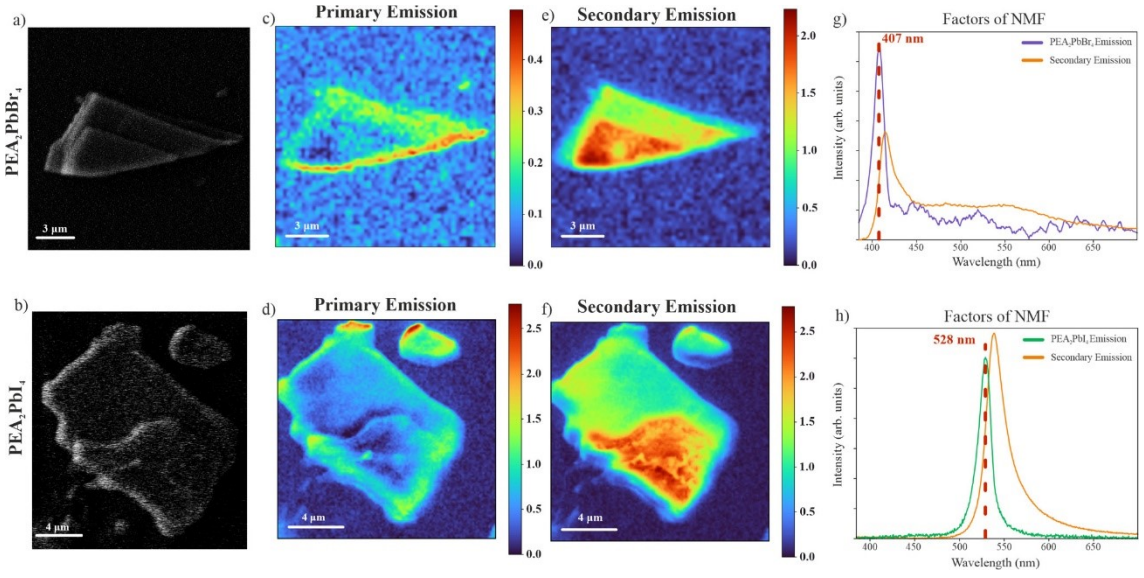

Figure 3.16. a, b) Secondary electron images of the microflakes. Spatial CL distributions of the pristine PEA_2PbBr_4 sample showing c) primary and e) secondary emissions, and of the pristine PEA_2PbI_4 sample showing d) primary and f) secondary emissions. g, h) Decomposition components extracted from CL hyperspectral maps for

the pristine PEA_2PbBr_4 and PEA_2PbI_4 structures, respectively. Reproduced with permission from ref. 87, copyright 2023 Nanotechnology.

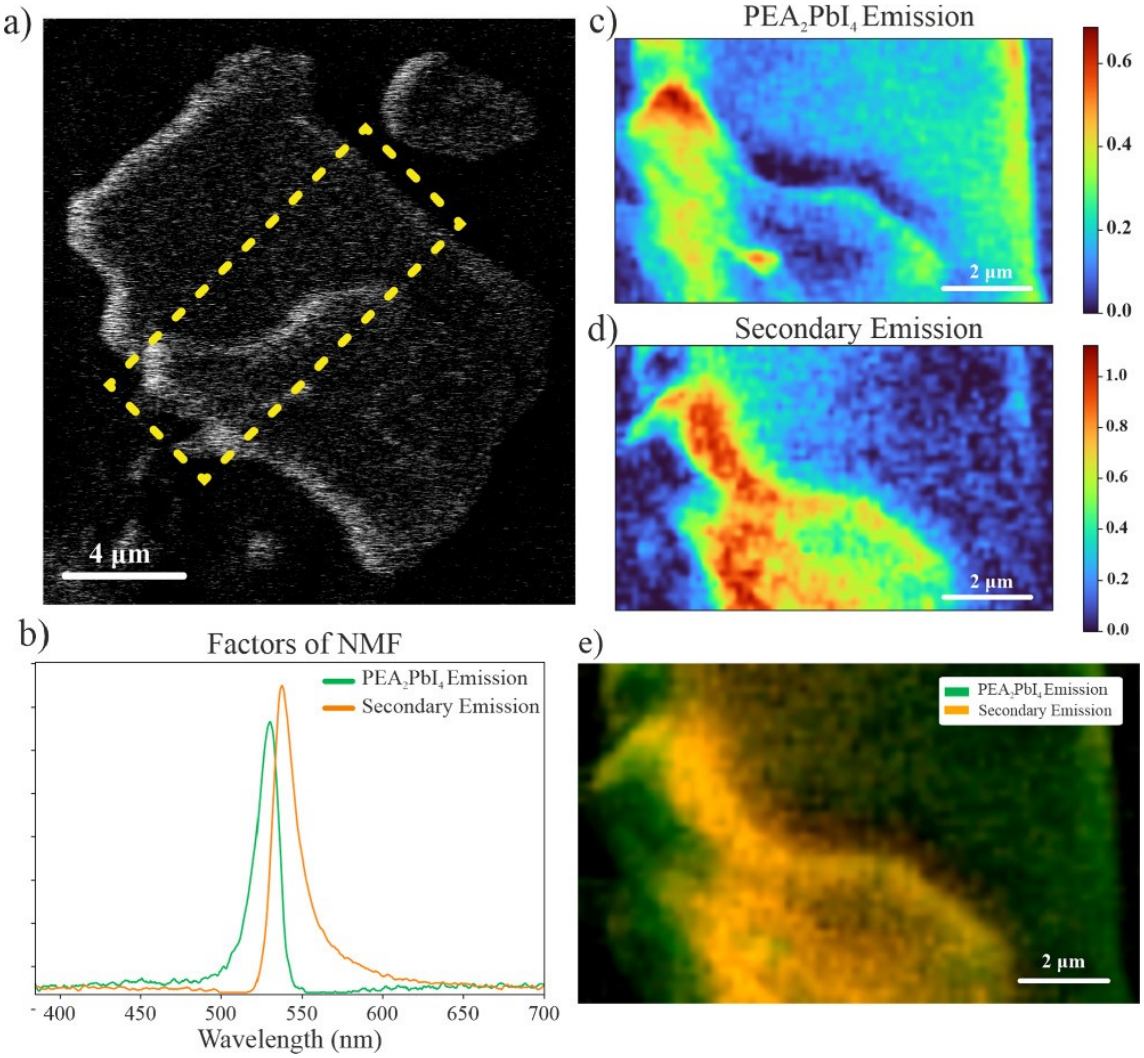

Figure 3.17. a) Secondary electron image of a pristine PEA_2PbI_4 microflake. b) The decomposition component was extracted from CL hyperspectral maps of the same microflake. Spatial CL emission intensity maps showing c) primary, d) secondary, and e) overall emissions, respectively. Reproduced with permission from ref. 87, copyright 2023 Nanotechnology.

3.4 CL mapping on PEA_2PbBr_4-PEA_2PbI_4 in-plane heterojunction

CL mapping was applied to investigate the halide-exchanged heterojunctions under similar experimental conditions. For the pristine microflakes, the CL data showed overall qualitative consistency with the PL results (**Figure 3.18**). On the other hand, the CL hyperspectral dataset analysis showed that the emission from the phase can be clearly separated, and that the single PEA_2PbBr_4 and PEA_2PbI_4 crystal phases also exhibit internal differences. It is possible to identify three main components. The first two components are the emission from bromide- and iodide-based 2D perovskites, resembling those exhibited in pristine structures. The third component modeled the

secondary emissions, which visibly altered the wavelength and the shape of the emission band related to the bromide-based phase.

There is no secondary emission regarding the PEA_2PbI_4 section of the heterosjunction, since it has been localized along the edges, where the secondary component is weaker. The PEA_2PbI_4 segment shows a slight blueshift from 528 to 522 nm, while the PEA_2PbBr_4 emission exhibited a redshift from 407 to 410 nm, comparable with the pristine phases' emission. The emission from PEA_2PbBr_4 originates from the bulk and along the edges of the microflakes and is homogenous in regions lacking significant morphology features, as represented in **Figure 3.19**. The strongest emission remains concentrated at the crystal edges as a secondary emission component is present (orange plot in **Figure 3.18a**). The secondary emission is significantly related to the bromide-based phase, as PEA2PbBr4 constitutes most of the structure, while the PEA2PbI4 phase is confirmed mainly along the edges. A line profile was extracted by integrating over a region of interest to quantify the PEA_2PbI_4 emission across the crystal boundary and assess the co-presence of the bromide signal. **Figure 3.19** demonstrates that strong CL features from both phases are observed within ~500 nm from the surface.

Furthermore, considering inside the microflake, the bromide-based phase is still emissive, while the iodide-based emission has ceased. The SEM-EDX elemental mapping demonstrates the co-presence of iodide and bromide in the region next to the edges. It also shows that both the new iodide and remaining bromide phases are optically active, showing CL's potential to control the halide exchange process. The edge-localized exchange directly results from the 2D layered perovskite crystal structure. The octahedra along the out-of-plane direction are passivated by large organic cations, considerably slowing halide exchange vertically. On the other hand, the in-plane octahedra have a significantly faster exchange rate because they are not passivated. This behavior is consistent with earlier findings in gas-phase exchange methods that use PEA_2PbI_4 vapor and HBr as starting materials [90].

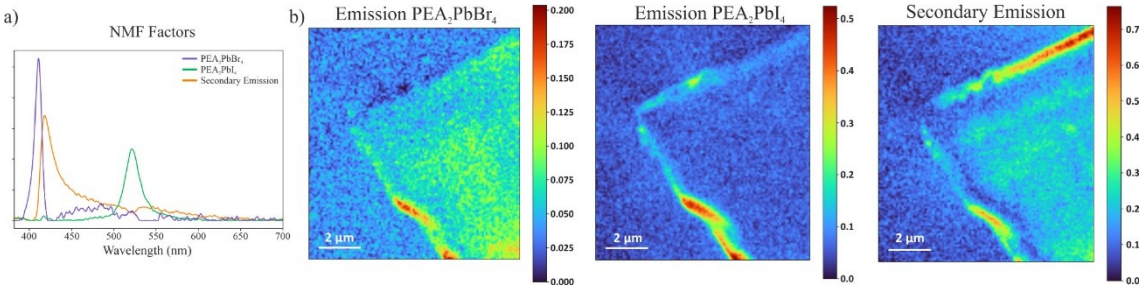

Figure 3.18. a) Decomposition component from CL hypermaps of PEA2PbBr4-PEA2PbI4 heterojunction. b) Spatial distribution of perovskites' primary and secondary emissions. Reproduced with permission from ref. 87, copyright 2023 Nanotechnology.

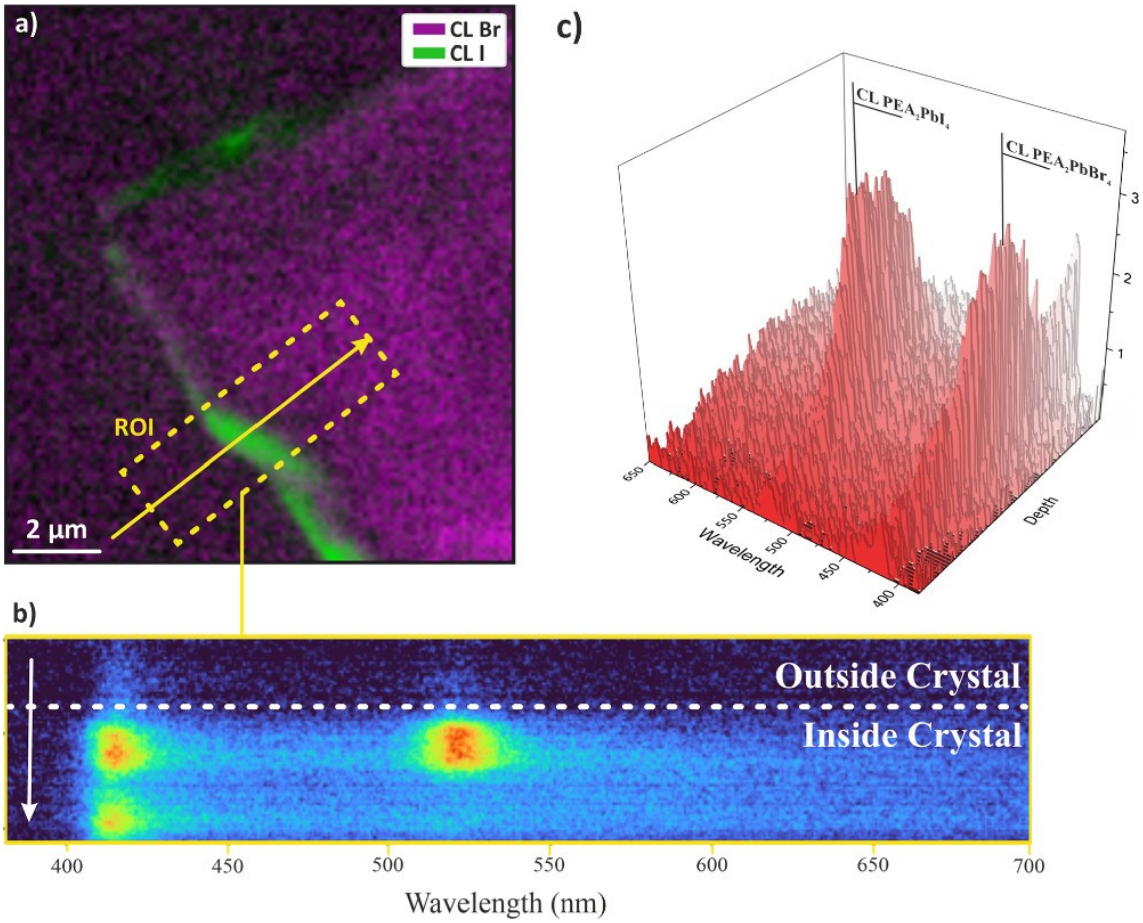

Figure 3.19. a) spatial distribution emission of pristine PEA2PbI4 (green) and PEA2PbBr4 (purple), with the region of interest (ROI) in yellow. b) ROI across emission intensity in line profile through the edge (x-axis: wavelength, and y-axis: distance along line profile). c) Emission profile plot as a function of depth in the microsheet. Reproduced with permission from ref. 87, copyright 2023 Nanotechnology.

3.5 Iodide to the bromide exchange process, core-frame PEA2PbI4-PEA2PbBr4 lateral heterostructure formation

This section investigates the iodide-to-bromide exchange, as the PEA2PbI4 microflakes were exposed to PEABr in an octanol solution. The results represented very different behaviors and mechanisms from those shown in the bromide-to-iodide exchange process. Accordingly, based on in situ controlling of the Iodide to bromide exchange with confocal hyperspectral imaging, it represents a gradual change in the PL spectral position that is shown predominantly along defects, like cracks, and at the edges, at the early exchange reaction times, as shown in **Figure 3.20a, 3.21, 3.21b and 3.22c**. Consequently, the PL spectrum in **Figure 3.20b** shows the location of the most dominant intensive PL band shifts by increasing reaction time from 525 to 507 nm, and a new PL band at 470 nm emerged in parallel. The PL spectroscopy data and Uv-vis

absorption recorded from the Iodide to bromide exchange reactions applied to microflake powders are shown in **Figure 3.23a**. Interestingly, there is no sign of a dominant PL peak at 415 nm, which is related to the formation of the pristine PEA2PbBr4 frame as it was expected, but only resolve a very weak PL band at the mentioned wavelength (**Figure 3.24**).

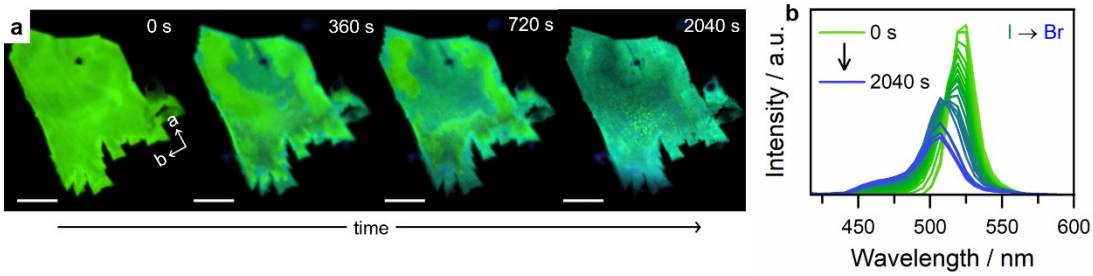

Figure 3.20. In situ tracking of the spatial and temporal dynamics using the iodide to bromide exchange (exciting at 400 nm and scale bar 20 µm) recorded by confocal hyperspectral imaging. **Figures 3.21 and 3.22** provide the full PL confocal images and their correlation with XRD and confocal data. b) The PL spectra extracted from the sequence of the PL confocal images in panel a) show a blue shift from the central emission peak and the appearance of additional emission bands on its high-energy side. Reproduced with permission from ref. 81, copyright 2024 Advanced Materials.

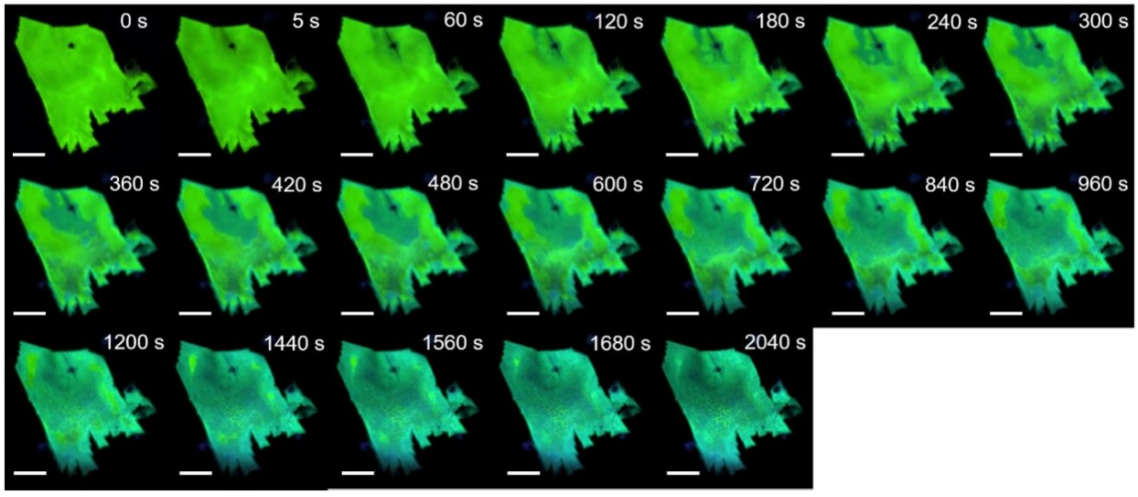

Figure 3.21. Time progression of confocal PL images of a PEA2PbI4 microflake during the iodide to bromide exchange (excited at 400 nm, scale bar 20 µm). Reproduced with permission from ref. 81, copyright 2024 Advanced Materials.

On the other hand, new bands at 512, 502, and 474 nm were resolved, associated with the formation of multiple alloyed phases, and the confocal images show that they are predominantly positioned in the edge region of the microcrystals [117,118]. The UV-vis absorption spectra confirm the formation of mixed alloyed phases, with a

broad, blueshifted absorption band compared to the pristine PEA2PbI4. **Figure 3.25** shows that the position of the new PL bands does not shift by increasing the exchange reaction times, showing a discrete transition from the pure iodide phase to the bromide and mixed alloyed phases. As shown in **Figure 3.25**, however, the relatively intensive single bands are altered by increasing the exchange reaction time, showing changes in the volume ratio of the various phases. In this case, the PL intensity is not a good representative of the size of the different phases, as the photoexcited carriers can relax across the heterostructures into phases with a lower bandgap. As an example, **Figure 3.24** confirms that a peak centered at 406 nm in the PLE spectrum with the detection at 510 nm, therefore, in the emission band of a mixed alloyed phase, which evidences a relaxation pathway from an almost pure bromide phase to a mixed alloyed phase. Intriguingly, the mentioned signal is absent in the PLE spectrum recorded at 522 nm of the more iodide-rich phases. This behavior rationalizes if it has been hypothesized that the Iodide bromide exchange observed using ion diffusion from the outside to the inside of the microflakes, forming onion-type spatially localized mixed alloyed phases in the exchanged frame area. In this scenario, the photo-excited carriers are efficiently harvested by the nearby phase with a lower bromide content or lower band gap.

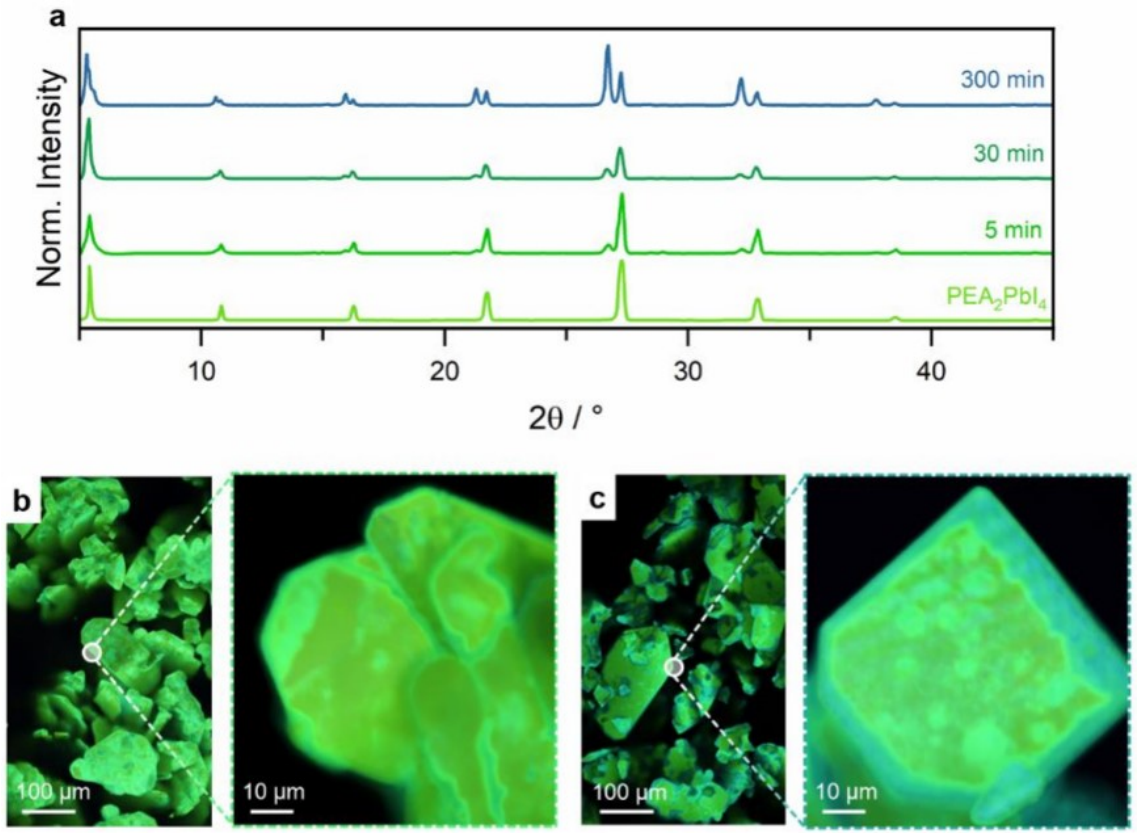

Figure 3.22. a) full XRD patterns related to pristine PEA2PbI4 microflake powders before and after 5, 30, and 300 min of iodide to bromide exchange. b) and c) lower and higher magnification PL confocal images of PEA2PbI4 after 5 and 300 min of iodide to bromide exchange process. Reproduced with permission from ref. 81, copyright 2024 Advanced Materials.

Figure 3.23b shows that the XRD patterns follow a similar trend to those in the bromide-to-iodide exchange process. After immediate exposure to the exchange reaction, a set of new reflexes appeared close to the position of the pristine PEA2PbBr4, which gained intensity by increasing reaction time and eventually became the dominant peak. **Figure 3.26c** shows that the positions of the peaks agree well with the pristine PEA2PbBr4 2D layered perovskites. However, investigation of the various mixed alloyed

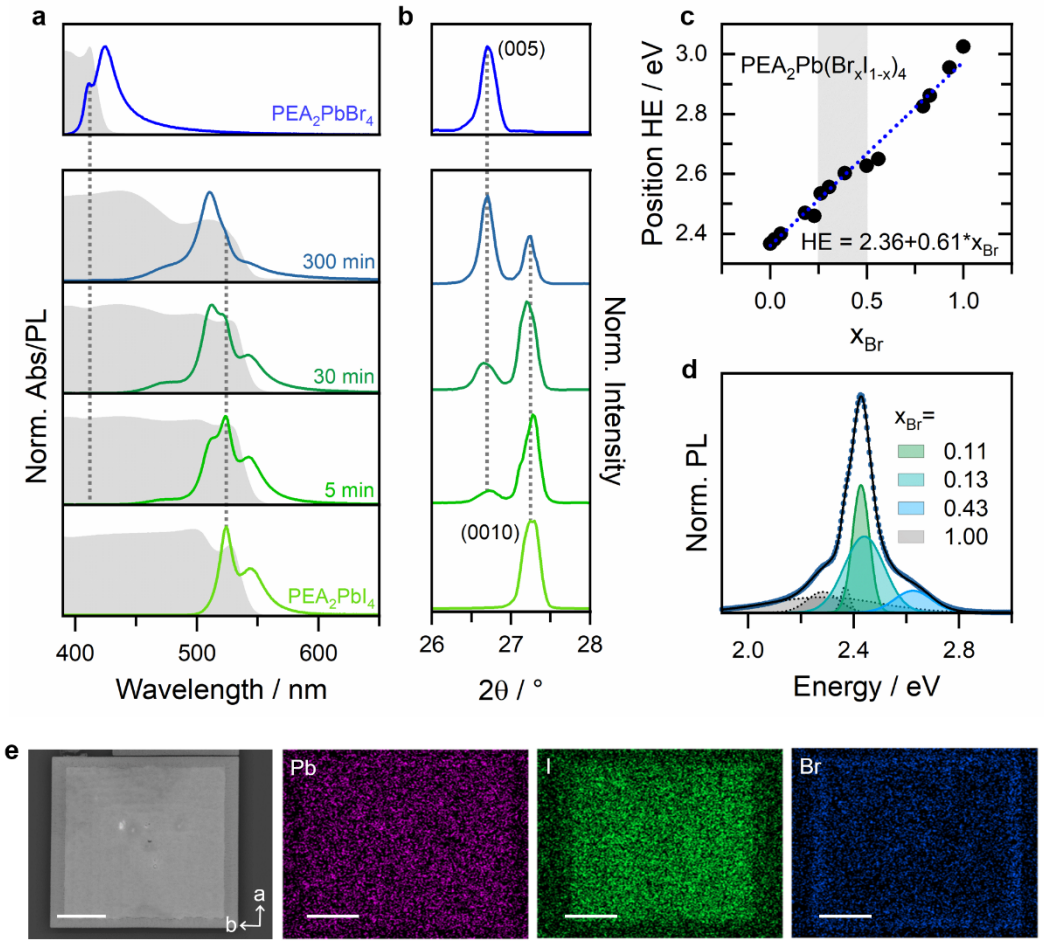

Figure 3.23. Structural and optical properties of heterojunctions acquired by iodide to bromide exchange compared to the pristine structures. a) UV-vis absorption (shaded area) and PL (continuous lines, excited at 350 nm) spectra of pristine PEA2PbI4 powder treated for 5, 30, and 300 min with PEABr in octanol solution. b) XRD pattern of the heterojunction exchanged powder samples centered on the (0010) and (005) reflexes of PEA2PbI4 and PEA2PbBr4, respectively (Figure X provides full patterns). c) PL peak position correlated with bromide content (XBr) of alloyed mixed powder samples of the form PEA2Pb(BrxI1-x)4, synthesized for reference analysis. The grey-shaded area shows the region of phase segregation (Figure X). d) PL spectrum acquired from a pristine PEA2PbI4 powder sample after a long exchange time of 300 min, fitted by a sum of Gaussians. Based on the correlation with the XBr in panel c), the acquired XBr value

was assigned to the various PL bands that emerged from the exchange reaction. e) SEM images and EDX elemental mapping of a single pristine PEA2PbI4 microflake after exposure to PEABr in octanol solution for 10 min (scale bar 2.5 µm). Reproduced with permission from ref. 81, copyright 2024 Advanced Materials.

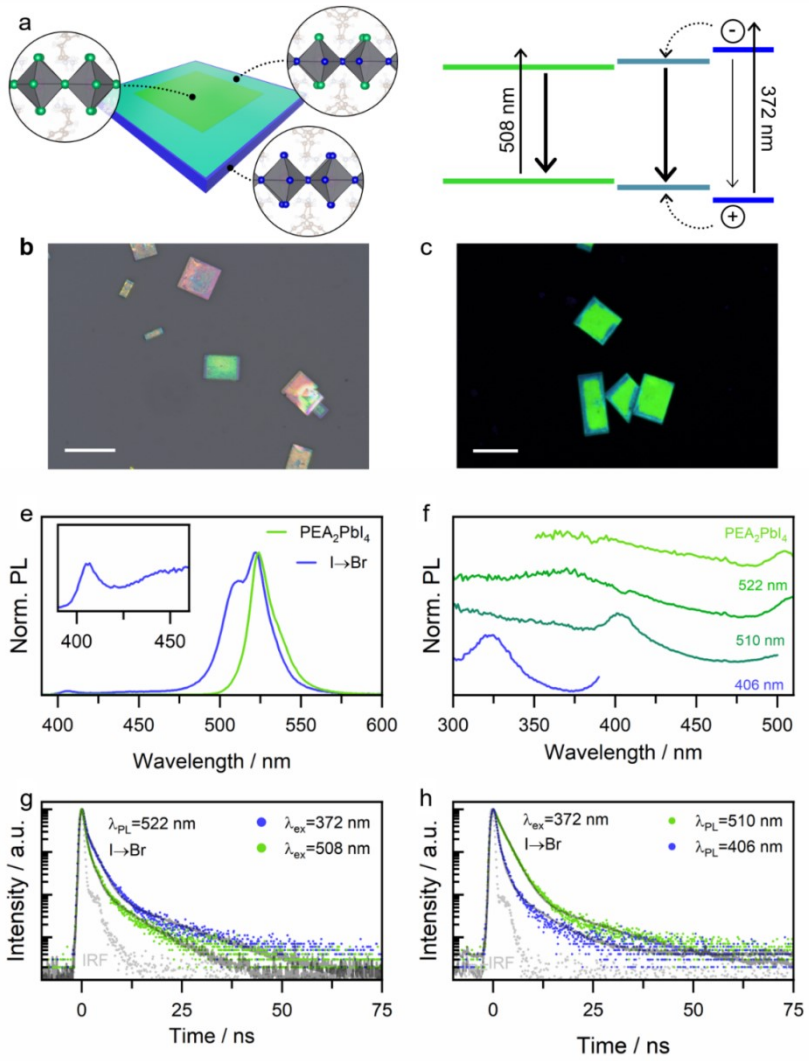

Figure 3.24. PL, PLE, and TRPL of microflakes for the iodide to bromide exchange. a) Scheme of the core-frame architecture and the excitation-relaxation mechanism in the heterojunctions for excitation above (372 nm) and below (508 nm) the band gap and alignment of PEA2PbI4 and PEA2PbBr4. Optical b) and confocal PL c) images with scale bars of 20 µm and 10 µm, respectively. d) Normalized PL spectra of pristine PEA2PbI4 microflakes and iodide to bromide exchange PEA2PbI4-PEA2PbBr4 heterojunctions on glass. The inset also represents a magnification of the spectrum, showing an emission peak corresponding to an almost pure bromide phase. e) PLE spectra measured from the iodide to bromide heterojunction microflakes at the indicated wavelengths. The PLE spectrum of pristine PEA2PbI4 was measured at 525 nm. f) Decay of the PL bands at 406 and 510 nm (excited at 372 nm). g) PL decay at 522 nm

of the exchanged microflakes when excited with 372 nm and 508 nm, respectively. PL decay traces were fitted with two components. The results are summarized in Table 2. Reproduced with permission from ref. 81, copyright 2024 Advanced Materials.

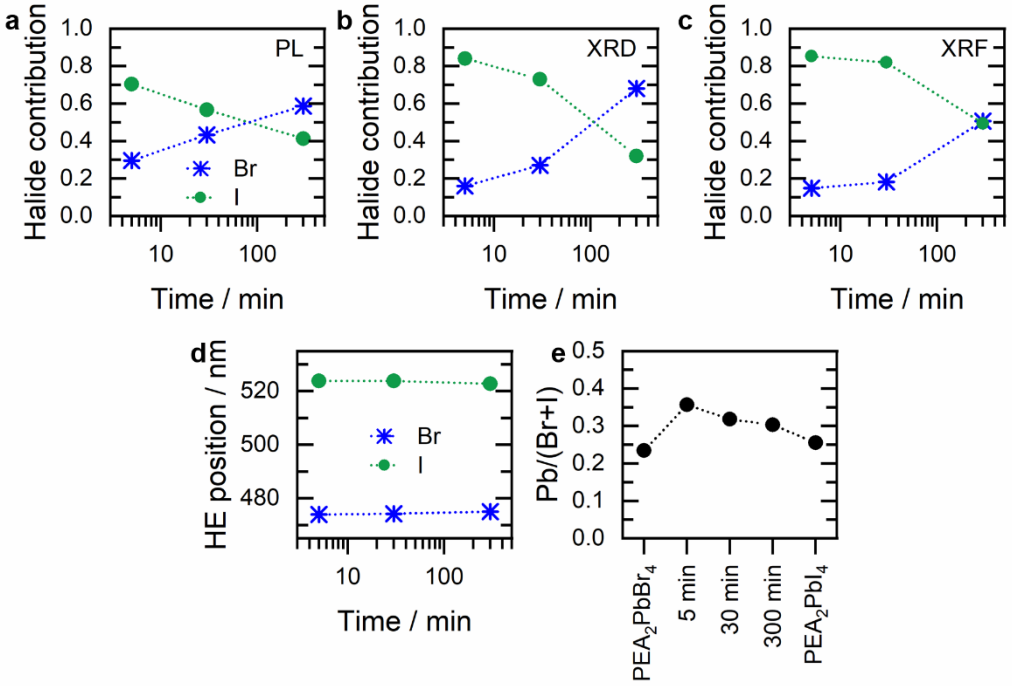

Figure 3.25. The contribution of the iodide and bromide signals to the overall signal of a) PL, b) XRD, and c) XRF indicates a similar trend for the various techniques. d) Position of the HE band for iodide and bromide, where the bromide band corresponds to the highest energy band of the newly appearing PL features. e) [Pb]/([Br]+[I]) ratio extracted from the XRF data. An increase in the ratio shows slight changes in the composition, e.g., due to the leaching of iodide ions into the solution. Reproduced with permission from ref. 81, copyright 2024 Advanced Materials.

Phases show that the location of the 005 XRD peak remains nearly constant for the bromide content (xBr) from 0.5 to 1. Additionally, after the short exchange reaction time of 5 and 30 minutes, a small shoulder indicated the presence of the mixed alloyed phases. The bromide-to-iodide contribution was evaluated using XRF and XRD yields of 0.51 and 0.69, an almost equal ratio of the two bromide and iodide halides (**Figure 3.27**). To confirm the approximation of XBr in the mixed alloyed phases, which show the new PL bands, a series of mixed alloyed phases microflake powder of PEA2Pb(BrxI1-x)4 were synthesized (**Table 4**) and characterized, and their PL were recorded in **Figure 3.27**. A sum of Gaussians fitted the PL spectra (**Figure 3.23c**), and the highest energy band (HE) was correlated to XBr of the mixed alloy phases determined by XRF. HE band was

considered for this correction because it can be assigned to the free exciton emission. The linear relationship between XBr and the HE band, as shown in **Figure 3.23c**, closely resembles Vegard's law [119]. To evaluate XBr of the mixed alloyed phases (**Figure 3.23d**), the fitting of the PL spectra of the exchanged samples by a sum of Gaussians, fixing the position of the pristine PEA2PbI4 band, was used, which yields XBr = 0.11, 0.13, and 0.43. This can confirm the coexistence of multiple mixed alloyed phases in microflakes, most likely positioned at the defect and edge regions. The SEM images in **Figure 3.23e** show the iodide-to-bromide exchanged microcrystals with a sharp interface between the outer frame of the different mixed bromide phases (dark contrast) and the central PEA2PbI4 region (bright contrast). The EDX elemental mapping can confirm this composition distribution. However, the bromide-to-iodide exchange process data show a well-defined and smooth boundary between the two phases. The homogenous thickness and smooth boundary point to anion diffusion, preserving the lattice structure as the mechanism of the exchange reaction.

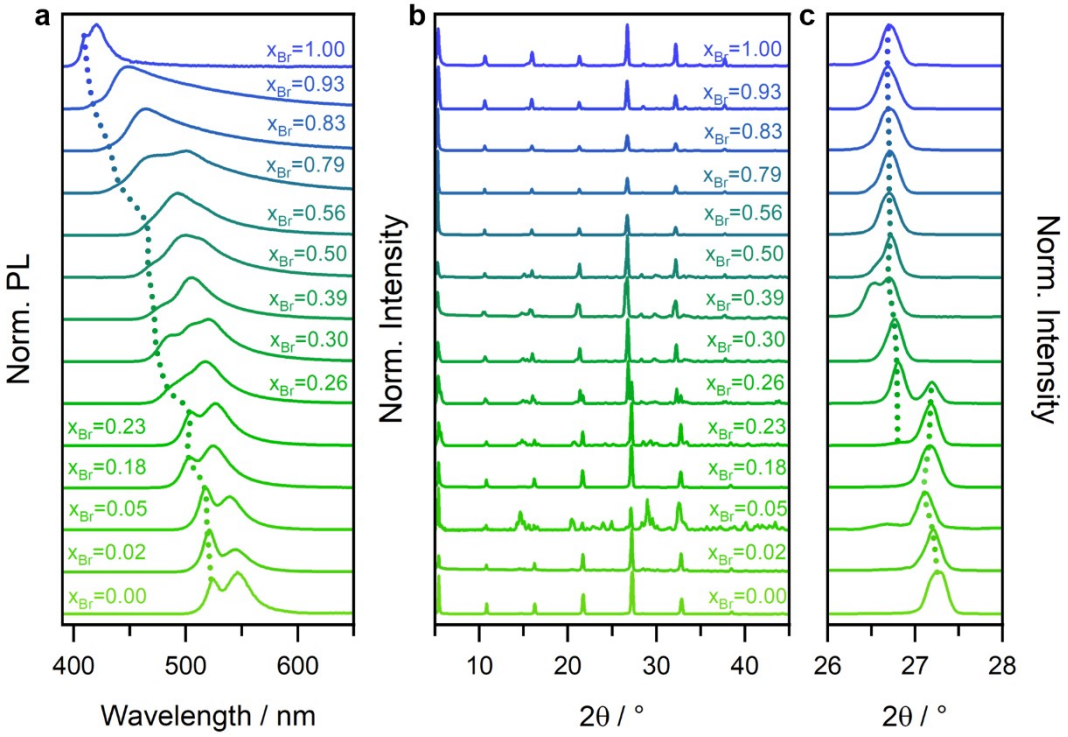

Figure 3.26. Microflake powders in the form of mixed alloyed PEA2Pb(BrxI1-x)4 phases, a) PL spectra, and b) XRD patterns. c) XRD patterns centered on the (0010) and (005) reflexes of PEA2PbI4 and PEA2PbBr4, respectively. The represented XBr by XRF experimentally determined values directly from powders. The dotted line in panel a) shows the position of the HE band extracted from fitting the spectra by a sum of Gaussians. The presence of two reflexes within the range of XBr = 0.23 to 0.5 in c) implied the segregation into bromide- and iodide-rich phases, showing a solubility gap that

results in the coexistence of multiple alloyed phases in the edge regions in the iodide to bromide exchange. Reproduced with permission from ref. 81, copyright 2024 Advanced Materials.

It can be concluded that the iodide-to-bromide exchange leads to a core-frame heterojunction with a smooth heterostructure interface, with a mixed alloyed bromide-iodide phase at the edges and PEA2PbI4 in the center. The mixed alloyed phases with various compositions are presented at the defects and edges, and the optical properties are determined. To get insights into the heterostructure morphology of iodide to bromide exchange on the nanoscale, as mentioned in the experimental section, small and thin crystals were fabricated, which are suitable for transmission electron microscopy (TEM) measurements, and performed scanning TEM-EDX (STEM-EDX) measurements are shown in **figures 3.28-3.33**, including morphological images and EDX elemental mapping of the pristine PEA2PbI4 and PEA2PbI4, and STEM-EDX elemental mapping recorded after the exchange reaction are reported in figures. These investigations with higher spatial resolution revealed a heterostructure with a width of 200 nm and confirmed the core-frame heterojunction. **Figure 3.28a** represents the high-angle annular dark field (HAADF)-STEM images of the overgrowth of the PEA2PbBr4 core with the iodide phase. For those tiny crystals, the irregularity of the frame is improved for the larger crystals that are represented in **Figure 3.11**. As a result, these images can confirm the assignment of a recrystallization process for the growth of the iodide phase. To estimate the extension of the heterostructure interface, **Figure 3.28b** focuses on a relatively regular, where the effects of vertical overgrowth should be minimized. However, a mixed alloyed region of both bromide and iodide contents has still been observed, which can be attributed to the vertical overlap of the two phases (**Figure 3.28d**). On the other hand, the bromide signal remains close to zero for the outer frame region, verifying the purest iodide phase presented there. For the iodide-to-bromide exchange process, as shown in **Figure 3.28f, g**, the exchange region follows a relatively smooth morphology at the interface between the two areas and the morphology of the pristine crystal formation in a regular frame. The iodide content rises almost immediately at the microflake edge, which confirms the mixed alloyed composition in the frame; as shown in **Figure 3.28i**, it goes along with a gradual decrease in the bromide content. The preferential occupancy of specific octahedral sites for different halide types can be used to discuss the possible origin of the two exchange processes [97,98,100]. Accordingly, the bromide anions preferentially occupy the equatorial positions, while the iodide ones prefer to occupy the axial positions. XBr = 0.5 composition is favored where all equatorial positions are occupied by bromide and all axial positions are occupied by iodide. The theoretical investigation predictions illustrated that this is the most stable configuration, which can be confirmed by reports on the photostability of mixed alloyed PEA2Pb(Br0.5I0.5)4 [99,120,121]. The solubility gap in the PEA2Pb(BrxI1-x)4 structure can explain the multiple mixed alloyed phase formation [118]. The reported XRD

patterns in **Figure 3.26b, c** related to mixed alloyed samples can represent a splitting into two reflexes at XBr = 0.23 to 0.5, showing the separation into bromide-rich and iodide-rich phases. During the iodide-to-bromide exchange process, reaching this bromide concentration can lead to phase segregation and the propagation of a phase-segregated process reaction front, which can explain mixed alloyed phases produced in the iodide-to-bromide exchange process. In the case of the bromide to the iodide exchange process, it can be hypothesized that the preferred occupation of iodide in the axial sites leads to instability since it influences the bands to the organic layer, which triggers a local/partial dissolution at the reaction process, from where the iodide phase recrystallizes. Thus, the recrystallized iodide phase slowly degrades over several days, which can be revealed by HAADF-STEM images (**Figure 3.34**) and spatially resolved emission (**Figure 3.35**) after various storage times. Nevertheless, in the case of the iodide to bromide exchange reaction, as shown in **Figure 3.36**, there is no significant sign of degradation.

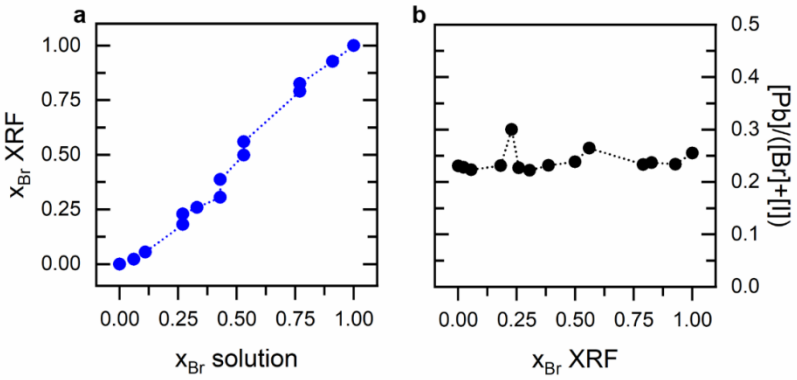

Figure 3.27. a) Br composition (XBr XRF) microflakes in PEA2Pb(BrxI1-x)4 powders versus the Br composition in the precursor solution (XBr solution), as determined experimentally. b) Pb/X ([Pb]/([Br]+[I])) ratio versus the XBr XRF represents a ratio very close to the ideal value of 0.25. Reproduced with permission from ref. 81, copyright 2024 Advanced Materials.

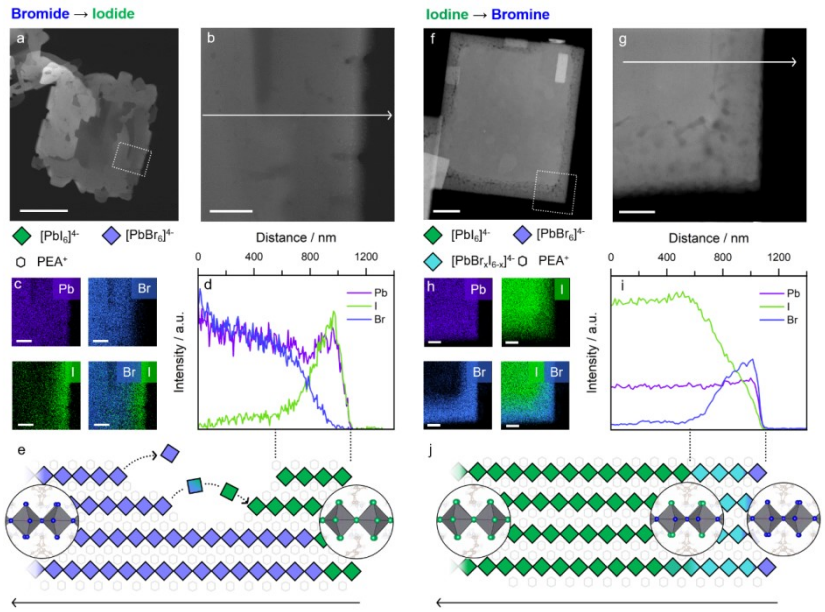

Figure 3.28. Structural and compositional properties of the interface in exchanged heterojunctions. a) HAADF-STEM elemental mapping of an indicative PEA2PbBr4 microflake after the exchange process (scale bar 2 µm). b) Higher magnification image from the marked region in panel a) (scale bar 300 nm). c) Corresponding STEM-EDX elemental mapping (scale bar 300 nm), d) line scan along the arrow in panel b). f) HAADF-STEM imaging of an indicative PEA2PbI4 microflake after the exchange process (scale bar 1.5 µm). g) Higher magnification image from the marked region in panel f) (scale bar 300 nm). h) Corresponding STEM-EDX elemental mapping. e) and i) line scan along the arrow in panel g). j) Illustrate the proposed scheme for the bromide to iodide and iodide to bromide exchange processes. The bromide to iodide exchanges follow a dissolution and recrystallization mechanism, while the iodide to bromide exchange process follows a diffusion mechanism. Reproduced with permission from ref. 81, copyright 2024 Advanced Materials.

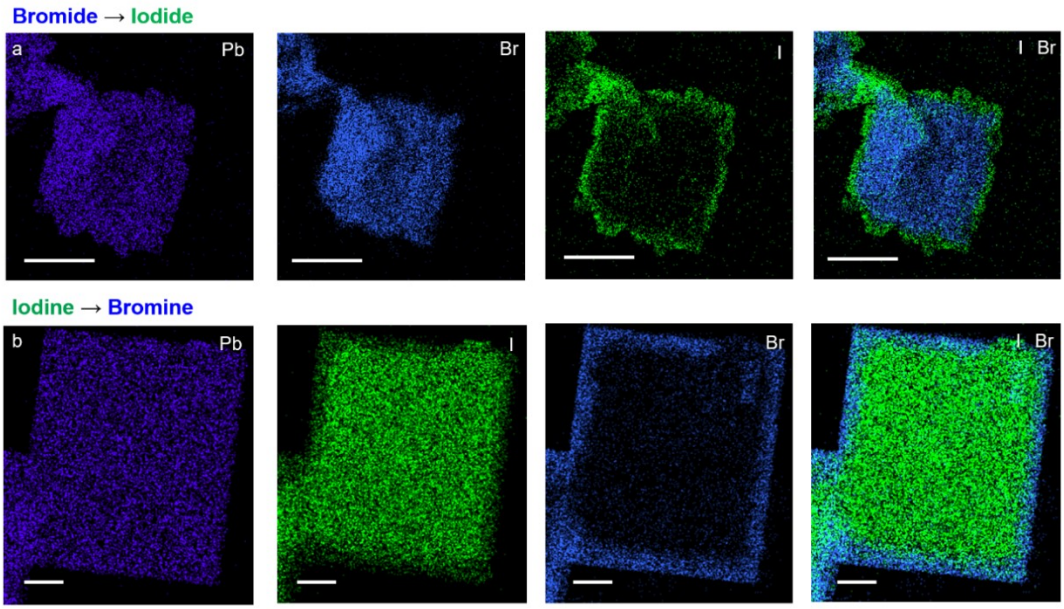

Figure 3.29. HAADF-STEM images of pristine, a) PEA2PbBr4, b) PEA2PBI4 structures, and the corresponding EDX elemental mapping for halide (Br and I), and Pb. Reproduced with permission from ref. 81, copyright 2024 Advanced Materials.

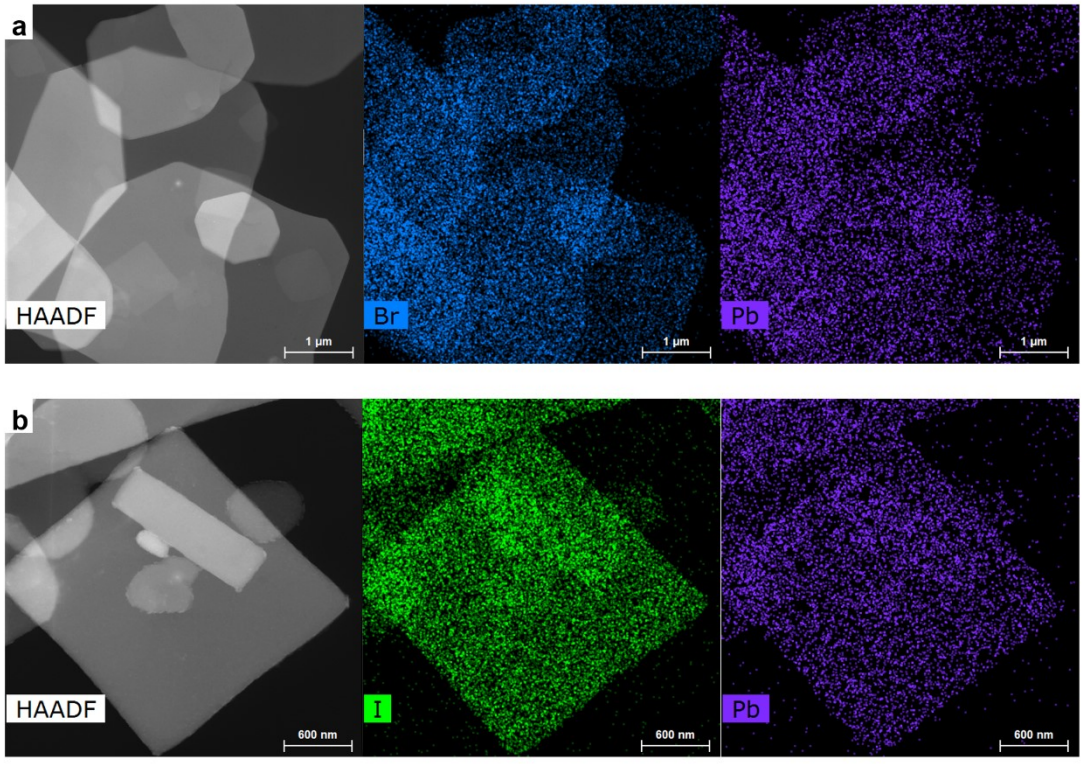

Figure 3.30. STEM-EDX elemental mappings for a) bromide to iodide, and b) iodide to bromide heterojunctions corresponding to the HAADF-STEM images in figure

Xa and Xf in the main text. Scale bars are 2 µm and 1.5 µm, respectively. Reproduced with permission from ref. 81, copyright 2024 Advanced Materials.

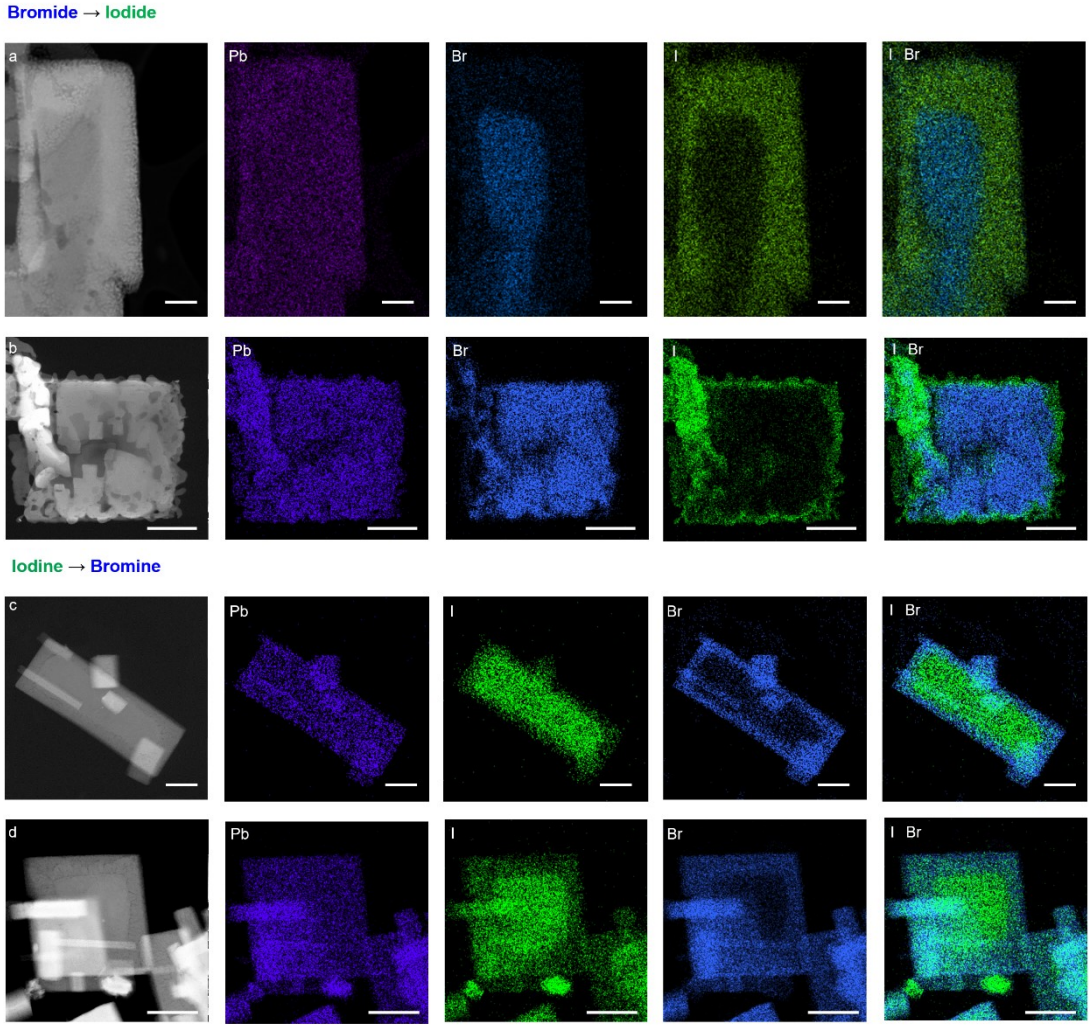

Figure 3.31. Additional STEM-EDX elemental mapping and HAADF-STEM images for the bromide to iodide (a and b, scale bar 200 nm and 2 µm, respectively) and iodide to bromide (c and d, scale bar 1 µm and 2 µm, respectively) exchange processes indicate the consistency of the exchange processes across various samples. Line scans in Figure X were extracted from the marked regions in b and d. Reproduced with permission from ref. 81, copyright 2024 Advanced Materials.

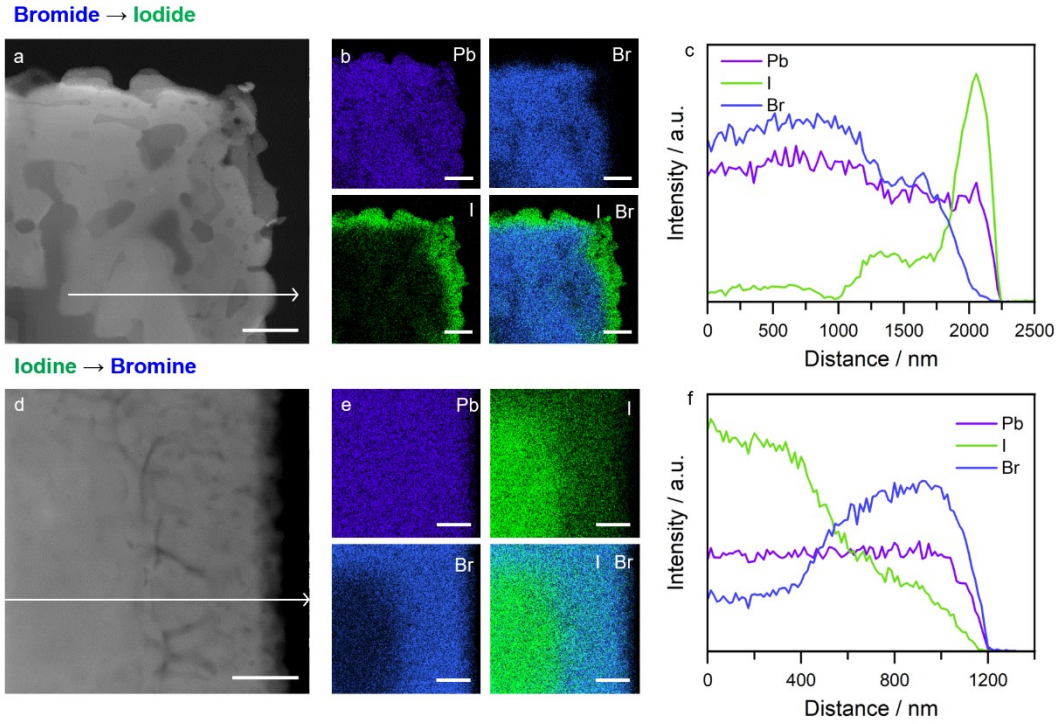

Figure 3.32. HAADF-STEM elemental mappings of the marked regions in figure Xb and Xd with corresponding STEM-EDX elemental mappings (b and e) and line scans (c and f) extracted along the arrow in a and d. Reproduced with permission from ref. 81, copyright 2024 Advanced Materials.

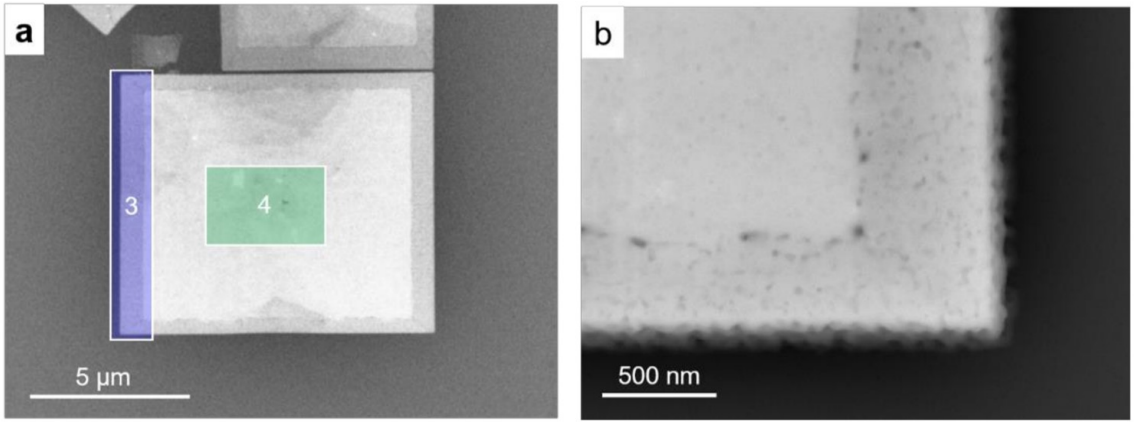

Figure 3.33. a) SEM image of a PEA2PbI4 microflake with the represented region to determine the edge and center composition (**Table 3**). b) A higher magnification SEM image of the same microflake in panel a) represents a sharp boundary in the junction region, and pores mainly appear in the edge region. Reproduced with permission from ref. 81, copyright 2024 Advanced Materials.

Table 4. Elemental composition of the regions 1 and 2 in **Figure 3.33**.

Spectrum 3	At. %	XBr	Spectrum 4	At. %	XBr
Br	51.31	0.66	**Br**	17.78	0.23
I	26.89		**I**	58.99	
Pb	21.80		**Pb**	23.23	

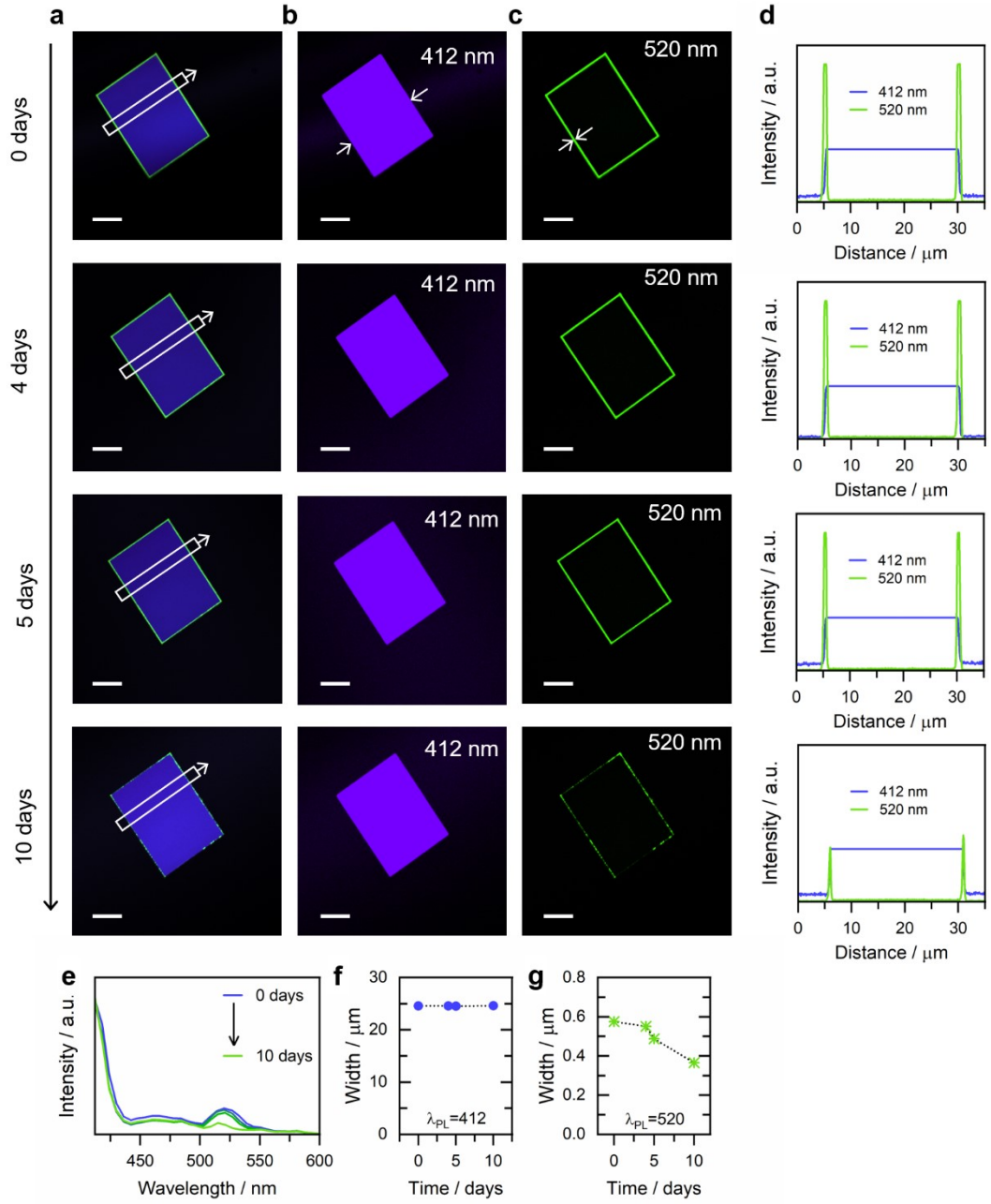

Figure 3.34. Stability test of the junction region after the bromide to iodide exchange over time in ambient conditions in the dark. a) Series of PL confocal images

directly after the exchange process and up to 10 days after storing in ambient conditions (excited at 400 nm, scale bar 10 µm). b), and c) spatial distribution of the PL at 412 and 500 nm (spectral bandwidth 6 nm), respectively. The arrows mark the width of the bromide (412 nm) and (520 nm) region, d) intensity profile of 412 and 520 nm PL extracted along the in a) represented regions for the different storage times. e) PL spectra extracted from the regions in a) are represented over time. f) and g) evolution of the width of the bromide region (412 nm) and iodide region (520nm) extracted from the intensity profile in panel d). Reproduced with permission from ref. 81, copyright 2024 Advanced Materials.

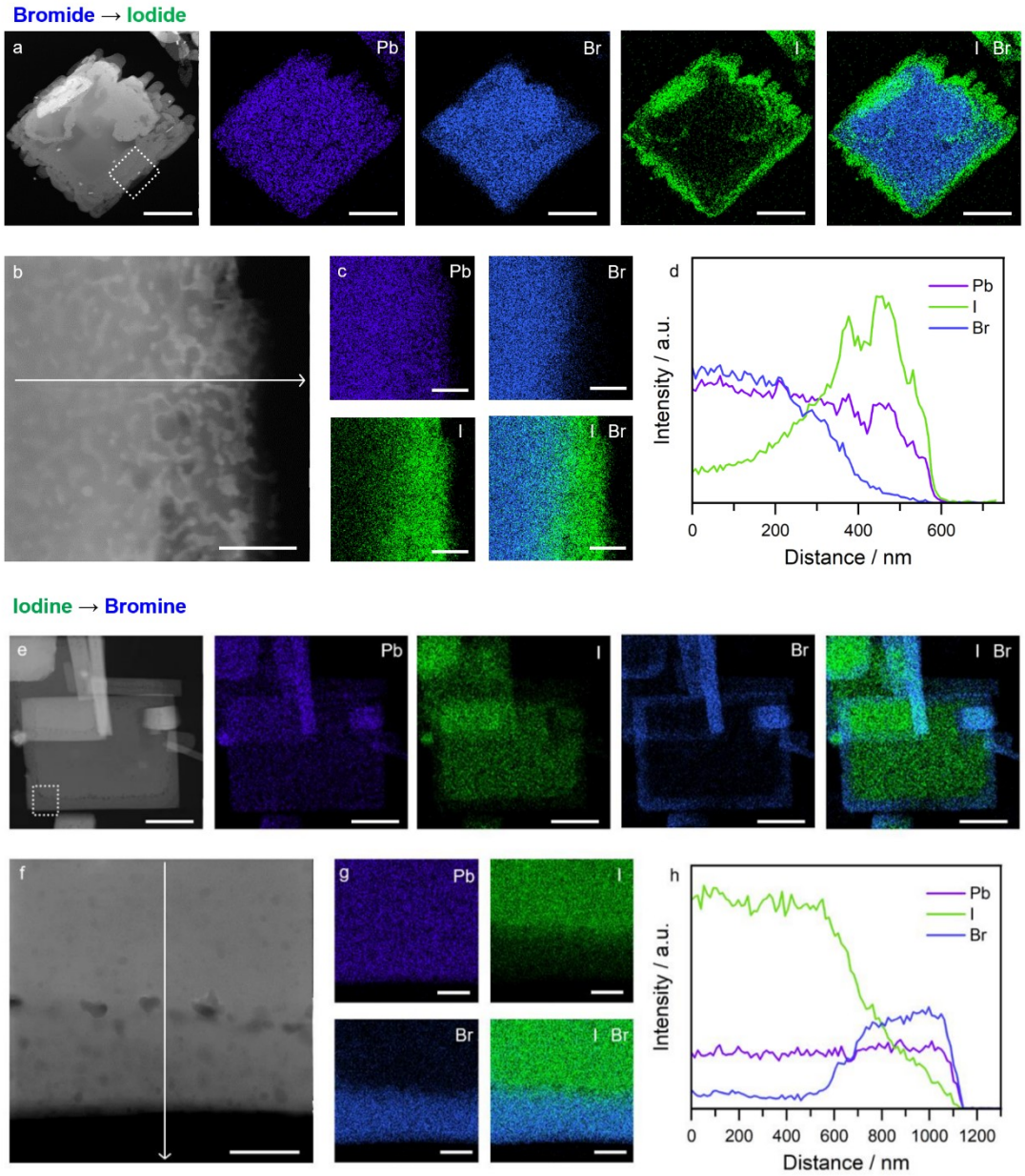

Figure 3.35. Stability of the heterostructures investigated by HAADF-STEM and EDX elemental mapping. a) Lower magnification HAADF-STEM image and STEM-EDX elemental mappings of the bromide to iodide exchange microflakes after storing the TEM grid for 6 days in ambient conditions (scale bar 3 µm). b) Higher magnification

HAADF-STEM images (scale bar 200 nm) of the region marked in panel a). c) corresponding STEM-EDX elemental mapping (scale bar 200 nm), and d) line scan along the arrow in panel b). e) Lower magnification HAADF-STEM images and STEM-EDX elemental mappings of an iodide to bromide exchanged midroflake after storing in the TEM grid for 3 days in ambient conditions (scale bar 2 µm). f) Higher magnification HAADF-STEM image (scale bar 300 nm) of the region marked in panel e). g) Corresponding STEM-EDX elemental mappings (scale bar 300 nm), and h) line scan along the arrow in panel f). The data were obtained from the same samples presented in Figure X in the main text, but not from the same microflake, to avoid regions where the electron beam might have been damaged. Reproduced with permission from ref. 81, copyright 2024 Advanced Materials.

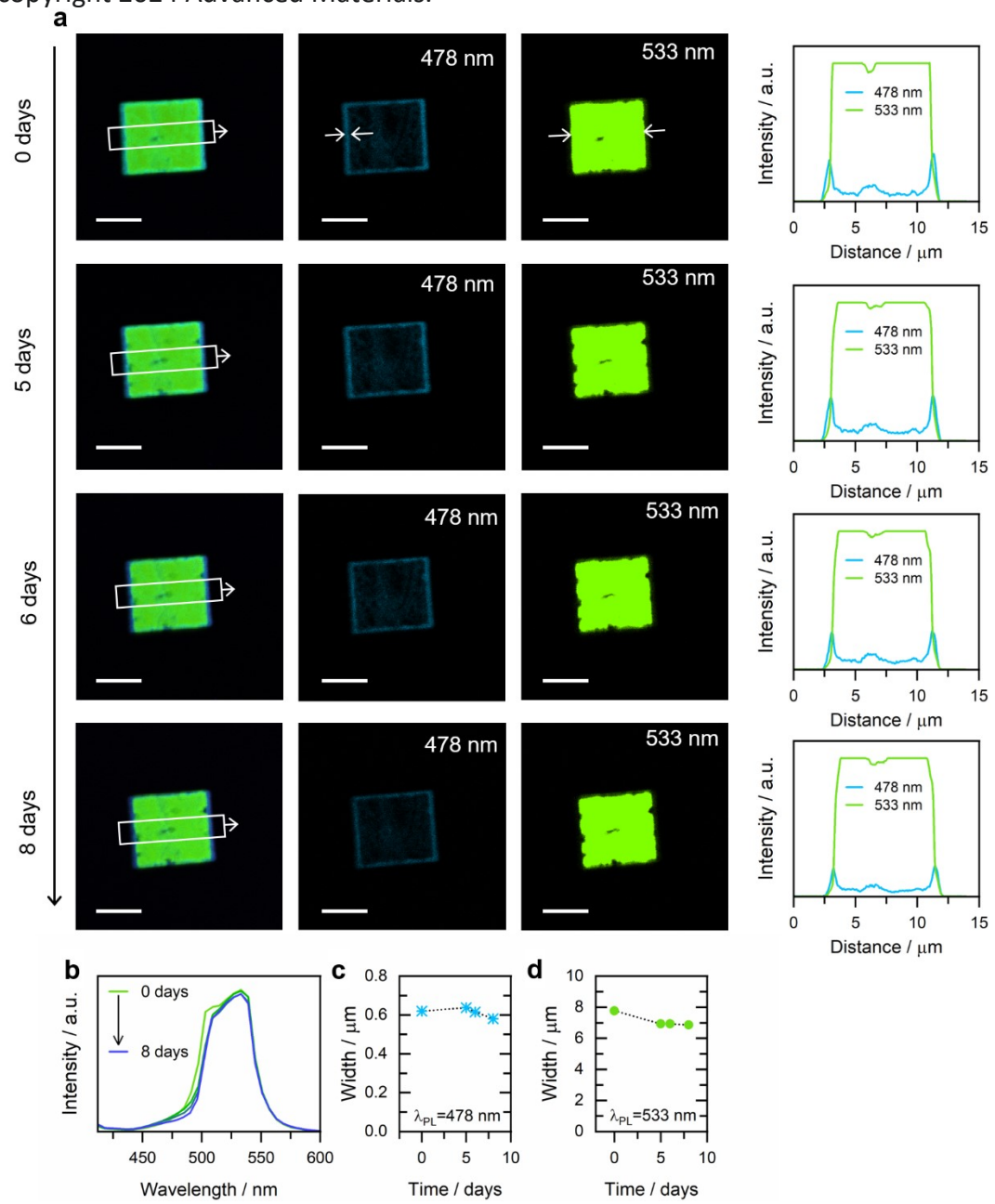

Figure 3.36. Stability test of the junction region after iodide to bromide exchange by storing in ambient conditions in the dark. a) Series of PL confocal images directly after

the exchange process and up to 8 days after storing in ambient conditions (excited at 400 nm, scale bar 5 µm). b), and c) spatial distribution of the PL at 478 and 533 nm (spectral bandwidth 6 nm), respectively. The arrows mark the width of the alloyed (478 nm) and iodide (533 nm) region d) Intensity profile of 478 and 533 nm PL extracted along the in panel a) represented regions for the different storage times. e) PL spectra extracted from the panel a) represented regions over time. f), and g) evolution of the sidth of the alloyed region (478 nm) and iodide region (533 nm) extracted from the intensity profile in panel d). Reproduced with permission from ref. 81, copyright 2024 Advanced Materials.

3.6 Conclusion

Using PEA as an organic cation space, a scalable and facile solution-based anion exchange process to produce in-plane 2D lead halide perovskite heterojunctions. By tracking the evolution of the structure and optical properties in and ex-situ, it has been shown that the bromide-to-iodide exchange process morphology resembles a core-frame-like structure with a bromide core and an iodide frame. Solvation recrystallization mechanisms can explain the rugged phase boundary between the iodide and bromide phases. On the other hand, in the case of iodide to bromide, it has been observed that the formation of multiple mixed alloyed phases in the edge region of the exchange process samples with a comparatively smooth interface between the center and frame, which is likely to result from a vacancy-assisted anion exchange process. The different anion exchange mechanisms can be ascribed to the preferential occupation of the halides in the octahedral lattice of the 2D layered perovskites. Therefore, the solution-based exchange process in 2D layered perovskites is more complex than their 3D counterparts since the preferential occupation of distinct octahedral positions must be considered. The strategy of lateral heterostructure formation using anion exchange in 2D layered perovskites leads to heterostructures in strongly confined quantum wells, which can open exciting opportunities for band gap engineering design and optoelectronic applications. Lateral heterojunctions show an intriguing platform to engineer and investigate energy and charge transfer processes across the introduced heterostructures, paving the way toward fully solution-based systems.

3.7 Experimental Synthesis

3.7.1 Chemicals and Materials

Lead (II)iodide (PbI2, 99%), Lead(II)bromide (PbBr2, ≥98%), hydroiodic acid (HI, 57%, distilled, 99.999% trace metal basis), hydrobromic acid (HBr, 48%), hypophosphorous acid (H3PO2, 50%), phenethylammonium bromide (PEABr, ≥98%), phenethylammonium iodide (PEAI, ≥98%), phenethylamine (PEA, 99%), chlorobenzene (CB, anhydrous, 99.8%), acetonitrile (ACN, anhydrous, 99.8%), 2-propanol (ACS reagent, ≥99.5%), 1-octanol (≥99%), toluene (≥99.7%, anhydrous), *N, N*-dimethylformamide

(DMF, 99.8%, anhydrous), ethyl acetate (≥99.5%), acetone (≥99.5%) were purchased without any further purification from Sigma-Aldrich.

3.7.2 Synthesis of pristine PEA_2PbI_4, PEA_2PbBr_4, and mixed alloyed $PEA_2Pb(Br_xI_{1-x})_4$ microcrystalline powders

Pristine PEA2PbBr4 microflakes were synthesized using the B. Dhanabalan et al. protocol with minor modifications [101]. Accordingly, 0.25 mmol (92 mg) of PbBr2 salt was dissolved in 226 µL of HBr, and 2 mL of acetone was added to dilute the solution as an antisolvent. This was followed by injecting 0.6 mmol (75 µL) of PEA into the solution; as a result, PEA2PbBr4 microflakes were immediately formed. The reaction mixture was continuously stirred for at least 3 h to ensure the reaction was complete. Consequently, the microflakes were first precipitated from the solution by centrifuging at 6000 rpm for 2 min, followed by redispersion in 2 ml of acetone. The washing process was repeated at least two more times, and the microcrystals were dried under a vacuum for 1 hour. For the synthesis of pristine PEA_2PbI_4, the same procedure was employed, except that $PbBr_2$ and HBr were replaced with PbI_2 (0.25 mmol, 115 mg) and a mixture of HI (132 µL) and H_3PO_2 (108 µL), respectively. Moreover, ethyl acetate was employed as the antisolvent to accommodate the higher solubility of PEA_2PbI_4 in acetone. Notably, the synthesis approach described here is versatile and can be applied to various 2D layered perovskites featuring different organic spacers, metal centers, and halide ions. **Table 1** lists the related microflakes for various 2D layered perovskites. To synthesize the mixed-phase alloy $PEA_2Pb(Br_xI_{1-x})4$ microflake powders, the same protocol was followed for the synthesis of PEA2PbI4, with the difference that the I precursor was mixed before the addition of Br precursors and PEA in the desired ratio. **Table 4** lists the reported desire ratios and required precursors.

3.7.3 Growth of pristine PEA2PbI4 and PEA2PbBr4 micro flakes on substrate

2 mg of the as-synthesized and dried microflakes line powders of pristine PEA2PbI4 were dissolved in 1.1 ml of ACN, 10 µL of DMF, *and 900 µL of IPA.* Subsequently, 5 mL CB was added as an antisolvent. A transparent, clear solution was dropped onto the desired substrate in a Petri dish, and the solvent was allowed to evaporate at 50 °C. For PEA2PbBr4 microflakes, 2 mg of the as-synthesized and dried microflake line powders of PEA2PbBr4 were dissolved in 4 mL ACN. After the complete solvation of the microflakes, 2.6 ml of toluene was added to the solution to precipitate tiny PEA2PbBr4 microcrystals. The solution was heated at 50 °C to become transparent and clear. The warm solution was dropped on a clean, arbitrary substrate and positioned in a petri dish. The drop volume was selected to cover the substrate fully. Subsequently, the petri dish was sealed and left to allow complete solvent evaporation at room temperature for 1-2 h.

Table 4. Composition of the precursor solutions for the synthesis of PEA2Pb(BrxI1-x)4. The amount of H3PO2 (108 µl), PEA (75 µl) and ethyl acetate (2 ml) was fixed for the differentsolutions.

XBr Solution	XBr XRF	$PbBr_2$ (g)	PbI_2 (g)	HBr (µl)	HI (µl)
0.00	0.00	-	0.115	-	200
0.06	0.02	0.005	0.109	10	190
0.11	0.05	0.009	0.104	20	180
0.27	0.18	0.024	0.087	50	150
0.27	0.23	0.024	0.087	50	150
0.33	0.26	0.028	0.081	60	140
0.43	0.30	0.037	0.069	80	120
0.43	0.39	0.037	0.069	80	120
0.53	0.5	0.046	0.057	200	200
0.77	0.79	0.069	0.030	150	50
0.77	0.83	0.069	0.030	150	20
0.91	0.93	0.083	0.012	180	20
1.00	1.00	0.092	-	200	-

3.7.4 Solution-based anion exchange of microflakes powders and on substrate

The bromide to iodide and iodide to bromide up to 0.1 mmol PEAI and 0.05 mmol PEABr were dissolved in 1 ml of octanol to form saturated solutions. The solutions were added to a vial containing 20 mg of PEA2PbX4 microflakes line powder. The mixtures were shaken for the desired time and followed the centrifugation process at 6000 rpm for 2 min. After removing the supernatant, toluene was added to the vial with the exchanged microflakes. The washing with toluene was repeated two more times. Subsequently, the powders were dried in a vacuum for 1 h. Microflakes were changed on an arbitrary substrate by dropping the respective PEAX in octanol solution directly on the substrate. After completion of the exchange process, the substrate was tilted to remove the remaining octanol solution and was further washed with toluene and dried under a stream of nitrogen.

3.7.5 Exfoliation of Pristine PEA2PbBr4 and PEA2PbI4 microflakes and the formation of PEA2PbBr4-PEA2PbI4 in-plane heterojunctions

For SEM, energy-dispersive X-ray (EDX), and CL spectroscopy analysis and height profile measurements, the as-prepared pristine PEA2PbBr4 and PEA2PBI4 microflakes were exfoliated by one-sided 3M scotch tape on a precleaned silicone substrate. The fabrication of heterojunctions using the exchange process was initiated by exposing the silicon substrate containing the parent microflake to a 0.1 mol.l-1

solution of PEAX in octanol for 5 min. Then the substrate containing the heterojunction was washed thoroughly with toluene to remove any excess of the PEAX solution.

3.8 Characterization

3.8.1 X-ray Diffraction

XRD patterns collected in this thesis were collected on a PANalytical Empyrean X-ray diffractometer equipped with a 1.8 KW Cu Kα ceramic X-ray tube and a PIXcel 3D 2 × 2 area detector, operating at 40 mA and 45 kV. The microcrystalline powder was pressed on a glass slide *and* placed on a zero-diffraction silicon substrate for the measurement. The diffraction patterns were recorded under ambient conditions using a parallel beam geometry and symmetric reflection mode.

3.8.2 X-ray Fluorescence Analysis

The measurements were performed via a Bruker M4 Tornado µ-XRF spectrum *equipped* with an air-cooled Rh anode X-ray tube operated at 200 µA and 50 kV. An energy-dispersive silicon drift detector with a 30 mm2 sensitive area and energy resolution of <145 eV for Mn *Kα was used. The polychromatic beam was focused to a spot size of* ≈25 µm for Mo K by using poly-capillary optics. *The measurements were implemented directly on the samples previously positioned on the* µ-XRF platform under 20 mbar vacuum conditions. Spectra acquisition, elemental map evaluation, and quantification were implemented based on the fundamental parameter approach via the Esprit software from Bruker. The reported values were the average of at least three measurements on the same sample.

3.8.3 Atomic Force Microscopy:

AFM images and topological analysis of the heterojunctions were performed using an XE-100 AFM system (Park Scientific, Suwon, South Korea), operating in a non-contact mode. The samples for the AFM imaging were prepared by performing an anion exchange on PEA2PbBr4 microflakes grown on glass.

3.8.4 Optical Characterization:

The absorption spectra were recorded from dried microflakes via a Varian Cary 5000 ultraviolet-visible-near-infrared (Uv-vis-NIR) spectrophotometer equipped with an external diffuse reflectance accessory and operating in absorption geometry. The PL and PLE spectra were acquired with an Edinburgh Instruments (FLS920) fluorescence spectrometer equipped with a monochromator and a Xenon lamp for steady-state PL excitation. The PL was recorded in the 415 and 600 nm with a resolution of 6 nm. Time-resolved PL measurements were implemented with a time-correlated single-photon counting (TCSPC) unit coupled with a diode laser. The samples were excited at 508 or 372 nm with 50-ps pulses at a repetition rate of 1 µs. PLQY values of the powder samples were measured in an integrating sphere attached to the same instrument with an

excitation wavelength of 370 nm. The confocal images were recorded with a Nikon A1R+/A1+ confocal laser microscope equipped with a 60× oil immersion or 20× 0.6 numerical aperture air objective. The samples were excited with a 400 nm laser.

3.8.5 Scanning Transmission Electron Microscopy:

To acquire desirable thin crystals for scanning transmission electron microscopy (STEM), this thesis adopted a method reported by X et al. [122]. The PEA2PbI4 and PEA2PbBr4 crystals were dispersed in toluene and were drop-casted onto Cu grids with a carbon-coated film. STEM-energy-Dispersive X-ray (EDX) compositional analysis and High-Angle Annular Dark Field (HAADF) images were implemented using an image-Cs-corrected JEOL JEM-2200FS with a Schottky emitter gun operated at 200 kV, equipped with a Bruker XFlash5060 silicon-drift EDX detector (SSD). For the analysis of pristine PEA2PbI4 and PEA2PbBr4, in-plane heterojunctions, crystals were drop-casted onto ultrathin holey carbon-coated copper grids and exposed to 0.1 mol.L-1 PEABr and 0.02 mol.L-1 PEAI solutions in octanol for 5 min and 1.5 min, respectively. STEM images were recorded via aHAADF detector on a probe- and image-abberation-corrected ThermoFisher Spectra 300 S/TEM with an XFEG source, operated at 300 kV. Line scan profiles and elemental distribution maps were recorded by collecting EDX signals on a Dual-X system comprising two EDX detectors on either side of the sample.

3.8.6 Scanning electron microscopy and Energy dispersive X-ray spectroscopy:

This thesis investigated the influences on composition and morphology of the exchanged process with Zeiss GeminiSEM 560 (Zeiss, oberkochen, Germany) scanning electron microscopy equipped with a field-emission gun and operating at 10kV acceleration voltage. The back-scattered VPBSE detector was used to improve the difference in the elements presented in the samples according to their brightness. The SEM was equipped with energy-dispersive X-ray spectroscopy (EDX, Oxford instrument, X-Max, 80 mm2) operating at 30 kV.

3.8.7. Cathodoluminescence

CL hypermapping was acquired in an Attolight Allalin 4027 Chronos SEM-CL. The spectra were performed with an Andor 1024 pixel charge-coupled device (readout rate of 50 MHz and 100 ms acquisition time per pixel) and an iHR320 spectrometer (focal length of 320 mm, 150 gratings per mm blazed at 500 nm, 700 μm entrance slit). All the measurements were recorded under high vacuum ($<10^{-7}$ mbar) at room temperature with a current of approximately 100 pA as measured by a Faraday cup, an acceleration voltage of 10 kV, and a pulsed beam with a frequency of 80 MHz and a duration of $\sim$7 ps.

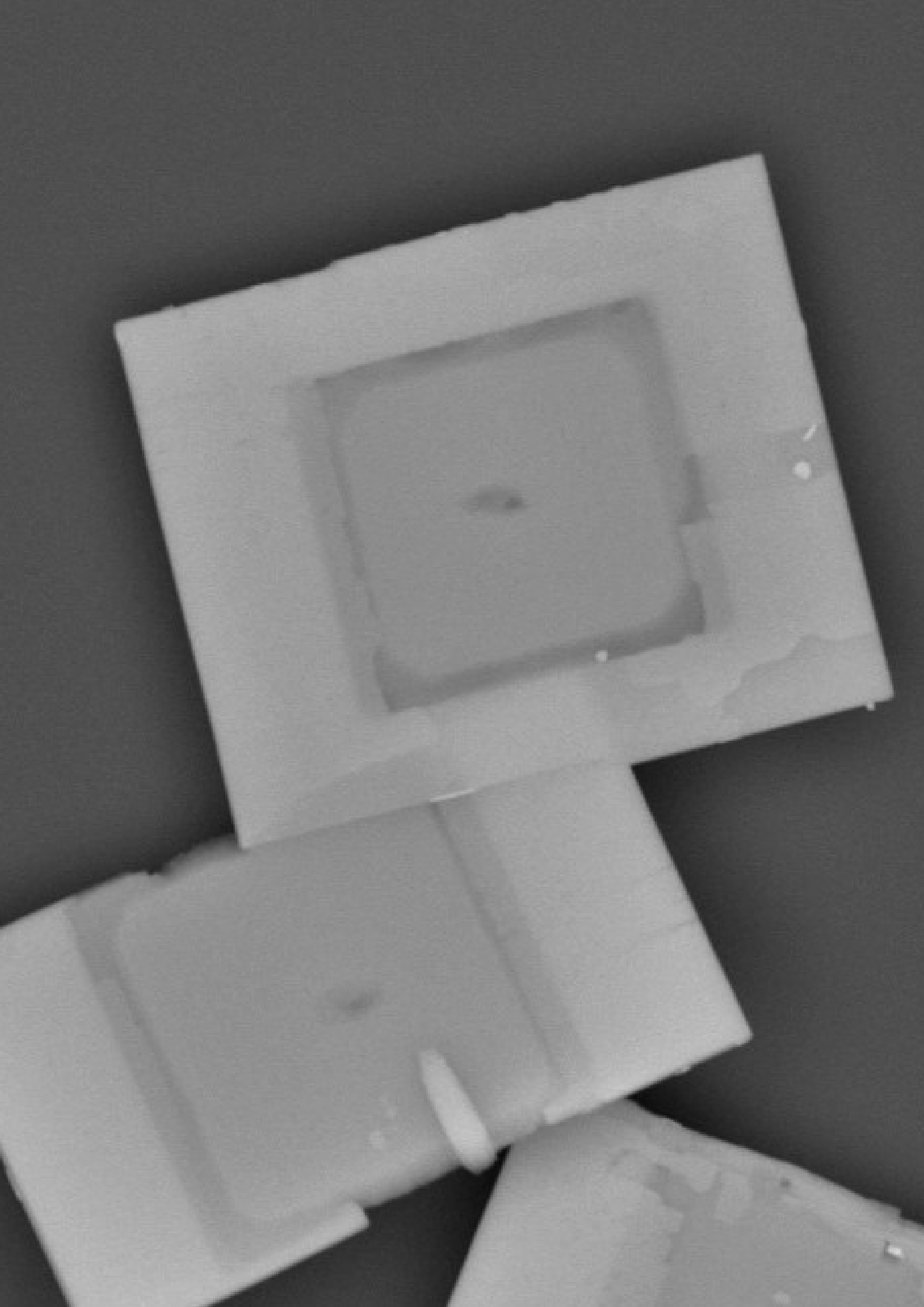

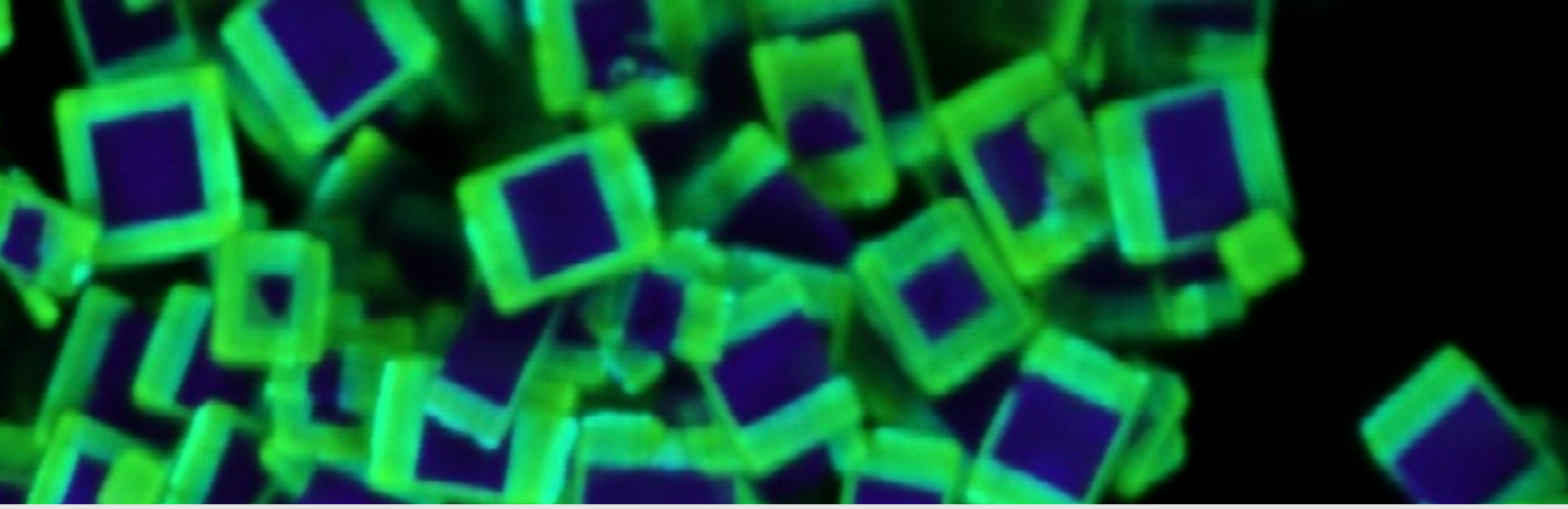

Chapter IV:

Formation of 2D perovskite lateral heterostructure via sequential growth

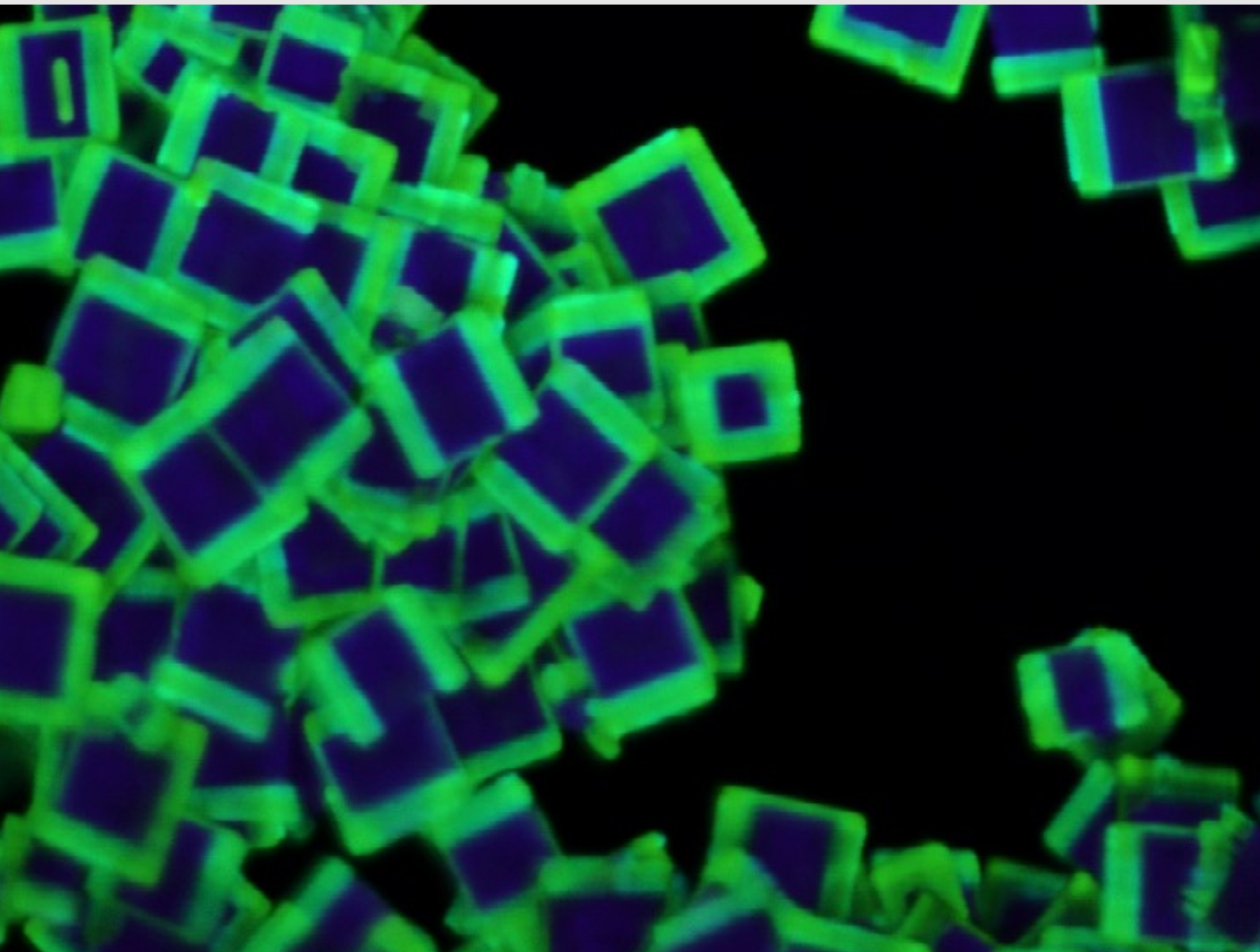

Chapter IV: Formation of 2D perovskite lateral heterostructure via sequential growth

Abstract: *2D layered perovskites have emerged as one of the most promising semiconductors for optoelectronic applications. Controlling charge-carrier flow, band gap, and position is essential for device efficiency, and the band-gap dependence in 2D layered perovskite compositions can be used to tune the energy-level structure. Developing in-plane heterojunctions that leverage the band-gap reliance on the various compositions of 2D layered perovskites can provide significant benefits, such as forming epitaxial junctions with low energy barriers and tailoring band offsets. In this Chapter, a one-pot synthesis approach for creating 2D-layered perovskite lateral heterojunctions with different metal cations and/or halide anions is demonstrated. The key parameter in this method is the differential solubility of 2D-layered perovskites with varying compositions in a carefully controlled solvent mixture. This enables sequential crystallization of distinct 2D-layered perovskites, yielding core-shell or dumbbell-shaped heterojunction architectures. Additionally, the compositional control can be maintained by adjusting the injection timing of the secondary perovskite materials. For example, reacting with a mixture of bromide- and iodide-based 2D layered perovskites yields heterojunctions of various bromide- iodide alloyed phases. Conversely, delaying the injection of the iodide-based 2D perovskite precursor, when a bromide-based phase has already formed in the antisolvent/solvent mixture, leads to the formation of nearly phase-pure lateral heterojunctions. Furthermore, this sequential injection strategy can be used to form heterojunctions with various metal cations and halide anions, enabling the creation of multiple heterojunctions, such as triple halide chloride-bromide-iodide core-frame heterostructures. It has also been demonstrated that the quality of crystallites and heterostructures can be evaluated with high-resolution 4D STEM, which yields single-crystal diffraction patterns. Confocal hyperspectral optical microscopy reveals emission properties through spatial emission mapping, and the combination of various bandgap regions with time-resolved photoluminescence indicates optical coupling that enhances emission from low-bandgap regions. Kelvin Probe Force Microscopy shows extended charge delocalization at the junction interface. At the same time, compositional analysis reveals sharp heterostructure interfaces, generating an electrostatic potential landscape and providing insights into the work function. It is expected that the design of a versatile one-pot synthesis approach to fabricate microflake heterojunctions will strongly stimulate the development of nanostructure-based photonics and optoelectronic devices that require band-gap engineering, especially for multicolor emission, sensing, and photocatalytic applications.*

4.1 Introduction

2D layered perovskites are an emerging semiconductor family in which bulky organic cation molecules separate the metal-halide octahedral layers [11,82,83]. The structure and composition of these 2D layered perovskites have been extensively discussed in Chapter 2. In 2D layered perovskites, strong excitonic effects are combined with compositional and structural tunability, making them promising materials for electronic and optoelectronic applications [123,124]. There is an essential challenge for the applications above: the rational control of bandgap and local compositions, which govern charge-carrier and energy flow, in devices [125,126]. Similar to transitional-metal dichalcogenide structures, the formation of in-plane heterojunctions, in which the composition varies laterally, suggests a promising approach toward defined energy funnels, integrated multifunctional interfaces, and defined junctions within a single crystal [69,127]. Getting a high-quality junction, ideally through epitaxial interfaces, is therefore significant. A very soft structure and lattice of 2D layered perovskites can preserve such interfaces even in the presence of considerable lattice mismatch, especially along the vertical direction, where the organic spacer decouples the inorganic slabs [81,128].

Post-synthesis methods, like the solution-based halide-exchange process, are practical for producing macroscopically uniform junctions but are limited to halide-anion substitution because metal cations are deeply embedded in these 2D layered perovskite structures [10,90,129]. These junctions often face halide-dependent limitations and poor quality, making it challenging to adapt strategies for more complex heterojunctions [10]. Epitaxial growth of 2D perovskite heterojunctions has been achieved at higher temperatures under substrate-constrained conditions. In multi-step processes that require careful control of temperature and solvents, these strategies lack versatility and are challenging to implement [79–81]. Furthermore, the resulting heterojunctions typically have a thickness of less than 100 nm, which complicates their use as open cavities capable of supporting optical resonances [130,131].

In this chapter, a solution-based one-pot crystallization strategy is introduced that enables the rational design of in-plane heterojunctions in 2D layered perovskites and affords considerable flexibility in selecting the interface architecture and material composition. First, the focus is on heterjunctions with various halide contents, and then on the applicability of our approach to heterjunctions with various metal cations. To overcome the restrictions above, a solution-based, sequential crystallization technique is introduced that enables the rational design of in-plane heterojunctions in 2D layered perovskites under mild conditions. Using controlled antisolvent injection, it has been demonstrated that the solubility differences of the chosen 2D layered perovskites in good solvents such as γ-butyrolactone (GBL) and acetonitrile (ACN) enable heterojunction formation in a pot process. The method itself allows for several strategies. Accordingly, by combining two 2D layered perovskites with various halide compounds in the starting solution of the reaction, the core-frame heterostructures

consist of alloyed phases with graded junctions when two different halide compositions are premixed. By instead injecting the second precursor solution at a later stage of antisolvent addition, double-halide heterojunctions are formed with phase-pure cores and nearly phase-pure frames. The frame composition can be further tuned by controlling the halide ratio of the injected solution, thereby enabling lateral bandgap engineering. Additionally, dumbbell structures form alongside the mentioned conventional core-frame structures, with the secondary phase growing preferentially along the long edges of rectangular crystals. Finally, the approach has been extended to a more complex system, including triple-halide (chloride-bromide-iodide) heterojunctions, within a single microcrystal, and to core-frame structures with lead-based PEA_2PbBr_4 in the core, and AgBi-based $PEA_4AgBiBr_8$ double-perovskite in the frame. The findings established a generalized framework for the solution-based synthesis of in-plane heterojunctions in 2D layered perovskites. This strategy shows opportunities for bandgap engineering, exciton funnels in electronics and optoelectronic devices, and fundamental investigations of exciton dynamics and charge transfer in hybrid semiconductors.

4.2 Formation of lateral heterojunction in 2D layered perovskites

The concept of this one-pot sequential growth method is shown in **Figure 4.1a**: irregularly shaped, presynthesized 2D layered perovskite powders [101] (**Figures 4.2** and **4.3**) are dissolved in a suitable solvent, such as ACN or GBL. By controlling the solvent-to-antisolvent ratio over time by adjusting the antisolvent injection rate, we can regulate crystallization kinetics (**Figure 4.4**). The recrystallization of irregularly shaped 2D-layered perovskite powders offers the advantage of starting from pure-phase materials, thereby avoiding the formation of unwanted byproducts. Using a similar approach, well-defined 2D layered perovskite microflakes are produced, serving as open optical cavities and exhibiting nearly flat, smooth surfaces (**Figure 4.5**) [132].

To create heterojunctions, a second material precursor can be either incorporated into the mixture from the outset or added after a specified period. Subsequently, the 2D layered perovskite with the lowest solubility will crystallize first, whereas delayed crystallization of the second 2D layered perovskite with higher solubility results in dumbbell- or core-frame architectures of heterojunctioned microcrystals. In the latter approach, the formation of a homogeneous interface is suppressed by slow antisolvent injection, which gradually saturates the solution and yields highly pure heterojunctions. The experimentally observed various solubilities of 2D layered perovskites with different metals and halides are shown in **Figure 4.1b**. This sequential injection approach enables the fabrication of more complex systems, such as core/frame/frame heterostructures comprising up to three distinct halides. To demonstrate the versatility of this strategy, SEM and EDX images of microcrystals with various heterojunction compositions are shown in **figures 4.1c-g**: c) PEA_2PbCl_4/PEA_4PbBr_4 chloride-bromide core-frame, d) PEA_2PbBr_4/PEA_2PbI_4 bromide-iodide dumbbell, e) $PEA_2PbCl_4/PEA_2PbBr_4/PEA_2PbI_4$ chloride-bromide-iodide core/

frame/ frame, and f) alloyed $Br_{x'}/I_{y'}$ and Br_x/I_y (with x>x') phases with different compositions in dumbbell and core-frame heterostructure architectures, and g) heterojunctions with PEA2PbBr4 at the core center and the double perovskite $PEA_4AgBiBr_8$ at the frame edges [80]. This chapter initially focuses on the formation of heterojunctions, beginning with a mixture of PEA2PbBr4 and PEA2PbI4 microcrystal precursors dissolved in ACN (Figure 4.5), to gain deeper insights into the fabrication process.

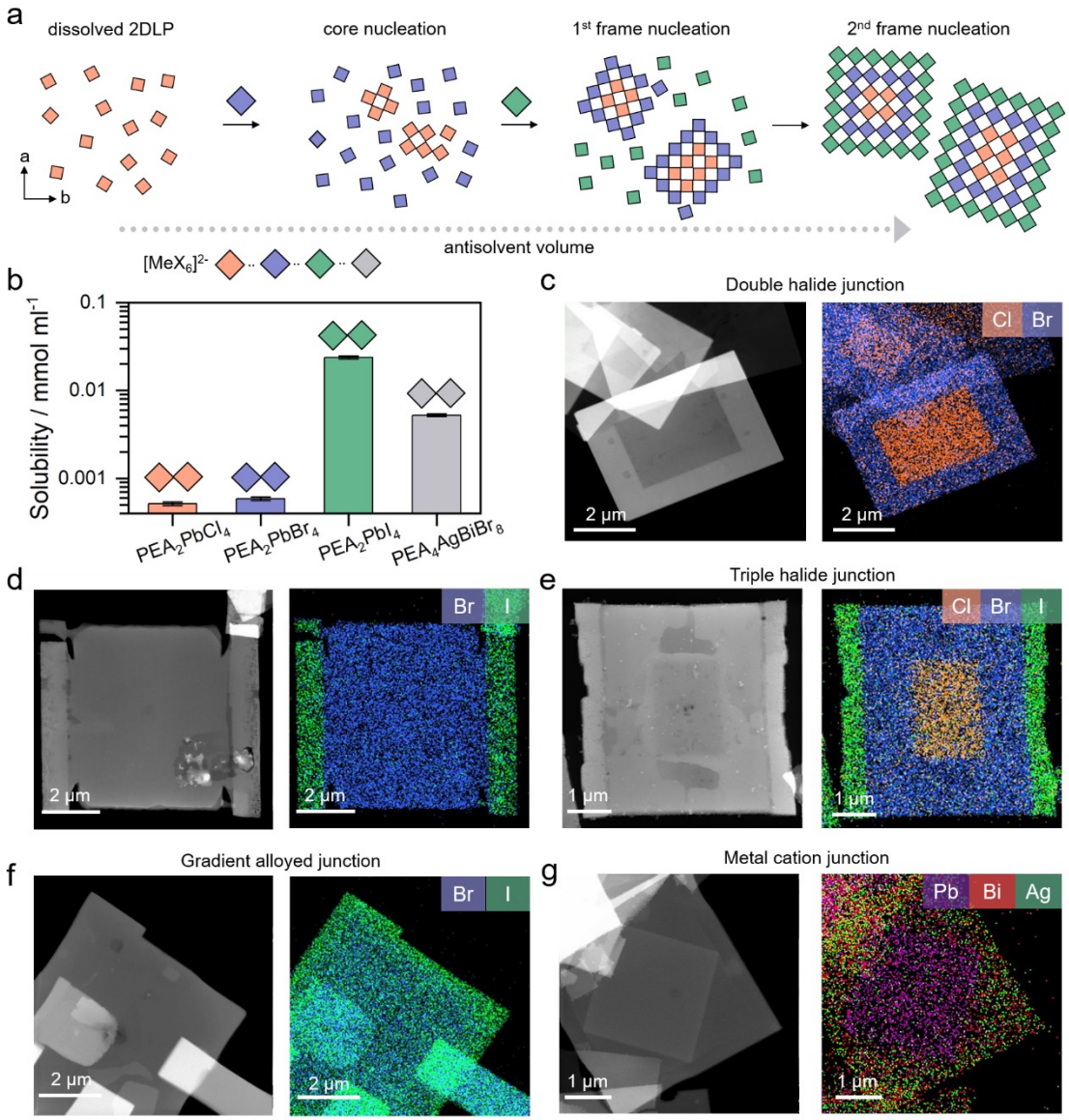

Figure 4.1. a) Sequential crystallization protocol and its ability to fabricate heterojunction microflakes with core-frame (or dumbbell-shaped) architecture. b) Solubility of 2D layered perovskite powders in the ACN as solvent determined by ICP. c-g) SEM and EDX images representing heterojunction microflake with various compositions, as shown by the headlines and labels.

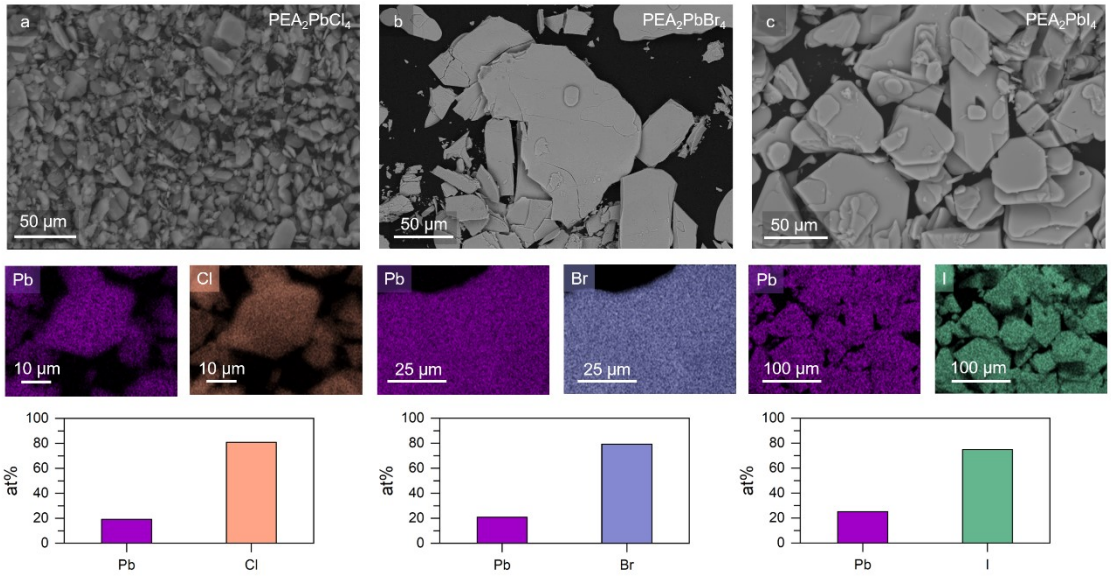

Figure 4.2. SEM images and EDX elemental mapings of a) PEA_2PbCl_4, b) PEA_2PbBr_4, and c) PEA_2PbI_4 microflake powder samples with irregular shapes, sizes, and thicknesses, which are used as starting material for the sequential growth process. The elemental composition extracted from the EDX map is reported in **Table 1**.

Table 1. The EDX elemental composition analysis of the 2D layered powders.

perovskite Powder	Pb (At. %)	Halide (At. %)	Halide: Pb Ration
PEA_2PbCl_4	19.17	80.83 (Cl)	4.2
PEA_2PbBr_4	20.82	79.18 (Br)	3.8
PEA_2PbI_4	25.06	74.94 (I)	3.0

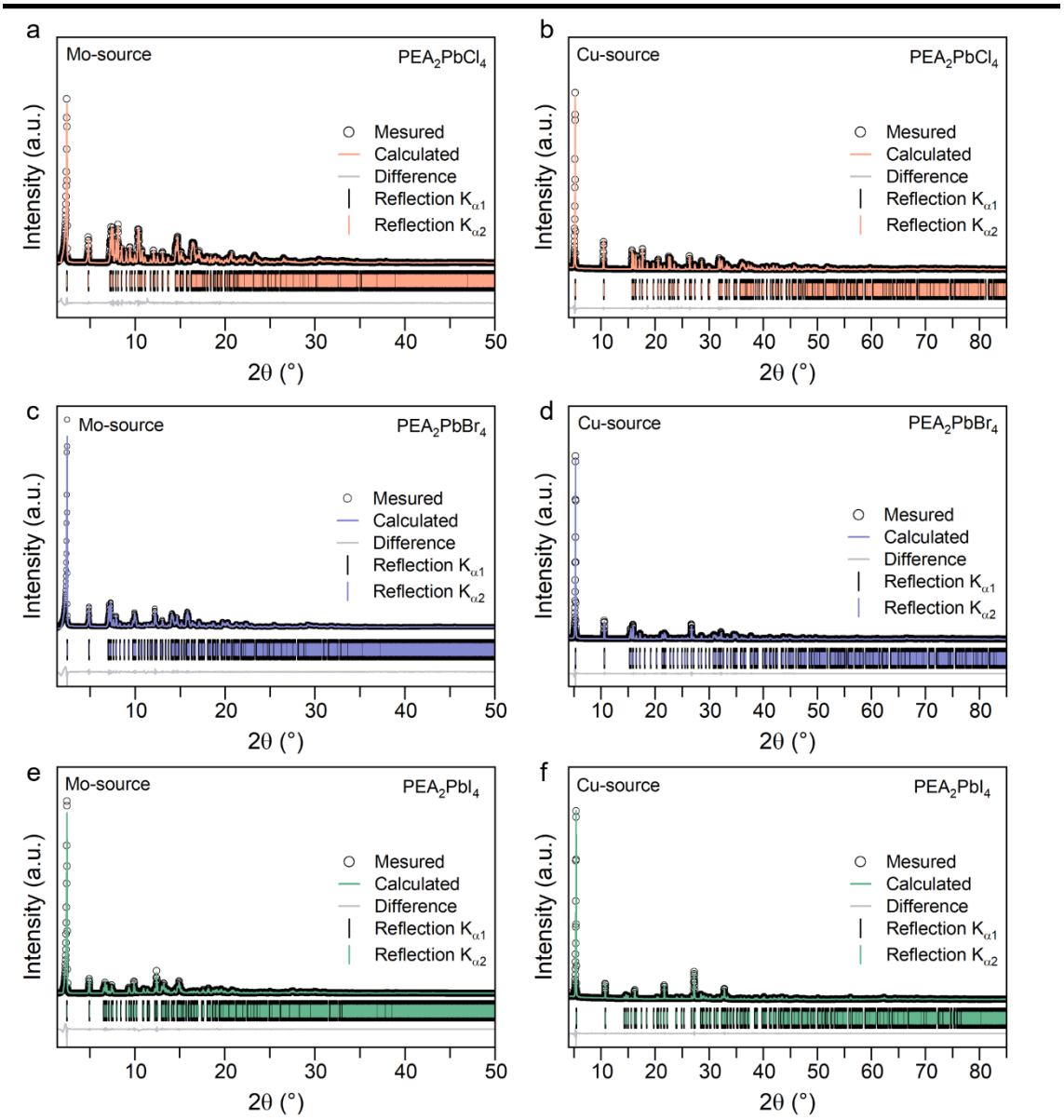

Figure 4.3. Rietveld refinements of powder XRD patterns recorded using Mo and Cu sources, as represented, for (a, b) PEA_2PbCl_4, (c, d) PEA_2PbBr_4, and (e, f) PEA_2PbI_4 microflake powder samples. Rotating capillaries were used to obtain complete diffraction patterns without preferred orientation for all measurements (see Experimental Section for details).

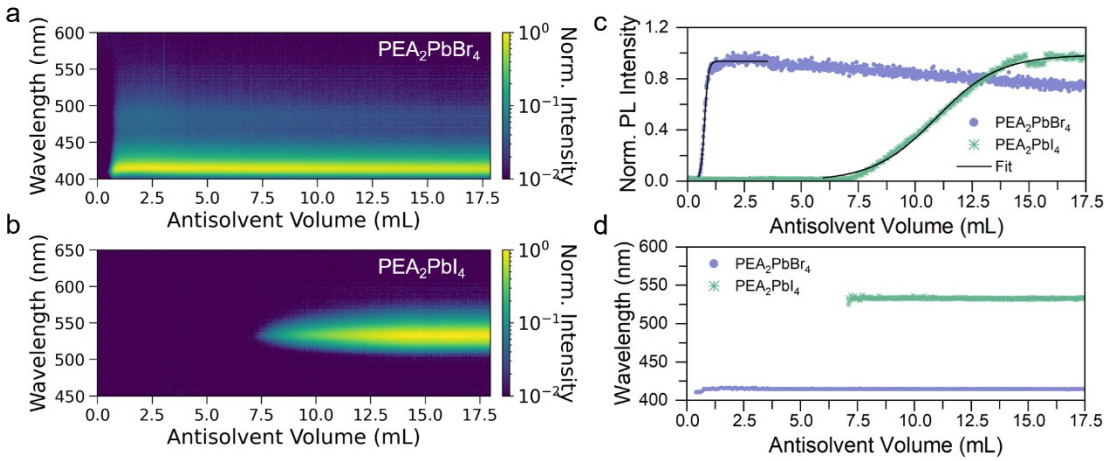

Figure 4.4. In-situ PL spectroscopy during the recrystallization of pristine a) PEA_2PbBr_4, and b) PEA_2PbI_4 microflakes from ACN by injecting toluene (1 mL/min) as an antisolvent. c) Evolution of the PL intensity with antisolvent injection volume in the range of 400-420 nm for PEA_2PbBr_4, and 500-550 nm for PEA_2PbI_4. d) Position of the PL maximum during antisolvent injection.

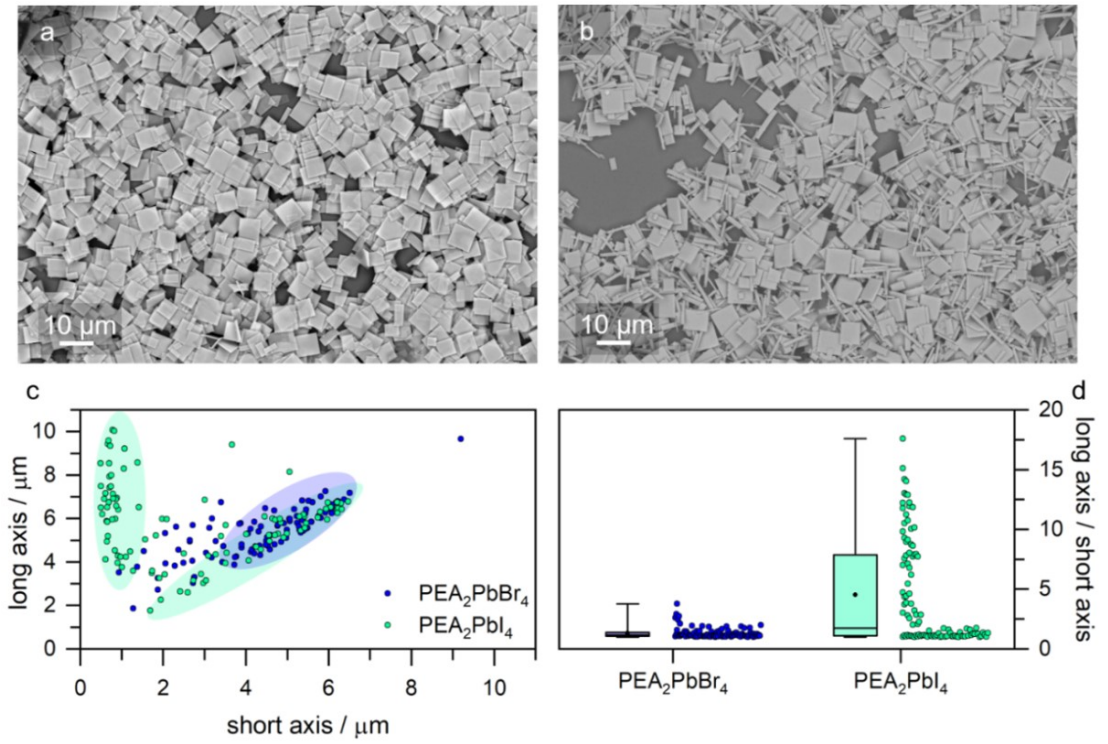

Figure 4.5. Morphology images and size distribution of recrystallized pristine 2D layered perovskites. a), and b) SEM images of pristine PEA_2PbBr_4 and PEA_2PbI_4 recrystallized with toluene antisolvent (injection rate 1 ml/min) with a final solvent-to-antisolvent ratio of 0.2. c) Scatter plots from the SEM images in a) and b) determined dimensions of the respective crystals. The shaded areas serve as visual guides to distinguish one bromide-size population from two iodide-size populations. d) Box plots showing the aspect ratio (long axis/short axis) for PEA_2PbBr_4 and PEA_2PbI_4 crystals.

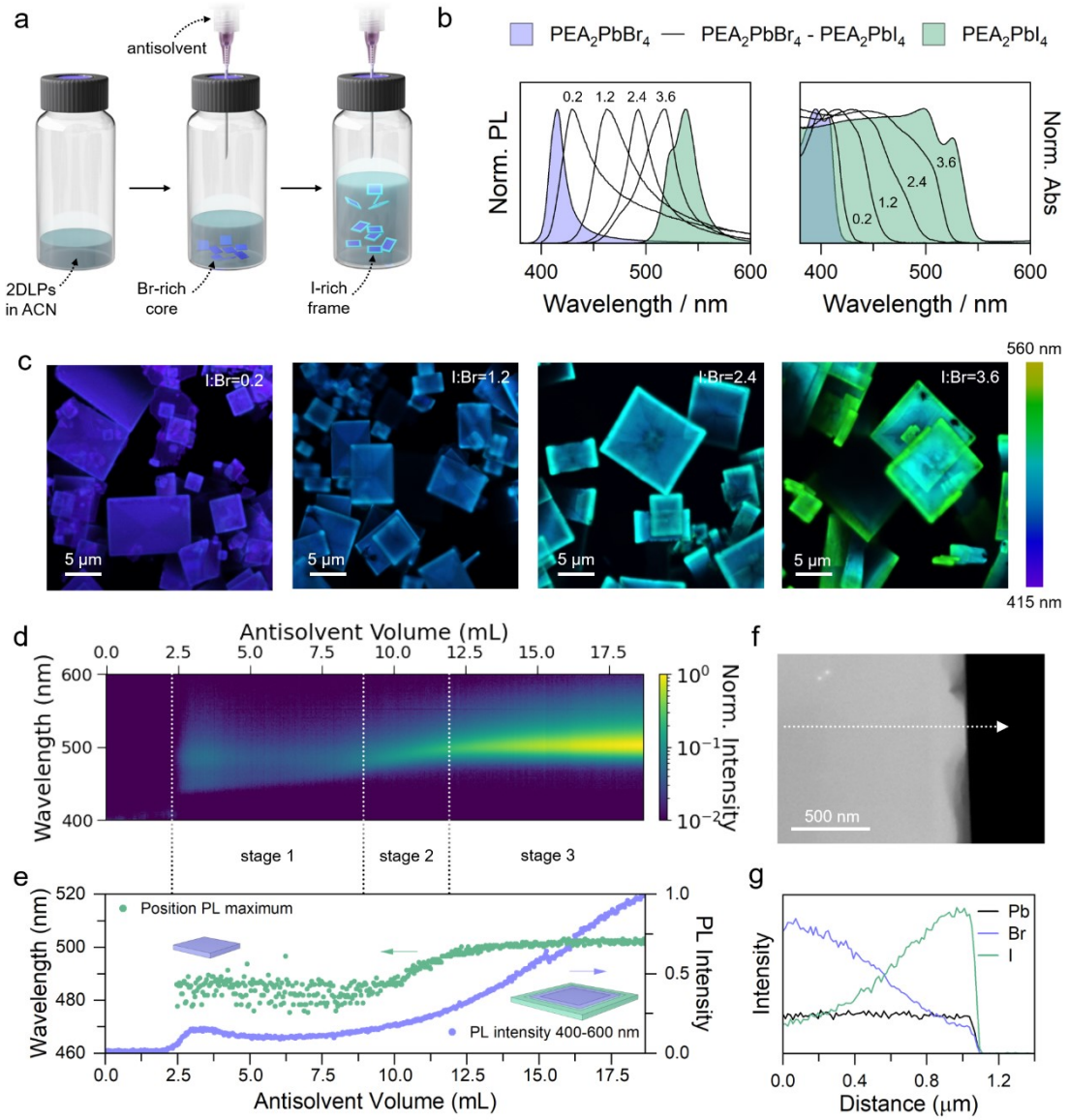

Figure 4.6. Lateral heterojunctions in 2D layered perovskites from mixed-halide precursor solutions**.** a) Representation of the formation processes. b) PL (λ_{ex}=350 nm) and absorption spectra recorded from microflakes formation with various I:Br ratios, indicating that the molar composition of the dissolved 2D layered perovskites can tune the optical band gap of the mixed phases. c) Confocal hyperspectral PL (λ_{ex}=400 nm) images of heterojunction microflakes composed of alloyed PEA_2PbBr_x/I_y phases with various compositions. d) Tracking the reaction kinetics by in-situ PL recorded during the formation process (λ_{ex}=365 nm). e) Integrated PL intensity (400-600 nm) and extracted position of the PL maximum. f) HAADF-STEM image of the heterostructure (I:Br=2.4) at the junction of a core-frame microcrystal, and g) EDX line scans for Pb, Br, and I along the represented arrow in (f).

4.3 Alloyed Heterojunctions formation using mixture precursors

When the reaction begins with a mixture of dissolved precursors for iodide- and bromide-based 2D layered perovskites, the heterojunctions consist of alloyed mixed-halide phases, including an iodide-rich phase at the edges or frame and a bromide-rich core. The relative concentrations of different precursors in the initial solution can control the composition of the heterojunctions, thereby enabling tailoring of the band gap and band gap offset within the heterostructure, subject to phase-pure constraints. The absorption and PL spectra in Figure 4.5b demonstrate this control over the PL center and absorption edge wavelength. It is worth noting that the emergence of new bands cannot be explained by overlapping optical behaviors of the two pristine bromide- and iodide-based 2D layered perovskite structures. Instead, this is associated with alloyed phases, most likely formed from distinct Pb-Br-I solvent complexes in the solution, which most probably predetermined the core-frame composition of the resulting heterojunctions (**Figure 4.7**).

Figure 4.6c represents a series of hyperspectral confocal PL emission images that evidence the change in PL emission color for different iodide to bromide structure ratios in the initial mixture (see **figure 4.7** for lower magnification confocal PL images, and SEM images, and **Figures 4.9-4.11** for other analysis including EDX elemental mapping, hyperspectral confocal, and XRD data), and the core-frame heterojunction structure formation. During the crystallization process, in situ control of the PL emission (**Figure 4.6d-e**) provided direct information on the band gap of microflakes (and therefore halide composition) from the spectral position of the PL emission maximum, along with details on the different crystallization events from the evolution of the integrated PL emission intensity. The onset of PL emission at 2.5 ml of antisolvent marks the onset of crystallization of the bromide-rich phase (PL emission centred at 485 nm), which remains stable up to ca. 9 ml (stage 1). In stage 2, the pronounced shift of the PL emission maximum from 485 nm to 500 nm and the rise in the PL emission signal indicate the progressive formation of halide mixed-phase alloys with changing composition, resulting in a graded heterojunction region, as verified by STEM-EDX (**Figures 4.6f-g**). Finally, in stage 3 (12.5-18 ml), the PL emission position stabilized around 500 nm, while the PL emission intensity increased, associated with the growth of an iodide-rich phase with a stable composition. To determine the spatial and size distributions of the blue and green PL emission signals (**Figure 4.12**), the reaction was stopped at different volumes of injected antisolvent (3.3, 6.7, 10, and 13.4). The increase in PL emission intensity (with wavelength corresponding to the shell composition) indicates efficient energy transfer from the core to the shell region (**Figure 4.6e**). As shown in **Figure 4.6f**, STEM-EDX reveals a gradual decrease in the bromide-based signal toward the edge, which correlates with an increase in the iodide-based signal, while the Pb signal remains constant. This suggests that the interface involves a gradual change in compositions extending over several hundred nanometers. The homogeneous

morphology of the heterostructure microflakes indicates an epitaxial (single-crystal) interface. The graded shell structure most likely results in a low density of defects [133] and alleviates lattice strain.

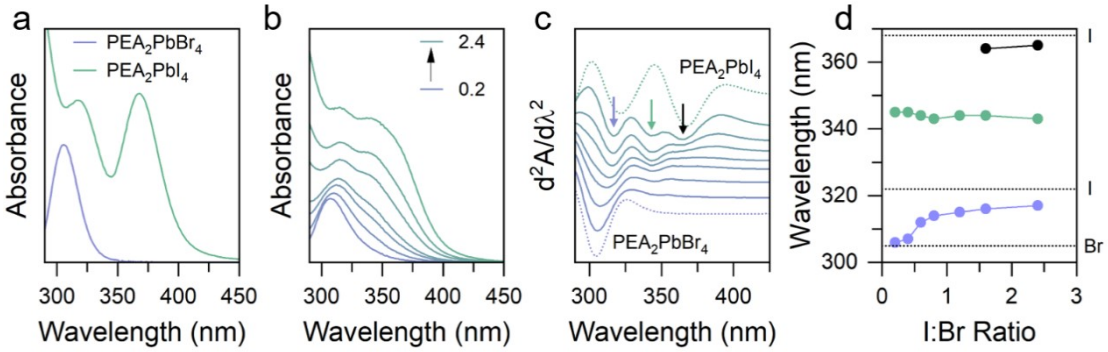

Figure 4.7. Representation of mixed halide precursor formation during the mixing of 2D perovskite powder precursor solutions of various halides (PEA_2PbBr_4 and PEA_2PbI_4) in ACN. a) UV-Vis absorption spectra of PEA_2PbBr_4 and PEA_2PbI_4 in ACN, representing typical bands for the polyhalide plumbate species formation. b) UV-Vis absorption spectra after mixing PEA2PbX4-ACN solutions in the represented ratios. c) Second derivative of the spectra illustrated in b), showing the formation of bands distinct from the pristine precursor solutions. d) Position of the bands with respect to the I:Br ratio extracted from c) (shown with arrows with corresponding colors). The horizontal lines represent the band positions of the pristine precursor solutions of PEA_2PbBr_4 and PEA_2PbI_4 in ACN.

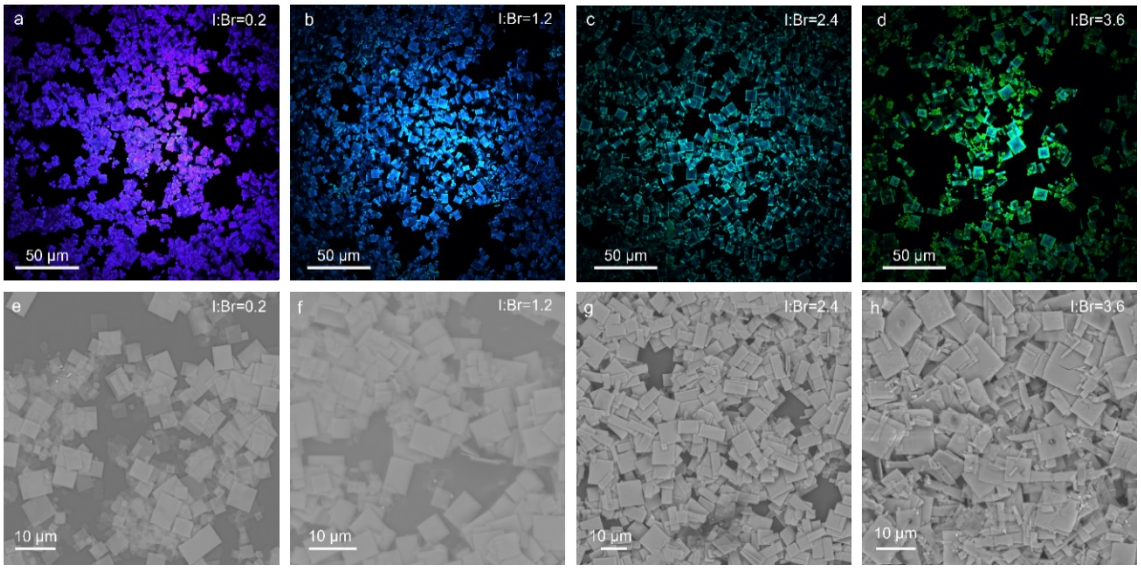

Figure 4.8. a-d) Low-magnification confocal PL images of the various I:Br ratio series that are represented in **Figure 4.6**. The confocal images represent a homogeneous size distribution of the microcrystals.

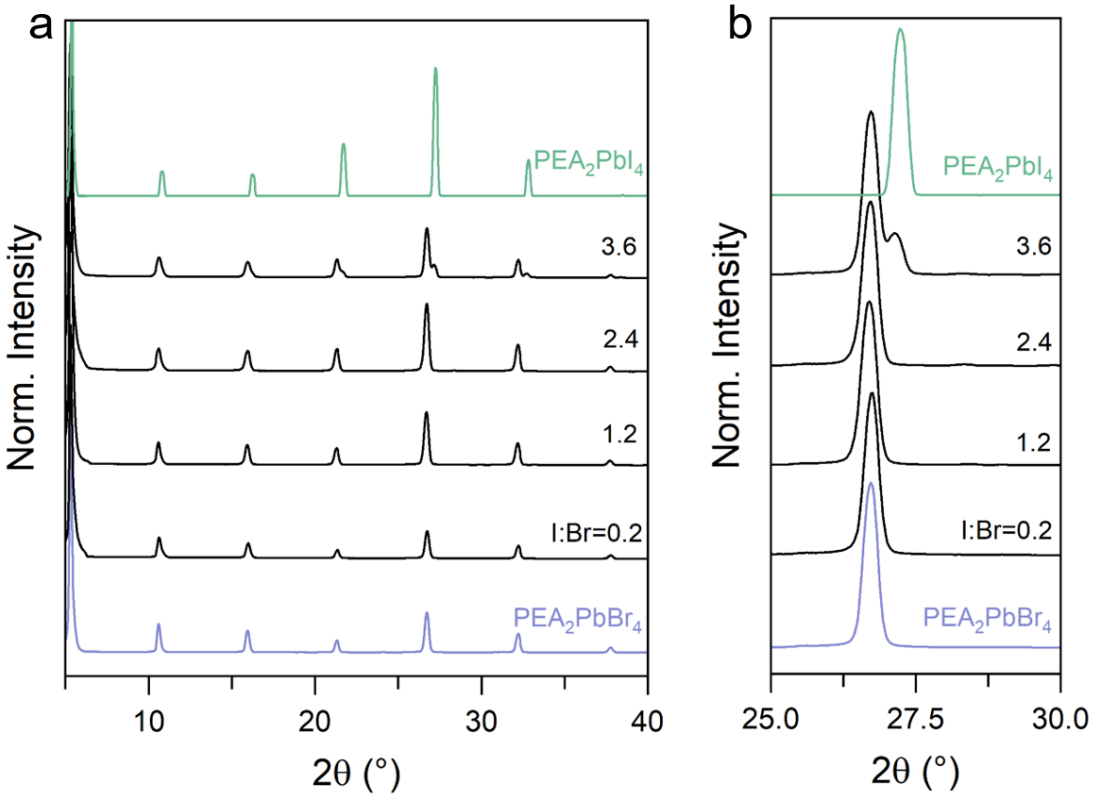

Figure 4.9. a) Overview of XRD patterns and b) a magnified view focused on the (0010) and (005) reflections of PEA_2PbI_4 and PEA_2PbBr_4 of heterojunctions obtained from mixed precursor solutions with varying I:Br ratios.

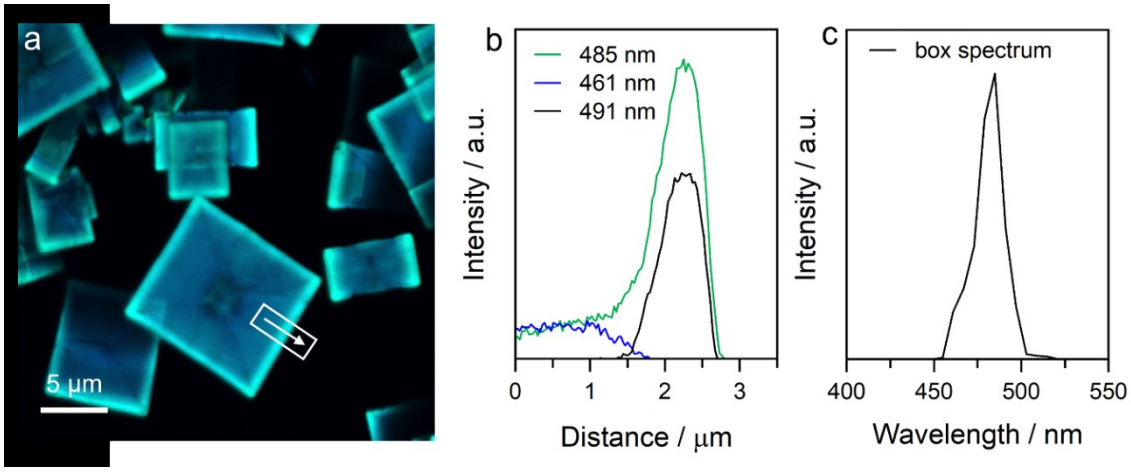

Figure 4.10. Confocal PL images as represented in Figure 4.5 (I:Br=2.4), with b) extracted intensity profile for 461, 485, and 491 nm and c) spectrum along the box marked in panel a. The width of the frame region is approximately 500 nm, which closely matches the EDX line scans shown in **Figure 4.6**.

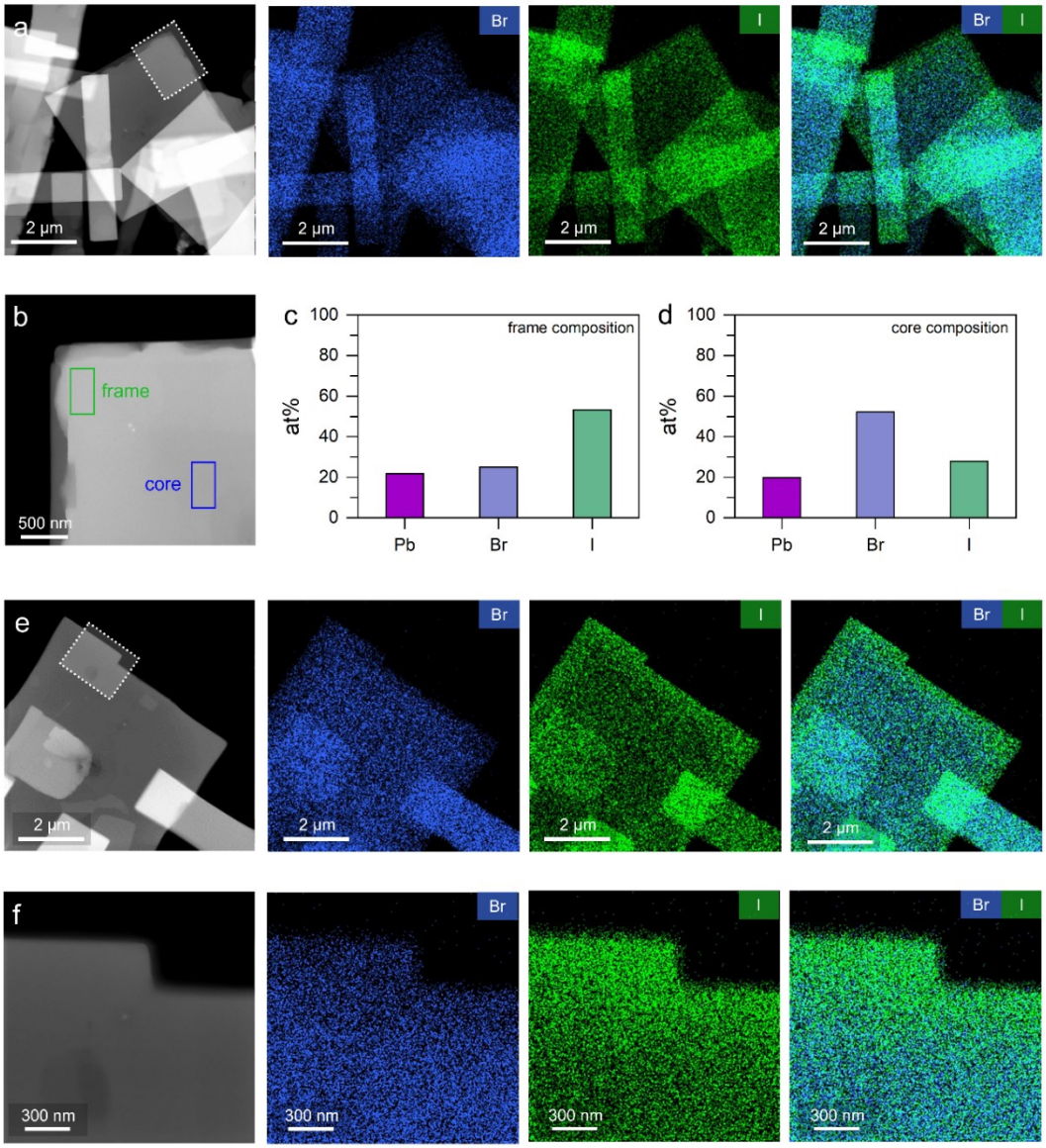

Figure 4.11. a) STEM image and EDX elemental mapping at lower magnification of the image represented in Figure 4.5 (I:Br=2.4). b) STEM image of **Figure 4.6** with the regions where the core and frame composition were extracted. c), and d) Elemental contribution for the regions marked in b). e) Additional lower and f) higher magnification STEM and EDX images of the same sample.

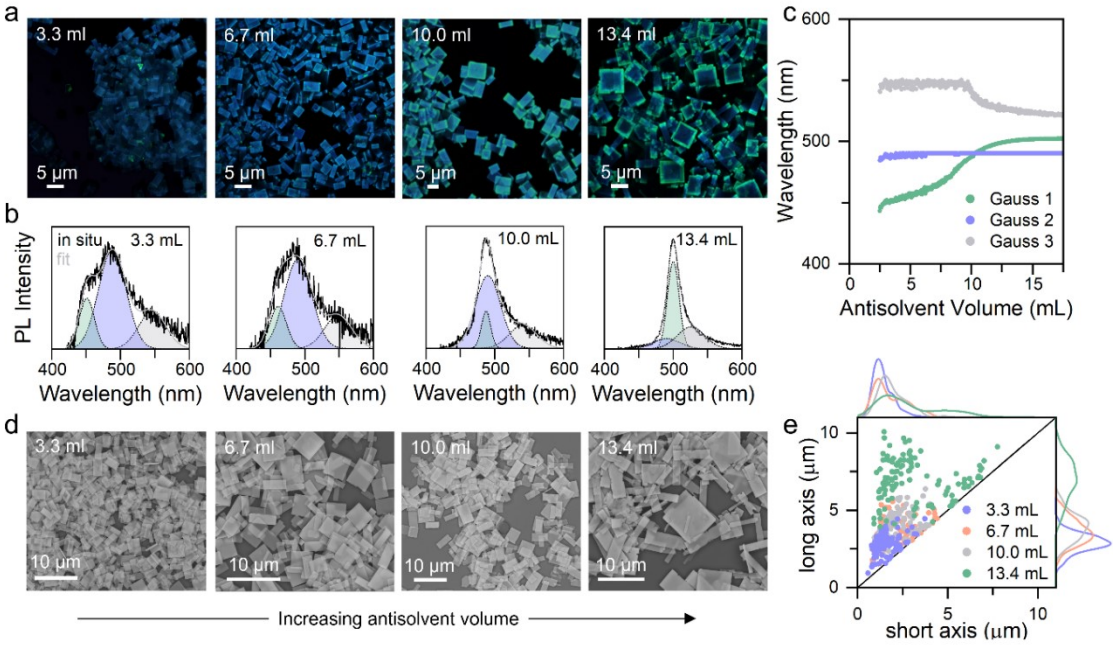

Figure 4.12. Details on the formation mechanism of heterojunctions from mixed precursor solutions. a) Confocal PL images (λex=400 nm) of microflakes from stopped recrystallizations at the shown antisolvent volume and b) corresponding in situ PL spectra fitted with the sum of three Gaussians. c) Position of the fitted Gaussians relative to the antisolvent volume. d) SEM images of the same microflakes represented in a). e) Size distribution of microflakes extracted from the SEM images in d), showing populations of rectangular- and square-shaped microflake heterojunctions. The diagonal line shows an aspect ratio of 1.

4.4 Phase-pure triple-halide heterostructure formation via sequential injection process

In this process, instead of using a precursor mixture to fabricate a 2D perovskite heterostructure, the process starts by dissolving presynthesized 2D layered perovskites in good solvents such as GBL and ACN, then injecting another precursor (dissolved 2D layered perovskite), and finally injecting a higher amount of antisolvent. The process initially leads to the formation of pristine 2D layered perovskite (core structure) by recrystallization, then, by the injection of second precursors and the continuous injection of antisolvent, the second layer is recrystallized (Frame). This process can be extended to two precursor secondary and third precursor injections to form a triple lateral heterostructure. The schematic illustration of the process is represented in **Figure 4.13a**. This sequential injection has two benefits: it forms phase-pure layers and leads to the formation of more complex heterojunction structures, such as triple halide heterostructures. Initially, PEA2PbBr4 was used as the core of a PEA2PbI4 frame via

delayed secondary injection of a PEA2PbI4 precursor dissolved in GBL, and the process was subsequently extended to other 2D layered perovskites and more complex heterostructures.

Figure 4.13b (hyperspectral confocal microscopy images) shows a deep blue emission from the core and a uniform green emission from the frame. The extracted PL emission intensity profile in **Figure 4.14** indicates a sharp transition from the green-emission frame to the blue-emission core. The PL spectra in **Figure 4.13c** confirm high color purity, with distinct PL peaks at 411 nm and 513 nm that correspond to the PL peak positions of the pure PEA_2PbBr_4 phase and are very close to those of the pure PEA_2PbI_4 phase, respectively. Additionally, the UV-vis absorption spectra display features of the pure PEA_2PbBr_4 phase, while the PEA_2PbI_4 frame shows a slightly blue-shifted absorption edge compared to pure PEA_2PbI_4. Therefore, the sequential injection strategy offers the opportunity to tune the band gap and frame components by injecting a mixed halide solution with varying xI = [I]/([I]+[Br]) content, as shown in **Figures 4.15-4.16**. Accordingly, the PL band and absorption edge of the frame could shift gradually toward higher wavelengths with increasing xI, indicating band-gap tuning via the halide ratio in the injected solutions. Interestingly, the spectral features of the PEA2PbBr4 core, regardless of iodide frame phase, remain unchanged. This confirms that the strategy preserves the purity of the core 2D-layered perovskite. **Figure 4.17** represents the size distribution of pristine and heterojunction microflakes. It has been observed that heterojunction structures are larger than pristine bromide-based crystals, and adjusting the antisolvent injection rate can tune their size. The slight batch-to-batch variation in the size distribution can further illustrate the high reproducibility of this strategy.

To control crystallization kinetics, in situ PL measurements are also performed for the sequential injection approach (**Figures 4.13e and 4.18** for homostructures). Accordingly, a weak band at 570 nm was observed, which is related to $[PbBr_3]^-$-GBL complexes generated in the solution (see **Figure 4.19**). With 2 ml of antisolvent injection, the emission of pristine PEA_2PbBr_4 crystals emerges at 410 nm, marking the onset of PEA_2PbBr_4 recrystallization. To confirm the consistency of precursor consumption and the completion of PEA_2PbBr_4 microcrystal formation, the PL emission intensity sharply increases and then gradually saturates. After injecting 9 ml of antisolvent in GBL containing the PEA_2PbI_4 precursor solution, there is an instantaneous drop in the PEA_2PbBr_4 PL intensity, likely caused by the absorption of PEA_2PbBr_4 emission by the dissolved PEA_2PbI_4 precursor (see **Figure 4.19**). After injecting 12 ml of antisolvent, the PL band corresponding to the PEA_2PbI_4 2D layered perovskite phase (at 500 nm) appears and progressively shifts to 510 nm, indicating the formation of I:Br halide alloyed phases in the heterostructure with decreasing bromide content until a stable composition—around 20% Br, as recorded by EDX, is reached at 20 ml of antisolvent injection, enabling emission at 510 nm. The alloyed halide composition of the framework may be related to incomplete consumption of the bromide phase prior to the injection of PEA_2PbI_4

dissolved in GBL (which can be further optimized to reduce bromide content in the alloy), and to interdiffusion of anions at the interface. Simultaneously, a relatively pure iodide phase begins to recrystallize on the edge of the PEA_2PbBr_4 core.

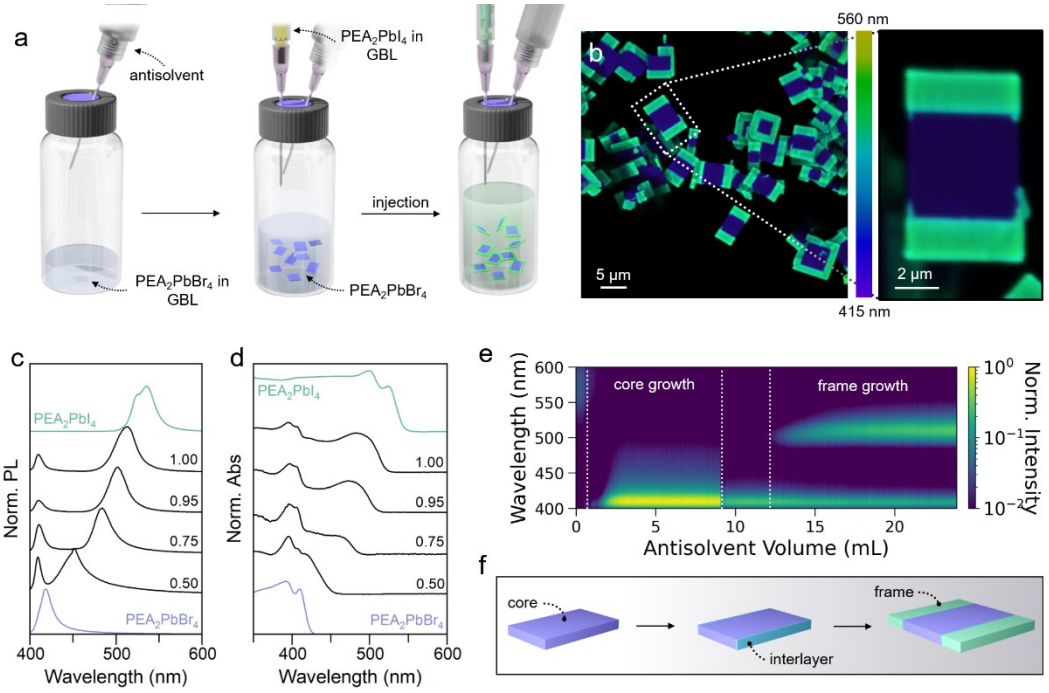

Figure 4.13. Sequential growth of heterojunctions with sharp interfaces. a) Representation of the sequential injection growth process. b) Confocal hyperspectral microscopy PL images indicating PEA_2PbBr_4-$PEA_2PbBr_xI_{4-x}$ heterojunctions in core-frame geometry that consist of nearly pure bromide phase in the core and slightly alloyed Br:I composition at the edges (λ_{ex}=400 nm). c-d) PL and absorption spectra recorded from the heterojunction microflakes fabricated by sequential injection with various frame compositions. The spectra of pure phases (PEA_2PbBr_4 and PEA_2PbI_4 homostructures) are reported for comparison (λ_{ex}=370 nm). e) In-situ recording of PL emission (λ_{ex}=365 nm) during the sequential growth, where the evolution is represented versus injected antisolvent volume. f) Schematic illustration of the growth process of the dumbbell-shaped heterojunctions.

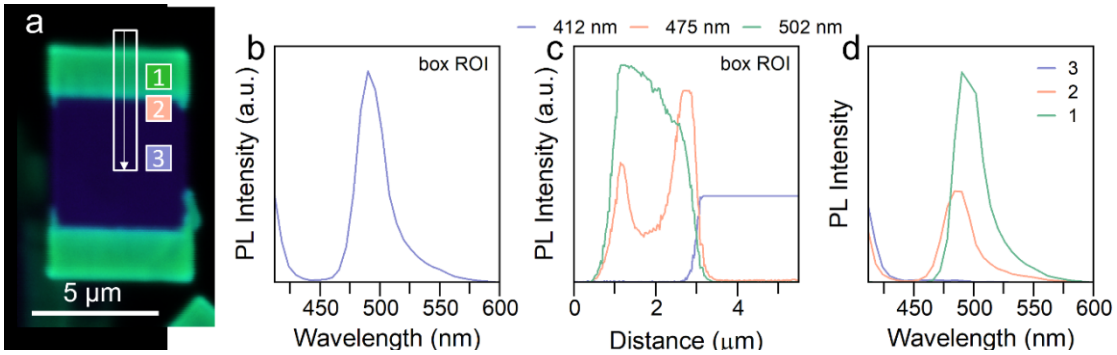

Figure 4.14. a) Confocal PL image (λ_{ex}=400 nm) as represented in **Figure 4.13**, with b) a spectrum extracted from the box in a). c) PL emission intensity profiles at 412, 475, and 502 nm, indicating the sharp transition between blue and green emitting regions. d) PL spectra extracted from the region marked with 1, 2, and 3, respectively.

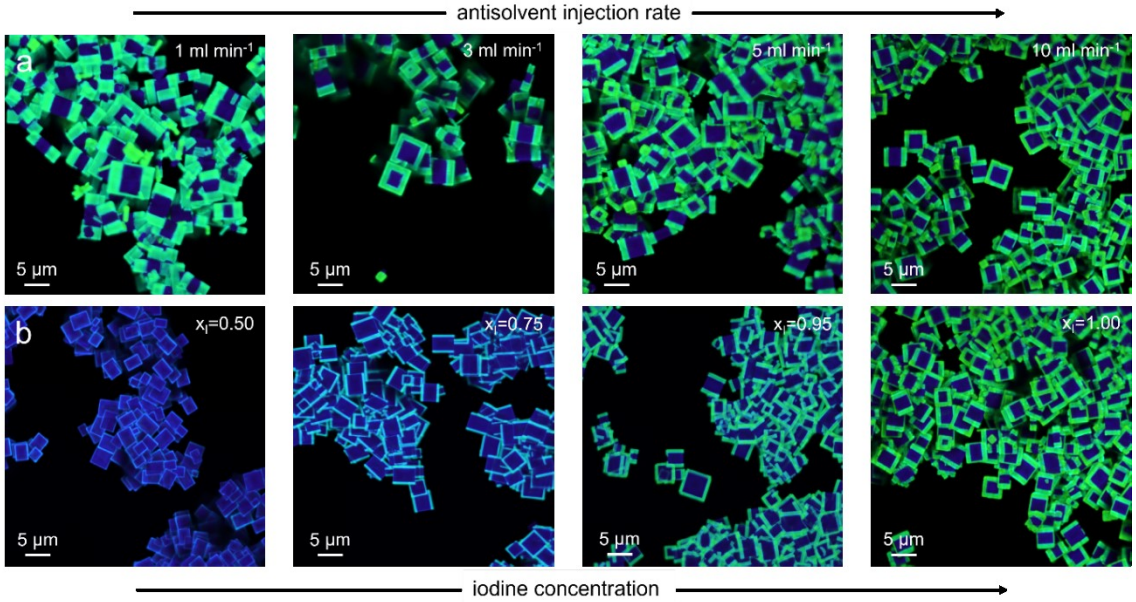

Figure 4.15. a) Confocal PL images (λ_{ex}=400 nm) of PEA_2PbBr_4–PEA_2PbI_4 in-plane heterojunctions prepared using the represented antisolvent injection rates. b) Confocal PL images of PEA_2PbBr_4–PEA_2PbI_4 heterojunctions prepared with precursor solutions containing the represented iodide fraction (x_I=[I]/([I]+[Br])).

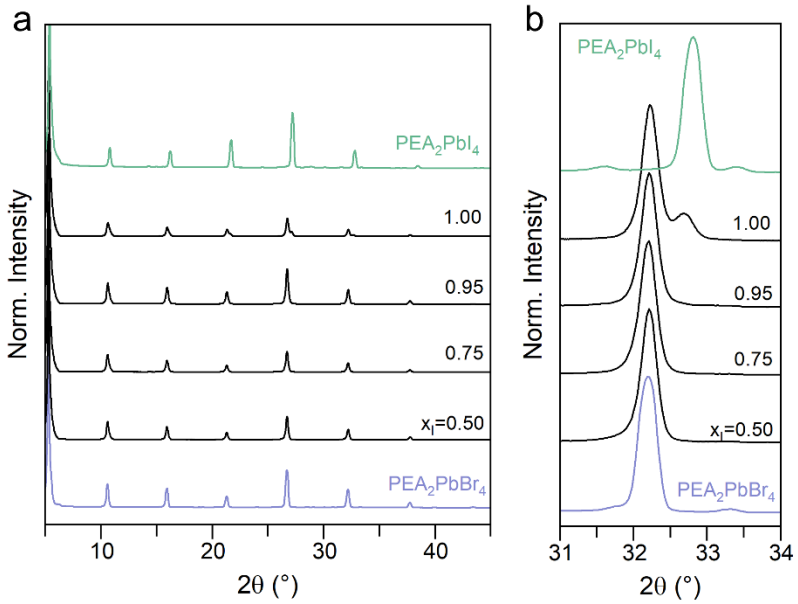

Figure 4.16. XRD pattern of PEA_2PbBr_4–PEA_2PbI_4 heterojunction structures prepared with precursor solutions containing the represented iodide fraction (x_I=[I]/([I]+[Br])). a) Overview and b) magnified view centered on the (0012) and (006) reflections of PEA_2PbI_4 and PEA_2PbBr_4.

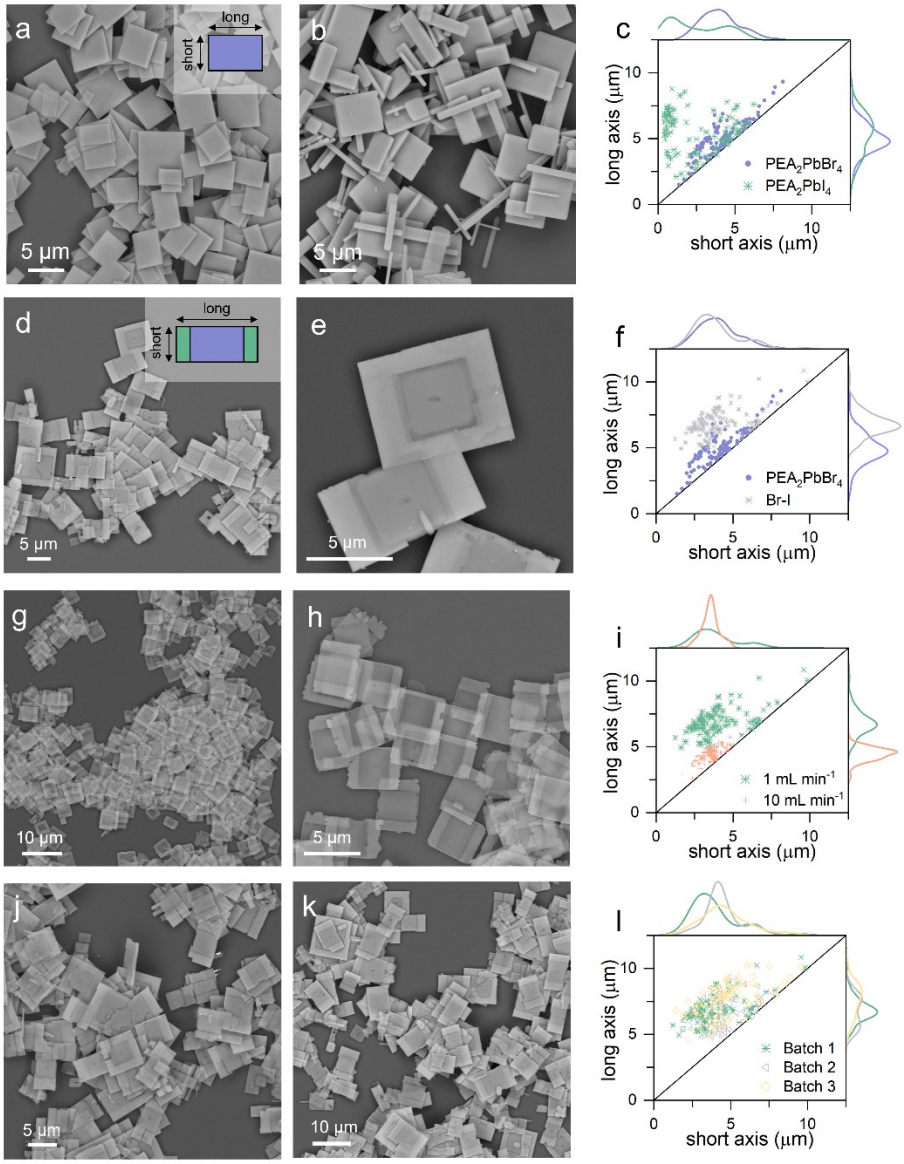

Figure 4.17. SEM images and size distributions of pristine PEA_2PbBr_4, PEA_2PbI_4, microcrystals, and their heterojunction structures obtained via controlled antisolvent injection from GBL solutions using DCB as the antisolvent. (a, b) SEM images of pristine PEA_2PbBr_4 and PEA_2PbI_4 microcrystals, respectively. c) Corresponding size distributions extracted from the SEM images. (d, e) Low- and high-magnification SEM images of PEA_2PbBr_4–PEA_2PbI_4 heterostructures obtained with an antisolvent injection rate of 1 mL/min. (f) Size distribution representing the asymmetric growth. (g, h) Low- and high-magnification SEM images of heterojunction structures prepared with an increased injection rate of 10 mL/min. (i) Comparison of the size distributions for both injection rates, illustrating that higher injection rates yield smaller heterojunctions. (j, k) Low-magnification SEM images of heterojunctions from two batches produced at 1 mL/min. (l) Size distributions of three independent batches, representing highly consistent results

and confirming the reproducibility of the injection strategy. The PEA_2PbBr_4 and Br–I size distributions are replotted in panels (f–l) for convenience and comparison.

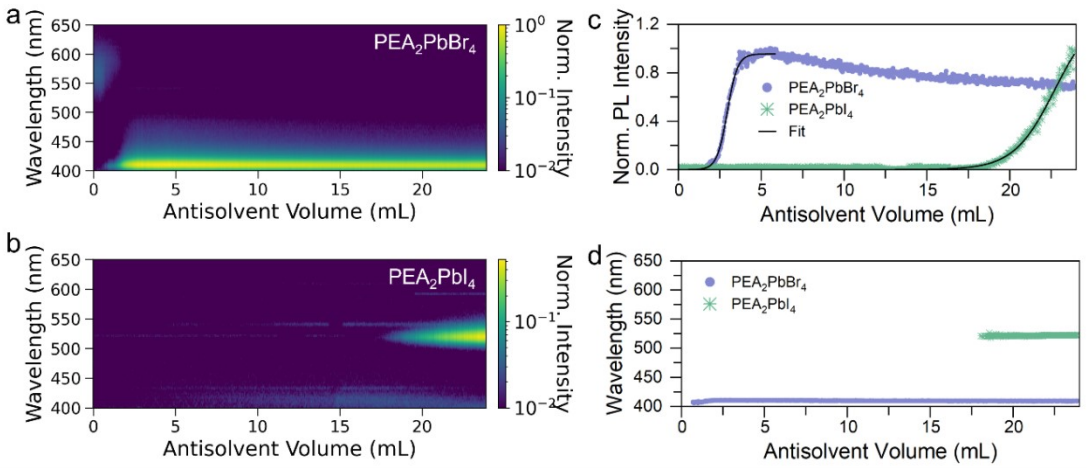

Figure 4.18. a-b*) In situ* PL spectra (λ_{ex}=365 nm) recorded during the recrystallization of PEA_2PbBr_4 and PEA_2PbI_4 from GBL with DCB as the antisolvent with an injection rate of 10 mL/min. c) Evolution of the PL intensity as a function of injected antisolvent volume, integrated over 408–410 nm for PEA_2PbBr_4 and 520–524 nm for PEA_2PbI_4. The growth rates (r_c) and crystallization points (V_{50}) are 3.2 mL and 2.9 mL for V_{50}, and 0.8 mL^{-1} and 3.2 mL^{-1} for r_c, respectively, for PEA_2PbI_4 and PEA_2PbBr_4. d) Position of the PL maximum during antisolvent injection.

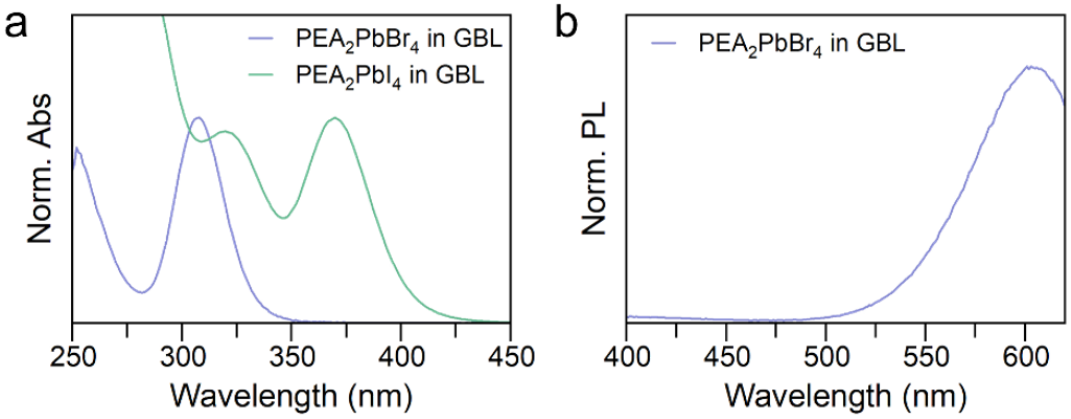

Figure 4.19. a) UV-Vis absorption spectra of PEA_2PbBr_4 and PEA_2PbI_4 powder crystals dissolved in GBL. b) PL spectrum (λ_{ex}=320 nm) of PEA_2PbBr_4 dissolved in GBL.

Based on this perfect matching between the core (high bandgap with UV or blue light) and frame (lower bandgap) heterostructures, they could enable optical coupling between the core and frame, or facilitate optical excitation from the higher bandgap core to the lower bandgap frame region, resulting in efficient compensation of the green emission from the frame. The heterojunctions exhibit blue and bright green emissions from the core and frame, respectively, under wide- field UV excitation (**Figures 4.20a, 4.20c,** and **4.21**). As shown in **Figure 4.21b**, the core of the heterojunctions is selectively

illuminated with a pulsed femtosecond laser at 375 nm through a 100 x objective (NA 1. 1.3 oil), and the resulting spatially and spectrally resolved images of the light emission are recorded, as shown in **Figures 4. 20d** and **4.20 e**. The observation of homogeneous, bright green emission from the frame regions demonstrates efficient optical coupling between the core and frame, which may arise from waveguiding, reabsorption, exciton diffusion, or energy transfer. The directional nature of this coupling (**Figure 4.22**) is confirmed by the selective excitation of one of the two iodide extremities, which results in no detectable emission from the bromide phase. To gain deeper insight into the optical coupling process, time-resolved photoluminescence (TRPL) and photoluminescence quantum yield (PLQY) measurements were performed on the heterojunction ensembles (see details in **Figures 4.23** and **4.24**). The results indicate that the PEA_2PbBr_4 core-related blue emission decays faster in the heterojunctions than in the pristine PEA_2PbBr_4 core, and the PLQY (blue emission intensity) decreases from 14% to 1%. In comparison, the overall blue and green (PLQY) emissions of the heterojunctions are around 6%. This suggests a loss channel with rapid decay for PEA_2PbBr_4 phase recombination, whereas the vigorous emission intensity from the PEA_2PbI_4 frame region indicates efficient core-to-frame coupling. Consequently, it is observed that the lifetime in the heterojunctions (compared to the pristine microflakes) is longer for the green emission of the frames, and the green emission intensity can be significantly increased from 1% in the pristine PEA_2PbI_4 microflakes to 6% in the heterojunctions. Therefore, radiative recombination in the PEA_2PbI_4 phase is strongly enhanced, as optical pumping from the core region may reduce non-radiative defects by preferentially localizing excitons near the heterostructure's crystalline interface.

The heterostructure interface reported with the sequential injection is well-defined, as evidenced by the elemental mapping using STEM-EDX, along with the compositional line scan as shown in **Figure 4.25a-e** that represents a sharp change in intensity for no iodide content and the Br/I signal in the core. The selective area electron diffraction (SAED) pattern, as shown in **Figure 4.25f-g**, from both the core and frame, confirms that each phase is crystalline with a monoclinic unit cell. Additionally, it has been observed that two distinct populations of heterojunctions are presented, one with core-frame morphology (almost 15%) and another with dumbbell shape, in which the PEA_2PbI_4 phase is grown only on two opposite edges. The lattice orientation in the core also determines the edge termination, which can be either armchair ([-110]/[110]) or zigzag ([100]/[010]). It has been hypothesized that the origin of these two growth morphologies lies in the orientation of the core lattice octahedra, with edge terminations running along the 45°-rotated [-110]/[110] or [100]/[010] directions, as shown in **Figure 4.26.** The microflake style, with corners truncated at 45°, is observed in the optical microscope images (**Figure 4.26**), supporting the possible occurrence of both edge terminations. Various lattice orientations in the cores are recorded by 4D-STEM SAED for these two populations (**Figures 4.25f-g**). Particularly, the asymmetry leading to

the dumbbell-shaped structures could stem from an uncertainty in the bromide site within the equatorial plane of the octahedra along the [010] direction. In contrast, along [100], only a single bromide site is observed in the monoclinic cell (**Figure 4.25h**). The asymmetry described above is not observed in the 45° lattice rotation with the [-110]/[110] orientation, which exhibits a symmetric distribution of this positional uncertainty at the equatorial positions along the edges, as shown in **Figure 4.25h.** This interpretation can be confirmed by SAED, which identifies the [100]/[010] lattice direction in the cores of the dumbbell-shaped heterojunctions, and the [-110]/[110] configuration for the core-frame heterojunctions (**Figures 4.25f-g**).

To observe the PEA_2PbBr_4 lattice along the [001] direction, two distinguished termination edges appear, either along the 45°-rotated [-110]/[110] or the [100]/[010] directions. The [-110]/[110] edges expose two halides in an armchair configuration, while the [100]/[010] edges expose a single halide atom in a zigzag configuration. The [-110]/[110] edges are expected to be thermodynamically less stable and more reactive. It has been assumed that the core-frame heterojunctions are less available; thus, likely, their core structures correspond to [-110]/[110] crystal orientation direction. Furthermore, they cannot fully account for the anisotropic formation behavior observed in core-dumbbell structures because both edge configurations are symmetric. Nevertheless, the configuration of the organic spacer ligand likely plays a decisive role. In the [100]/[010] configuration, two distinct behaviors are observed: the [010] edge shows parallel alignment, whereas the [100] edge exhibits alternating phenyl-ring orientations. Whereas in the [-110]/[110] configuration, the orientation of the phenyl ring alternates between edges. Therefore, the directional formation in the core-dumbbell heterojunctions is due to this anisotropy in organic-layer conformation.

Using sequential injection of precursors, multiple heterostructure sequences can be fabricated; for instance, triple halide microflakes with decreasing bandgap toward the edges, which can funnel photoexcited charges toward the edges and therefore be attractive for photocatalytic applications. It has been demonstrated that such a heterostructure, including a PEA_2PbCl_4 phase as the core, and then sequential injection of PEA_2PbBr_4 as a first frame, and PEA_2PbI_4 phase as a second frame, as represented in **Figures 4.1e** and recorded by the STEM and EDX images. Similar to PEA2PbBr4-PEA2PbI4 double halide heterojunctions, the iodide-rich phase is significantly alloyed, by up to 0.45 bromide, as recorded by STEM-EDX line scan. It has also been found that the amount of bromide signal in the core region is considerable, however, associated with two vertically separated phases in the bromide region (frame) and the chloride region (core) geometry as a result of overlapping diffraction features in the SAED patterns. Furthermore, this core-frame geometry is also observed when sequential injection is used to grow PEA_2PbCl_4-PEA_2PbBr_4 heterojunctions, and a similar core-frame architecture is observed in PEA_2PbBr_4-$PEA_4AgBiBr_8$ heterojunctions. More

data on metal cation heterojunctions and triple halide heterojunctions are provided in **Figures 4.27-4.30**.

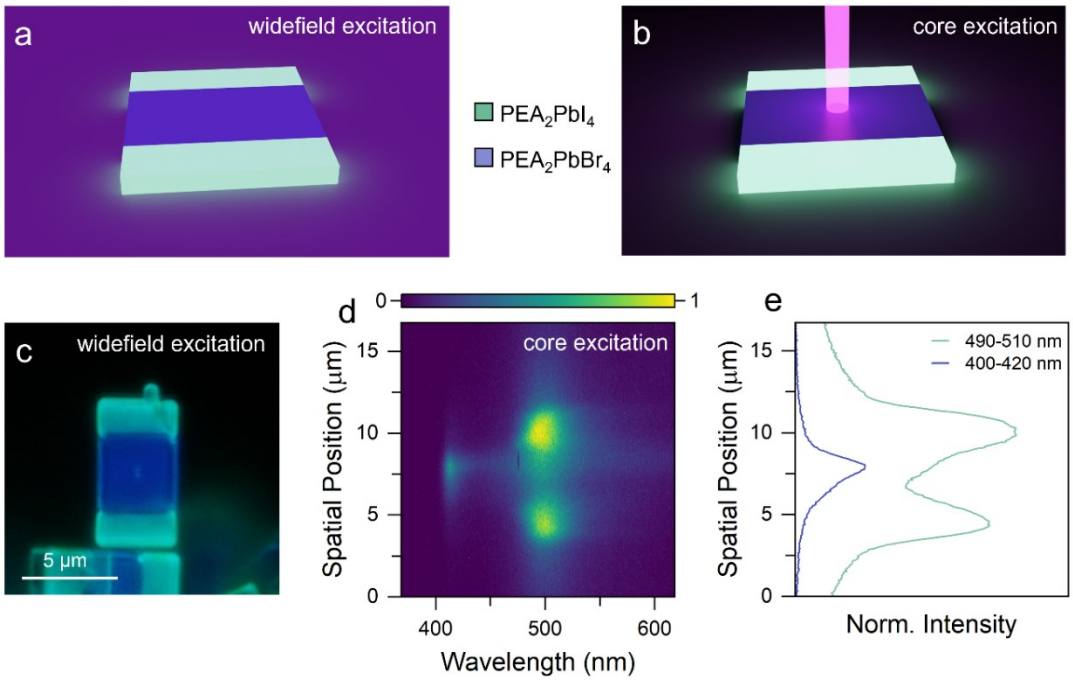

Figure 4.20. Optical coupling between the PEA_2PbI_4 and PEA_2PbBr_4 phases in a dumbbell-shaped heterostructure. (a, b) Schematic representation of selective core excitation and wide-field illumination. (c) Optical emission image of a dumbbell-shaped heterojunction (λ_{ex}=365 nm). (d) Spatially resolved emission spectra of a similar heterojunction under selective excitation of the bromide-based core (λ_{ex} = 375 nm), representing emission from the PEA_2PbI_4 extremities. (e) Spatial intensity distributions of the PEA_2PbBr_4 emission (400–420 nm) and the PEA_2PbI_4 emission (490–510 nm) extracted from d).

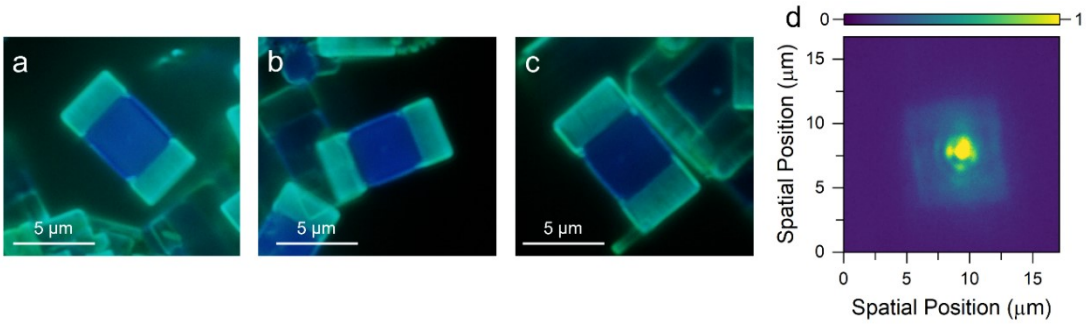

Figure 4.21. a-c) Additional optical PL image of a dumbbell-shaped heterojunction microflake under UV-light excitation, d) Spatially resolved emission intensity of a dumbbell-shaped heterojunction with localized excitation of the core with a focused sub-micron size laser spot (fs-pulsed laser at 375 nm). The spectral dispersion is represented in **Figure 4.20**.

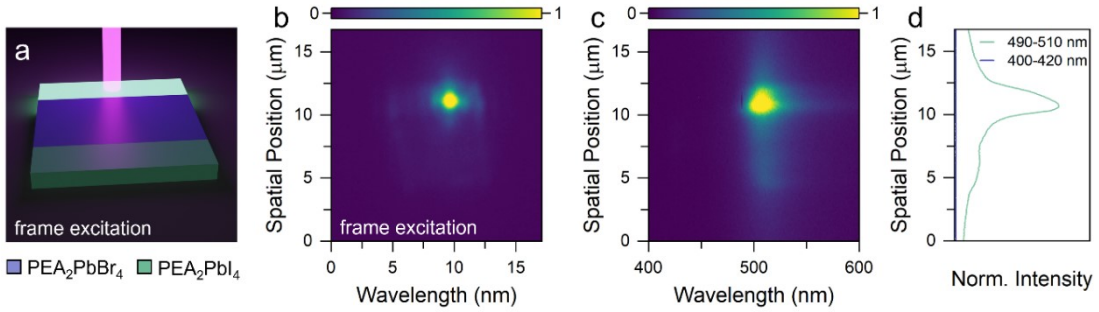

Figure 4.22. a) Representation of the selective excitation of the iodine phase. b) Spatially resolved emission intensity obtained by selectively exciting one of the two iodine extremities with a sub-micron focused 375 nm fs-pulsed laser. c) Spectral and spatial dispersion of the same crystal represented in b). d) Intensity distributions in the 400–420 nm and 490–510 nm ranges extracted from c), indicating no detectable emission from the core.

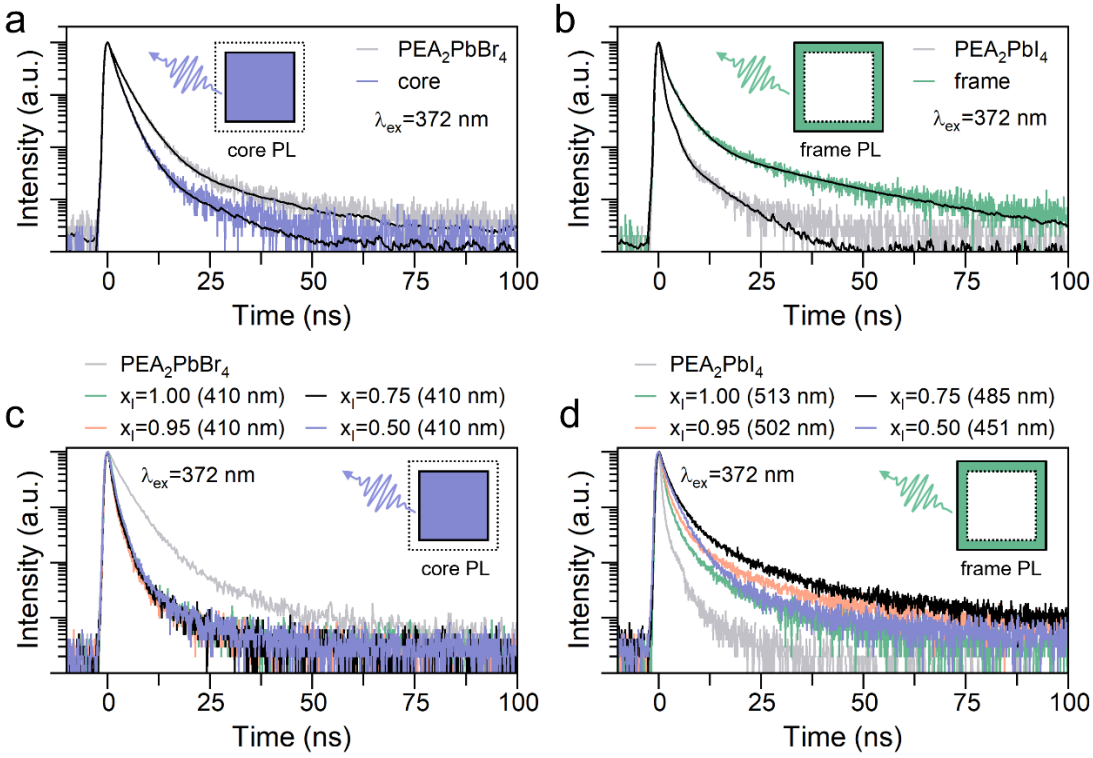

Figure 4.23. a) TRPL of the PEA_2PbBr_4 core and (b) the iodine-rich frame following 372 nm excitation for a representative heterojunction prepared with an antisolvent injection rate of 1 mL/min. (c, d) Core and frame decay traces of heterojunctions with varying frame compositions prepared using an antisolvent injection rate of 10 mL/min (see also **Figure 4.13**).

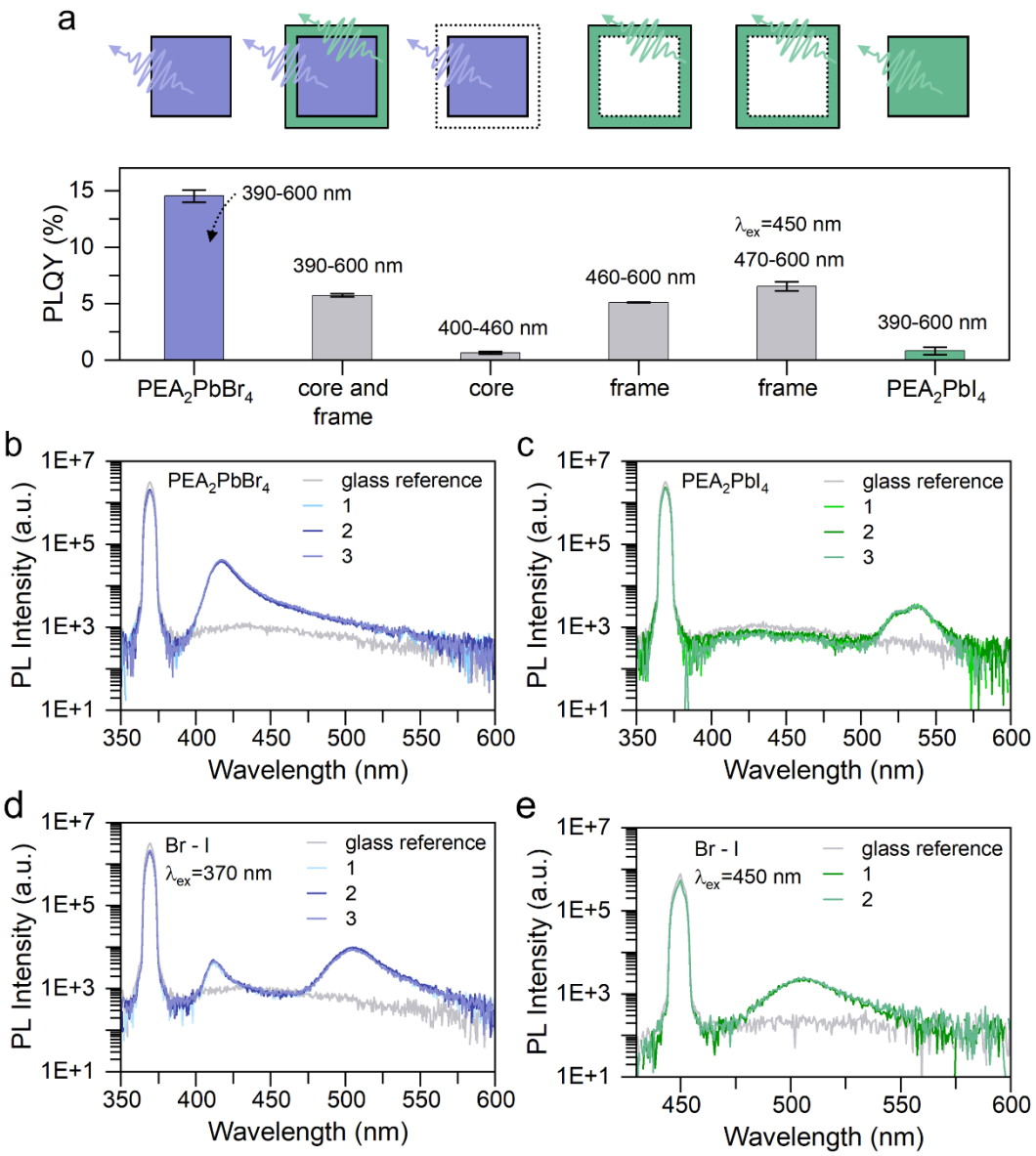

Figure 4.24. a) PLQY measurements of pristine and heterojunction microflakes (injection rate 1 mL/min). The PLQY was measured over the indicated spectral range using excitation wavelengths of 370 nm and 450 nm, as specified. (b–e) Corresponding PL spectra used for PLQY measurement. All spectra for both pristine and heterojunction microflakes were recorded from the same drop-cast sample on glass at various locations.

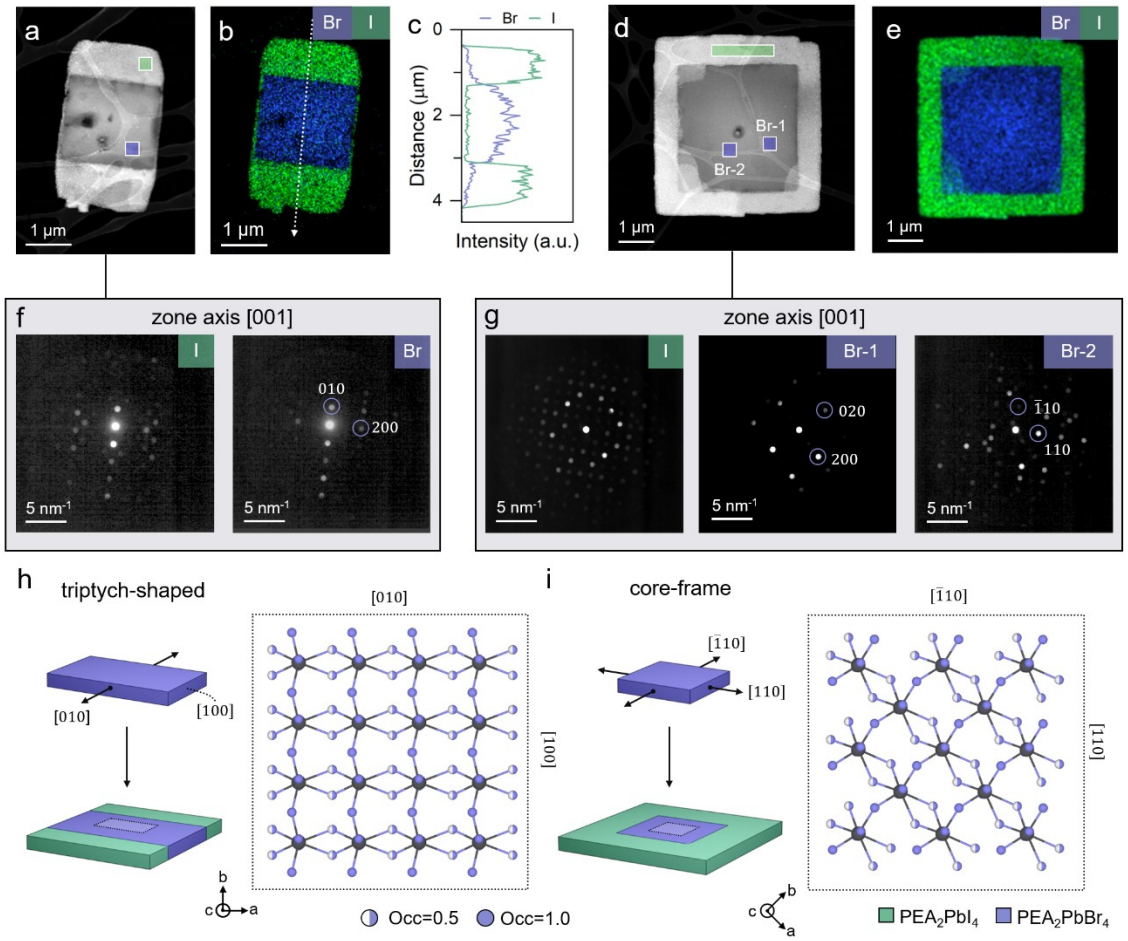

Figure 4.25. Crystallographic origin of dumbbell-shaped and core–frame heterojunctions. a) STEM image and (b) corresponding EDX map of a typical dumbbell-shaped heterojunction. c) EDX line scan along the arrow in (b) representing the sharp change in bromide and iodide intensities at the interface. (d, e) STEM image and (e) corresponding EDX map of a core-frame heterojunction. f) SAED patterns of the iodide wings and bromide core regions of the dumbbell-shaped configuration are marked in (a). g) SAED patterns of the bromide core, and iodide frame regions of the core-frame heterojunction are marked in (d). The prominent reflexes in the SAED patterns in f-g are identified with labels indicating the crystallographic direction. h) Representation of the directional growth leading to the dumbbell-shaped configuration and top view on the octahedra lattice of the core with [100]/[010] lattice direction. i) Scheme of the symmetric core-frame growth originating from a core with a 45° rotated lattice.

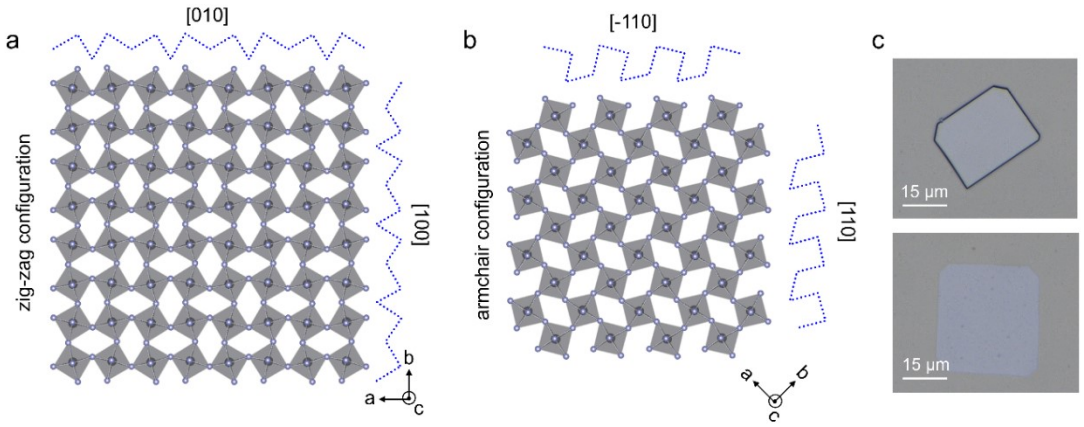

Figure 4.26. Lattice configurations influencing the edge termination of the inorganic layer. a) Zig-zag ([100]/[010]) and b) armchair ([−110]/[110]) configurations, the latter obtained by a 45° rotation of the lattice. (c) Optical microscope images of PEA_2PbBr_4 microcrystals grown on glass substrates using our previously reported method [132].

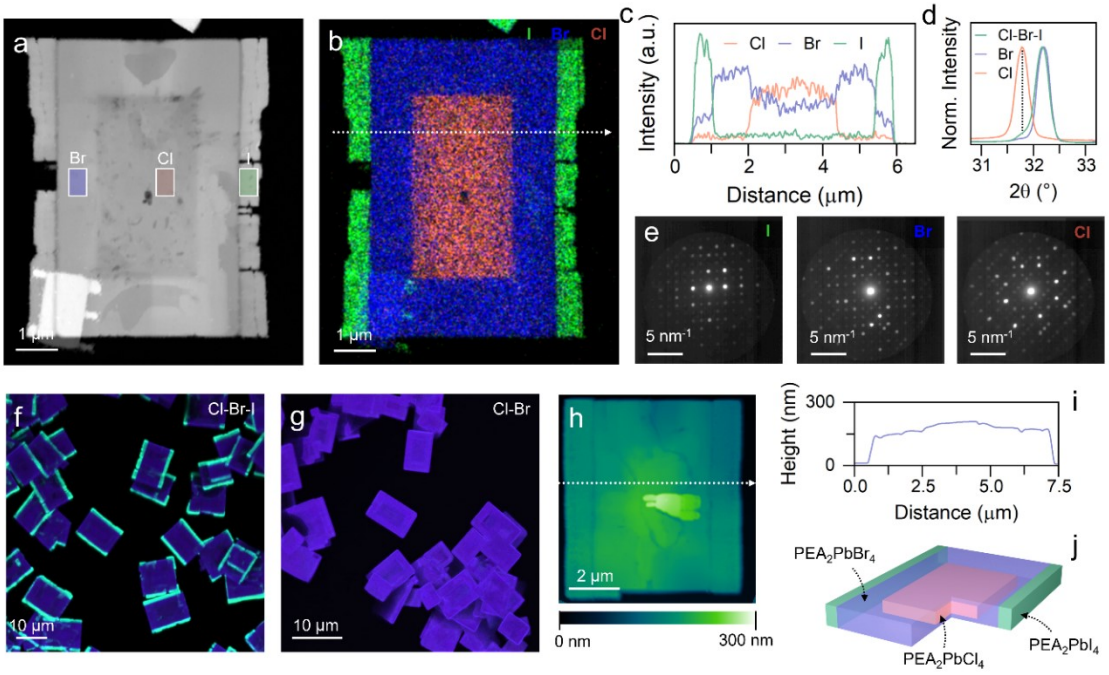

Figure 4.27. Formation of triple halide core-frame-frame heterojunctions by sequential injection. a) STEM and b) corresponding STEM-EDX map displaying the three different halide regions. c) EDX line scan along the arrow indicated in b). d) e) SAED pattern of the iodide-, bromide-, and chloride-regions represented in a). f) Confocal hyperspectral mapping of triple chloride-bromide-iodide and g) double chloride-bromide heterojunctions. h) AFM image and i) corresponding height profile of a single triple halide heterojunction microflakes. j) Representation of the phase distribution

within the triple halide heterojunctions, with the chloride core embedded in the bromide phase.

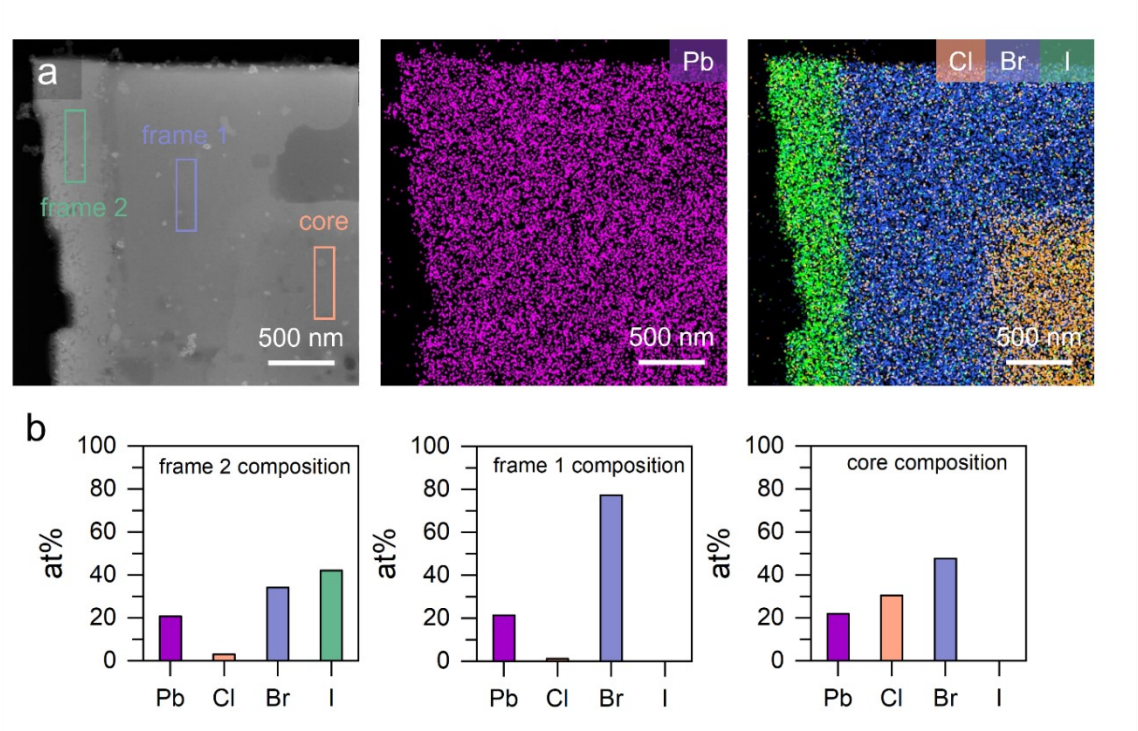

Figure 4.28. STEM images and EDX maps of PEA_2PbCl_4-PEA_2PbBr_4-PEA_2PbI_4 triple halide heterojunction. a) Higher magnification image with the corresponding EDX elemental maps of the images represented in **Figure 4.1. b**) Composition of frame 1 and frame 2, along with the core extracted from the regions marked in a).

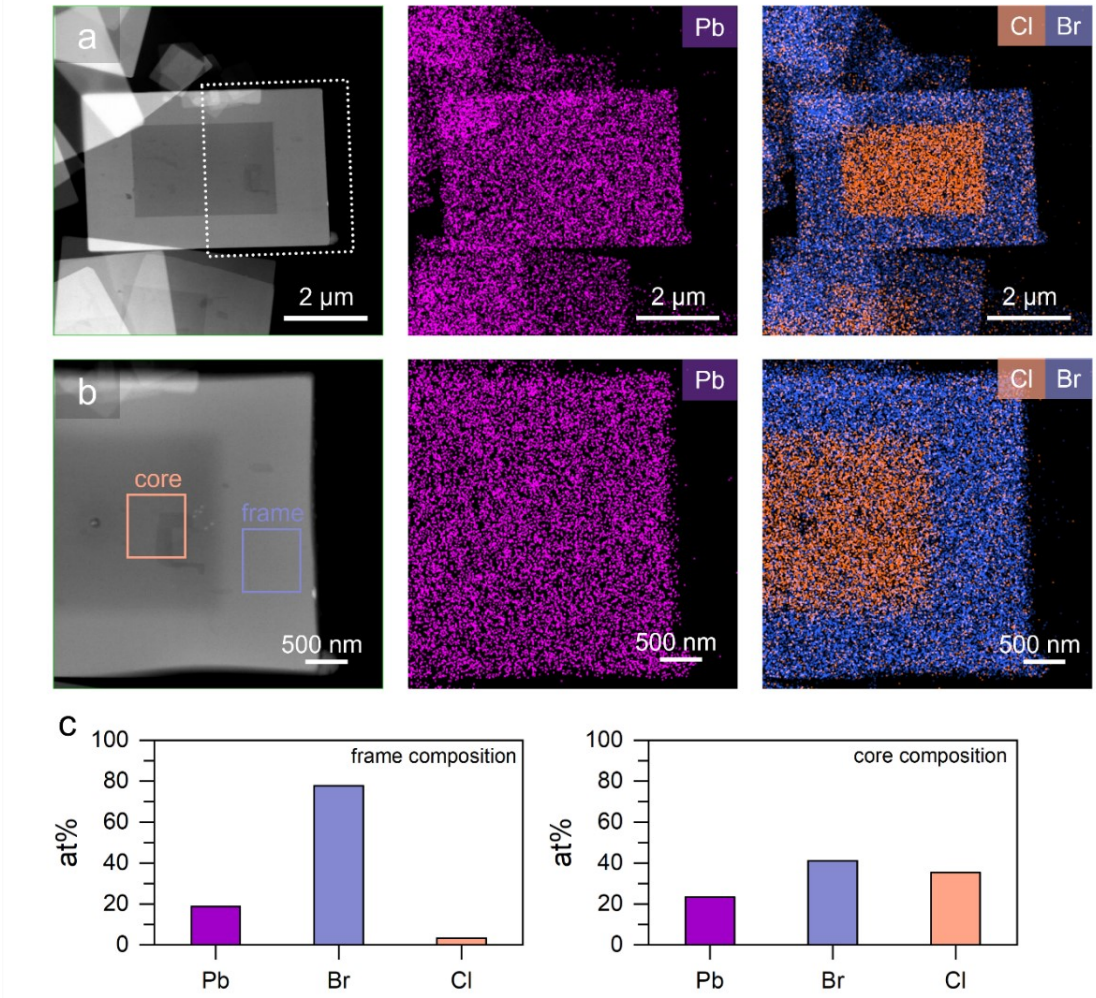

Figure 4.29. Additional STEM images and EDX elemental maps of PEA_2PbCl_4-PEA_2PbBr_4 core-frame heterojunction. a) and b) lower and higher magnification images with the corresponding EDX elemental maps. c) Composition of core and frame extracted from the regions marked in b).

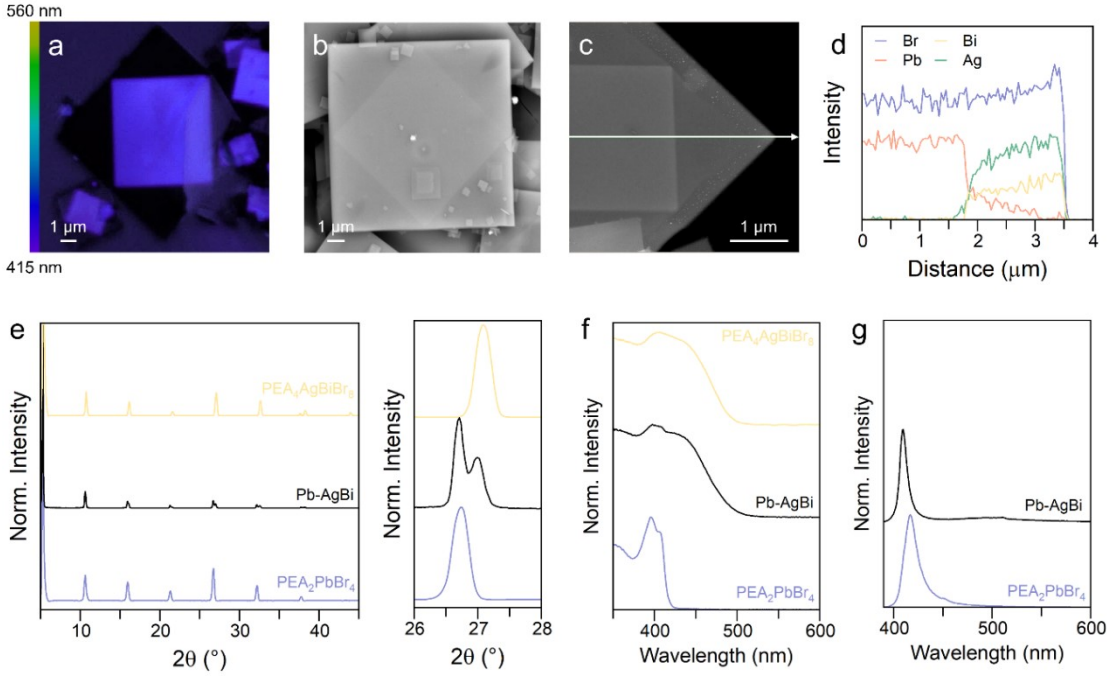

Figure 4.30. Heterojunctions made of a PEA_2PbBr_4 core and a double $PEA_4AgBiBr_8$ perovskite frame. a) Confocal hyperspectral PL microscopy image (λ_{ex} = 400 nm) of a PEA_2PbBr_4–$PEA_4AgBiBr_8$ core–frame heterojuunction, indicating the blue-emitting core surrounded by a non-emissive frame. b) SEM image of a single heterojunction showing the 45° rotation of the frame relative to the core. c) STEM image of the heterojunction and (d) corresponding EDX line scan along the arrow marked in c), confirming the core–frame configuration. e) Overview and zoomed-in XRD patterns of PEA_2PbBr_4, $PEA_4AgBiBr_8$, and the core–frame heterojunctions, representing two distinct reflections for the heterojunction. (f, g) UV–Vis absorption and PL spectra (λ_{ex} = 370 nm) of PEA_2PbBr_4, $PEA_4AgBiBr_8$, and the core–frame heterojunctions. As also shown in a), the $PEA_4AgBiBr_8$ phase shows no observable PL.

4.5 Electric potential mapping with Kelvin Probe Force Microscopy

One of the main benefits of the capability to design in-plane heterojunctions is the ability to control changes in energy levels and energy flow, and to shape the potential landscape within single microcrystals. Therefore, the electrostatic potential of heterostructure microflakes can be evaluated using Kelvin Probe Force Microscopy (KPFM), which enables measurement of relative changes in electrostatic potential across the interface and absolute work function values [134]. The work function strongly depends on charge trapping, band bending, and surface chemistry [135], and thus KPFM provides crucial information about the electronic and surface chemical properties at the nanoscale. This section focuses on heterojunctions with various halides (chloride, bromide, and iodide). Initially, a set of phase-pure 2D microflakes for each halide was

measured, and the corresponding work function was obtained and listed in **Table 2** and shown in **Figure 4.31a**. It is worth noting that the order of increasing work function does not correlate with an increase in band gap of these 2D layered perovskites. **Figure 4.31b** represents dumbbell-shaped PEA2PbBr4-PEA2PbI4 heterojunctions generated by sequential injection, therefore with pure or pristine PEA2PbBr4 core, and a nearly phase-pure PEA_2PbI_4 frame that contains a tiny amount of bromide phase. The high quality of the heterojunctions in terms of phase and interface homogeneity is demonstrated in **Figure 4.31b** (hyperspectral confocal PL images). The KPFM and atomic force microscopy (AFM) images of the dumbbell heterojunction microflakes are reported in **Figures 4.31b** and **4.31c**. The higher work function of the PEA_2PbBr_4 phase, indicated by the lower contact potential difference (CPD) signal, is clearly observed in the core regions. In contrast, the dumbbell represents the higher CPD signal expected for the iodide phase. It is worth noting that the variation in the CPD signal between the two regions is less than the work function variation of pristine PEA_2PbBr_4 and PEA_2PbI_4 structures, given by the fraction of bromide phase presented in the iodide phase. As shown in **Figure 4.31d**, the iodide-bromide interface section of the magnified scale demonstrates a slightly larger thickness of the bromide core than the two iodide sections and a tiny dip in height at the interface. A gradual increase in CPD signal is observed in the CPD profile from the bromide-based core to the iodide-based region, spanning approximately 500 nm (see **Figure 4.31e**), indicating a charge redistribution that extends significantly beyond the morphological interface. The migration of positive charge from bromide to iodide phases rationalizes the relative decrease in CPD in the iodide region toward the interface. In contrast, the absence of a positive charge in the bromide heterojunction region explains the increase in CPD toward the interface. **Figure 4.31a** shows the band alignment, with a larger valence-band offset resulting from the ca. 120 meV work-function difference, which is consistent with such charge-migration processes. Interestingly, no charge-accumulation peaks in CPD or localized valleys at the interface have been observed, suggesting that they may be related to defects, charge traps, or vacancies. Interestingly, in PEA_2PbCl_4-PEA_2PbBr_4 heterojunctions, the variation in work function between the phases is much smaller than in PEA2PbBr4-PEA2PbI4 heterojunctions, around 60 meV, as reported in **figures 4.32-4.34**. As a result, less pronounced charge redistribution effects are expected. The observation indicates that, in KPFM maps of the full crystals, in many cases an increase in CPD from the PEA2PbCl4 core to the PEA2PbBr4 frame region, as depicted in **Figure 4.34**, implies that opposite work-function values are expected. However, this could be an edge or interface effect. **Figure 4.28** shows that, in some cases, an increase in the CPD signal at the edge of PEA2PbCl4 microflakes is observed. Additionally, the band alignment of the PEA2PbCl4 and PEA2PbBr4 phases could lead to electron transfer from PEA2PbCl4 to PEA2PbBr4 at the interface, as shown in **Figure 4.31a**, resulting in an increase of the CPD signal at the PEA2PbBr4 to PEA2PbCl4 side of the heterostructure. A local maximum of CPD at the

interface was identified in the PEA2PbCl4-PEA2PbBr4 heterojunctions using higher spatial resolution. However, the CPD maximum could also be related to edge effects, as this interface corresponds to a step in microflake height.

Regarding triple halide heterojunctions, as shown in **Figure 4.33**, it has been found that interface effects play a crucial role; therefore, the local CPD maximum occurs at the PEA2PbCl4-PEA2PbBr4 heterostructure, and the CPD increases from PEA2PbBr4 to PEA2PbI4.

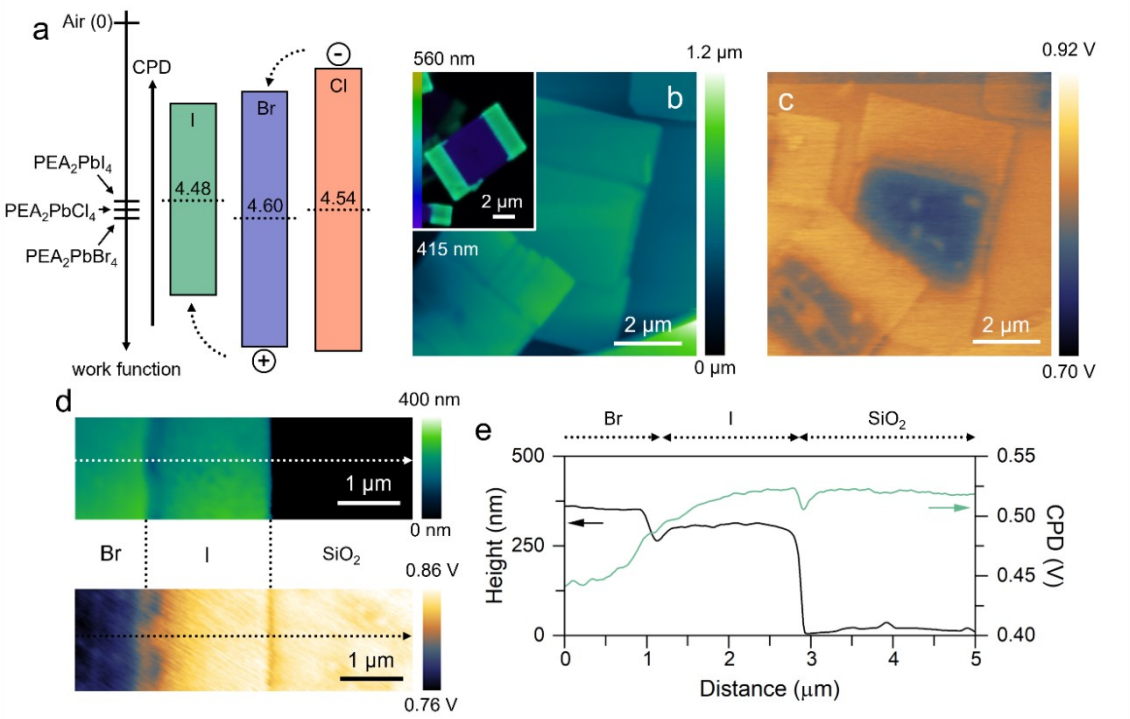

Figure 4.31. Electrical potential landscape in heterojunction microcrystals grown by sequential injection. a) Work functions of the 2D layered perovskites with pure halide phases measured by KPFM from homostructures, and a representation of the band alignment of the three different materials, indicating the hypothesized charge transfer upon contact formation. The opposite polarity of CPD relative to the work function is shown by the arrows. The band gap, determined from the excitonic peak in absorption, is represented by the height of the colored rectangles. b) AFM topography (inset shows a typical hyperspectral confocal fluorescence image of a single microcrystal from this batch), and c) CPD signal measured by KPFM of single dumbbell-shaped heterojunction microflakes. d) Topography and CPD measurements on a magnified region extending from the center to the edge of the microflakes. e) Averaged height and CPD profiles derived from the data in d). For the KPFM experiments, the microcrystals were deposited on SiO2 substrates.

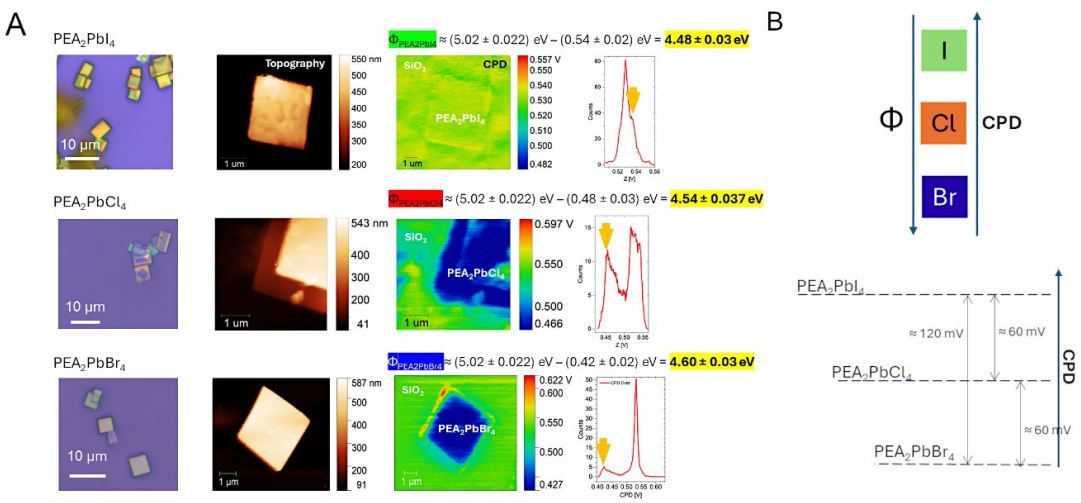

Figure 4.32. a) Optical microscope, AFM topography, and CPD images obtained by KPFM; each series is related to a homostructure based on iodide, bromide, or chloride. By relating the CPD signal to the work function of the tip ($V_{CPD} = (\Phi s - \Phi p)/e$), the absolute work function values of the microcrystal materials can be obtained. V_{CPD} values extracted are indicated by the orange arrows in the three graphs reporting the CPD distribution. Right end schemes (B) are reported to visualize better relative differences in work function values between the three compositions.

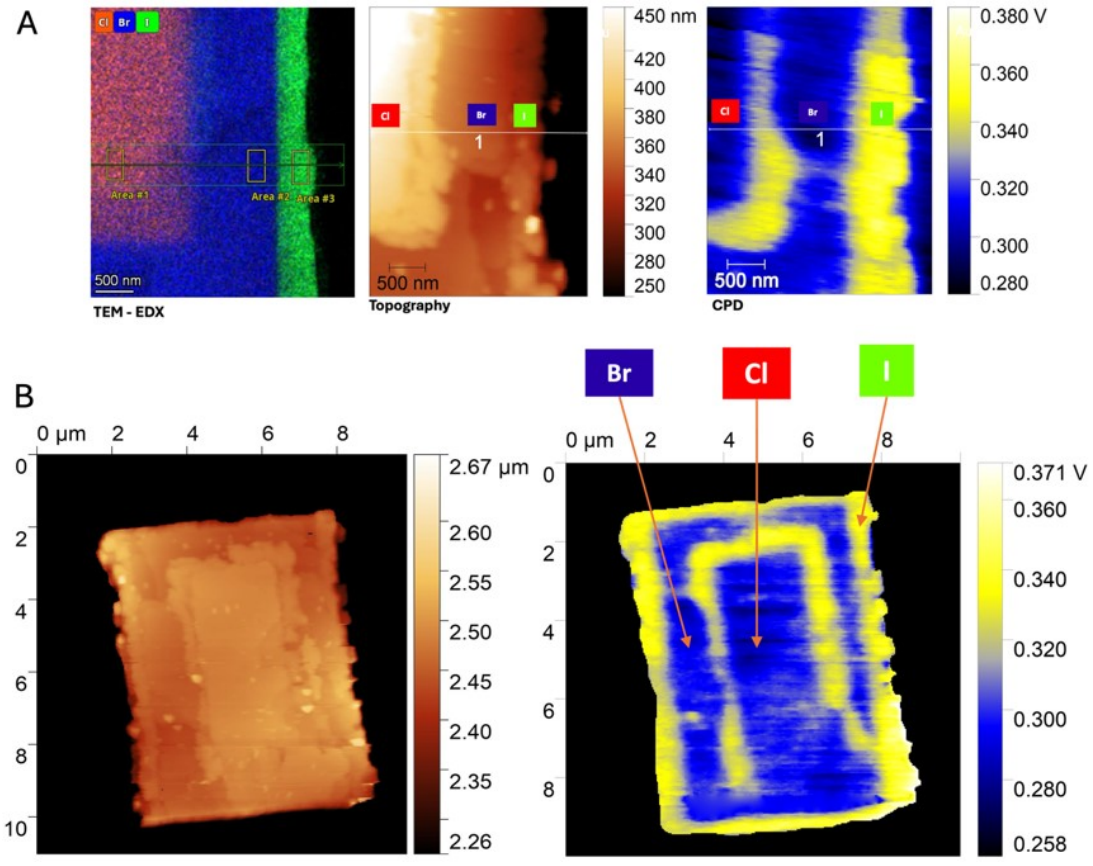

Figure 4.33. A) Compositional EDX elemental map, AFM topography and KPFM-CPD images of chloride-bromide-iodide core-frame-frame triple-halide heterojunction. B) AFM and KPFM-CPD images of an entire microcrystal, evidencing the correlation of CPD signal with the composition and morphology.

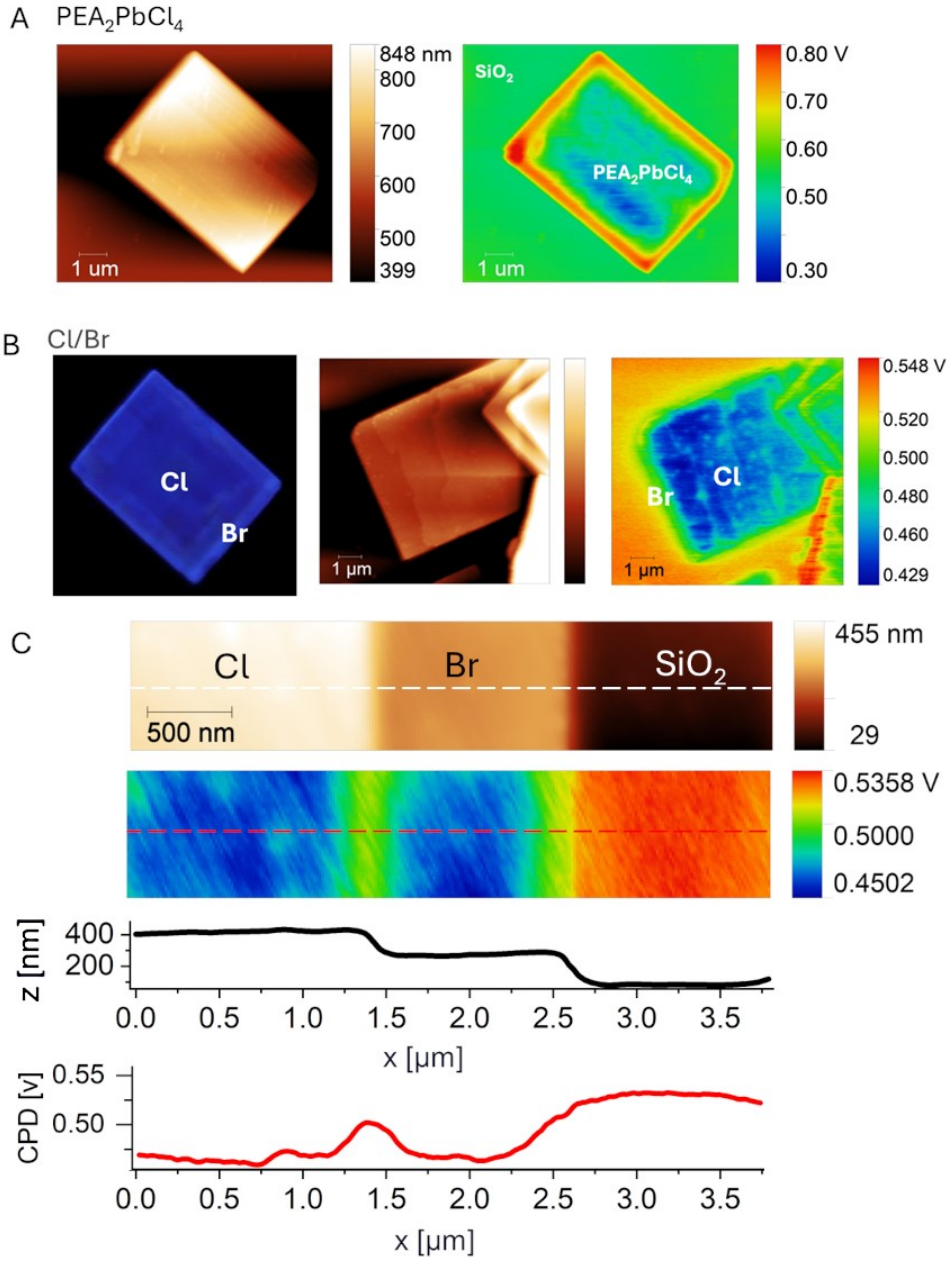

Figure 4.34. A) AFM and KPFM images of a single PEA2PbCl4 microflake. A pronounced edge effect is observed in the CPD map, with an accumulation of negative charges at the edges of the microflake. B) Hyperspectral PL confocal, AFM topography, and KPFM-CPD images of a chloride-bromide single crystal heterojunction. Small z-steps in the microcrystal topography are observed, which correlate with slight increases in the CPD image. C) AFM topography and KPFM-CPD map measured on a 1µm wide stripe

from the center to the edge of the microcrystal heterojunction with a representative line profile. A localized increase in CPD signal at the interface is observed, most likely originating from the step-like discontinuity in microflake height and resulting in negative charge accumulation at the edges.

4.6 Conclusion

This chapter presents an innovative sequential growth method for creating in-plane heterojunctions in 2D layered perovskite microflakes through antisolvent-triggered recrystallization, allowing precise control over composition and structure. The composition and band gap of the heterojunctions can be tuned by adjusting the solvation concentration of the pristine 2D layered perovskites, which have irregular shapes and structures, as well as by the associated interfacial offset. This enables the customization of recombination dynamics, charge transfer, and emission color at the junction. The sequential injection of different 2D-layered perovskites during fabrication offers flexibility and sharp interfaces, allowing tailored perovskite sequences in heterostructures and the formation of multiple heterojunctions. This growth strategy provides a versatile platform for engineering the electrical potential landscape and energy band gap in 2D layered perovskites, making them highly suitable for optoelectronic applications such as photodetectors, LEDs, energy harvesting, and photocatalysis. Additionally, the fundamental concept of heterojunctions formed via sequential recrystallization can likely be extended to other organic-inorganic structures, like metal-organic chalcogenides.

4.7 Experimental Synthesis

4.7.1 Chemicals and Materials

Lead(II)chloride ($PbCl_2$), Lead(II)bromide ($PbBr_2$, ≥98%), Lead (II)iodide (PbI_2, 99%), hydrobromic acid (HBr, 48%), hypophosphorous acid (H_3PO_2, 50%), hydroiodic acid (HI, 57%, distilled, 99.999% trace metal basis), phenethylammonium iodide (PEAI, ≥98%), phenethylammonium bromide (PEABr, ≥98%), phenethylamine (PEA, 99%), acetonitrile (ACN, anhydrous, 99.8%), N, N-dimethylformamide (DMF, 99.8 %, anhydrous), toluene (≥99.7%, anhydrous), ethyl acetate (≥99.5%), acetone (≥99.5%), 1,3-dichlorobenzene (DCB, anhydrous, 99%), γ-Butyrolactone (GBL, anhydrous, 99%) were purchased without any further purification from Sigma-Aldrich.

4.7.2 Synthesis of pristine irregular-shaped powder 2D layered perovskites

The pristine powder of 2D-layered perovskites was prepared using a previously reported fast-crystallization method [101], which produces irregularly shaped, large microflakes (see Figures 4.2 and 4.3). By dissolving these microflakes in ACN and GBL (good solvents) and then recrystallizing via controlled injection of an antisolvent (toluene or DCB) at 1

ml/min, the process yields consistently well-defined microflakes with a uniform, narrow size distribution, as shown in Figures 4.17. The gradual addition of an antisolvent reduces precursor solubility, increases saturation, and triggers nucleation. As the solute is consumed during nucleation, the saturation decreases but remains sustained by ongoing solvent addition, promoting crystal growth. Ultimately, the system reaches equilibrium, halting further growth and nucleation.

The solubility in a good solvent like ACN, as reported from ICP analysis, is 2×10^{-2} mmol/mL for PEA_2PbI_4 and 6×10^{-4} mmol/mL for PEA_2PbBr_4 (see Figure 4.1b). The variation in the solubility of pristine microflakes reflects differences in recrystallization behavior. In situ PL spectroscopy was performed to monitor recrystallization from ACN precursor solutions at a concentration similar to that used during toluene injection (Figure 4.4). In in situ PL, the final spectrum does not match the ex situ spectrum. To understand this discrepancy and assess the duration of a typical in situ experiment, the prepared sample was directly exposed to the excitation source of a 365- or 385-nm LED, without any washing after synthesis. It became clear that light exposure causes quenching and a blue shift of the PL emission (Figure 4.24). The confocal images before and after exposure show that the green-emission frame nearly disappears, indicating preferential degradation of the iodide-rich phase upon light exposure in the solution mixture. The absorption spectra of the supernatant after light exposure reveal two bands at 295 and 363 nm, attributed to I3- formed during light-induced degradation of the iodide-rich phase, as discussed in the literature [136,137]. To reduce degradation of this phase in the heterojunctions, dodecanthiol (DDT) was added to the antisolvent to convert I3- and I2 back to I-, maintaining the iodide-rich phase during in situ measurements. Adding DDT to the heterojunction solution does not quench or shift the PL emission under 385 nm LED illumination. Additionally, after light exposure, the supernatant lacks bands associated with I3- compounds, and the unchanged microlakes suggest successful mitigation of heterojunction degradation, as indicated by the steepness of the PL intensity-recrystallization rate (rc) correlation at maximum intensity. Recrystallization onset was estimated using V50, the antisolvent volume at which 50% of the maximum PL emission is reached. Both rc and V50 were determined by fitting the integrated PL intensity to a logistic function. Pristine bromide-based microflakes (here PEA_2PbBr_4) begin to recrystallize at rc = 12 mL^{-1} and V50 = 0.8 mL, while pristine iodide-based microflakes (here PEA_2PbI_4) recrystallize later at rc = 0.7 mL^{-1} and V50 = 10.9 mL. Due to pronounced variation in solvation and recrystallization behavior, two distinct methods were developed to fabricate in-plane heterojunctions in 2D layered perovskites. The first method employs a co-dissolution strategy, in which bromide- and iodide-based pristine powder 2D layered perovskite precursors in ACN are mixed at a specified bromide-to-iodide (Br:I) ratio. The second maintains a one-pot process, relying on delayed injection of the second component after the first has recrystallized. Analysis of the shape and size of the microflakes revealed

two populations, one with a rectangular shape and another with a square shape, confirmed by statistical analysis in Figure 4.5. For pristine PEA_2PbI_4 microflakes, it was found that they consist of a population with square shapes, as well as another with a high aspect ratio of short to long in-plane sides.

The monitored recrystallization of pristine PEA2PbBr4 and PEA2PbI4 using toluene as an antisolvent, an injection rate of 1 ml.min-1, and an optimized solvent-to-antisolvent ratio of 0.2 yielded a relatively narrow size distribution of regular-shaped microflake crystals. As mentioned above, the pristine PEA2PbBr4 microflakes represent a slightly rectangular or mainly a square crystal shape, whereas for pristine PEA2PbI4 microflakes, two distinct populations of crystals were identified. The first population is similar in shape and size to those pristine PEA2PbBr4 microflakes, while the second consists of elongated structures with a high aspect ratio. The appearance of two various crystal morphologies for pristine PEA2PbI4 is associated with the special solvent/antisolvent ratio at the recrystallization point compared to PEA2PbBr4 microflakes (see **Figure 4.4a and b**). Because PEA2PbI4 microflakes recrystallize with 7.5 ml of toluene antisolvent injection, and the recrystallization occurs in a much more nonpolar solvent environment compared to pristine PEA2PbBr4 microflakes.

Table 2. Parameters obtained from a series of PLQY measurements.

Sample	Excitation (nm)	Spectral Range (nm)	PLQY (%)	PLQY (%)	PLQY (%)	Mean PLQY (%)	Error (%)
PEA_2PbBr_4	370	390-600	15.1	14.4	14.1	14.5	0.5
core/frame	370	390 - 600	5.6	5.7	5.9	5.7	0.1
core	370	400 - 460	0.5	0.7	0.8	0.6	0.1
frame	370	460 - 600	5.1	5.1	5.1	5.1	0.0
frame	450	470-600	6.4	6.2	7.0	6.5	0.4
PEA_2PbI_4	370	390-600	0.7	1.2	0.6	0.8	0.3

Table 3. Workfunction and bandgap of the homo-materials

Material	**PEA_2PbI_4**	**PEA_2PbBr_4**	**PEA_2PbCl_4**
Work Function (eV)	4.48 +/-0.03	4.60+/-0.03	4.54 +/-0.04
Band Gap (eV) from Abs	2.34	3.1	3.54

4.7.3 Microcrystal alloyed phase heterojunctions design and control

To fabricate heterostructures using various halide precursor mixtures, the concentration ratio between halide precursors (e.g., bromide and iodide) can control the alloyed composition of the core (bromide) and frame (iodide). **Figures 4.6**, **4.8**, and **4.9** present results for different Br: I ratios of dissolved microflake powders of pristine PEA2PbBr4 and PEA2PbI4.

4.7.4 Pure phase formation of heterostructure via sequential injection of dissolved microflake powders: optical coupling and interface characterization

Time-resolved PL spectroscopy with varying compositions elucidates the relationship between PL decay dynamics and the frame composition of the PEA_2PbBr_4 core. The bromide-based core in all heterojunctions is substantially independent of the frame composition, exhibiting a considerably shorter lifetime than pristine PEA_2PbBr_4, indicating the presence of compositional and fast, independent recombination channels introduced during the sequential recrystallization process. On the other hand, by increasing the iodide content (x_I = [I]/([I]+[Br]), the PL decay time measured at the wavelength associated with the bandgap of the frame increases. The PL decay for the perfectly shaped pristine PEA_2PbI_4 (xI=1.00) microflakes, which are produced by solvation and recrystallization of irregularly shaped PEA_2PbI_4 powders, however, is faster than that of alloyed phases. The PLQY of the heterojunctions represents a pronounced decrease in the emission of PEA_2PbBr_4 core, decreasing from 14.5% in the pristine phase to about 1% in the heterojunctions. This reduction is associated with a faster average PL decay, from 6 ns in the pristine phase to 3 ns in the heterojunctions, showing the presence of additional decay channels. The reported PLQYs of 5% and 6.5% for the iodide-based frame, excited at 370 nm and 450 nm, respectively, are below the core's bandgap; therefore, the iodide-based frame is excited selectively.

4.7.5 Synthesis of large size and irregular shape PEA_2PbX_4 (X = Cl, Br, and I), and $PEA_2Pb(Br_xI_{1-x})$ microflake powders

PEA_2PbX_4 (X = Cl, Br, and I) microflake powders were synthesized via a method previously reported protocol with minor modifications [101]. Particularly, 0.25 mmol of PbX_2 was dissolved in 200 µL of HX, followed by diluting with 2 ml of acetone regarding PEA2PbBr4 and PEA2PbCl4, and 2 ml of ethyl acetate regarding PEA2PbI4. Moreover, ethyl acetate was used as an antisolvent because PEA2PbI4 is more soluble in acetone, and 108 µL of H3PO2 was added to the PEA2PbI4 solution to prevent the oxidation of I- to I2. Subsequently, 0.6 mmol of PEA was injected into the solution, resulting in the immediate formation of large sizes (micrometers) and irregular shapes of PEA2PbX4 2D layered perovskite microflakes. The reaction mixture was stirred continuously for at

least 3 h to ensure complete formation of the product. Subsequently, the microflakes were precipitated and separated from the solution by centrifugation at 6000 rpm for 2 min, followed by redispersion in 2 ml of acetone and ethyl acetate for the PEA2PbI4 microflakes. The washing step was repeated at least twice more, and the purified microflakes were dried under vacuum for 1 h. To synthesize alloyed halide phases of $PEA_2Pb(Br_xI_{1-x})_4$ microflake powders, the same protocol was used as for PEA2PbI4 formation, with the variation that before injection of PEA, the iodide and bromide precursors were mixed in the desired ratios (Table X).

4.7.6 Making PEA_2PbX_4 (X = Cl, Br, and I) and PEA2AgBiBr8 precursors solution

As synthesized, PEA2PbX4 microflakes with irregular shape and size are dissolved in ACN and GBL, good solvents, separately to form the corresponding precursors. Accordingly, 5 mg (0.0084 mmol) of PEA2PbCl4 is dissolved in 18.75 ml of ACN and 2.5 ml of GBL, 5 mg (0.0065 mmol) of PEA2PbBr4 is dissolved in 7.5 ml of ACN and 1 ml of GBL, and 5 mg (0.0052 mmol) of PEA2PbI4 is dissolved in 0.261 ml of ACN and 0.125 ml of GBL. Additionally, 5 mg (0.0035 mmol) of PEA2AgBiBr8 is dissolved in 1.7 ml of ACN. Any undissolved material was removed by filtration through a syringe filter. For solubility details, see Table X.

4.7.7 PEA_2PbBr_4-PEA_2PbI_4 epitaxial core-frame heterojunctions

4.7.7.1 Precursor mixture approach

To form a lateral 2D layered perovskite heterojunction using a precursor mixture, accordingly, 2 ml of PEA2PbBr4-ACN precursor solution was mixed with 150 µL of PEA2PbI4-ACN precursor solution in a 40 ml vial, and toluene as an antisolvent was injected into the solution using a syringe pump with a certain injection rate of 1 ml/min until 24 ml of toluene. Afterward, the prepared heterostructure microflakes were separated and washed by centrifugation at 3000 rpm for 2 min, and the centrifugation was repeated twice. The heterostructure microflakes were dried on glass under a fume hood.

4.7.7.2 Sequential injection of precursors

In this method, unlike in the precursor mixture, the first core structure is formed by injecting an antisolvent into the core PEA2PbBr4-ACN precursor solution; after recrystallization of the PEA2PbBr4 (core), the second precursor, PEA2PbI4-ACN (frame), is injected while antisolvent injection continues. Therefore, 2 ml of PEA2PbBr4-ACN or 1.2 ml of PEA2PbBr4-GBL is added to a 40 ml vial, and toluene or DCB as an antisolvent is added to the solution using a syringe pump. After recrystallization of the core PEA2PbBr4 structure (5 min), 150 µL of PEA2PbI4-ACN or PEA2PbI4-GBL (the solubility of PEA2PbI4 is almost the same in ACN and GBL) is swiftly injected into the

solution. The syringe pump is allowed to continue injecting antisolvent until the full 24 ml is used.

4.7.8 PEA_2PbCl_4-PEA_2PbBr_4 epitaxial core-frame heterojunctions

For the growth of the PEA2PbCl4-PEA2PbBr4 core-frame heterojunction via the sequential injection of the aprecursor approach, 600 µL of PEA2PbCl4-GBL precursor solution was initially placed in a 40 mL vial, and DCB was injected as the antisolvent at 1 mL/min via a syringe pump. after the recrystallization of the PEA2PbCl4 core structure (5 min), 1.2 ml of PEA_2PbBr_4-GBL precursor solution was swiftly injected into the solution, and the antisolvent injection process continued until the whole 24 ml volume had been injected at the same rate. Once the antisolvent injection was completed, the solution, including the heterojunction microflakes, was stirred for an additional 5 min to ensure the stabilization of the structures. Finally, the same precipitation and washing procedure used in the previous formation protocol is applied to precipitate and wash the heterostructure microflakes.

4.7.9 PEA_2PbBr_4-$PEA_4AgBiBr_8$ epitaxial core-frame heterojunctions

As in the previous protocols, for the growth of PEA2PbBr4-PEA4AgBiBr8 heterojunction microflakes, 3 ml of PEA2PbBr4-ACN precursor solution was placed in a 40 ml vial, and toluene as the antisolvent was injected into the solution using a syringe pump. After 5 min (formation of PEA2PbBr4 core microlakes), 680 µL of $PEA_4AgBiBr_8$-ACN precursor solution was swiftly injected into the solution. The syringe pump was then allowed to continue injecting the antisolvent until the full 24 ml of toluene had been used.

4.7.10 Synthesis of *PEA_2PbCl_4-PEA_2PbBr_4-PEA_2PbI_4* triple halide heterostructures

To form a heterojunction with triple halide layers, 0.6 mL of PEA_2PbCl_4-GBL precursor solution was added to a 40 mL vial. Under constant stirring, DCB, as the antisolvent, was added at a rate of 1 mL/min. After 5 min reaction duration, when PEA_2PbCl_4 core microcrystals are formed, 1.2 ml of the PEA2PbBr4 precursor solution was rapidly injected into the solution to create the first frame of the heterojunctions. The third iodide frame was formed by adding 150 µL of PEA2PbI4-GBL precursor solution after 15 min (reaction duration) and by injecting 15 mL of antisolvent. The addition of DCB antisolvent was continued until a total of 24 ml of DCB had been injected. Following completion of the final DCB addition, the mixture was stirred for an additional 5 minutes to facilitate stabilization. Consequently, the same washing and precipitation procedure was implemented.

4.8 Characterization

As the heterostructures are formed in the same institute (IIT), the characterization and analysis devices and protocol, like XRD, Uv-vis absorption, PL

emission, confocal microscopy, PLQY, SEM, EDX, TEM, are the same as reported in chapter three, except as described in the following.

4.8.1 Time-resolved PL measurements

Time-resolved PL measurements were carried out with a time-correlated single-photon counting (TCSPC) unit coupled to a pulsed diode laser. The samples were excited at 372 nm and 508 nm using 50-ps pulses at a repetition rate of 1 µs.

4.8.2 4D-Scanning tunneling electron microscopy

4D-STEM datasets were recorded in microprobe mode on an aberration-corrected ThermoFisher Spectra 300 S/TEM microscope with an X-FEG source, operated at 300 kV and a semi-convergence angle of 0.5 mrad. The diffraction pattern was recorded on a post-filter Gatan Continuum camera. 4D-STEM data cubes were analyzed in Gatan DigitalMicrograph.

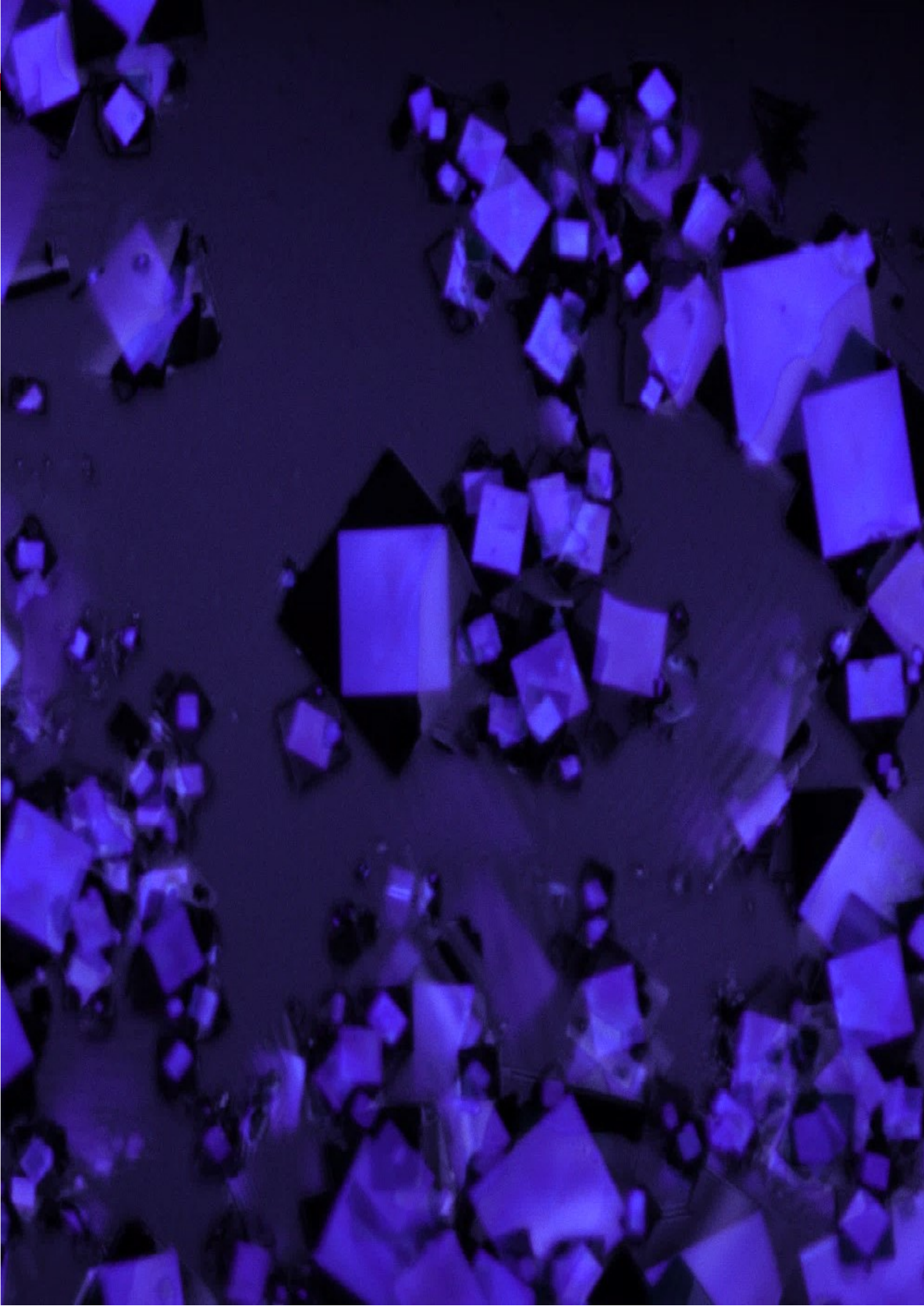

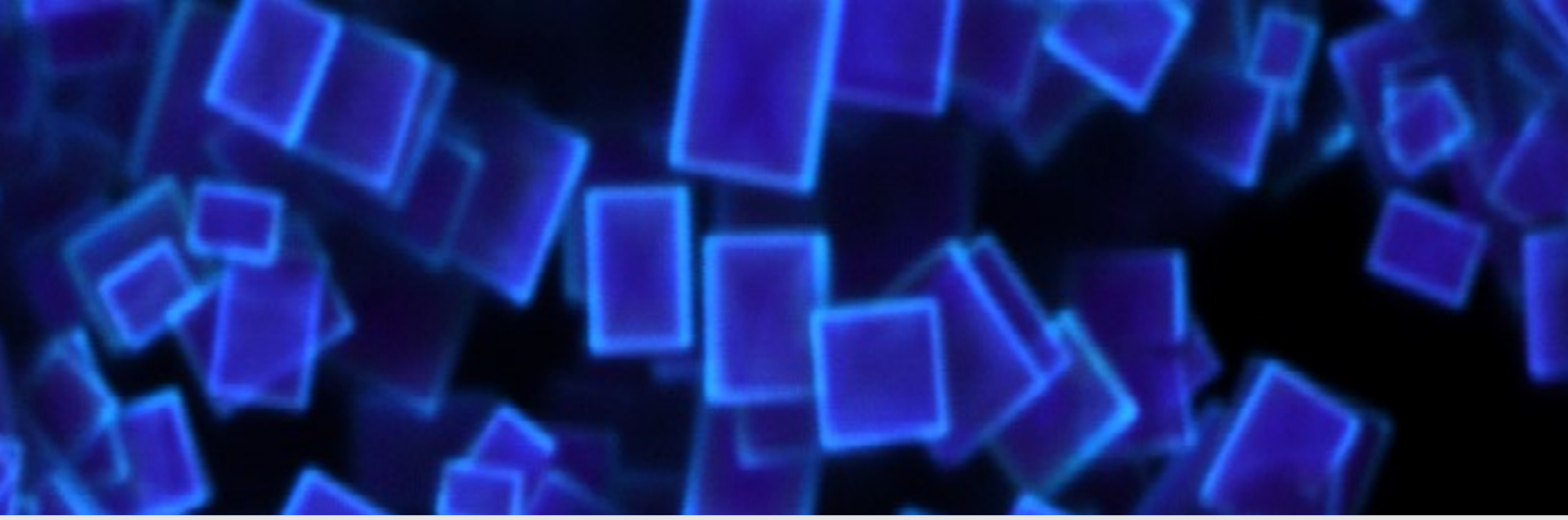

Chapter V:

Summary and outlook

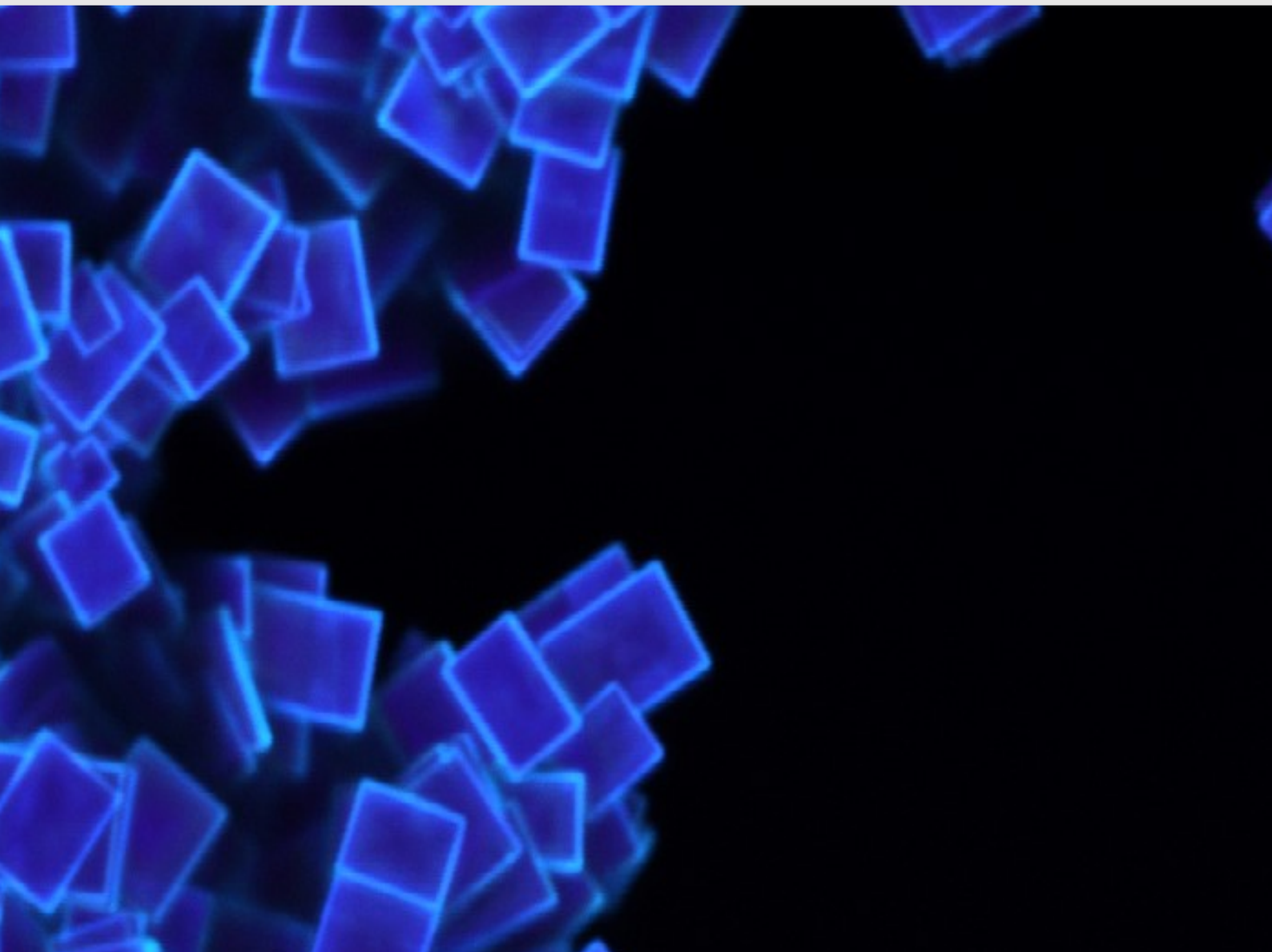

Chapter V: Summary and outlook

Summary

In this thesis, 2D layered halide perovskite lateral heterojunctions have been designed, fabricated, and characterized from several aspects. Initially, the formation of lateral heterostructures between halides was investigated using two solution-based strategies: anion exchange (Chapter III) and direct formation via a solvation-crystallization approach (Chapter IV). Based on differences in solubility and recrystallization, triple-halide and dual metal-based heterostructures comprising chloride-, bromide-, and iodide-based 2D layered perovskites and Pb- and AgBi-based metals, respectively, are designed, fabricated, and investigated. In Chapter III, a scalable, facile, solution-based method for the synthesis of 2D layered perovskite in-plane heterostructures was evaluated. After evaluating the structural and optical properties of the heterostructures, it was found that, in bromide-to-iodide exchange structures, core-frame heterostructures form via solvation and recrystallization. In contrast, iodide-to-bromide heterostructures exhibit a different mechanism: the formation of multiple alloyed phases has been used to confirm the vacancy-assisted anion-exchange process. This leads to preferential occupation of the halide sites in the octahedral lattice of 2D layered perovskites. Therefore, the solution-based exchange process is more complex than in 3D perovskites because the preferential occupation of distinct octahedral sites is explicitly accounted for. In Chapter IV, an innovative fabrication method is introduced to produce 2D layered perovskite lateral heterostructures via antisolvent-triggered recrystallization, offering a low-cost, flexible design and fabrication technique. The composition of the heterostructures was controlled by the concentrations of dissolved materials in the growth solution, thereby enabling band-gap tuning and associated interfacial offsets, tailoring emission colors, charge transfer, and recombination dynamics at the junction. Sharp interfaces can be achieved by sequentially injecting different 2D-layered perovskites, thereby tailoring the material sequence of the heterostructures; this approach can be extended to multiple heterojunctions. The method provides a versatile platform for designing and fabricating heterostructures with tunable band gaps and electric potential landscapes in perovskite materials, which could be of interest for optoelectronic applications.

Outlook

This thesis provides new insight into the design, synthesis, and characterization of 2D layered perovskites heterostructures. However, many challenges remain before 2D layered perovskite heterostructures can be used in consumer devices. However, AgBi-based perovskites are used to form lateral heterostructures; one of the main issues with 2D layered perovskite heterostructures is that they are typically formed with Pb-based 2D perovskites, which are highly toxic metals. Due to the highly polar nature of 2D laterally heterostructured perovskites, they readily dissolve in polar solvents, including water, posing serious safety and health risks. To date, some efforts have been made to

replace Pb with Sn; however, because Sn-based perovskites are sensitive to oxidation, the heterostructures become less stable. This could also lead to a type-II heterostructure, which can quench PL emission and is unfavorable for optoelectronic applications. Therefore, no feasible alternatives to Pb-based structures have been identified, as most replacements would result in reduced PLQY, significant broadening of the PL spectrum, large Stokes shifts, and stability issues. Additionally, due to size-dependent properties, heterostructures, especially those with pure layers, require size-dependent tuning. To make the heterostructures usable in electronic, optoelectronic, and quantum applications. Based on experience and the literature, it should be possible to tune the size of the heterostructures by varying or replacing the solvents and antisolvents used in these sequential solvation-recrystallization growth approaches. Therefore, future research on these 2D layered perovskite heterostructures will primarily focus on identifying a suitable Pb replacement and on tuning the microheterostructure size to achieve high emission and enhanced optoelectronic performance.

List of abbreviations

0/1/2/3/4D 0/1/2/3/4 Dimensional
AFM Atomic Force Microscopy
CB Conduction Band
CPD contact potential difference
EDX Energy-Dispersive X-Ray Spectroscopy
HAADF High-Angle Annular Dark-Field
HRTEM High Resolution Transmission Electron Microscopy
KPFM Kelvin probe force Microscope
LED Light Emitting Diode
PEA Phenethylamine
PLE Photoluminescence Excitation
PXRD Powder X-ray Diffraction
SAED Selected Area Electron Diffraction
STEM Scanning Transmission Electron Microscope
UPS Ultraviolet Photoelectron Spectroscopy
VdW Von der Waals
Abs Absorption
ACN Acetonitrile
CL Chatodoluminescence
DFT Density Functional Theory
DOS Density of States
GBL Gamma butyrolactone
HOMO Highest Occupied Molecular Orbital
ICP Inductively Coupled Plasma Optical Emission Spectroscopy
LUMO Lowest Unoccupied Molecular Orbital
PL Photoluminescence
PLQY Photoluminescence Quantum Yield
RP Ruddlesden popper
RT Room Temperature
SEM Scanning Electron Microscope
TRPL Time-resolved photoluminescence
UV Ultra Violet
VB Valence Band
XRF X-Ray fluorescence

Acknowledgments

Here, at the end of my thesis, my PhD is coming to an end. I would like to express my sincere gratitude to those mentioned below for sharing the past four years in a truly incredible experience.

I would like to start by thanking Dr. **Roman Krahne**, my supervisor and the head of the optoelectronic group at iit. Without his support, I would not have started my PhD at the University of Genoa and iit, nor would I have achieved what I have accomplished to date. I am sincerely grateful to him for the opportunity to work in his group and for his guidance, supervision, and support throughout these 4 years.

I would like to express my sincere gratitude to Dr. **Alex Schleusener**. He played an essential role in the development of this research through his generosity and scientific compassion during my studies at iit. His careful guidance, deep insight, experiences, and support at critical moments not only contributed to the scientific advancement of the thesis but also gave me encouragement and confidence in the research process. I am very grateful to him.

Throughout these 4 years at iit, many have helped me, and my work at iit would not have been possible without the support of the many essential staff members. I give my sincere thanks to **Iulia Manolache Orlatan** and **Francesca Canu**, as well as **Simone Coralluzzo**, who handled all administrative work, making my stay at iit, as well as travel plans for conferences and visits around the world, much easier. The work in the chemistry lab, of course, would not have been possible without the help of all the excellent technicians, including **Simone Nitti, Gabriele La Rosa, Giammarino Pugliese, Filippo Drago,** and **Francesco De Donato**, who always helped me out with all the chemicals and glassware I needed, as well as with shipping samples and performing measurements. Another big thanks to all other staff members and researchers at IIT who supported me in conducting measurements and trained me to use the equipment, including **Lea Pasquale**, **Simone Lauciello**, and **Dorwal Marchelli**.

There are also a lot of collaborators I have had the joy and honor to work with over the past few years: **Giorgio Divitini, Sirous Khabbaz Abkenar, Sergey Artyukhin, Aditya Putatunda, Andrea Griesi, Mattia Lizzano, Sudhir Kumar Saini, Aswin V. Asaithambi, Liberato Manna, Matteo Lorenzoni, and Mirko Prato.** Thank you for all the excellent scientific work you involved me in.

I am deeply grateful to Prof. **Letian Dou** for their exceptional support and kindness in allowing me to visit their labs at Purdue University and Emory University. His exemplary character, generosity, and guidance have enriched and inspired my skills.

Undoubtedly, I would like to thank my mother, **Mahin Choulchi**, and my sister, **Fatemeh Faraji**, who supported me over these 4 years as I overcame challenges and problems, and in loving memory of my father and older brother.

And so, here it is, the end of my thesis. I wish health, hope, happiness, and all the wonderful things life can offer to all of you, including any I may have inadvertently omitted.

About the Author

Mehrdad Faraji was born on Wednesday, the 13th of December 1989, in Tabriz, Iran. He obtained his Bachelor's degree in chemical engineering in 2011. In 2018, moved to Ankara to pursue a Master's degree in Micro- and Nanotechnology at TOBB University of Economics and Technology and conducted his Master's project on the synthesis and characterization of a ZnO/CdX photocathode for photoelectrochemical water splitting to produce hydrogen. His work contributed to a publication. During the COVID-19 pandemic and the subsequent remote-work period, he worked on DFT-based modeling and simulation of semiconductors and published 50 papers.

Finally, in 2021, Mehrdad joined Roman Krahne's group and started the PhD journey. At the beginning of his PhD, he began working on 2D layered perovskites, focusing on fabricating a lateral heterostructure via a solution-based anion-exchange and sequential growth method; the results are presented in this thesis. During his PhD, he has contributed to three papers, one as the first author. In 2025, he visited Prof. Letian Dou's group at Purdue and subsequently moved to Emory University to research 2D metal-organic Chalcogenides.

Publications

1- Griesi, A.; **Faraji**, **M.**; Kusch, G.; Khabbazabkenar, S.; Borreani, M.; Lauciello, S.; Schleusener, A.; Oliver, R. A.; Krahne, R.; Divitini, G. Mapping Emission Heterogeneity in Layered Halide Perovskites Using Cathodoluminescence. *Nanotechnology* 2023, *35* (10), 105204.

2- Krahne, R.; Schleusener, A.**; Faraji**, **M.**; Li, L.-H.; Lin, M.-L.; Tan, P.-H. Phonon Directionality Impacts Electron–Phonon Coupling and Polarization of the Band-Edge Emission in Two-Dimensional Metal Halide Perovskites. *Nano Lett.* 2024, *24* (35), 11124–11131.

3- Schleusener, A.; **Faraji**, **M.**; Borreani, M.; Lauciello, S.; Pasquale, L.; Khabbaz Abkenar, S.; Divitini, G.; Krahne, R. Heterostructures via a Solution-Based Anion Exchange in Microcrystalline 2D Layered Metal-Halide Perovskites. *Adv. Mater.* 2024, *36* (31), 2402924.

4- **Faraji, M.**; Schleusener, A.; Khabbaz Abkenar, S.; Griesi, A.; Lizzano, M.; Kumar Saini, Sufhir.; Asaithambi, A. V.; Manna, Liberato.; Lorenzoni, M.; Prato, M.; Divinitini, G.; Krahne, R. Heterostructure Design in Two-Dimensional Perovskites by Sequential Recrystallization. arXiv. 2025. 2512.13299.

References

(1) Atkins, P. W, S., D. F. *Inorganic Chemistry*, 4th ed.; Oxford University Press, 2001.

(2) Würfel, P. *Physics of Solar Cells: From Basic Principles to Advanced Concepts*; Wiley, John & Sons, 2010.

(3) Boles, M. A.; Ling, D.; Hyeon, T.; Talapin, D. V. The Surface Science of Nanocrystals. *Nat. Mater.* **2016**, *15* (2), 141–153. https://doi.org/10.1038/nmat4526.

(4) Rabouw, F. T.; de Mello Donega, C. Excited-State Dynamics in Colloidal Semiconductor Nanocrystals. *Top. Curr. Chem.* **2016**, *374* (5), 58. https://doi.org/10.1007/s41061-016-0060-0.

(5) Protesescu, L.; Yakunin, S.; Bodnarchuk, M. I.; Krieg, F.; Caputo, R.; Hendon, C. H.; Yang, R. X.; Walsh, A.; Kovalenko, M. V. Nanocrystals of Cesium Lead Halide Perovskites (CsPbX3, X = Cl, Br, and I): Novel Optoelectronic Materials Showing Bright Emission with Wide Color Gamut. *Nano Lett.* **2015**, *15* (6), 3692–3696. https://doi.org/10.1021/nl5048779.

(6) Alivisatos, A. P. Semiconductor Clusters, Nanocrystals, and Quantum Dots. *Science* **1996**, *271* (5251), 933–937. https://doi.org/10.1126/science.271.5251.933.

(7) Grundmann, M., B., D.; Ledentsov, N. N. *Quantum Dot Heterostructures*, 1st ed.; Wiley: Sussex, 1999.

(8) Hunklinger, S., K., C. *Einführung in Die Festkörperphysik*, 15th ed.; Oldenbourg: Munchen, 2013.

(9) Griffiths, D. J. *Introduction to Quantum Mechanics*, 2nd ed.; Pearson Prentice Hall: Upper Saddle River, 2005.

(10) Schleusener, A.; Faraji, M.; Borreani, M.; Lauciello, S.; Pasquale, L.; Khabbaz Abkenar, S.; Divitini, G.; Krahne, R. Heterostructures via a Solution-Based Anion Exchange in Microcrystalline 2D Layered Metal-Halide Perovskites. *Adv. Mater.* **2024**, *36* (31), 2402924. https://doi.org/10.1002/adma.202402924.

(11) Ishihara, T.; Takahashi, J.; Goto, T. Exciton State in Two-Dimensional Perovskite Semiconductor (C10H21NH3)2PbI4. *Solid State Commun.* **1989**, *69* (9), 933–936. https://doi.org/10.1016/0038-1098(89)90935-6.

(12) Mitzi, D. B.; Feild, C. A.; Harrison, W. T. A.; Guloy, A. M. Conducting Tin Halides with a Layered Organic-Based Perovskite Structure. *Nature* **1994**, *369* (6480), 467–469. https://doi.org/10.1038/369467a0.

(13) Mitzi, D. B.; Wang, S.; Feild, C. A.; Chess, C. A.; Guloy, A. M. Conducting Layered Organic-Inorganic Halides Containing 〈110〉-Oriented Perovskite Sheets. *Science* **1995**, *267* (5203), 1473–1476. https://doi.org/10.1126/science.267.5203.1473.

(14) Stoumpos, C. C.; Kanatzidis, M. G. The Renaissance of Halide Perovskites and Their Evolution as Emerging Semiconductors. *Acc. Chem. Res.* **2015**, *48* (10), 2791–2802. https://doi.org/10.1021/acs.accounts.5b00229.

(15) Mitzi, D. B.; Chondroudis, K.; Kagan, C. R. Organic-Inorganic Electronics. *IBM J. Res. Dev.* **2001**, *45* (1), 29–45. https://doi.org/10.1147/rd.451.0029.

(16) Saparov, B.; Mitzi, D. B. Organic–Inorganic Perovskites: Structural Versatility for Functional Materials Design. *Chem. Rev.* **2016**, *116* (7), 4558–4596. https://doi.org/10.1021/acs.chemrev.5b00715.

(17) Hong, X.; Ishihara, T.; Nurmikko, A. V. Dielectric Confinement Effect on Excitons in \mathrmPbI_4-Based Layered Semiconductors. *Phys Rev B* **1992**, *45* (12), 6961–6964. https://doi.org/10.1103/PhysRevB.45.6961.

(18) Chen, Y.; He, M.; Peng, J.; Sun, Y.; Liang, Z. Structure and Growth Control of Organic–Inorganic Halide Perovskites for Optoelectronics: From Polycrystalline Films to Single Crystals. *Adv. Sci.* **2016**, *3* (4), 1500392. https://doi.org/10.1002/advs.201500392.

(19) Kamminga, M. E.; Fang, H.-H.; Filip, M. R.; Giustino, F.; Baas, J.; Blake, G. R.; Loi, M. A.; Palstra, T. T. M. Confinement Effects in Low-Dimensional Lead Iodide Perovskite Hybrids. *Chem. Mater.* **2016**, *28* (13), 4554–4562. https://doi.org/10.1021/acs.chemmater.6b00809.

(20) Katan, C.; Mercier, N.; Even, J. Quantum and Dielectric Confinement Effects in Lower-Dimensional Hybrid Perovskite Semiconductors. *Chem. Rev.* **2019**, *119* (5), 3140–3192. https://doi.org/10.1021/acs.chemrev.8b00417.

(21) Slavney, A. H.; Smaha, R. W.; Smith, I. C.; Jaffe, A.; Umeyama, D.; Karunadasa, H. I. Chemical Approaches to Addressing the Instability and Toxicity of Lead–Halide Perovskite Absorbers. *Inorg. Chem.* **2017**, *56* (1), 46–55. https://doi.org/10.1021/acs.inorgchem.6b01336.

(22) Dhanabalan, B.; Leng, Y.-C.; Biffi, G.; Lin, M.-L.; Tan, P.-H.; Infante, I.; Manna, L.; Arciniegas, M. P.; Krahne, R. Directional Anisotropy of the Vibrational Modes in 2D-Layered Perovskites. *ACS Nano* **2020**, *14* (4), 4689–4697. https://doi.org/10.1021/acsnano.0c00435.

(23) Dhanabalan, B.; Castelli, A.; Ceseracciu, L.; Spirito, D.; Di Stasio, F.; Manna, L.; Krahne, R.; Arciniegas, M. P. Mechanical Switching of Orientation-Related Photoluminescence in Deep-Blue 2D Layered Perovskite Ensembles. *Nanoscale* **2021**, *13* (7), 3948–3956. https://doi.org/10.1039/D0NR08043H.

(24) Kutkan, S.; Dhanabalan, B.; Lin, M.-L.; Tan, P.-H.; Schleusener, A.; Arciniegas, M. P.; Krahne, R. Impact of the Organic Cation on the Band-Edge Emission of Two-Dimensional Lead–Bromide Perovskites. *Nanoscale* **2023**, *15* (31), 12880–12888. https://doi.org/10.1039/D3NR02172F.

(25) Dhanabalan, B.; Biffi, G.; Moliterni, A.; Olieric, V.; Giannini, C.; Saleh, G.; Ponet, L.; Prato, M.; Imran, M.; Manna, L.; Krahne, R.; Artyukhin, S.; Arciniegas, M. P. Engineering the Optical Emission and Robustness of Metal-Halide Layered Perovskites through Ligand Accommodation. *Adv. Mater.* **2021**, *33* (13), 2008004. https://doi.org/10.1002/adma.202008004.

(26) Dhanabalan, B.; Pothuraju, R. D.; Marras, S.; Pasquale, L.; Manna, L.; Krahne, R.; Arciniegas, M. P. Reversible Emission Tunability from 2D-Layered Perovskites with Conjugated Organic Cations. *Adv. Photonics Res.* **2021**, *2* (6), 2100005. https://doi.org/10.1002/adpr.202100005.

(27) Lee, Y. H.; Tang, Y.; Dani, R.; Lee, W.-J.; Kim, J. H.; Lee, G.; Sun, J.; Ma, K.; Jeong, S. H.; Xu, W.; Mei, J.; Dou, L. Self-Aligned Fluorinated-Organic Ligand for Boosting the Performance of Perovskite Solar Cells. *ACS Appl. Mater. Interfaces* **2025**, *17* (18), 26751–26758. https://doi.org/10.1021/acsami.5c03012.

(28) Baek, S.-D.; Shao, W.; Feng, W.; Tang, Y.; Lee, Y. H.; Loy, J.; Gunnarsson, W. B.; Yang, H.; Zhang, Y.; Faheem, M. B.; Kaswekar, P. I.; Atapattu, H. R.; Qin, J.; Coffey, A.

H.; Park, J. Y.; Yang, S. J.; Yang, Y.-T.; Zhu, C.; Wang, K.; Graham, K. R.; Gao, F.; Qiao, Q.; Guo, L. J.; Rand, B. P.; Dou, L. Grain Engineering for Efficient Near-Infrared Perovskite Light-Emitting Diodes. *Nat. Commun.* **2024**, *15* (1), 10760. https://doi.org/10.1038/s41467-024-55075-3.

(29) Tang, Y.; Yang, H.; Sun, J.; Wu, Z.; Shao, W.; Joy, S.; Kim, J. H.; Xu, W.; Coffey, A. H.; Lee, Y. H.; Lin, C.; Wang, L.; Ma, K.; Zhu, C.; Graham, K. R.; Tao, S.; Huang, L.; Dou, L. Triplet Management at Ligand-Perovskite Interface to Enhanced Photovoltaics Performance. *ACS Energy Lett.* **2024**, *9* (9), 4323–4330. https://doi.org/10.1021/acsenergylett.4c01853.

(30) Wang, K.; Lin, Z.-Y.; De, A.; Kocoj, C. A.; Shao, W.; Yang, H.; He, Z.; Coffey, A. H.; Fruhling, C. B.; Tang, Y.; Varadharajan, D.; Zhu, C.; Zhao, Y. S.; Boltasseva, A.; Shalaev, V. M.; Guo, P.; Savoie, B. M.; Dou, L. Two-Dimensional-Lattice-Confined Single-Molecule-like Aggregates. *Nature* **2024**, *633* (8030), 567–574. https://doi.org/10.1038/s41586-024-07925-9.

(31) De, A.; Mora Perez, C.; Liang, A.; Wang, K.; Dou, L.; Prezhdo, O.; Huang, L. Tunneling-Driven Marcus-Inverted Triplet Energy Transfer in a Two-Dimensional Perovskite. *J. Am. Chem. Soc.* **2024**, *146* (6), 4260–4269. https://doi.org/10.1021/jacs.4c00236.

(32) Seo, J.; Wang, K.; Coffey, A. H.; He, G.; Yang, H.; Lee, Y. H.; Ma, K.; Sun, J.; Park, J. Y.; Zhao, H.; Yuan, C.; Zhu, C.; Sfeir, M. Y.; Dou, L. Reduced Energetic Disorders in Dion–Jacobson Perovskites for Efficient and Spectral Stable Blue LEDs. *Adv. Opt. Mater.* **2023**, *11* (24), 2301164. https://doi.org/10.1002/adom.202301164.

(33) Wang, K.; Lin, Z.-Y.; Zhang, Z.; Jin, L.; Ma, K.; Coffey, A. H.; Atapattu, H. R.; Gao, Y.; Park, J. Y.; Wei, Z.; Finkenauer, B. P.; Zhu, C.; Meng, X.; Chowdhury, S. N.; Chen, Z.; Terlier, T.; Do, T.-H.; Yao, Y.; Graham, K. R.; Boltasseva, A.; Guo, T.-F.; Huang, L.; Gao, H.; Savoie, B. M.; Dou, L. Suppressing Phase Disproportionation in Quasi-2D Perovskite Light-Emitting Diodes. *Nat. Commun.* **2023**, *14* (1), 397. https://doi.org/10.1038/s41467-023-36118-7.

(34) Liang, A.; Gao, Y.; Asadpour, R.; Wei, Z.; Finkenauer, B. P.; Jin, L.; Yang, J.; Wang, K.; Chen, K.; Liao, P.; Zhu, C.; Huang, L.; Boudouris, B. W.; Alam, M. A.; Dou, L. Ligand-Driven Grain Engineering of High Mobility Two-Dimensional Perovskite Thin-Film Transistors. *J. Am. Chem. Soc.* **2021**, *143* (37), 15215–15223. https://doi.org/10.1021/jacs.1c06337.

(35) Wang, K.; Jin, L.; Gao, Y.; Liang, A.; Finkenauer, B. P.; Zhao, W.; Wei, Z.; Zhu, C.; Guo, T.-F.; Huang, L.; Dou, L. Lead-Free Organic–Perovskite Hybrid Quantum Wells for Highly Stable Light-Emitting Diodes. *ACS Nano* **2021**, *15* (4), 6316–6325. https://doi.org/10.1021/acsnano.1c00872.

(36) Wei, Z.; Wang, K.; Zhao, W.; Gao, Y.; Hu, Q.; Chen, K.; Dou, L. A Selenophene-Containing Conjugated Organic Ligand for Two-Dimensional Halide Perovskites. *Chem Commun* **2021**, *57* (87), 11469–11472. https://doi.org/10.1039/D1CC04679A.

(37) Gao, Y.; Shi, E.; Deng, S.; Shiring, S. B.; Snaider, J. M.; Liang, C.; Yuan, B.; Song, R.; Janke, S. M.; Liebman-Peláez, A.; Yoo, P.; Zeller, M.; Boudouris, B. W.; Liao, P.; Zhu, C.; Blum, V.; Yu, Y.; Savoie, B. M.; Huang, L.; Dou, L. Molecular Engineering of Organic–Inorganic Hybrid Perovskites Quantum Wells. *Nat. Chem.* **2019**, *11* (12), 1151–1157. https://doi.org/10.1038/s41557-019-0354-2.

(38) Sun, J.; Ma, K.; Lin, Z.-Y.; Tang, Y.; Varadharajan, D.; Chen, A. X.; Atapattu, H. R.; Lee, Y. H.; Chen, K.; Boudouris, B. W.; Graham, K. R.; Lipomi, D. J.; Mei, J.; Savoie, B. M.; Dou, L. Tailoring Molecular-Scale Contact at the Perovskite/Polymeric Hole-Transporting Material Interface for Efficient Solar Cells. *Adv. Mater.* **2023**, *35* (26), 2300647. https://doi.org/10.1002/adma.202300647.

(39) Koutselas, I. B.; Ducasse, L.; Papavassiliou, G. C. Electronic Properties of Three- and Low-Dimensional Semiconducting Materials with Pb Halide and Sn Halide Units. *J. Phys. Condens. Matter* **1996**, *8* (9), 1217. https://doi.org/10.1088/0953-8984/8/9/012.

(40) Umebayashi, T.; Asai, K.; Kondo, T.; Nakao, A. Electronic Structures of Lead Iodide Based Low-Dimensional Crystals. *Phys Rev B* **2003**, *67* (15), 155405. https://doi.org/10.1103/PhysRevB.67.155405.

(41) Muljarov, E. A.; Tikhodeev, S. G.; Gippius, N. A.; Ishihara, T. Excitons in Self-Organized Semiconductor/Insulator Superlattices: PbI-Based Perovskite Compounds. *Phys Rev B* **1995**, *51* (20), 14370–14378. https://doi.org/10.1103/PhysRevB.51.14370.

(42) Mosconi, E.; Amat, A.; Nazeeruddin, Md. K.; Grätzel, M.; De Angelis, F. First-Principles Modeling of Mixed Halide Organometal Perovskites for Photovoltaic Applications. *J. Phys. Chem. C* **2013**, *117* (27), 13902–13913. https://doi.org/10.1021/jp4048659.

(43) Even, J.; Pedesseau, L.; Dupertuis, M.-A.; Jancu, J.-M.; Katan, C. Electronic Model for Self-Assembled Hybrid Organic/Perovskite Semiconductors: Reverse Band Edge Electronic States Ordering and Spin-Orbit Coupling. *Phys Rev B* **2012**, *86* (20), 205301. https://doi.org/10.1103/PhysRevB.86.205301.

(44) Sourisseau, S.; Louvain, N.; Bi, W.; Mercier, N.; Rondeau, D.; Boucher, F.; Buzaré, J.-Y.; Legein, C. Reduced Band Gap Hybrid Perovskites Resulting from Combined Hydrogen and Halogen Bonding at the Organic−Inorganic Interface. *Chem. Mater.* **2007**, *19* (3), 600–607. https://doi.org/10.1021/cm062380e.

(45) Even, J.; Pedesseau, L.; Katan, C.; Kepenekian, M.; Lauret, J.-S.; Sapori, D.; Deleporte, E. Solid-State Physics Perspective on Hybrid Perovskite Semiconductors. *J. Phys. Chem. C* **2015**, *119* (19), 10161–10177. https://doi.org/10.1021/acs.jpcc.5b00695.

(46) Manser, J. S.; Christians, J. A.; Kamat, P. V. Intriguing Optoelectronic Properties of Metal Halide Perovskites. *Chem. Rev.* **2016**, *116* (21), 12956–13008. https://doi.org/10.1021/acs.chemrev.6b00136.

(47) Shao, W.; Yang, S.; Wang, K.; Dou, L. Light-Emitting Organic Semiconductor-Incorporated Perovskites: Fundamental Properties and Device Applications. *J. Phys. Chem. Lett.* **2023**, *14* (8), 2034–2046. https://doi.org/10.1021/acs.jpclett.2c03882.

(48) Shao, W.; Kim, J. H.; Simon, J.; Nian, Z.; Baek, S.-D.; Lu, Y.; Fruhling, C. B.; Yang, H.; Wang, K.; Park, J. Y.; Huang, L.; Yu, Y.; Boltasseva, A.; Savoie, B. M.; Shalaev, V. M.; Dou, L. Molecular Templating of Layered Halide Perovskite Nanowires. *Science* **2024**, *384* (6699), 1000–1006. https://doi.org/10.1126/science.adl0920.

(49) Yan, L.; Gloor, C. J.; Moran, A. M.; You, W. Non-Covalent Interactions Involving π Effect between Organic Cations in Low-Dimensional Organic/Inorganic Hybrid

Perovskites. *Appl. Phys. Lett.* **2023**, *122* (24), 240501. https://doi.org/10.1063/5.0148876.

(50) Passarelli, J. V.; Mauck, C. M.; Winslow, S. W.; Perkinson, C. F.; Bard, J. C.; Sai, H.; Williams, K. W.; Narayanan, A.; Fairfield, D. J.; Hendricks, M. P.; Tisdale, W. A.; Stupp, S. I. Tunable Exciton Binding Energy in 2D Hybrid Layered Perovskites through Donor–Acceptor Interactions within the Organic Layer. *Nat. Chem.* **2020**, *12* (8), 672–682. https://doi.org/10.1038/s41557-020-0488-2.

(51) Mauck, C. M.; Tisdale, W. A. Excitons in 2D Organic–Inorganic Halide Perovskites. *Trends Chem.* **2019**, *1* (4), 380–393. https://doi.org/10.1016/j.trechm.2019.04.003.

(52) Chen, P.; Bai, Y.; Lyu, M.; Yun, J.-H.; Hao, M.; Wang, L. Progress and Perspective in Low-Dimensional Metal Halide Perovskites for Optoelectronic Applications. *Sol. RRL* **2018**, *2* (3), 1700186. https://doi.org/10.1002/solr.201700186.

(53) Agranovich, V. M.; Gartstein, Yu. N.; Litinskaya, M. Hybrid Resonant Organic–Inorganic Nanostructures for Optoelectronic Applications. *Chem. Rev.* **2011**, *111* (9), 5179–5214. https://doi.org/10.1021/cr100156x.

(54) Blancon, J.-C.; Stier, A. V.; Tsai, H.; Nie, W.; Stoumpos, C. C.; Traoré, B.; Pedesseau, L.; Kepenekian, M.; Katsutani, F.; Noe, G. T.; Kono, J.; Tretiak, S.; Crooker, S. A.; Katan, C.; Kanatzidis, M. G.; Crochet, J. J.; Even, J.; Mohite, A. D. Scaling Law for Excitons in 2D Perovskite Quantum Wells. *Nat. Commun.* **2018**, *9* (1), 2254. https://doi.org/10.1038/s41467-018-04659-x.

(55) D'Innocenzo, V.; Grancini, G.; Alcocer, M. J. P.; Kandada, A. R. S.; Stranks, S. D.; Lee, M. M.; Lanzani, G.; Snaith, H. J.; Petrozza, A. Excitons versus Free Charges in Organo-Lead Tri-Halide Perovskites. *Nat. Commun.* **2014**, *5* (1), 3586. https://doi.org/10.1038/ncomms4586.

(56) Ema, K.; Inomata, M.; Kato, Y.; Kunugita, H.; Era, M. Nearly Perfect Triplet-Triplet Energy Transfer from Wannier Excitons to Naphthalene in Organic-Inorganic Hybrid Quantum-Well Materials. *Phys Rev Lett* **2008**, *100* (25), 257401. https://doi.org/10.1103/PhysRevLett.100.257401.

(57) Sun, J.; Wang, K.; Ma, K.; Park, J. Y.; Lin, Z.-Y.; Savoie, B. M.; Dou, L. Emerging Two-Dimensional Organic Semiconductor-Incorporated Perovskites–A Fascinating Family of Hybrid Electronic Materials. *J. Am. Chem. Soc.* **2023**, *145* (38), 20694–20715. https://doi.org/10.1021/jacs.3c02143.

(58) Simbula, A.; Wu, L.; Pitzalis, F.; Pau, R.; Lai, S.; Liu, F.; Matta, S.; Marongiu, D.; Quochi, F.; Saba, M.; Mura, A.; Bongiovanni, G. Exciton Dissociation in 2D Layered Metal-Halide Perovskites. *Nat. Commun.* **2023**, *14* (1), 4125. https://doi.org/10.1038/s41467-023-39831-5.

(59) Tao, W.; Zhou, Q.; Zhu, H. Dynamic Polaronic Screening for Anomalous Exciton Spin Relaxation in Two-Dimensional Lead Halide Perovskites. *Sci. Adv.* **2020**, *6* (47), eabb7132. https://doi.org/10.1126/sciadv.abb7132.

(60) Franchini, C.; Reticcioli, M.; Setvin, M.; Diebold, U. Polarons in Materials. *Nat. Rev. Mater.* **2021**, *6* (7), 560–586. https://doi.org/10.1038/s41578-021-00289-w.

(61) Zhu, X.-Y.; Podzorov, V. Charge Carriers in Hybrid Organic–Inorganic Lead Halide Perovskites Might Be Protected as Large Polarons. *J. Phys. Chem. Lett.* **2015**, *6* (23), 4758–4761. https://doi.org/10.1021/acs.jpclett.5b02462.

(62) Smith, M. D.; Karunadasa, H. I. White-Light Emission from Layered Halide Perovskites. *Acc. Chem. Res.* **2018**, *51* (3), 619–627. https://doi.org/10.1021/acs.accounts.7b00433.
(63) Tao, W.; Zhang, Y.; Zhu, H. Dynamic Exciton Polaron in Two-Dimensional Lead Halide Perovskites and Implications for Optoelectronic Applications. *Acc. Chem. Res.* **2022**, *55* (3), 345–353. https://doi.org/10.1021/acs.accounts.1c00626.
(64) Smith, M. D.; Jaffe, A.; Dohner, E. R.; Lindenberg, A. M.; Karunadasa, H. I. Structural Origins of Broadband Emission from Layered Pb–Br Hybrid Perovskites. *Chem Sci* **2017**, *8* (6), 4497–4504. https://doi.org/10.1039/C7SC01590A.
(65) Ni, L.; Huynh, U.; Cheminal, A.; Thomas, T. H.; Shivanna, R.; Hinrichsen, T. F.; Ahmad, S.; Sadhanala, A.; Rao, A. Real-Time Observation of Exciton–Phonon Coupling Dynamics in Self-Assembled Hybrid Perovskite Quantum Wells. *ACS Nano* **2017**, *11* (11), 10834–10843. https://doi.org/10.1021/acsnano.7b03984.
(66) Cortecchia, D.; Yin, J.; Bruno, A.; Lo, S.-Z. A.; Gurzadyan, G. G.; Mhaisalkar, S.; Brédas, J.-L.; Soci, C. Polaron Self-Localization in White-Light Emitting Hybrid Perovskites. *J Mater Chem C* **2017**, *5* (11), 2771–2780. https://doi.org/10.1039/C7TC00366H.
(67) Emin, D. Optical Properties of Large and Small Polarons and Bipolarons. *Phys Rev B* **1993**, *48* (18), 13691–13702. https://doi.org/10.1103/PhysRevB.48.13691.
(68) Xie, S.; Tu, L.; Han, Y.; Huang, L.; Kang, K.; Lao, K. U.; Poddar, P.; Park, C.; Muller, D. A.; DiStasio, R. A.; Park, J. Coherent, Atomically Thin Transition-Metal Dichalcogenide Superlattices with Engineered Strain. *Science* **2018**, *359* (6380), 1131–1136. https://doi.org/10.1126/science.aao5360.
(69) Sahoo, P. K.; Memaran, S.; Xin, Y.; Balicas, L.; Gutiérrez, H. R. One-Pot Growth of Two-Dimensional Lateral Heterostructures via Sequential Edge-Epitaxy. *Nature* **2018**, *553* (7686), 63–67. https://doi.org/10.1038/nature25155.
(70) Zhang, Z.; Chen, P.; Duan, X.; Zang, K.; Luo, J.; Duan, X. Robust Epitaxial Growth of Two-Dimensional Heterostructures, Multiheterostructures, and Superlattices. *Science* **2017**, *357* (6353), 788–792. https://doi.org/10.1126/science.aan6814.
(71) Gong, Y.; Lin, J.; Wang, X.; Shi, G.; Lei, S.; Lin, Z.; Zou, X.; Ye, G.; Vajtai, R.; Yakobson, B. I.; Terrones, H.; Terrones, M.; Tay, B. K.; Lou, J.; Pantelides, S. T.; Liu, Z.; Zhou, W.; Ajayan, P. M. Vertical and In-Plane Heterostructures from WS2/MoS2 Monolayers. *Nat. Mater.* **2014**, *13* (12), 1135–1142. https://doi.org/10.1038/nmat4091.
(72) Bernevig, B. A.; Hughes, T. L.; Zhang, S.-C. Quantum Spin Hall Effect and Topological Phase Transition in HgTe Quantum Wells. *Science* **2006**, *314* (5806), 1757–1761. https://doi.org/10.1126/science.1133734.
(73) Lugli, P.; Goodnick, S. M. Nonequilibrium Longitudinal-Optical Phonon Effects in GaAs-AlGaAs Quantum Wells. *Phys Rev Lett* **1987**, *59* (6), 716–719. https://doi.org/10.1103/PhysRevLett.59.716.
(74) Ahn, C. H.; Rabe, K. M.; Triscone, J.-M. Ferroelectricity at the Nanoscale: Local Polarization in Oxide Thin Films and Heterostructures. *Science* **2004**, *303* (5657), 488–491. https://doi.org/10.1126/science.1092508.
(75) Ziffer, M. E.; Ginger, D. S. How Hybrid Perovskites Get Their Groove. *Science* **2016**, *353* (6306), 1365–1365. https://doi.org/10.1126/science.aai7682.

(76) Snaith, H. J. Present Status and Future Prospects of Perovskite Photovoltaics. *Nat. Mater.* **2018**, *17* (5), 372–376. https://doi.org/10.1038/s41563-018-0071-z.
(77) Pan, D.; Fu, Y.; Chen, J.; Czech, K. J.; Wright, J. C.; Jin, S. Visualization and Studies of Ion-Diffusion Kinetics in Cesium Lead Bromide Perovskite Nanowires. *Nano Lett.* **2018**, *18* (3), 1807–1813. https://doi.org/10.1021/acs.nanolett.7b05023.
(78) Huang, Z.; Proppe, A. H.; Tan, H.; Saidaminov, M. I.; Tan, F.; Mei, A.; Tan, C.-S.; Wei, M.; Hou, Y.; Han, H.; Kelley, S. O.; Sargent, E. H. Suppressed Ion Migration in Reduced-Dimensional Perovskites Improves Operating Stability. *ACS Energy Lett.* **2019**, *4* (7), 1521–1527. https://doi.org/10.1021/acsenergylett.9b00892.
(79) Shi, E.; Yuan, B.; Shiring, S. B.; Gao, Y.; Akriti; Guo, Y.; Su, C.; Lai, M.; Yang, P.; Kong, J.; Savoie, B. M.; Yu, Y.; Dou, L. Two-Dimensional Halide Perovskite Lateral Epitaxial Heterostructures. *Nature* **2020**, *580* (7805), 614–620. https://doi.org/10.1038/s41586-020-2219-7.
(80) Singh, A.; Yuan, B.; Rahman, Md. H.; Yang, H.; De, A.; Park, J. Y.; Zhang, S.; Huang, L.; Mannodi-Kanakkithodi, A.; Pennycook, T. J.; Dou, L. Two-Dimensional Halide Pb-Perovskite–Double Perovskite Epitaxial Heterostructures. *J. Am. Chem. Soc.* **2023**, *145* (36), 19885–19893. https://doi.org/10.1021/jacs.3c06127.
(81) Xia, M.; Wang, T.; Lu, Y.; Li, Y.; Li, B.; Shen, H.; Guo, Y.; Yu, Y.; Dong, J.; Dou, L.; Liu, Y.; Shi, E. Kinetic Wulff-Shaped Heteroepitaxy of Phase-Pure 2D Perovskite Heterostructures with Deterministic Slab Thickness. *Nat. Synth.* **2025**, *4* (3), 380–390. https://doi.org/10.1038/s44160-024-00692-5.
(82) Arciniegas, M. P.; Manna, L. Designing Ruddlesden–Popper Layered Perovskites through Their Organic Cations. *ACS Energy Lett.* **2022**, *7* (9), 2944–2953. https://doi.org/10.1021/acsenergylett.2c01415.
(83) Li, X.; Hoffman, J. M.; Kanatzidis, M. G. The 2D Halide Perovskite Rulebook: How the Spacer Influences Everything from the Structure to Optoelectronic Device Efficiency. *Chem. Rev.* **2021**, *121* (4), 2230–2291. https://doi.org/10.1021/acs.chemrev.0c01006.
(84) Cao, F.; Yu, D.; Telychko, M.; Lu, J.; Pang, P.; Su, C.; Xing, G. Navigating the Site-Distinct Energy Conversion Properties of Perovskite Quantum Wells. *ACS Energy Lett.* **2023**, *8* (2), 1236–1265. https://doi.org/10.1021/acsenergylett.2c02080.
(85) Motti, S. G.; Kober-Czerny, M.; Righetto, M.; Holzhey, P.; Smith, J.; Kraus, H.; Snaith, H. J.; Johnston, M. B.; Herz, L. M. Exciton Formation Dynamics and Band-Like Free Charge-Carrier Transport in 2D Metal Halide Perovskite Semiconductors. *Adv. Funct. Mater.* **2023**, *33* (32), 2300363. https://doi.org/10.1002/adfm.202300363.
(86) Oddo, A. M.; Gao, M.; Weinberg, D.; Jin, J.; Folgueras, M. C.; Song, C.; Ophus, C.; Mani, T.; Rabani, E.; Yang, P. Energy Funneling in a Noninteger Two-Dimensional Perovskite. *Nano Lett.* **2023**, *23* (24), 11469–11476. https://doi.org/10.1021/acs.nanolett.3c03058.
(87) Griesi, A.; Faraji, M.; Kusch, G.; Khabbazabkenar, S.; Borreani, M.; Lauciello, S.; Schleusener, A.; Oliver, R. A.; Krahne, R.; Divitini, G. Mapping Emission Heterogeneity in Layered Halide Perovskites Using Cathodoluminescence. *Nanotechnology* **2023**, *35* (10), 105204. https://doi.org/10.1088/1361-6528/ad12ec.

(88) Lee, Y. H.; Park, J. Y.; Niu, P.; Yang, H.; Sun, D.; Huang, L.; Mei, J.; Dou, L. One-Step Solution Patterning for Two-Dimensional Perovskite Nanoplate Arrays. *ACS Nano* **2023**, *17* (14), 13840–13850. https://doi.org/10.1021/acsnano.3c03605.

(89) He, C.; Li, J.; Bao, Y.; Li, J.; Wang, H.; Zhang, M.; Li, H.; Tang, H.; Sun, Z.; Zhang, Q.; Fang, Y.; Xu, J.; Yang, Y. Robust Heterostructures in Two-Dimensional Perovskites by Threshold-Dominating Anion Exchange. *Small* **2022**, *18* (31), 2203036. https://doi.org/10.1002/smll.202203036.

(90) Roy, C. R.; Pan, D.; Wang, Y.; Hautzinger, M. P.; Zhao, Y.; Wright, J. C.; Zhu, Z.; Jin, S. Anion Exchange of Ruddlesden–Popper Lead Halide Perovskites Produces Stable Lateral Heterostructures. *J. Am. Chem. Soc.* **2021**, *143* (13), 5212–5221. https://doi.org/10.1021/jacs.1c01573.

(91) Nedelcu, G.; Protesescu, L.; Yakunin, S.; Bodnarchuk, M. I.; Grotevent, M. J.; Kovalenko, M. V. Fast Anion-Exchange in Highly Luminescent Nanocrystals of Cesium Lead Halide Perovskites (CsPbX3, X = Cl, Br, I). *Nano Lett.* **2015**, *15* (8), 5635–5640. https://doi.org/10.1021/acs.nanolett.5b02404.

(92) Lai, M.; Shin, D.; Jibril, L.; Mirkin, C. A. Combinatorial Synthesis and Screening of Mixed Halide Perovskite Megalibraries. *J. Am. Chem. Soc.* **2022**, *144* (30), 13823–13830. https://doi.org/10.1021/jacs.2c05082.

(93) Akkerman, Q. A.; D'Innocenzo, V.; Accornero, S.; Scarpellini, A.; Petrozza, A.; Prato, M.; Manna, L. Tuning the Optical Properties of Cesium Lead Halide Perovskite Nanocrystals by Anion Exchange Reactions. *J. Am. Chem. Soc.* **2015**, *137* (32), 10276–10281. https://doi.org/10.1021/jacs.5b05602.

(94) Dou, L.; Lai, M.; Kley, C. S.; Yang, Y.; Bischak, C. G.; Zhang, D.; Eaton, S. W.; Ginsberg, N. S.; Yang, P. Spatially Resolved Multicolor $CsPbX_3$ Nanowire Heterojunctions via Anion Exchange. *Proc. Natl. Acad. Sci.* **2017**, *114* (28), 7216–7221. https://doi.org/10.1073/pnas.1703860114.

(95) Akriti; Lin, Z.-Y.; Park, J. Y.; Yang, H.; Savoie, B. M.; Dou, L. Anion Diffusion in Two-Dimensional Halide Perovskites. *APL Mater.* **2022**, *10* (4), 040903. https://doi.org/10.1063/5.0088538.

(96) Yuan, Y.; Huang, J. Ion Migration in Organometal Trihalide Perovskite and Its Impact on Photovoltaic Efficiency and Stability. *Acc. Chem. Res.* **2016**, *49* (2), 286–293. https://doi.org/10.1021/acs.accounts.5b00420.

(97) Hope, M. A.; Cordova, M.; Mishra, A.; Gunes, U.; Caiazzo, A.; Datta, K.; Janssen, R. A. J.; Emsley, L. Axial–Equatorial Halide Ordering in Layered Hybrid Perovskites from Isotropic–Anisotropic 207Pb NMR. *Angew. Chem. Int. Ed.* **2024**, *63* (13), e202314856. https://doi.org/10.1002/anie.202314856.

(98) Toso, S.; Gushchina, I.; Oliver, A. G.; Manna, L.; Kuno, M. Are Mixed-Halide Ruddlesden–Popper Perovskites Really Mixed? *ACS Energy Lett.* **2022**, *7* (12), 4242–4247. https://doi.org/10.1021/acsenergylett.2c01967.

(99) Chen, Z.; Xue, H.; Brocks, G.; Bobbert, P. A.; Tao, S. Thermodynamic Origin of the Photostability of the Two-Dimensional Perovskite PEA2Pb(I1–xBrx)4. *ACS Energy Lett.* **2023**, *8* (2), 943–949. https://doi.org/10.1021/acsenergylett.2c02463.

(100) Wright, N. E.; Qin, X.; Xu, J.; Kelly, L. L.; Harvey, S. P.; Toney, M. F.; Blum, V.; Stiff-Roberts, A. D. Influence of Annealing and Composition on the Crystal Structure of

Mixed-Halide, Ruddlesden–Popper Perovskites. *Chem. Mater.* **2022**, *34* (7), 3109–3122. https://doi.org/10.1021/acs.chemmater.1c04213.
(101) Dhanabalan, B.; Castelli, A.; Palei, M.; Spirito, D.; Manna, L.; Krahne, R.; Arciniegas, M. Simple Fabrication of Layered Halide Perovskite Platelets and Enhanced Photoluminescence from Mechanically Exfoliated Flakes. *Nanoscale* **2019**, *11* (17), 8334–8342. https://doi.org/10.1039/C9NR00638A.
(102) Tutantsev, A. S.; Udalova, N. N.; Fateev, S. A.; Petrov, A. A.; Chengyuan, W.; Maksimov, E. G.; Goodilin, E. A.; Tarasov, A. B. New Pigeonholing Approach for Selection of Solvents Relevant to Lead Halide Perovskite Processing. *J. Phys. Chem. C* **2020**, *124* (20), 11117–11123. https://doi.org/10.1021/acs.jpcc.0c03661.
(103) Du, K.; Tu, Q.; Zhang, X.; Han, Q.; Liu, J.; Zauscher, S.; Mitzi, D. B. Two-Dimensional Lead(II) Halide-Based Hybrid Perovskites Templated by Acene Alkylamines: Crystal Structures, Optical Properties, and Piezoelectricity. *Inorg. Chem.* **2017**, *56* (15), 9291–9302. https://doi.org/10.1021/acs.inorgchem.7b01094.
(104) Nobuaki Kitazawa, N. K. Stability of (C6H5C2H4NH3)2Pb(BrxI4-x) Mixed Crystals. *Jpn. J. Appl. Phys.* **1997**, *36* (11R), 6876. https://doi.org/10.1143/JJAP.36.6876.
(105) Yoon, S. J.; Stamplecoskie, K. G.; Kamat, P. V. How Lead Halide Complex Chemistry Dictates the Composition of Mixed Halide Perovskites. *J. Phys. Chem. Lett.* **2016**, *7* (7), 1368–1373. https://doi.org/10.1021/acs.jpclett.6b00433.
(106) Chen, S.; Xiao, X.; Gu, H.; Huang, J. Iodine Reduction for Reproducible and High-Performance Perovskite Solar Cells and Modules. *Sci. Adv.* **2021**, *7* (10), eabe8130. https://doi.org/10.1126/sciadv.abe8130.
(107) Awtrey, A. D.; Connick, R. E. The Absorption Spectra of I2, I3-, I-, IO3-, S4O6= and S2O3=. Heat of the Reaction I3- = I2 + I-. *J. Am. Chem. Soc.* **1951**, *73* (4), 1842–1843. https://doi.org/10.1021/ja01148a504.
(108) Lyu, D.; Miao, Y.; Li, B.; Xiao, Z.; Wu, X.; Hu, X.; Jiang, X.-F.; Xu, Q.-H. Dual Blue Emission in Ruddlesden–Popper Lead-Bromide Perovskites Induced by Photon Recycling. *J. Phys. Chem. C* **2021**, *125* (33), 18308–18316. https://doi.org/10.1021/acs.jpcc.1c04891.
(109) Sheikh, T.; Shinde, A.; Mahamuni, S.; Nag, A. Possible Dual Bandgap in (C4H9NH3)2PbI4 2D Layered Perovskite: Single-Crystal and Exfoliated Few-Layer. *ACS Energy Lett.* **2018**, *3* (12), 2940–2946. https://doi.org/10.1021/acsenergylett.8b01799.
(110) Merano, M.; Collin, S.; Renucci, P.; Gatri, M.; Sonderegger, S.; Crottini, A.; Ganière, J. D.; Deveaud, B. High Brightness Picosecond Electron Gun. *Rev. Sci. Instrum.* **2005**, *76* (8), 085108. https://doi.org/10.1063/1.2008975.
(111) Ferrer Orri, J.; Tennyson, E. M.; Kusch, G.; Divitini, G.; Macpherson, S.; Oliver, R. A.; Ducati, C.; Stranks, S. D. Using Pulsed Mode Scanning Electron Microscopy for Cathodoluminescence Studies on Hybrid Perovskite Films. *Nano Express* **2021**, *2* (2), 024002. https://doi.org/10.1088/2632-959X/abfe3c.
(112) Cacovich, S.; Matteocci, F.; Abdi-Jalebi, M.; Stranks, S. D.; Di Carlo, A.; Ducati, C.; Divitini, G. Unveiling the Chemical Composition of Halide Perovskite Films Using Multivariate Statistical Analyses. *ACS Appl. Energy Mater.* **2018**, *1* (12), 7174–7181. https://doi.org/10.1021/acsaem.8b01622.

(113) Shrestha, S.; Li, X.; Tsai, H.; Hou, C.-H.; Huang, H.-H.; Ghosh, D.; Shyue, J.-J.; Wang, L.; Tretiak, S.; Ma, X.; Nie, W. Long Carrier Diffusion Length in Two-Dimensional Lead Halide Perovskite Single Crystals. *Chem* **2022**, *8* (4), 1107–1120. https://doi.org/10.1016/j.chempr.2022.01.008.

(114) Milot, R. L.; Sutton, R. J.; Eperon, G. E.; Haghighirad, A. A.; Martinez Hardigree, J.; Miranda, L.; Snaith, H. J.; Johnston, M. B.; Herz, L. M. Charge-Carrier Dynamics in 2D Hybrid Metal–Halide Perovskites. *Nano Lett.* **2016**, *16* (11), 7001–7007. https://doi.org/10.1021/acs.nanolett.6b03114.

(115) Kuo, M.-Y.; Spitha, N.; Hautzinger, M. P.; Hsieh, P.-L.; Li, J.; Pan, D.; Zhao, Y.; Chen, L.-J.; Huang, M. H.; Jin, S.; Hsu, Y.-J.; Wright, J. C. Distinct Carrier Transport Properties Across Horizontally vs Vertically Oriented Heterostructures of 2D/3D Perovskites. *J. Am. Chem. Soc.* **2021**, *143* (13), 4969–4978. https://doi.org/10.1021/jacs.0c10000.

(116) Dar, M. I.; Jacopin, G.; Hezam, M.; Arora, N.; Zakeeruddin, S. M.; Deveaud, B.; Nazeeruddin, M. K.; Grätzel, M. Asymmetric Cathodoluminescence Emission in CH3NH3PbI3–xBrx Perovskite Single Crystals. *ACS Photonics* **2016**, *3* (6), 947–952. https://doi.org/10.1021/acsphotonics.6b00290.

(117) Dong, Y.; Gao, G.; Deng, Y.; Liu, X.; Zhu, T. Ultrafast Energy Funneling in Two-Dimensional Mixed-Halide Perovskites Caused by Intrinsic Halide Immiscibility. *J. Phys. Chem. C* **2024**, *128* (1), 279–286. https://doi.org/10.1021/acs.jpcc.3c07170.

(118) Roy, C. R.; Zhou, Y.; Kohler, D. D.; Zhu, Z.; Wright, J. C.; Jin, S. Intrinsic Halide Immiscibility in 2D Mixed-Halide Ruddlesden–Popper Perovskites. *ACS Energy Lett.* **2022**, *7* (10), 3423–3431. https://doi.org/10.1021/acsenergylett.2c01631.

(119) Vegard, L. Die Konstitution Der Mischkristalle Und Die Raumfüllung Der Atome. *Z. Für Phys.* **1921**, *5* (1), 17–26. https://doi.org/10.1007/BF01349680.

(120) Liu, Y.; Wang, M.; Ievlev, A. V.; Ahmadi, A.; Keum, J. K.; Ahmadi, M.; Hu, B.; Ovchinnikova, O. S. Photoinduced Iodide Repulsion and Halides-Demixing in Layered Perovskites. *Mater. Today Nano* **2022**, *18*, 100197. https://doi.org/10.1016/j.mtnano.2022.100197.

(121) Mathew, P. S.; DuBose, J. T.; Cho, J.; Kamat, P. V. Spacer Cations Dictate Photoinduced Phase Segregation in 2D Mixed Halide Perovskites. *ACS Energy Lett.* **2021**, *6* (7), 2499–2501. https://doi.org/10.1021/acsenergylett.1c01015.

(122) Weidman, M. C.; Seitz, M.; Stranks, S. D.; Tisdale, W. A. Highly Tunable Colloidal Perovskite Nanoplatelets through Variable Cation, Metal, and Halide Composition. *ACS Nano* **2016**, *10* (8), 7830–7839. https://doi.org/10.1021/acsnano.6b03496.

(123) Fieramosca, A.; Polimeno, L.; Ardizzone, V.; De Marco, L.; Pugliese, M.; Maiorano, V.; De Giorgi, M.; Dominici, L.; Gigli, G.; Gerace, D.; Ballarini, D.; Sanvitto, D. Two-Dimensional Hybrid Perovskites Sustaining Strong Polariton Interactions at Room Temperature. *Sci. Adv.* **2019**, *5* (5), eaav9967. https://doi.org/10.1126/sciadv.aav9967.

(124) Tsai, H.; Nie, W.; Blancon, J.-C.; Stoumpos, C. C.; Asadpour, R.; Harutyunyan, B.; Neukirch, A. J.; Verduzco, R.; Crochet, J. J.; Tretiak, S.; Pedesseau, L.; Even, J.; Alam, M. A.; Gupta, G.; Lou, J.; Ajayan, P. M.; Bedzyk, M. J.; Kanatzidis, M. G.; Mohite, A. D. High-Efficiency Two-Dimensional Ruddlesden–Popper Perovskite Solar Cells. *Nature* **2016**, *536* (7616), 312–316. https://doi.org/10.1038/nature18306.

(125) Tatarinov, D. A.; Schleusener, A.; Krahne, R. Controlling Energy Flow in Perovskite Heterostructures Through Dimensionality and Phase Engineering. *Adv. Sci.* **2025**, *12* (34), e05971. https://doi.org/10.1002/advs.202505971.
(126) Ziegler, J. D.; Cho, Y.; Terres, S.; Menahem, M.; Taniguchi, T.; Watanabe, K.; Yaffe, O.; Berkelbach, T. C.; Chernikov, A. Mobile Trions in Electrically Tunable 2D Hybrid Perovskites. *Adv. Mater.* **2023**, *35* (18), 2210221. https://doi.org/10.1002/adma.202210221.
(127) Li, J.; Yang, X.; Zhang, Z.; Yang, W.; Duan, X.; Duan, X. Towards the Scalable Synthesis of Two-Dimensional Heterostructures and Superlattices beyond Exfoliation and Restacking. *Nat. Mater.* **2024**, *23* (10), 1326–1338. https://doi.org/10.1038/s41563-024-01989-8.
(128) Yang, H.; Shao, W.; Sun, J.; Kim, J. H.; Lee, Y. H.; Huang, L.; Dou, L. Ligand-Variant Two-Dimensional Halide Perovskite Lateral Heterostructure. *MRS Bull.* **2024**, *49* (8), 771–777. https://doi.org/10.1557/s43577-024-00718-5.
(129) Walsh, K. M.; Smith, R. T.; Gamelin, D. R. Anion Exchange and Lateral Heterostructure Formation in Ferromagnetic PEA2Cr(Cl,Br)4 Two-Dimensional Perovskites. *J. Am. Chem. Soc.* **2024**, *146* (42), 29159–29168. https://doi.org/10.1021/jacs.4c11490.
(130) Borreani, M.; Saini, S. K.; Schleusener, A.; Krahne, R. Direct Growth of Rectangular 2D Layered Metal-Halide Perovskite Microcrystal Photonic Cavities on Functional Substrates. *Adv. Opt. Mater.* **2025**, *13* (27), e01276. https://doi.org/10.1002/adom.202501276.
(131) Wu, S.-C.; Wu, C.-S.; Chien, C.-H.; Zhang, Y.-W.; Yang, C.-X.; Liu, C.; Li, M.-H.; Lin, C.-F.; Wu, Y.-H.; Lin, B.-H.; Chou, Y.-H.; Chang, Y.-C.; Chen, P.; Hsu, H.-C. Carrier–Phonon Interaction Induced Large Negative Thermal-Optic Coefficient at Near Band Edge of Quasi-2D (PEA)2PbBr4 Perovskite. *Adv. Funct. Mater.* **2023**, *33* (25), 2213427. https://doi.org/10.1002/adfm.202213427.
(132) Borreani, M.; Saini, S. K.; Schleusener, A.; Krahne, R. Direct Growth of Rectangular 2D Layered Metal-Halide Perovskite Microcrystal Photonic Cavities on Functional Substrates. *Adv. Opt. Mater.* **2025**, *13* (27), e01276. https://doi.org/10.1002/adom.202501276.
(133) Jang, Y.; Shapiro, A.; Isarov, M.; Rubin-Brusilovski, A.; Safran, A.; Budniak, A. K.; Horani, F.; Dehnel, J.; Sashchiuk, A.; Lifshitz, E. Interface Control of Electronic and Optical Properties in IV–VI and II–VI Core/Shell Colloidal Quantum Dots: A Review. *Chem Commun* **2017**, *53* (6), 1002–1024. https://doi.org/10.1039/C6CC08742F.
(134) Melitz, W.; Shen, J.; Kummel, A. C.; Lee, S. Kelvin Probe Force Microscopy and Its Application. *Surf. Sci. Rep.* **2011**, *66* (1), 1–27. https://doi.org/10.1016/j.surfrep.2010.10.001.
(135) Lin, L.; Jacobs, R.; Ma, T.; Chen, D.; Booske, J.; Morgan, D. Work Function: Fundamentals, Measurement, Calculation, Engineering, and Applications. *Phys. Rev. Appl.* **2023**, *19* (3), 037001. https://doi.org/10.1103/PhysRevApplied.19.037001.
(136) Mathew, P. S.; Szabó, G.; Kuno, M.; Kamat, P. V. Phase Segregation and Sequential Expulsion of Iodide and Bromide in Photoirradiated Ruddlesden–Popper 2D Perovskite Films. *ACS Energy Lett.* **2022**, *7* (11), 3982–3988. https://doi.org/10.1021/acsenergylett.2c02026.

(137) Samu, G. F.; Balog, Á.; De Angelis, F.; Meggiolaro, D.; Kamat, P. V.; Janáky, C. Electrochemical Hole Injection Selectively Expels Iodide from Mixed Halide Perovskite Films. *J. Am. Chem. Soc.* **2019**, *141* (27), 10812–10820. https://doi.org/10.1021/jacs.9b04568.